A MANIFOLD DESTINY: ADVANCING THE FRONTIERS OF THE ADOR PROCESS

Daniel Sean Firth

A Thesis Submitted for the Degree of PhD
at the
University of St Andrews

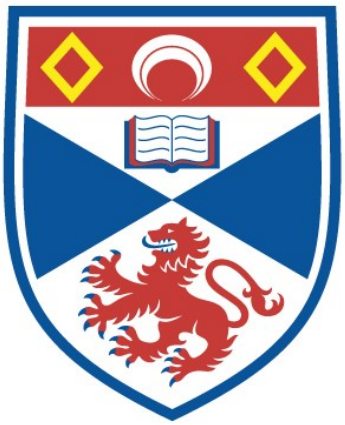

2017

A Manifold Destiny: Advancing the Frontiers of the ADOR Process

By Daniel Sean Firth

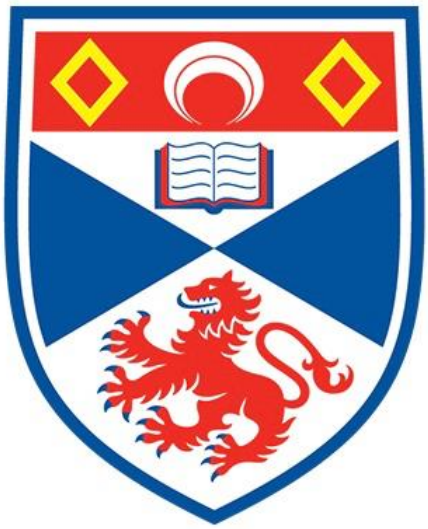

University of
St Andrews

This thesis is submitted in partial fulfilment for the degree of

Doctor of Philosophy

at the

University of St Andrews

Date Submitted: 17 August 2017

Declaration

I, Daniel Sean Firth, hereby certify that this thesis, which is approximately 80,000 words in length, has been written by me, and that it is the record of work carried out by me, or principally by myself in collaboration with others as acknowledged, and that it has not been submitted in any previous application for a higher degree.

I was admitted as a candidate for the degree Doctor of Philosophy in August 2013; the higher study for which this is a record was carried out in the University of St Andrews between 2013 and 2017.

Date: 17 August 2017

Signature of Candidate

I hereby certify that the candidate has fulfilled the conditions of the Resolution and Regulations appropriate for the degree of Doctor of Philosophy in the University of St Andrews and that the candidate is qualified to submit this thesis in application for that degree.

Date 17 August 2017

Signature of Supervisor

In submitting this thesis to the University of St Andrews I understand that I am giving permission for it to be made available for use in accordance with the regulations of the University Library for the time being in force, subject to any copyright vested in the work not being affected thereby. I also understand that the title and the abstract will be published, and that a copy of the work may be made and supplied to any bona fide library or research worker, that my thesis will be electronically accessible for personal or research use unless exempt by award of an embargo as requested below, and that the library has the right to migrate my thesis into new electronic forms as required to ensure continued

access to the thesis. I have obtained any third-party copyright permissions that may be required in order to allow such access and migration, or have requested the appropriate embargo below.

The following is an agreed request by candidate and supervisor regarding the publication of this thesis – everyone has access to the printed and electronic copy of this thesis through the University of St Andrews.

Date 17 August 2017

Signature of Candidate Signature of Supervisor

Courses Attended

The School of Chemistry at the University of St Andrews requires that a PhD student complete a number of taught courses. The courses attended were:

Electron Microscopy – Prof Wuzong Zhou

EaStCHEM Paper Writing Course – University of St Andrews

Thesis Writing Workshop – University of Edinburgh

Powder Diffraction for Materials Chemists – Dr Yuri Andreev

Conferences Attended

6th FEZA Conference in Leipzig, Germany (September 2014)

Post-FEZA Zeolite Workshop in Třešť, Czech Republic (September 2014)

BZA Annual Meeting in Chester, UK (July 2015)

6th International Workshop on Layered Materials in Třešť, Czech Republic (September 2015)

18th International Zeolite Conference in Rio de Janeiro, Brazil (June 2016)

Prizes

Best Postgraduate Poster – Industry Chemistry Forum 2016 (St Andrews)

Best Oral Presentation – Postgraduate Symposium 2016 (St Andrews)

Acknowledgements

First, I would like to thank Russell for taking a chance on me and giving me the opportunity to study under his supervision. Without your support, guidance, and understanding these past four years would have been a far more inferior experience. I would most like to thank you for allowing me to pursue my dream career (not in academia), without which I would not be on the path that I am on now.

I would also like to thank the Morris group, both past and present members, for their help, support, chat (both professional and personal), and the cakes. I would particularly like to thank the ever-present Paul Wheatley for his words of advice (sometimes kind); your guidance, knowledge and solitaire skills have been unparalleled. I would also particularly like to thank Sam Morris, Marta Navarro-Rojas, Yuyang Tian, Laura McCormick, and Matthew McPherson who helped me so much during their time in the Morris group.

I wish all the current PhDs good luck in their respective futures: Giulia Bignami, Samantha Russell, Lauren McHugh, Susan Henkelis and Simon Vornholt. Keep up the good research, the far more superior baking, and try to enjoy a gin or two along the way.

I would also like to thank all the technical staff at the University of St Andrews, in particular Daniel Dawson for his expertise in solid-state NMR and Ross Blackley for his training and knowledge on the SEM/EDX. Special thanks also go to Dr Alvaro Mayoral, from the University of Zaragoza, for the beautiful TEM images he has produced for part of this thesis, the quality of such images has been amazing, despite the low-quality of some samples.

I would also like to thank all the friends I have made in and out of St Andrews, who have made my time here all the more enjoyable. I would particularly like to thank Charlotte Dixon for keeping things fun during our time as undergraduates and postgraduates at St Andrews.

I would like to thank my family for the support and kind words, despite never quite understanding what I've been doing over these past four years. In particular, I would like to thank my mum and dad for their encouragement and support despite being on the other side of the country.

Finally, I would like to thank my partner Halvor whose love and support have made these four years far easier. Your belief in me has helped me achieve things in these four years that I would have never expected.

"Every new beginning comes from some other beginnings end."

Seneca

Abstract

This thesis deals with the various attempts to expand the ADOR (Assembly, Disassembly, Organisation and Reassembly) process. This includes the use of the ADOR process to incorporate new elements into a zeolite framework, the expansion of the ADOR process to other germanosilicate frameworks, and the first ever synthesis of a new ADORable germanosilicate and its subsequent daughters.

Chapter 4 deals with the expansion of the ADOR process to the already known ADORable zeolite **UTL**, using the organisation and reassembly steps to incorporate Al and P, resulting in the formation of a zeolite-AlPO hybrid with distinct silicate layers connected by AlPO based *s4r* linkages. The material was shown to contain Al and P species and was unstable to acidic medium, atypical of the wholly silica zeolite frameworks produced by the ADOR process. MAS NMR studies showed the presence of both tetrahedral P and Al species in the material and that the presence of Si-OH groups was limited. Indicating that the layers had been reconnected with Al and P now present, forming a zeolite-AlPO hybrid. ^{29}Si-enriched materials were synthesised to confirm the presence of P-O-Si bonds, through 2D MAS NMR correlation experiments; however, results were limited due to the lack of signal strength.

Chapter 5 deals with attempts to expand the ADOR process by applying the ADOR process to other already known germanosilicates. It was found that the non-ideal ADORable candidates NUD-1 and ITQ-33 were unable to undergo a controlled disassembly process, primarily due to their high Ge content and distribution of *d4r*/*d3r*. The zeolites ITQ-38 and IM-20 showed more promise. Both could undergo disassembly to form a layered material, which could then be organised and reassembled to form new materials. However, these materials were shown to not form perfect daughter zeolites and had a high degree of disorder. This was associated with the complexity of the ADOR process and the many factors that play a role in each step.

Chapter 6 deals with the use of a family of SDAs (with the same biphenyl backbone) to synthesise new ADORable zeolites. The synthesis of the SDAs and their use in various zeolite syntheses was discussed. The potential of these SDAs for the synthesis of new zeolites was then evaluated. The investigations were relatively successful with the successful formation of an ADORable zeolite, which was already known, **UTL**. However,

the suitability of such SDAs also put into question, due to their instability under hydrothermal conditions.

Chapter 7 discussed the first successful *a priori* synthesis of a parent germanosilicate and its daughter zeolites by the ADOR process. The successful synthesis of an ADORable zeolite (SAZ-1) was conducted with the use of an imidazolium-naphthalene based SDA. Investigations were first conducted into changing the synthesis condition, exploring the impact of these changes on the resulting products, and optimising the synthesis conditions to favour the formation of the new zeolite SAZ-1. These investigations led to the new zeolite framework SAZ-1, which showed similarities to the zeolites NUD-2 and CIT-13, which were developed simultaneously by other institutions. The properties of the SAZ-1 framework were discussed and were found to be highly suitable for the ADOR process. SAZ-1 was then successfully disassembled, organised, and reassembled to form two new daughter zeolites SAZ-2 and SAZ-3. The alumination of SAZ-1P to form aluminated SAZ-2 and SAZ-3 was also attempted. Both zeolites showed an increase in catalytic activity, compared to the typical pure-silica daughter zeolites. The layers of SAZ-1P were also able to undergo the same shifting process as seen for the 'unfeasible' zeolites IPC-9 and IPC-10, but the resultant products were not as ordered as these previous examples. This in addition to the previous work highlighted some of the non-ideal properties of SAZ-1 compared to other ADORable zeolites, like **UTL**.

Publications

Publications Arising from this Thesis

Firth, D. S.; Morris, S. A.; Wheatley, P. S.; Russell, S. E.; Slawin, A. M. Z.; Dawson, D. M.; Mayoral, A.; Opanasenko, M.; Položij, M.; Čejka, J.; Nachtigall, P; Morris R.E. Assembly–Disassembly–Organisation–Reassembly Synthesis of Zeolites Based on cfi -Type Layers. *Chem. Mater*. **2017**, *29* (13), 5605–5611.

Publications Outside the Scope of this Thesis

Shamzhy, M. V.; Eliášová, P.; Vitvarová, D.; Opanasenko, M. V.; Firth, D. S.; Morris, R. E. Post-Synthesis Stabilization of Germanosilicate Zeolites ITH, IWW, and UTL by Substitution of Ge for Al. Chem. - A Eur. J. **2016**, *22* (48), 17377–17386.

Morris, S. A.; Bignami, G. P. M.; Tian, Y.; Navarro, M.; Firth, D. S.; Čejka, J.; Wheatley, P. S.; Dawson, D. M.; Slawinski, W. A.; Wragg, D. S.; et al. In situ solid-state NMR and XRD studies of the ADOR process and the unusual structure of zeolite IPC-6. *Nat. Chem*. **2017**, *9*, 1012-1018.

Table of Contents

1 Introduction

1.1 What are Zeolites?

Zeolites are primarily composed of tetrahedra (TO_4 where the T can be Al and/or Si). Different orientations and arrangements of these tetrahedra lead to different sized cavities and unique frameworks. There are now over 230 unique zeolite frameworks with differing properties that are fundamentally dictated by their structural architecture.[1] These materials have been of interest due to their thermal stability, high surface area and porosity. This has led to their use in many important industrial applications including industrial scale oil refining, automotive catalysis, ion exchange, water purification and as anti-microbial agents for medical purposes.[2]

1.2 Historical Development of Zeolites

Zeolites were first described in 1756 by Swedish mineralogist Axel Fredrik Cronstedt, when he observed, that upon heating a sample of stilbite, large amounts of steam were produced from water that had already been absorbed by the material. The material was hence given the name zeolite, from the Greek *zeo* meaning 'to boil' and *lithos* meaning 'stone'.[3]

1.2.1 Natural Zeolites

Since their discovery by Cronstedt zeolites have been found in many different areas around the globe. At present natural zeolites are used on a several million-tonne scale and their mining has been of great interest. Although there are fifty different varieties of naturally occurring zeolites, only eight make up much of the volcano sedimentary deposits in the world: analcime, chabazite, clinoptilolite-heulandite, erionite, ferrierite, laumonite, mordenite and phillipsite. All these natural zeolites contain the characteristic properties associated with zeolites including low density, high void volume and a high internal surface area.[4,5]

1.2.2 The First Man-Made Zeolites

The initial synthesis of man-made zeolites was based on observations and the analysis of natural zeolites. It was concluded that perhaps the best way of synthesising these interesting materials was to try to replicate the conditions that form them in the natural world.

While there are claims of the synthesis of man-made zeolites dating back to 1862, with the preparation of levynite reported by Henri E. Sainte-Claire Deville.[6] The preparation of

zeolites in a way that would be recognisable to today's researchers was first reported in the late 1940s. Richard Barrer and Robert Milton were the first to report the preparation of zeolites using what is now known as hydrothermal synthesis.[7] Both men used variations of hydrothermal synthesis to produce their zeolites. Barrer investigated the conversion of known minerals with the use of strong salt solutions and moderately high temperatures (170 °C - 270 °C). This resulted in the formation of the first synthetic zeolites, known as species P and Q, that had been previously unknown as natural minerals.[8] Milton was the first to use more reactive starting materials such as freshly precipitated aluminosilicate gels and he used milder conditions.[9] This research would eventually lead to the synthesis of 20 new man-made zeolites by 1953 (14 of which were previously unknown as natural minerals). The first commercial success of synthetic zeolites was achieved in the 1950s as **FAU**-type zeolite was first used in oil refining.[2,7,10]

1.2.3 New Methods and New Frameworks

These initial discoveries led to further developments in the 1960s when Mobil utilised organic cations, including quaternary ammonium ions, to create an even greater variety of new aluminosilicates. These experiments would eventually lead to synthesis of industrially important high silica zeolites such as ZSM-5 (**MFI**) in the 1970s.[10–12] Further developments in the synthesis of zeolites in the 1970s included the use of fluoride as a mineralising agent,[13] which has gained far more prominence in recent years, particularly in aiding the formation of larger crystals and novel structures.[14]

The discovery of the first aluminophosphate molecular sieves (AlPOs) in the 1980s was reported by Flanigen *et al*.[15] This research gained further prominence as such structures were able to incorporate more elements into the AlPO framework leading to many derivatives like silico- and metallo-aluminophosphates (SAPOs and MAPOs).[10] The discovery of AlPOs and their capacity for heterosubstitution led to propositions that much greater varieties of heterosubstitution were also possible for zeolites, than just same-group substitution (with Ga for Al and Ge for Si).[10]

1.2.4 The Search for Bigger Pores

The 1990s led to the use of other organic reagents, such as surfactants, to produce framework materials with uniform mesopores.[16–18] The potential of zeolites with large uniform mesopores and a quasi-amorphous character have since become more prevalent in research activities, with the hope of increasing the size of molecules that can be processed. Research was also started on 2D layered materials, with very different chemical

properties to their 3D framework cousins. The ability to synthesise layered materials also increased the number of framework structures.[19]

Research into zeolite-like materials with larger pores has been aided with the use germanosilicates and silicoaluminophosphates. The range of open structures formed shows the potential of such methods to produce these materials. However the inherent instability of these structures is still a challenge for research into their potential catalytic applications.[11]

1.2.5 The Current Outlook and Horizon

Areas of zeolite research have broadened with interests including: The synthesis of zeolites that can do reactions other than acid catalysed ones. The application of zeolites into areas like sensors, membranes and optoelectrics. The use of molecular modelling has also allowed for a better understanding of the role played by zeolites and their mechanism for molecular selectivity and catalysis of certain reactions. [20]

Since the turn of the century research activity has reached a current level of ~4,200 publications annually and the number of researchers affiliated with zeolite science has greatly increased. The breadth of research into zeolitic materials and their applications clearly shows that the area has come a long way, since Cronstedt heated that first sample of stilbite, and still has an important role to play in society. [11]

1.3 Defining Zeolite Frameworks

1.3.1 Zeolite Nomenclature

According to IUPAC, zeolites are defined as aluminosilicates with open 3-dimensional framework structures. These are composed of corner-sharing TO_4 tetrahedra, where T can be Al or Si. Cations that balances the charge of the anionic framework are loosely associated with the framework oxygens and the remaining pore volume is filled with water molecules.[11] The non-framework cations are generally exchangeable and the water molecules removable. This definition has since been expanded to include T-atoms other than Si and Al in the framework and organic species (cationic or neutral) in the pores.

Each time a new zeolite framework structure is reported the members of the IZA-SC (Structure Commission of the International Zeolite Association) will assign a framework type code, if the framework structure is found to be a unique framework type.[20] If this is the case, then the framework is given a unique 3-letter code. This 3-letter code is written in bold and consists of only capital roman letters derived from the original first material.[1]

For example, the first material to have the unique **UTL** framework type was IM-12. This was the 12th structure discovered by the **I**nstitut Français du Pétrole and University of **M**ulhouse, hence the material code IM-12. The 3-letter code was therefore designated **UTL** derived from M**u**lhouse **t**we**l**ve.[1]

This three-letter framework type code denotes only the framework type and does not indicate chemical composition, distribution of T-atoms, cell dimensions or symmetry. For example, the framework type **LTA** has 15 related materials listed on the IZA website, these include such examples as Linde Type A, ZK-4, SAPOs-42 and [Ga-P-O]-LTA, which all differ from each other chemically but have the same framework type.[1]

1.3.2 Primary Build Units

As discussed previously zeolites and are made of TO_4 tetrahedra (where T can be generally aluminium or silicon). These tetrahedra are arranged such that the T atom is in the centre surrounded by oxygens on each of the four corners of the tetrahedron. These are often defined as the primary build units (PBUs). By then linking these tetrahedra together it is possible to build larger structures, including channels, rings and secondary build units (SBUs).[21]

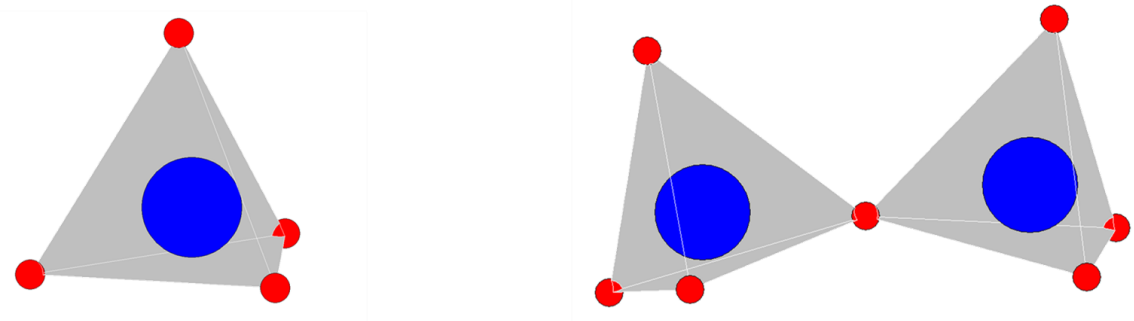

Figure 1.1 shows the typical primary building unit (left) consisting of the tetrahedron with a central T atom (blue) surrounded by oxygens at each corner (red) and how these PBUs connect through corner sharing oxygens (right).

1.3.3 Secondary Build Units

When discussing zeolites frameworks, it has often been more useful to describe the overall structure with the use of finite (secondary build units and composite build units) and infinite (chains, layers etc.) component units. Secondary building units (SBUs) can contain up to 16T atoms and are non-chiral. Every unit cell of a zeolite contains the same number of SBUs and some may have different combinations of SBUs within the zeolites framework.[22] Examples of some typical SBUs are shown in Figure 1.2.

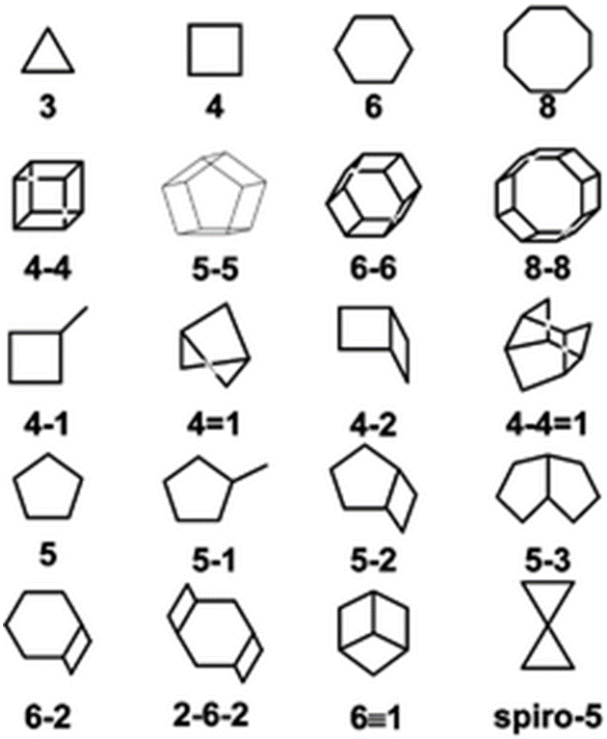

Figure 1.2 Shows examples of SBUs typically used to describe zeolite frameworks adapted from reference 23.

An important SBU is pentasil which is made from five-membered rings and is important in the framework of ZSM-5 one of the most used zeolites in the oil industry, particularly for use for hydrocarbon isomerisation. The finite pentasil SBU consists of eight five-membered rings joined together (Figure 1.3). These can then be linked together to form pentasil chains. These chains can then be interconnected by oxygen bridges to form ZSM-5 as shown below.

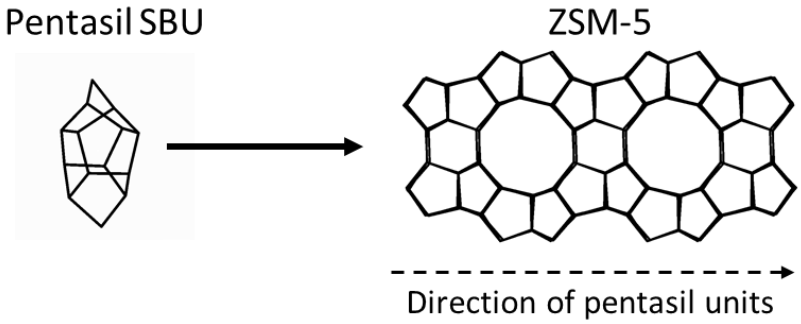

Figure 1.3 Shows the pentasil SBU (left) and the ZSM-5 framework, which is made from chains of pentasil SBU that are linked together by oxygen bridges, resulting in 10 ring channels between each pentasil chain. Each corner represents a T atom, oxygens are omitted for clarity.

The use of SBUs to describe frameworks has recently gone out of favour when describing frameworks as the number of SBUs started to increase and frameworks required more complicated combinations of SBUs to be completely defined.

1.3.4 Composite Build Units

The decline of SBUs lead to the use of CBUs and tiling schemes to define frameworks. CBUs differ from SBUs as they are not required to be achiral, can contain more than 16 T atoms and cannot always be used to build the entire framework. CBU units (like *d6r,* cancrinite and sodalite cages, and alpha cavities) appear in several different framework structures.[24] These can therefore be used to help better show the relationship between different but similar framework types. Extensive lists of CBUs have been compiled for known and hypothetical CBUs.[25,26] CBUs are typically assigned a three-character italic code and includes former SBUs like *d4r* and *d6r* as well as larger units *lta* and *clo* (Figure 1.4).[22]

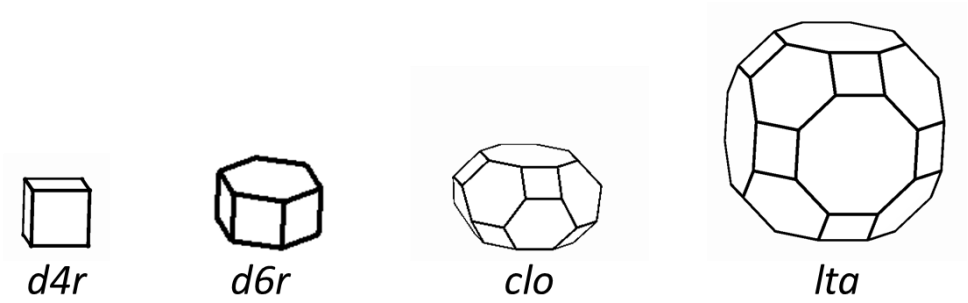

Figure 1.4 Shows some example CBUs including former SBUs (*d4r* and *d6r*) and new CBUs (*clo* and *lta*). Corners represent T atoms, oxygens omitted for clarity.

1.3.4.1 Using CBUs to Define a Zeolite Framework

In the example in Figure 1.5 zeolites sodalite (**SOD**), Linde type A (**LTA**), Faujasite (**FAU**) and **EMT** can be formed using the β-cage (or *sod* CBU). The *sod* consists of four-membered rings and six-membered rings in its structure. By fusing together, the square faces sodalite (**SOD**) is formed and is a well-known zeolite that occurs in nature. By bridging the square faces of the *sod* Linde type A (**LTA**) is formed. **LTA** does not occur in nature but is produced industrially on a large scale for use in ion exchange, gas separation etc. By bridging the six membered rings of the *sod* **FAU** or **EMT** can be formed, depending on the orientation of the *sod* SBUs to the next. **FAU** is formed by stacking the puckered sod layers so that they are related to one another by inversion. This stacking sequence can be described as ABCABC. This means the orientation of the *sod* in FAU is similar to the orientation of carbon atoms in diamond. The faujasite structure has large channels and voids and thus is useful in catalysis and as molecular sieves as its large microporous spaces allow for organic molecules to diffuse in and out, the most important use of this zeolite is in the cracking of large hydrocarbons into shorter chain length molecules. In contrast, **EMT** is formed by stacking the puckered *sod* layers in an ABAB sequence so that the layers

are related to each other by a mirror plane. This does not form a regular 3D net and so is less desirable for catalysis.[21]

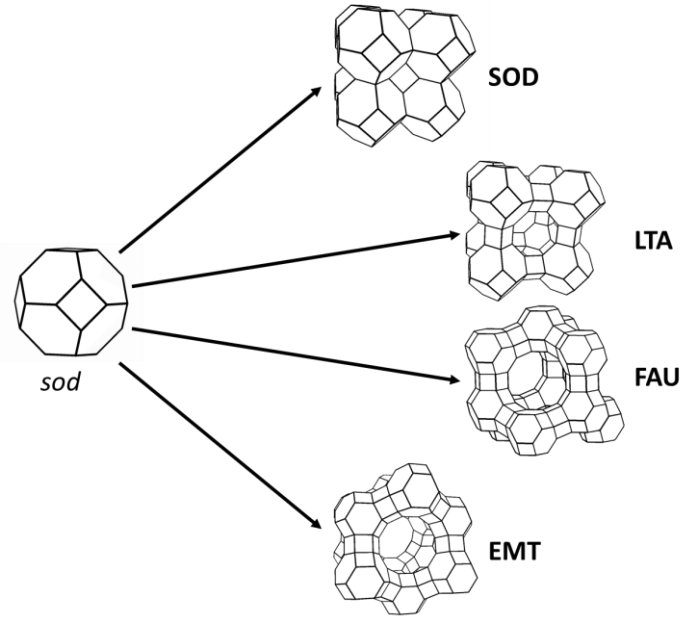

Figure 1.5 Shows the *sod*/β-cage CBU (left) made from *s4r* and *s6r* SBUs and the different frameworks possible by changing the connectivity of the β-cages. Direct fusion of the *s4r* results in SOD, bridging the *s4r* results in LTA and bridging of the *s6r* results in FAU and EMT. Where FAU and EMT differ depending on the orientation of opposite *sod*. Corners represent T atoms, oxygens omitted for clarity.

1.3.5 Zeolite Porosity

One of the key properties of zeolites is their porosity. The different frameworks, consisting of different combinations of SBUs and CBUs means that there is a large array of unique frameworks, with different pore sizes and channel systems. A zeolite's usefulness in certain applications is often determined by the pore size/topology of the framework.

Figure 1.6 Shows how the size of pores present in a zeolite increase with the increasing number of T-atoms. From small pore LTA (left), to medium pore FER (middle) and large pore SAF (right). T-atoms shown in blue, oxygens shown in red.

Most zeolites are microporous. This means that they have accessible pore openings smaller than 2 nm. Zeolites with accessible pore openings larger than 2 nm are defined as mesoporous. The pore openings are typically described as a function of T-atoms, where a pore consisting of 12 atoms (6 T atoms and 6 oxygens) is defined as a 6-ring pore. Zeolites

are typically described in terms of small, medium and large pore; depending on the number of T-atoms circumscribing the pore (Figure 1.6).[27] Small pore zeolites like **LTA** have pores made up of 8 T-atoms and a 0.4 nm diameter. Medium pore zeolites like **FER** have pores made up of 10 T-atoms and a 0.55 nm diameter. Large pore zeolites like **SAF** have pores made up of 12 T-atoms and a 0.75 nm diameter. Ultra-large pore zeolites typically consist of pores made up of more than 12 T-atoms. Assuming perfectly cylindrical pores zeolites can have a pore made of up to 20 T-atoms. After this the pore becomes larger than 2 nm and so according to IUPAC rules cannot be defined as a zeolite. An example like MCM-41, which although well ordered, should technically be referred to as a mesoporous ordered material and not as a zeolite.[16]

If these pores run through the zeolite structure, then this can be described as a channel. Channels are defined by their ring size and are typically straight, but zigzag channels are also known. The nature of the channel system can have a large impact on the reaction by limiting the rate of diffusion of molecules into/out of the zeolite. Channel systems are typically defined based on their interconnectivity. If all channels run parallel with each other and do not interconnect this creates a 1-Dimensional channel system, if channels interconnect in two directions this creates a 2-Dimensional channel system and if channels interconnect in all 3 directions then this creates a 3-Dimensional channel system.

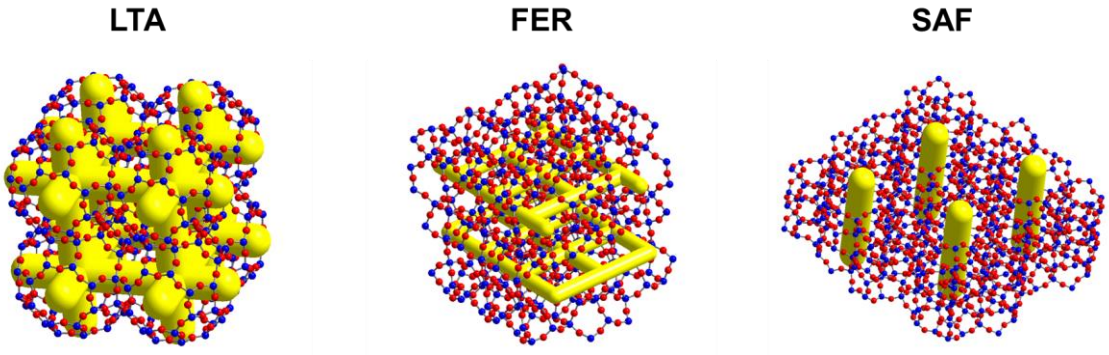

Figure 1.7 Shows the three zeolites LTA, FER and SAF with their channels highlighted in yellow. This shows that while the channel sizes increase in size from LTA < FER < SAF, the dimensionality of the channel systems decreases as LTA > FER > SAF.

This means that although **SAF** has a bigger channel size than **LTA,** the presence of a 1D channel system may make it unfavourable for applications due to the lower rate of diffusion of molecules. By comparison, **LTA** has smaller channels, but the 3D channel system makes the rate of diffusion within the structure faster (Figure 1.7).

1.4 Applications of Zeolites

Zeolites are used in a wide range of applications, with some being used on a multi-tonne scale. The main applications of zeolites fall into three categories: ion exchangers, molecular sieves, and catalysis (Figure 1.8).[2]

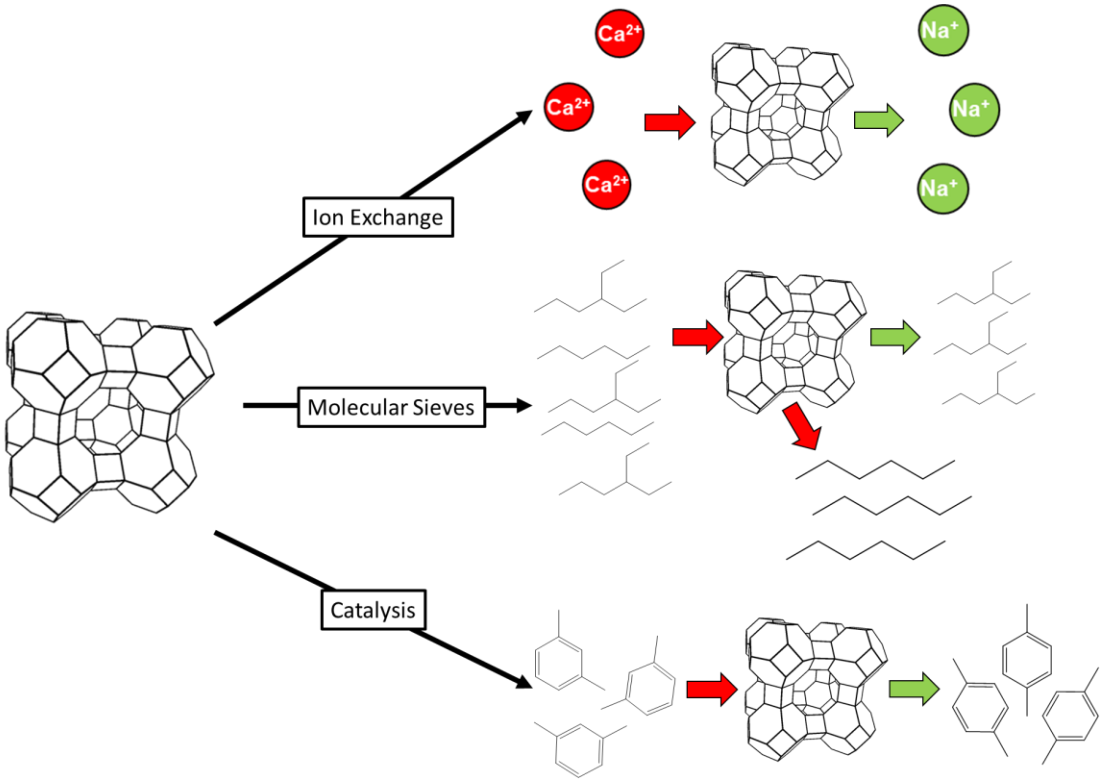

Figure 1.8 Shows the three main applications of zeolites and a schematic example of this application. Ion exchange (left) where Ca^{2+} ions are exchanged for Na^{+} ions already in the zeolite. Molecular sieves (middle) where branched- and straight-chain alkanes can be separated from each other as bulkier branched alkanes cannot pass through the zeolite pores. Catalysis (right) where zeolites can catalyse the isomerisation of meta-xylene to para-xylene.

The various applications that zeolites have found is down to their tunability. Through the synthesis of different zeolites and their post-synthesis modifications, it is possible to produce zeolites with different chemical compositions and framework properties fully optimised for the desired application.

The largest application (although reducing) of zeolites is as ion exchangers in detergents and washing powder.[2] By replacing silicon in the zeolite with aluminium a negative charge is introduced to the framework. This charge is then balanced out by the material incorporating inorganic cations like sodium. These cations are loosely bound and so can be exchanged for other cations. During ion exchange, the sodium cations in the zeolite exchange out of the framework to replace the calcium and magnesium ions present in 'hard' water thereby softening it.[11] Previously the removal of hard water ions used

environmentally damaging phosphates.[28] The ion exchange properties of zeolites have been exploited further in applications such as for cleaning-up nuclear waste, for example after the Fukushima disaster, sandbags containing zeolite were dropped into the seawater near the power plant to adsorb radioactive caesium.[29]

Zeolites are often called "molecular sieves". This is because there are many industrially available zeolite frameworks, each with unique pore size and channel systems. By choosing a specific zeolite and therefore channel system, it is possible to sort molecules from a mixture based on size exclusion, as the channel system contains very regular pore structures and channels. This limits the size of molecules that can pass through the channels. This is used on an industrial scale for the separation of more valuable branched hydrocarbons from straight chain alkanes.[30]

The acid derivatives of zeolites (H-zeolites) are also widely used in industrial catalysis. These acid catalysts can adsorb molecules into their channels and cavities, to then catalyse reactions, like dehydration and rearrangement, that would typically require strong acids.[30] The leading commercial processes where zeolites are used for catalysis is in Fluid Catalytic Cracking (FCC) and Hydro-Cracking (HC). The ability for a zeolite to simultaneously catalyse reactions and act as a molecular sieve allows for the introduction of reactant, product and/or transition state selectivity into the process. This means that the zeolite can either selectively adsorb only certain reactants, release only certain products from their structure, or limit the intermediates that can be accessed during a chemical reaction at the active site.

The application of zeolites is even wider with zeolites being used in concrete, soil conditioners, nutrient release agents in horticulture, odour control agents in cat litter, heat storage and the removal of NO_x from car exhausts.[31]

1.4.1 NO Delivery

The use of zeolites for the removal of nitric oxide from emissions is very important for improving air quality, particularly in areas with high congestion. This reason usually leads to the impression of NO as a toxic and 'bad' molecule.

However, it has been shown that low concentrations of NO play an important role in the body and has a variety of functions. The Nobel Prize in physiology or medicine was awarded to Furchtgott, Ignarro and Murad for their work identifying NO as a signalling molecule in the cardiovascular system.[32] NO has also been shown to play a role in relaxing

the arteries,[33] inhibiting platelet aggregation,[34] and show antibacterial properties.[35] NO is produced in the body through a two-step oxidation of L-arginine, facilitated by the enzyme nitric oxide synthase (NOS), to produce NO, water and L-Citrulline.

The delivery of NO has been investigated with the use of Co-exchanged zeolites as they are able to store NO and then release it upon contact with water. However Cu-exchanged zeolites, traditionally used for the removal of NO, have been shown to produce NO at lower tempertures.[36] Recent work by Russell *et al.* have shown the potential for Cu-exchanged zeolites to catalytically produce NO.[37] Where the Cu(I) in the framework reacts with nitrite to produce NO. After this reaction, the Cu(I) is reduced to Cu(II), which can then be re-oxidised back to Cu(I) in the presence of cysteine, regenerating the catalyst. As nitrites and cysteine are naturally present in the blood, this research could have the potential to lead to the zeolites being used in stent coatings to prevent stent thrombosis.

1.5 The Synthesis of Zeolites

The synthesis of new zeolite framework structures is of interest for those involved in the field. New topologies and chemical compositions will give rise to different activities and the roles that these materials might be able to play in differing applications. To synthesise new materials, it therefore imperative to have a full understanding of the many factors that can affect the synthesis. Since the first synthetic procedures performed by Barrer in the 1940s, where he tried to replicate the conditions under which natural zeolites are formed,[8] this understanding has only increased.

The mechanism for zeolite crystallisation is complex, however a typical zeolite crystallisation follows these key steps:

1. A mixture of amorphous reactants containing structure forming ions is placed in a usually basic medium. This leads to the formation of a heterogenous, partly reacted phase, referred to as the primary amorphous phase (varying between gel-like and colloidal in appearance).
2. Heating of the reaction follows (the reaction mixture may also be aged beforehand).
3. A secondary amorphous phase is formed at pseudo-equilibrium with a solution phase. This phase contains some short-range order due to structuring effect of cations in solution.
4. After an induction period the formation of nuclei takes place.
5. The growth of the zeolite continues at the expense of the amorphous solid.[38,39]

The knowledge of the crystallisation mechanism and of the roles played by the many factors in the synthesis has increased dramatically and so led to the discovery of new frameworks. Whether it has been the use of new more complex organic structure directing agents or the use of hydrofluoric acid to produce a fluoride route, researchers have advanced the field greatly in the past 60 years. The synthesis of new structures is influenced by many factors including gel composition, pH, temperature, digestion time, and starting materials (including the cations present).[40]

1.5.1 Batch Composition

One of the most important factors in zeolite synthesis is batch composition. Early work by Breck showed the impact of different batch compositions. Based on a Na_2O-Al_2O_3-SiO_2-H_2O system zeolites A (**LTA**), X (**FAU**), Y (**FAU**), B (**ANA**) and HS (**SOD**) were obtained in different regions (Figure 1.9), with two phases possibly co-existing in boundary regions. Breck also showed that reducing the water content to 60-85% resulted in solely zeolite HS (**SOD**) being obtained. Meanwhile exchanging sodium silicate for colloidal silica showed a different phase selectivity for **LTA**, and zeolites X and Y, while also introducing two new phases: zeolites R (**CHA**) and S (**GME**).[41]

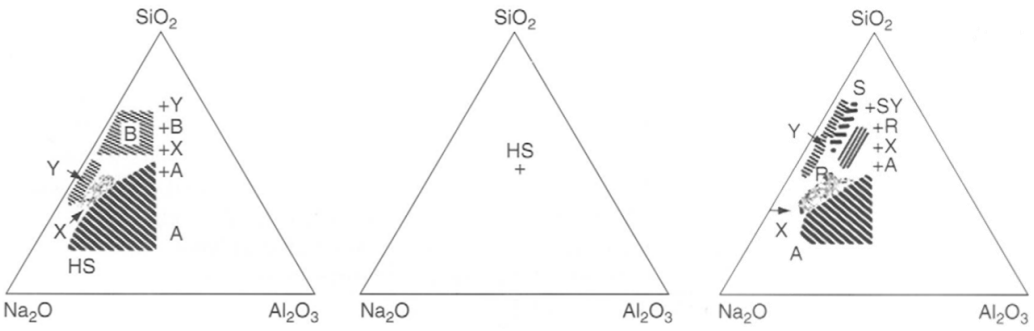

Figure 1.9 Shows reaction composition diagrams. Indicating the areas where a particular zeolite phase (with the corresponding letter) was synthesised. The + shows the typical chemical composition of the zeolite phase obtained (mol %). Left shows Na_2O-Al_2O_3-SiO_2-H_2O system at 100 °C with H_2O content of 98-100 mol%. Middle shows the same system as left but with the H_2O content of 60-85 mol%. Right shows the same system as left but with colloidal silica as the silica source. Taken from reference 41.

This clearly shows the impact different batch compositions can have. However, batch composition may include many more parameters like: the organic templating agents used, the heteroatoms present, the alkalinity of the composition, the type of mineralising agent used and solvent. The interplay of all these actors would come under the term 'batch composition'. However, for clarity it is better to talk about the specific impact of these factors individually.

1.5.2 Structure Directing Agents

Since the use of inorganic cations as structure directing agents (SDAs), the field has expanded greatly as their role in zeolite synthesis has been more fully understood. The role of SDAs is to aid in the directing of the condensation of the gel, through favourable interactions with the condensing nuclei and aid the formation of the metastable zeolite framework instead of more stable denser phases.

1.5.2.1 What are SDAs?

As described previously the first SDAs were inorganic metal hydroxides like NaOH, which are similarly present in the natural synthesis of zeolites. Current syntheses involve the use of organic SDAs like amines, ammonium and phosphonium cations. Work has been conducted to understand the chemistry in the building-up process of zeolite frameworks,[42–44] the mechanism behind the directing nature of these SDAs is still not wholly understood. The role played by the SDA can vary, with several terms being used interchangeably, sometimes incorrectly. Lobo *et al.* suggested that SDAs can be described as 'space filling agents', 'structure directing agents' and 'true templating agents':[45]

Firstly 'structure directing agents', now often used as a collective term, is defined by Lobo *et al*. as an additive; whose presence is required to direct the synthesis to a specific product, whose formation is impossible with another additive, but is not necessarily unique. The interaction between the SDA and the framework is typified as 'host-guest interactions' through Van der Waals interactions. This leads to a framework that tends to correlate with the size and shape of the SDA used. By comparison, the other two terms 'true templating agents' and 'space filling agents' describe a role played by the SDA that is more well-defined.

'True templating agents' originally referred to the role played by the alkali cations in earlier syntheses and their role in the formation of the smaller cage structures in the final zeolite. This has since been expanded to include organic cations whose shape, size and electronic configuration is replicated within the zeolite structure. To date there have been very few examples of true templating agent syntheses. The only example confirmed at the time by Lobo *et al*. was the use of a specific triquat molecule to synthesise ZSM-18 (**MEI**) by Lawton *et al* (Figure 1.10).[46] This is deemed a true templating agent as the triquat is prevented from not only translational deviation, typical of other SDAs, but also rotational by the guest-host interaction with the framework. More recent research by Pinar *et al*.

showed that pyrrolidine also behaves as a 'true templating agent' in the formation of **FER**.[47]

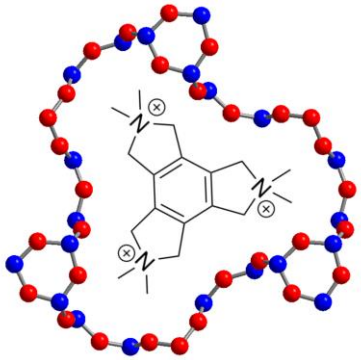

Figure 1.10 Shows the 'true templating' nature of the triquat molecule where the SDA is almost perfectly encapsulated in the pore of the ZSM-18 framework (T-atoms shown in blue, oxygens in red).

In contrast to these 'true templating agents', 'space filling agents' typically occlude themselves into the zeolite structure, stabilising the structure, but have no specific templating interaction within it and hence have no specific impact on the final structure produced. This means that many different SDAs can lead to the same structure, for example ZSM-5 can be formed by at least 22 different organic SDAs. Other frameworks that can also be synthesised using a variety of SDAs include ZSM-48, ZSM-12 and zeolite beta.[45,48] It has also been noted that one SDA can also lead to the formation of several different frameworks depending on the synthesis conditions. For example the tetramethylammonium cation is known to form at least 17 different framework structures.[40]

A lot of work has been conducted to ascertain the full nature of the relationship between the SDA size and shape, and the product framework. Early work by Gies *et al*. using silica, water, and organic molecule systems showed a correlation between molecule size and cage size; with larger molecules producing larger cages and smaller molecules smaller cages.[49] Another observation was the link between cage size and temperature, as they found that with some SDAs the size of the cages increased with higher temperatures. It was suggested that this could be linked to the higher thermal motion of the molecule, leading it to require more space to be occluded into the framework. These early assessments were summarised by Lobo *et al*. who linked the structure directing abilities of molecules to several factors including: 1) The molecule must have room within the particular cage of the clathrasil. 2) The guest compound must be stable in the presence of water under synthesis conditions. 3) The guest compound should fit the inner surface of the cage with

as many van der Waals contacts as possible without deformation. 4) The tendency of the guest substance to form complexes in solvent should be weak; those molecules with higher stiffness will tend to form a clathrasil. 5) The tendency to form a clathrasil will increase with basicity or polarisability of the molecule.[50]

Further analysis by Zones *et al*. investigating the relationship between the size (or C+N number) of quaternary ammonium molecules and their selectivity for a specific framework.[51] Their work showed that as a molecule increased in size they generally became more selective, as larger molecules placed more stringent requirements on the framework; to provide enough room for the molecule and provide favourable van der Waals interactions. These requirements can then be maximised by increasing the rigidity of the SDA, limiting the number of favourable van der Waals interactions, as a more flexible molecule can achieve a greater number of conformations decreasing its selectivity. Despite these advances, it is hard to not argue that these trends are more generalisations as it is still impossible to directly infer the efficiency of a specific compound as a templating agent for a specific framework strucuture.[52]

In a similar manner, the use of heteroatoms and mineralising agents like fluoride could also be described as structure directing agents as, for example, germanium and fluoride are both known to direct the formation of *d4r*-containing frameworks.[53,54]

1.5.3 Heteroatoms in Zeolites

While zeolites have included primarily aluminium and silicon the heteroatomic substitution of such zeolites has occurred frequently, as many seek to explore the properties that the addition of such atoms could yield.

1.5.3.1 Aluminium

The incorporation of aluminium into zeolites has a long and varied history with many frameworks producing a large array of Si/Al ratios. Examples like zeolites X/Y can exist in their high silicate and high aluminate forms.[1] The inclusion of aluminium into the zeolites structure has two major effects.

1.5.3.1.1 Defects or Lewis Acid Sites

One of the interesting properties of aluminosilicates is the formation of defects in the framework. SiO_4 units are neutral while AlO_4 units are negative, which results in the zeolite framework being negatively charged. This negative charge needs to be balanced. The presence of extra-framework species, such as the organic SDA cations, usually aids this. Without the presence of a charge balancing agent in the synthesis this often leads to

the formation of defects in the zeolite, as the zeolite structure compensates for the negative charge. This leads to the formation of Lewis acid sites (Figure 1.11), which can help to add to the catalytic ability of the zeolite.[55]

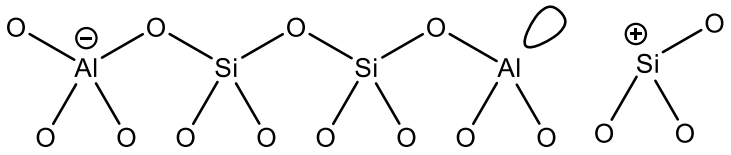

Figure 1.11 Shows a schematic representation of a Lewis acid site, where the negative charge of the AlO_4 unit results in the formation of a positive charge on the silicon, resulting in a defect site.

1.5.3.1.2 Brønsted Acid Sites

The presence of this net negative charge into the zeolite framework can also be compensated for by the incorporation of protons through ion exchange. The binding these protons to the lone pairs of bridging oxygens neutralises this negative charge and forms Brønsted acid sites (Figure 1.12).

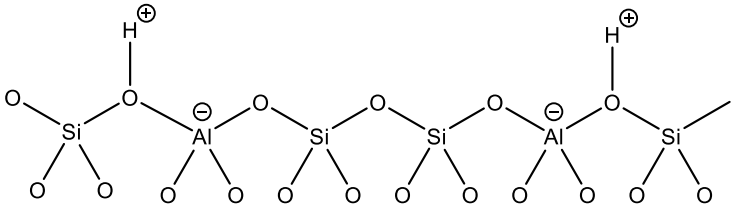

Figure 1.12 Shows a schematic representation of Brønsted acid sites, where the negative charge of the AlO_4 is counteracted by the addition of a proton to the lone pair of a bridging oxygen.

These acidic sites play a major role in the zeolite's catalytic activity and the framework becomes more hydrophilic due to this increase in charge. Another interesting feature of aluminium based zeolites frameworks is the lack of Al-O-Al bonds in the framework. This is explained by Löwenstein's avoidance rules, which explains that the oxygen bridge between two aluminium ions only has stability when at least one of the aluminium atoms has the enhanced coordination of five or six rather than 4. Therefore, in a zeolite framework consisting of tetrahedra no two aluminium ions can occupy the centres of the tetrahedra linked by one oxygen bridge. This further explains the fact that in all known cases when substituting silicon with aluminium the maximum substitution is only 50%.[56] Although recent literature has called into question Löwenstein's avoidance rules in some zeolite frameworks.[57]

1.5.3.2 Phosphorus in Zeolites

The presence of phosphorus in zeolite frameworks was first achieved through the formation of the first AlPOs. AlPOs have a similar framework structure to traditional

zeolites, with tetrahedral AlO_4^- and PO_4^+units bound together through corner sharing oxygens. The need for charge balancing leads to the formation of a zeolite framework with a 1:1 ratio of Al to P. There are over 50 phosphate containing structures recognised by the IZA, some of which are not known in their zeolite analogue forms.[58]

SAPOs consist of Al, P, and Si tetrahedra together in the same framework. This means that they have the properties of both zeolites and AlPOs. The structure can be thought of as and an AlPO with Si substituted into the framework. The substitution of Si into the framework avoids the formation of unfavourable bonds like P-O-P, P-O-Si and Al-O-Al. Si is therefore only incorporated into the SAPO structure in two ways: either into a hypothetical P site or five Si are incorporated into one hypothetical Al site and four hypothetical P sites. This can alternatively be described as a combination of the replacement of an Al-P atom pair and the three P atoms surrounding the replaced Al.[15,59–61] It is believed that the ability to easily make and break bonds during hydrothermal synthesis means that unfavourable P-O-Si bonds are avoided.

The distribution of Si in SAPOs has an impact on the number of acid sites and the catalytic activity of the framework. It is assumed that by increasing the amount of Si the number of acid sites will increase. However, these acid sites are weak as Si with more Si nearest neighbours will have a greater electronegativity and stronger acid sites. The inability to control the distribution of Si in SAPOs also leads to the formation of larger silica islands, where Si surround the internal Si and so no acid sites are formed. To maximise the acidity and catalytic activity, it is therefore desirable to increase the amount of Si while also minimizing the size of the Si islands.[62] This has been achieved with the use of mineralising agents to slowly release silicate into the synthesis gel during crystallisation.[63]

1.5.3.3 Germanium in Zeolites

The use of germanium has yielded the formation of several new framework structures. The fact that Ge and Si are in the same group on the periodic table suggests that they have similar chemistry and so Ge can be substituted into the framework for Si. However, the subtle differences between Ge and Si lead to certain nuances that makes Ge advantageous for the synthesis of new frameworks. The larger size of the Ge atom leads to a smaller Ge-O-Ge angles (≈130°) compared to Si-O-Si angles (≈146°). This allows for Ge to compensate for the additional strains present in *d4r* and *d3r* thereby stabilising frameworks that contain these SBUs.[53,64] The use of GeO_2 in syntheses has led to the formation of many new zeolite frameworks containing *d4r*, with lower framework densities, extra-large pores,

and large pore openings. The use of GeO_2 has also led to the formation of the first zeolites with *d3r*, which have even more strain present (ITQ-49 and ITQ-44).[65,66]

The presence of high levels of Ge also leads to increased thermal instability, due to the hydrolytically unstable Ge-O-Ge bonds, so some germanosilicates are unable to undergo calcination without prior modification. Also, the susceptibility of Ge to hydrolysis means that most of these structures, even uncalcined, are unstable in air and will breakdown over time. Such disadvantages, along with the higher price of GeO_2, means that the use of germanosilicates (or materials derived there from) in industrial processes is severely limited. Interest has increased in post-synthesis isomorphous substitution of the Ge in the framework structures for other elements like Si and Al.[67,68]

1.5.4 Mineralising Agents

A mineralising agent aids zeolite crystallisation through the dissolving of polymeric silicate anions into suitable monomeric/oligomeric anions. Without this ability to form and hydrolyse T-O-T bonds, introducing reversibility, fractal structures are formed.[41,62]

1.5.4.1 The Hydroxide Method

Most aluminosilicate zeolites are synthesised under highly alkaline conditions where OH^- acts as the mineralising agent. Increasing the alkalinity of the system typically leads to the increased solubility of Si and Al sources, decreases the polymerisation rate of silicate anions, and accelerates the polymerisation of the polysilicate and aluminate anions. This means that the increase in alkalinity often leads to an shorter induction and nucleation periods, due to the greater concentration of reactants in solution, leading to a shorter synthesis time.[69]

The hydroxide concentration also plays a role in controlling the alumina/silica ratio in zeolites. A higher pH often leads to a higher alumina content due to silicon's higher solubility in alkaline solutions compared to aluminium, preventing the silica condensing and oligomerising. If the concentration of hydroxide is too high it can also lead to lower yields, or even no zeolite formation as the silica species remain in solution.[62]

1.5.4.2 The Fluoride Method

The introduction of fluoride created a new avenue for the synthesis of zeolite frameworks. Since it was first reported by *Flanigen et al.* in the late 1970s,[13] the use of fluoride has led to a huge expansion in the number of, particularly large-pore, zeolite frameworks.

Fluoride's role as a mineralising agent is particularly important in high silica based syntheses where the reaction gel has a pH lower than 10-11. Fluoride is particularly noted for forming more homogeneous and larger crystalline products. This is thought to occur because nucleation is suppressed by the efficient cleavage of T-O-T bonds and due to the formation of T-F species, producing fewer ordered sites. This causes slower crystal growth kinetics and nucleation promoting larger crystalline phases. This effect is clearly seen in the work of Kuperman *et al*. who produced crystals between 0.5 and 4 mm using this low pH fluoride route.[70]

d

The replacement of OH^- with F^- results not only in a decrease in pH and the slowing of crystal growth but also results in the inclusion of F^- in the zeolite framework. The inclusion of fluoride allows for the formation of pentacoordinated SiO_4F^- species. This imparts a negative charge to balance the cationic template charge, decreasing siloxy defects. This has allowed the formation of all silica zeolites like pure Si **MFI**.[71] F^- has also been shown to play a key role in the stabilisation of *d4r* as the F^- is incorporated and resides in the centre of *d4r* units. This is particularly observed in frameworks that have no charge or when the charges are autocompensated.[71–73]

Due to fluoride's ability to direct small cage units like *d4r* its use has led to the formation of more open, low density frameworks like that obtained using germanium, boron, and aluminium in higher alkaline conditions. This is thought to be helped by the production of highly negative fluorosilicate ion concentration which increases the amount of SDA required to balance out the charge and so increases the void space of the framework due to the increased SDA space filling required.[74]

1.5.5 Solvent

The synthesis of crystalline materials can take place in the solid- or solution-state. However as solid-state requires high temperatures to facilitate the reactants and favour the thermodynamic product this is avoided for zeolite synthesis.

Most zeolite syntheses therefore take place in solution as this facilitates the transport of reactants, while allowing for the kinetic product to be formed. The most common method for zeolite synthesis is hydrothermal synthesis or the use of water. While water is the most common solvent, other solvents have been pursued including alcohols, hydrocarbons, and

pyridine with varying degrees of success. All methods involve the use of these solvents to produce autogenous pressure at elevated temperatures.[75]

1.5.5.1 Low Water Synthesis

Typically, zeolite synthesis has involved ratios of $H_2O:SiO_2$ >25 to facilitate the homogenisation of the reaction gels. The synthesis of high silica zeolite beta was achieved by Corma *et al* with the use of fluoride, a lower water concentration in the synthesis gel (typically $H_2O:SiO_2$ <10), and no seeds.[76] Until this point low framework density zeolites had only been achieved with the use of high aluminium content. More and more low framework density zeolite have now been produced using these methods.[71] The effect of water content has been investigated with some syntheses producing very different frameworks when the water content is varied. A general trend observed is that decreasing the $H_2O:SiO_2$ ratio leads to a lower framework density.

1.5.5.2 Ionothermal Synthesis

The search for new materials led to the questioning of the use of hydrothermal and solvothermal synthesis. The use of ionic liquids was pursued to impart particular properties on the synthesis, particularly the lack of autogenous pressure. The similarity between SDAs and ionic liquids also suggested the potential for ionic liquids to act as templates as well as solvents.[77] It was believed that by using solely ionic liquids in the synthesis of zeolites the impact of competition between the solvent and the template could be removed, thereby increasing the templating effect of the organic used (the ionic liquid). The use of ionic liquids has led to the synthesis of new interesting structures including the SIZ-*n* series of aluminophosphates and silica-based zeolites.[75]

1.5.6 Nonconventional Zeolite Synthesis

Even with an understanding of the role of various elements of hydrothermal synthesis, the process persists to have an unpredictable tendency, with planned hydrothermal syntheses never always leading to the exact intended product. It has therefore become more desirable to add more control to the synthesis using different methods.

1.5.6.1 Two Dimensional Zeolites

One method that has been pursued in the last two decades is the use of larger building units, to limit the number of possible products resulting from crystallisation. Interest in the use of 2D layered precursors began in the 1970s with research into the insertion of aluminium pillars into 2D layered smectite clays.[78,79] It was later found that during the synthesis of some 3D zeolite frameworks a 2D layered precursor was formed and could be

isolated as a stable solid. The first such case that was identified was for the 3D structure **MWW** and was designated MCM-22(P).[80] This 2D layered precursor was then used to form the first pillared zeolite MCM-36, with a high-activity, micro/mesoporous composite. However, such materials could not be considered 'true' zeolites as they do not contain fully coordinated tetrahedra.

It was found that by condensing these 2D precursors topotactically it was possible to form their 3D true zeolites counterparts.[81] This was first achieved through the calcinations of preFER and MCM-22(P) to produce **FER** and **MWW** respectively.[19,82,83] Such layered materials could also be manipulated with other organic molecules and silicon alkoxides to form other 3D zeolites like **CDO** from preFER.[84]

The synthesis of 2D layered zeolites has been achieved in 3 main ways. 1) By direct solvothermal preparation similar to traditional hydrothermal synthesis, but for unknown reasons produces a layered material instead of its 3D analogue, possibly due to low aluminium content and other factors.[85,86] 2) The use of surfactant style SDAs, consisting of a charged ammonium templating 'head' and a long hydrocarbon 'tail' helping to suppress the formation of the framework in a particular direction.[87,88] 3) The ADOR process, which will be discussed in far more detail in Section 1.6.

The use of 2D layered materials has led to a plethora of new methods for preparing interesting structures including layered disordered and ordered assemblies, self-supported layers and self-pillared materials,[89] as well as the synthesis of several 3D zeolites.

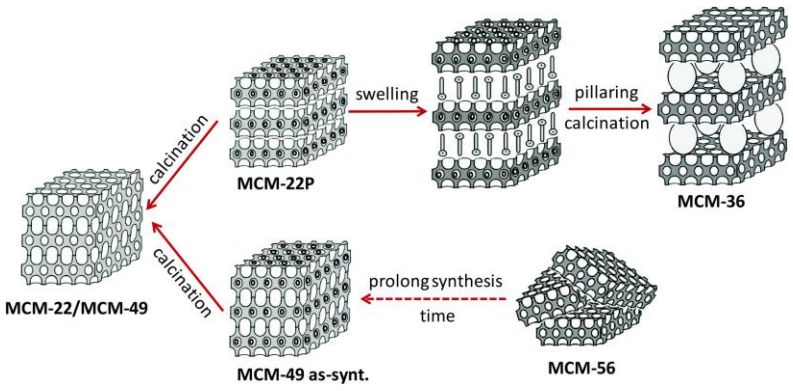

Figure 1.13 Shows the family of structures made from layered materials MCM-56 and MCM-22P including pillared material MCM-36 and fully connected 3D zeolite MCM-22 (taken from reference 90)

The use of 2D layered precursors although showing promise has had some limited success. Most of the 3D frameworks made through the formation of these 2D intermediates and subsequent condensation can be formed through traditional direct hydrothermal

synthesis. This implies that the synthesis of 2D precursors does not differ enough from direct 3D zeolite synthesis to produce unique frameworks.[91] The use of 2D layered precursors also adds further complications to the synthesis of 3D zeolite frameworks. The synthesis is forced to go through an additional intermediate step. The problem of controlling the direct hydrothermal synthesis of a 3D zeolite is then replaced by the 2 problems: 1) controlling the formation of these 2D layered materials and 2) controlling their subsequent arrangement to form the final 3D zeolite product.

1.6 The ADOR Process

1.6.1 Introduction

One of the most interesting recent developments in zeolite synthesis has been the discovery of a new method for the top-down synthesis of zeolites called the ADOR process. Since its inception in 2013,[92] the ADOR process has led to the synthesis of new all-silica frameworks, including high-energy 'unfeasible zeolites' and the synthesis of zeolite frameworks with other elements.[93,94] One of the key reasons for the successes of the ADOR process has been its ability to turn 'weakness into strength'.[95] It allows for the transformation of hydrolytically unstable germanosilicates into new stable high silica zeolites, with framework properties related to the original germanosilicate.

1.6.2 The First 3D-2D Transformation

The first indications of the ADOR process were reported in 2011,[96] where Roth *et. al.* showed that it was possible to use the known instability of germanosilicates, particularly the weakness of the Ge-dominated *d4r* units, to conduct a 3D to 2D zeolite transformation (Figure 1.14).[97] In this case the parent germanosilicate **UTL** was used to form the new 2D layered material IPC-1P. The use of this 3D-2D transformation allowed for the synthesis of silicate layers, based on **UTL**, which otherwise would be impossible to achieve through traditional hydrothermal synthesis. The use of such methods was particularly attractive as many of these parent germanosilicates contain large pore systems, **UTL** contains 14 x 12-ring 2D channels, that may be advantageous in catalysis. But the inherent instability of these germanosilicate large pore systems has prevented their use in such processes.

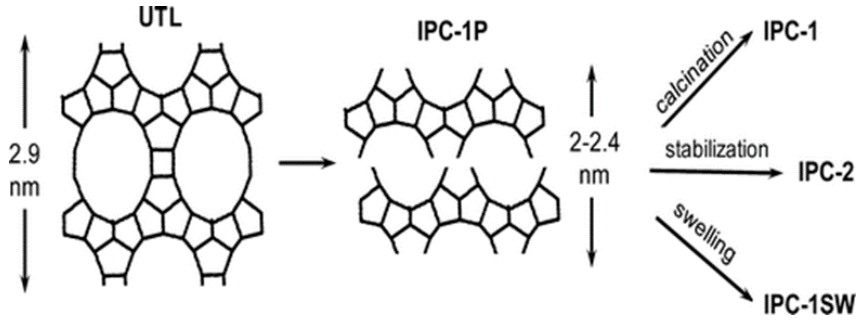

Figure 1.14 Schematic representation of the 3D-2D transformation and subsequent products produced by the degermanation of UTL (taken from reference 96)

Not only did Roth *et al*. show that the germanosilicate **UTL** could be successfully disassembled, they also showed that these layers could undergo similar treatments as reported for other 2D zeolites, such as the MCM-22 family. The treatment of this lamellar material, IPC-1P, under different conditions resulted in the formation of different products. Direct calcination of IPC-1P resulted in the formation of the IPC-1, a poorly defined structure with a reduced *d*-spacing between the layers and consequently a reduced BET surface area. These layers were also able to undergo different treatments to form other products IPC-2 and IPC-1SW. IPC-2 was a so-called interlamellar expanded zeolite (IZA), though unconfirmed), where a silicate source was used to form a product with a slightly larger *d*-spacing than IPC-1 after calcination. Swelling of IPC-1P with surfactants showed that these silicate layers could be expanded to even further *d*-spacing, while still resulting in the formation of the IPC-1 product after calcination of the layers.[96]

1.6.3 The ADOR Process Confirmed

In 2013 Roth *et al*. reported the full ADOR process.[92] In this landmark paper, they showed that not only was it possible to disassemble the **UTL** layers to form the lamellar product IPC-1P, but that these layers could be organised and then reassembled to form the new pure-silica daughter zeolites IPC-2 and IPC-4. This extra organisation step was key in overcoming the previous issues of disordered layers noted in 2011.[96] It was found that organic directing agents could hydrogen bond with the interlayer silanols, organise these layers, and create a more uniform sample.

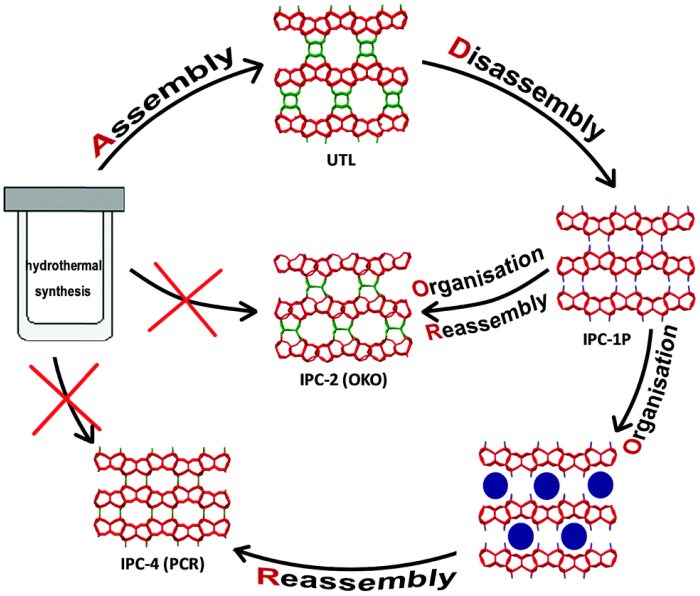

Figure 1.15 Shows a schematic representation of the first confirmed case of the ADOR process. Where the assembled UTL is disassembled into IPC-1P and then reassembled into IPC-2 (OKO framework) or IPC-4 (PCR framework). IPC-2 (OKO) consists of IPC-1P layers connected by *s4r* linkages between them, IPC-4 (PCR) consists of IPC-1P layers connected by direct O-linkages between them. Both structures were, at the time the paper was published, not available by traditional hydrothermal synthesis (Taken from reference 92).

This additional control over the synthesis produced IPC-2, which consisted on IPC-1P layers connected by *s4r* linkages between the layer and IPC-4, which consisted of IPC-1P layers connected by direct O-linkages between the layers. The resultant mother and daughter zeolites, were therefore isoreticular; with the same layers but different interlayer linkages and different channel systems. The reduction from *d4r*- to *s4r*- and direct O-linkages reduced the 14 x 12 ring channels to 12 x 10 and 10 x 8 ring channels respectively.

The desirability of the ADOR process was increased further due to this combination of control and predictability. Not only was it possible to predict the channel systems of the daughter zeolites, based on the parent zeolite, it was also possible to have the required control to produce the uniform sample that would be desirable for applications. Furthermore, as the ADOR process is a 3D-2D-3D transformation it could grant access to new frameworks that were not possible through traditional hydrothermal synthesis.

1.6.4 The Stages of the ADOR Process

The ADOR process stands for the Assembly, Disassembly, Organisation and Reassembly process**Error! Reference source not found.**. The fact that these four steps can be defined and separated from each other is a key element of the controllability of the ADOR process. It is important to have a full understanding of the chemistry and characteristics of each step, to gain a full understanding of their implications for the final products formed by the ADOR process.[91]

1.6.4.1 Assembly

The first stage (Assembly) involves the synthesis of the parent germanosilicate using traditional hydrothermal synthesis. As previously discussed there are many factors that play a role in hydrothermal synthesis and these will have an impact on the chemical and framework properties of the parent germanosilicate. The ADOR process has traditionally only been applied to already known zeolites, so this means that there is less of a requirement for a full exploration into the hydrothermal synthesis parameters. However, it is important to have a complete knowledge of the framework properties of candidate germanosilicates to ensure the ADOR process can be applied successfully (Figure 1.16).

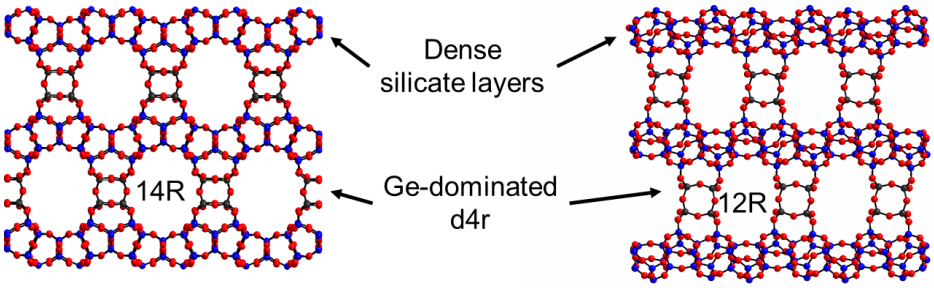

Figure 1.16 Shows the structure of UTL viewed along the 14- (left) and 12-ring (right) with the dense silicate layers and Ge-dominated *d4r* highlighted. The presence of the large channels, dense layers of silica and monodirectional Ge-dominated *d4r* make UTL an ideal zeolite for the ADOR process. Ge *d4r* T-atoms in black, Si T-atoms in blue and O in red.

Ideally the parent germanosilicate should consist of dense silicate layers, connected by Ge-containing *d4r* units in a monodirectional fashion. The *d4r* should be dominated by enough Ge to ensure that they are fully removed during disassembly. This allows for the successful removal of the *d4r* avoiding the presence of silica *s4r* in the *d4r* units, which would remain intact after the disassembly process. These *d4r* should be accessible through the framework's channel system to allow access for disassembly and organisation reagents.

1.6.4.2 Disassembly

The second stage (Disassembly) involves the removal of the Ge-dominated *d4r* by acid hydrolysis. The relative weakness of Ge-O-Ge and Ge-O-Si bonds under weakly acidic hydrolysis conditions results in the removal of Ge from these *d4r* and, if the Ge content is high enough, the full removal of the *d4r* connecting the layers. This results in an 'unzipping' of the **UTL** framework and the formation of the 2D lamellar product consisting of the dense silicate layers, with a similar appearance to preFER, that are no longer directly connected by *d4r* interlayer linkages (Figure 1.17). The loss of these *d4r* supports between

the layers also results in a contraction of the interlayer distance and the formation of Si-OH (silanols) that can hydrogen bond between the layers.

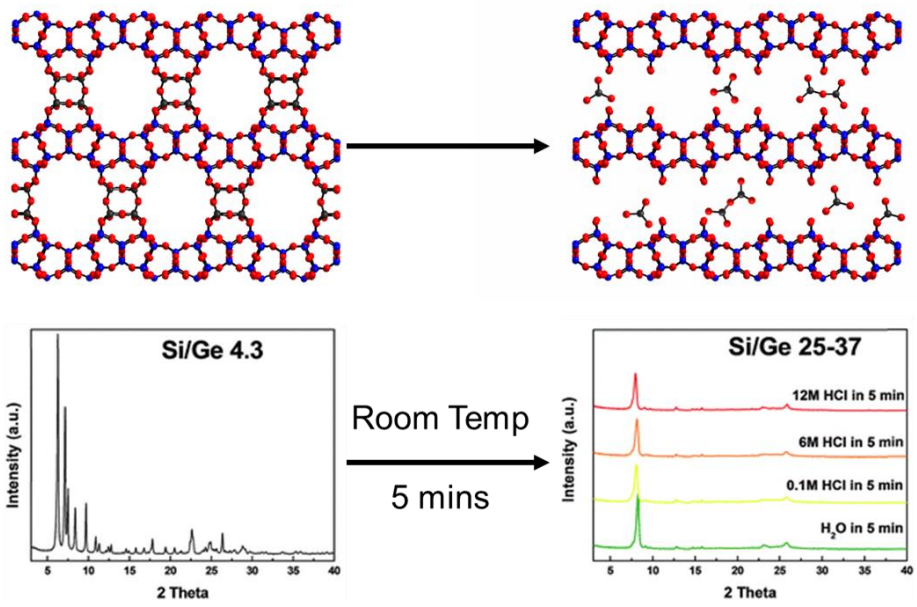

Figure 1.17 Shows a schematic representation of the disassembly process of UTL in water and various acid concentrations for 5 minutes at room temperature. The resultant PXRD patterns of the products differ from the parent UTL (left) and are dominated by a single broad peak (right). The similarity of the product PXRD patterns shows that the disassembly step is independent of acid concentration. Ge *d4r* T-atoms in black, Si T-atoms in blue and O in red. (Picture adapted from Reference 91).

These changes can be typically characterised by: the decrease in *d*-spacing is observed in the PXRD pattern as the interlayer peak moves to high 2θ angles, the removal of germanium can be observed by EDX spectroscopy and the formation of silanols is typically observed through solid-state ^{29}Si NMR.[91]

1.6.4.3 Organisation

The third stage (Organisation) is one of the most important and consequential steps of the ADOR process. If direct calcination is attempted on the dissembled zeolite then a poorly ordered material IPC-1 is obtained, where the layers are partially connected and partially collapsed onto each other to produce a material that is not a true zeolite.[96] During this step, different methods can be used to arrange the layers in the desired fashion, ready for the final reassembly stage, to produce different daughter zeolites.

1.6.4.3.1 Self-Organisation

The most direct method of organisation is to continue heating the sample after disassembly and allow for the layers to self-organise. The use of different acid concentrations results in a shift in the process occurring during organisation step (Figure 1.18). The use of strong acid concentrations not only results in the deintercalation of the

layers but also allows for formation of Si-O-Si bonds and the rearrangement of the silica species.

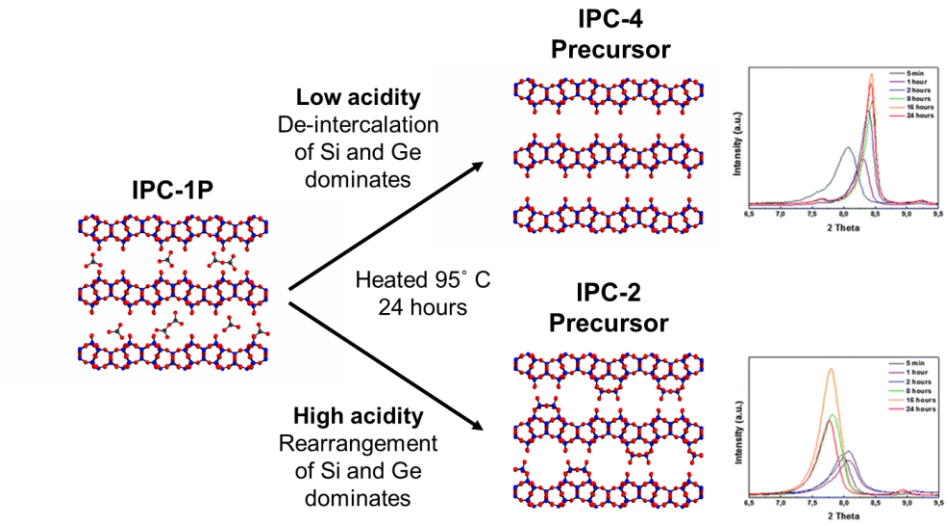

Figure 1.18 Shows a schematic representation of the acidity dependent self-organisation that occurs when heating IPC-1P under different acidic conditions. With high acidity (12 M HCl) an increase in the interlayer spacing is seen, corresponding to the rearrangement process. With low acidity (0.1 M HCl) a decrease in interlayer spacing is seen, corresponding to the full deintercalation of the layers. Ge T-atoms in black, Si T-atoms in blue and O in red (adapted from reference 91).

This would result in the formation of *s4r* units and consequently an increase in the interlayer spacing. The subsequent reassembly step forms *s4r* interlayer linkages and the IPC-2 framework. The amount of silicon atoms present in the now destroyed *d4r* is not enough to allow for the formation of these new units. It is believed that this additional silicon originates from migration of silicon from the intralayer region or from residual silicon present as a minor impurity. The former has been shown to occur with work by Hong *et al.* on the healing of defects in zeolite YNU-2.[98]

The use of water/very low acid concentration caused the deintercalation process to dominate as the acid strength is not strong enough to promote the formation of Si-O-Si bonds. The deintercalation of the layers leads to a decrease in the interlayer spacing as the *d4r* and residual units are completely removed. Reassembly of this species leads to the formation of direct oxygen linkages between the layers forming IPC-4.

It was also found that by varying the acid concentration it was possible to interplay these two processes, deintercalation and rearrangement. The use of 1.5 M HCl lead to the formation of IPC-6 with alternating *s4r* and direct O-linkages between the layers. A higher molarity of acid (5 M HCl) lead to the formation of IPC-7 with alternating *s4r* and *d4r* linkages between the layers.[99,100]

1.6.4.3.2 Organisation by Intercalation

The second method for the organisation of layers is the use of intercalating agents (Figure 1.19). The dense groups of silanols after the degradation of the *d4r* results in silanol quadruplets. These quadruplets are available for interactions with those quadruplets on the opposite layers. The correct orientation of these quadruplets to each other allows for their successful condensation and the formation of a fully connected zeolite.

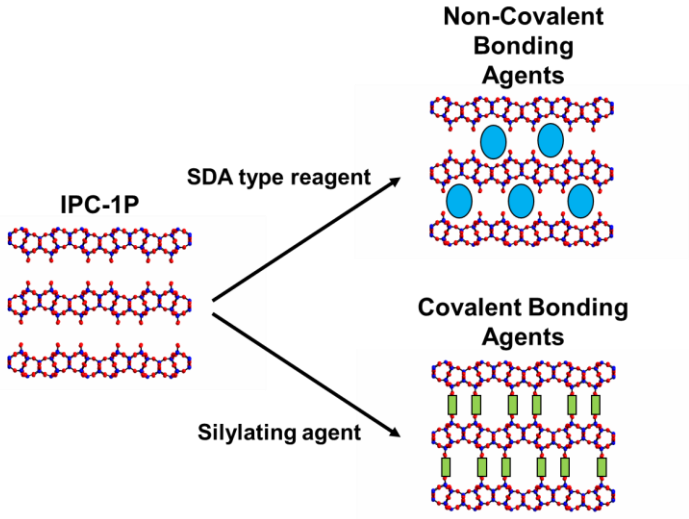

Figure 1.19 Shows the two methods for the organisation by intercalation of the IPC-1P layers. (Top) The use of SDA type reagents (blue circles) that exhibit a non-covalent bond interaction organizing the layers. (Bottom) The use of silylating agents (green rectangles) that covalently bond with the interlayer silanols to form columns in between the layers. Si T-atoms in blue and O in red.

1.6.4.3.3 Non-Covalent Bonding Agents

Non-covalent bonding agents can involve the use of organic SDA-like reagents (including octylamine, dipropylammonium hydroxide and hexylamine) that can, through hydrogen bonding, align the layers in the fashion desired. These reagents have been used with great success to form more crystalline products, swollen products, and high energy structures.[92,93,101]

1.6.4.3.4 Covalent Bonding Agents

Covalent bonding agents can also be used. These react with the interlayer silanols to form covalent bonds between the organised layers in a similar fashion to the formation of expanded interlamellar zeolites. The silylating agent diethoxydimethylsilane (DEDMS) intercalates between the layers, reacts with the available silanols to form covalent bonds between the layers. The two methyl groups on the DEDMS remain unreacted, allowing for their subsequent condensation together during the reassembly step. This approach has been used for other layered materials, however the presence of silanol quadruplets means

that the condensation of the silylating agent is complete and so results in a fully connected zeolite.[91]

1.6.4.4 Reassembly

The final stage (Reassembly) involves reconnecting these organised layers together, in a final irreversible step, using calcination. This requires the sample to be heated above 500 °C, to promote the formation of Si-O-Si bonds and form a fully connected zeolite.

This process has already been used on other 2D lamellar materials. The direct condensation of layers has been reported for preFER and MCM-22(P) to form **FER** and MCM-22. But direct condensation does not always lead to fully connected zeolites , as is the case for the calcination of EU-19 to form EU-20b.[102]

Marler *et al*. have suggested several factors that can affect the quality of the final condensed framework to optimise the quality of the final reassembled zeolite including: the impact of the interlayer hydrogen bonds and their stabilisation effect and the stacking order.[103]

Silylation of the other layered materials like preFER formed interlamellar expanded zeolites (IEZ).[104] These often do not form fully connected zeolites as the interlayer silanes are not tetrahedral, they are only connected to two other tetrahedrally coordinated silica. The ADOR process enables the formation of a fully connected zeolite, due to presence of the silanol quadruplets from the disassembly of the parent germanosilicate. This means that the silylating agents, will covalently bond with the silanols between the layers, to form quadruplets too. During the reassembly/calcination the geminal methylsilanes convert to geminal silanols. These silanols within the quadruplet are then close enough together that they condense together forming Si-O-Si bonds and *s4r* units between the layers, resulting in a fully connected daughter zeolite (Figure 1.20).[91]

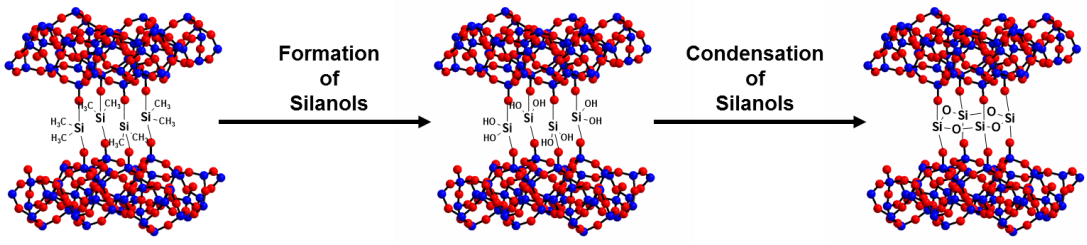

Figure 1.20 Shows a schematic representation of the reassembly process on a IPC-1P quadruplet that has been organised with a covalent bonding agent (left). The high temperatures and presence of oxygen cause the initial conversion of geminal methylsilanes to geminal silanols (centre). These are then able to condense together forming Si-O-Si bonds and a complete *s4r* interlayer linkage. Layer Si T-atoms in blue and O in red.

1.6.5 The ADOR Process Expanded

1.6.5.1 New Families

Since the first description of the ADOR process in 2013 it has since expanded to include the synthesis of daughter zeolites from other germanosilicates. The successful disassembly of the frameworks **ITH**, **ITR**, and **IWR** were reported in 2014.[105] These initial results were further advanced with the application of the whole ADOR process on germanosilicate **IWW** to yield the structure IPC-5,[106] a pure silicate version of **IWW**. Both parent and daughter zeolites showed similar powder patterns and adsorption isotherms. This showed that it was possible to not only incorporate *s4r* or direct O-linkages but also restore the *d4r* linkages between the layers. The impact of the Ge content of the parent germanosilicate was also highlighted. The acid hydrolysis of Ge-rich **IWW** resulted in the formation of a layered precursor IPC-5P, while Ge-poor **IWW** did not result in the full removal of the *d4r*. This however did allow for the incorporation of aluminium into the newly vacant sites left by the removed germanium.

The ADOR process has also been expanded to include the parent germanosilicate **UOV** resulting in the new daughter zeolite IPC-12 with the same layers as its parent germanosilicate, but with direct O-linkages between the layers.[94]

1.6.5.2 Use of ADOR Process to Produce Aluminosilicates

As previously discussed above the ADOR process can synthesise pure-silica zeolites from a parent germanosilicate. The incorporation of other elements, like aluminium, for catalytic purposes has also been of interest. The ADOR process was first used to incorporate aluminium into IPC-5, the daughter zeolite of the germanosilicate **IWW**.[106] This has been expanded to include the synthesis of other aluminium containing daughter zeolites from parent germanosilicates **IWW**, **UTL**, **ITH**.[68]

1.6.5.3 Use of ADOR Process to Synthesise 'Unfeasible' Zeolites

One of the biggest challenges in zeolite synthesis is the so-called "zeolite conundrum".[107] Zeolite frameworks are composed of relatively simple PBUs consisting of tetrahedra with a central T-atom and joined together by corner sharing oxygens. There are millions of ways to connect these simple PBUs and so the number of unique frameworks is expected to be relatively high.[108,109] Yet the number of known unique frameworks stands at merely 232 and the minority of these are pure or high silica frameworks, which are of most interest in catalysis.[1,110]

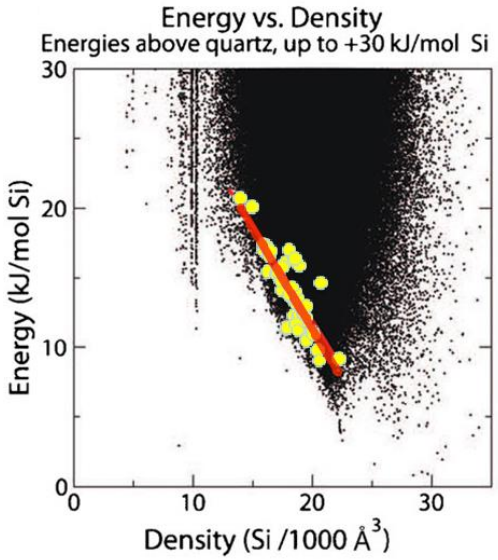

Figure 1.21 Shows an Energy vs. Density plot for computationally predicted zeolite structure, known zeolite structures are shown in yellow with the linear fit highlighted in red. Adapted from reference 111.

By plotting a graph of energy vs density of predicted and already known frameworks. All the known frameworks seem to follow a trend, adhering very closely to a particular energy vs density gradient (Figure 1.21).[111,112] Attempts to explain this trend have revolved around setting criteria to predict the likelihood of a predicted framework being synthesised. This first began with measuring proposed frameworks with a feasibility factor, based on how far the framework is from this energy vs. density trend.[113] More recent criteria have focused on local interatomic distances (LIDs), where feasible zeolites are those that only obey strict criteria based on limiting the values of interatomic distances and angles. There are five criteria that all known zeolite structures obey.[114] All the known zeolites are noted for showing a correlation between energy and density and obeying these five criteria. However, a large majority of hypothetical zeolites also obey these five LID criteria and so the range of structures should be far larger. The presence of all the known zeolites at the edge of this energy vs. density plot indicates that the problem of accessing such structures is not determined by the zeolite properties but by the kinetic limitation of the synthesis procedure.[93,111]

This indicates that the use of hydrothermal synthesis is a limiting factor in the formation of more new unique frameworks and exciting structures, like frameworks with odd membered rings.[111] This is most likely because, during hydrothermal synthesis, the system is able to easily make and break bonds and so avoid high energy framework structures. The ADOR process is an ideal methodology for the formation of interesting and 'unfeasible' zeolite frameworks. Particularly due to the presence of an irreversible

reassembly step, preventing the synthesis from avoiding unfavourable structures, which is possible under traditional hydrothermal conditions.

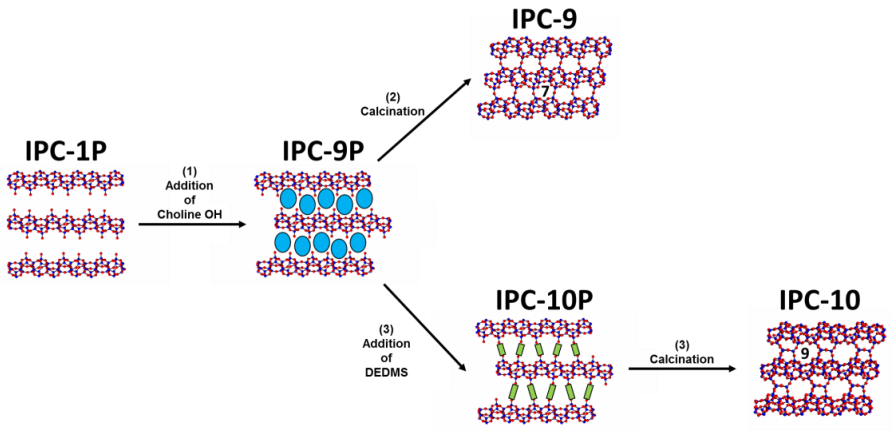

Figure 1.22 Shows a schematic representation of the formation of the 'unfeasible' zeolites IPC-9 and IPC-10. 1) After disassembly of UTL to form IPC-1P the addition of choline cation (blue circle) causes the layers to shift with respect to each other. The layers can then be reassembled in two ways. 2) Direct calcination to form IPC-9 (top). 3) Intercalation of the covalent bonding agent DEDMS (green rectangles) followed by calcination to form IPC-10 (bottom). The shift in the layers by the choline allows for the formation of 7 rings in IPC-9 and 9 rings in IPC-10 (highlighted). Ge *d4r* T-atoms in black, Si T-atoms in blue and O in red.

Mazur *et al.* proved this fundamental idea in 2016 with the formation of the first 'unfeasible' zeolites IPC-9 and IPC-10 (Figure 1.22).[93] These two new daughter zeolites are like IPC-4 and IPC-2, consisting of IPC-1P layers connected by direct O- and *s4r* linkages, respectively. However, IPC-9 and IPC-10 differ from their sister zeolites. The layers are slightly shifted resulting in the formation of frameworks containing 7- and 9-ring channels respectively. This was achieved using a surfactant (choline hydroxide) on the layered material IPC-1P to produce a shift in the layers by half a unit cell along the *c*-direction. The shifted layers could then be directly calcined to form IPC-9 or intercalated with DEDMS before calcination to form IPC-10. This shifting of the layers introduces strain into the final daughter zeolite frameworks leading to highly unfavourable energy/density properties (Figure 1.23). Both IPC-9 and IPC-10 failed to obey all five of the LID selection criteria (failing 2 and 3 respectively) hence they were deemed 'unfeasible' zeolites.[93]

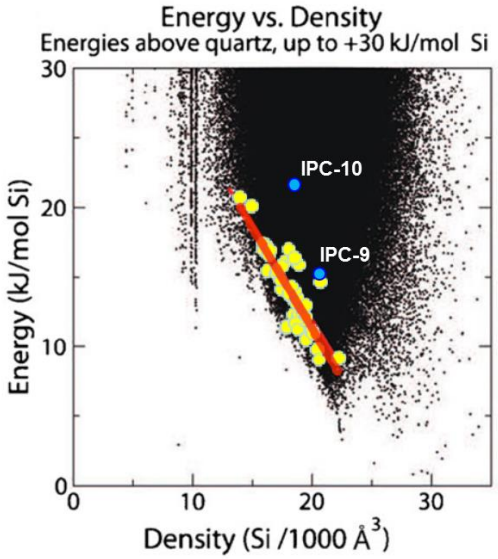

Figure 1.23 Shows an Energy vs. Density plot for computationally predicted zeolite structures, known zeolite structures are shown in yellow with the linear fit highlighted in red. The 'unfeasible' zeolites IPC-9 and IPC-10 are represented by blue circles. Adapted from reference III.

1.6.5.4 The Future of the ADOR Process

In just a few years the ADOR process has gone from strength to strength. Whether used to synthesise new all silica frameworks, incorporating new elements into frameworks or new unique frameworks originally deemed 'impossible' by conventional methods. The ADOR process has shown not just its adaptability but its potential to fundamentally change the field of zeolite research.

1.7 References

(1) Baerlocher, C.; McCusker, L. B. Database of Zeolite Structures http://www.iza-structure.org/databases/.

(2) Maesen, T.; Marcus, B. Chapter 1 The Zeolite Scene - An Overview. In *Introduction to Zeolite Science and Practice*; Čejka, J., Corma, A., Bekkum, H. van, Schüth, F., Eds.; 2007; Vol. 168, pp 1–12.

(3) Colella, C.; Gualtieri, A. F. Cronstedt's Zeolite. *Microporous Mesoporous Mater.* **2007**, *105* (3), 213–221.

(4) Ozaydin, S.; Kocer, G.; Hepbasli, A. Natural Zeolites in Energy Applications. *Energ. Source Part A* **2006**, *28* (15), 1425–1431.

(5) Sheppard, R. Zeolites in Sedimentary Deposits of the United States-A Review. In *Molecular Sieve Zeolites-I: Advances in chemistry series 101*; Advances in Chemistry;

American Chemical Society, 1974; Vol. 101, pp 279–209.

(6) Sainte-Claire-Deville, H. Reproduction de la Lévyne. *Comptes Rendus* **1862**, *54*, 324–327.

(7) Cundy, C. S.; Cox, P. A. The Hydrothermal Synthesis of Zeolites: History and Development from the Earliest Days to the Present Time. *Chem. Rev.* **2003**, *103* (3), 663–701.

(8) Barrer, R. M. Synthesis of a Zeolitic Mineral with Chabazite-like Sorptive Properties. *J. Chem. Soc.* **1948**, 127–132.

(9) Milton, R. M. Molecular Sieve Adsorbents. US Patent. 2,882,244, 1959.

(10) Flanigen, E. M. Chapter 2 Zeolites and Molecular Sieves an Historical Perspective. In *Studies in Surface Science and Catalysis*; 1991; Vol. 58, pp 13–34.

(11) Maesen, T.; Marcus, B. Chapter 1 The Zeolite Scene - An Overview. In *Studies in Surface Science and Catalysis*; van Bekkum, H., Flanigen, E. M., Jacobs, P. A., Jansen, J. C., Eds.; 2001; Vol. 137, pp 1–9.

(12) Robert J. Argauer, Kensington Md., George R. Landolt, A. N. J. Crystalline Zeolite ZSM-5 and Method of Preparing the Same. US Patent. 3,702,886, 1972.

(13) Flanigen, E. M.; Patton, R. L. Silica Polymorph and Process for Preparing the Same. US Patent. 4,073,865, 1978.

(14) Zones, S. I.; Hwang, S. J.; Elomari, S.; Ogino, I.; Davis, M. E.; Burton, A. W. The Fluoride-Based Route to All-Silica Molecular Sieves; a Strategy for Synthesis of New Materials Based upon Close-Packing of Guest-Host Products. *Comptes Rendus Chim.* **2005**, *8* (3–4), 267–282.

(15) Wilson, S. T.; Lok, B. M.; Messina, C. A.; Cannan, T. R.; Flanigen, E. M. Aluminophosphate Molecular Sieves: A New Class of Microporous Crystalline Inorganic Solids. *J. Am. Chem. Soc.* **1982**, *104* (4), 1146–1147.

(16) Kresge, C. T.; Leonowicz, M. E.; Roth, W. J.; Vartuli, J. C.; Beck, J. S. Ordered Mesoporous Molecular Sieves Synthesized by a Liquid-Crystal Template Mechanism. *Nature* **1992**, *359* (6397), 710–712.

(17) Inagaki, S.; Fukushima, Y.; Kuroda, K. Synthesis of Highly Ordered Mesoporous Materials from a Layered Polysilicate. *J. Chem. Soc. Chem. Commun.* **1993**, No. 8,

680–682.

(18) Yanagisawa, T.; Shimizu, T.; Kuroda, K.; Kato, C. The Preparation of Alkyltrimethylammonium-Kanemite Complexes and Their Conversion to Microporous Materials. *Bull. Chem. Soc. Jpn.* **1990**, *63* (4), 988–992.

(19) Leonowicz, M. E.; Lawton, J. A.; Lawton, S. L.; Rubin, M. K. MCM-22: A Molecular Sieve with Two Independent Multidimensional Channel Systems. *Science* **1994**, *264* (5167), 1910–1913.

(20) Martinez-Triguero, J.; Diaz-Cabañas, M. J.; Camblor, M. A.; Fornés, V.; Maesen, T. L. M.; Corma, A. The Catalytic Performance of 14-Membered Ring Zeolites. *J. Catal.* **1999**, *182* (2), 463–469.

(21) McCusker, L. B.; Baerlocher, C. Chapter 3 Zeolite Structures. In *Introduction to Zeolite Science and Practice*; 2001; Vol. 137, pp 37–67.

(22) Baerlocher, C.; McCusker, L. B.; Olson, D. H. Introduction and Explanatory Notes. In *Zeolites*; 1992; Vol. 12, pp 3–15.

(23) Morris, R. E.; McCusker, L. B.; Baerlocher, C.; Merrouche, A.; Kessler, H.; O'Keeffe, M.; Yaghi, O. M.; Yaghi, O. M.; Loiseau, T.; Férey, G. Modular Materials from Zeolite-like Building Blocks. *J. Mater. Chem.* **2005**, *15* (9), 931.

(24) McCusker, L. B.; Baerlocher, C. Chapter 2 - Zeolite Structures. In *Introduction to Zeolite Science and Practice*; Čejka, J., Corma, A., Bekkum, H. van, Schüth, F., Eds.; Elsevier, 2007; Vol. 168, pp 13–37.

(25) Smith, J. V. *Microporous and Other Framework Materials with Zeolite-Type Structures*; Springer, 2000.

(26) Koningsveld, H. Van. *Compendium of Zeolite Framework Types: Building Schemes and Type Characteristics*; Elsevier, 2007.

(27) Vogt, E. T. C.; Kresge, C. T.; Vartuli, J. C. Chapter 22 Beyond Twelve Membered Rings. In *Studies in Surface Science and Catalysis*; 2001; Vol. 137, pp 1003–1027.

(28) Smulders, E.; von Rybinski, W.; Nordskog, A. Laundry Detergents, 1. Introduction. In *Ullmann's Encyclopedia of Industrial Chemistry*; Wiley-VCH Verlag GmbH & Co. KGaA: Weinheim, Germany, 2011.

(29) Brumfiel, G. Fukushima Set for Epic Clean-Up. *Nature*. Nature Publishing Group

April 14, 2011, pp 146–147.

(30) Tanabe, K.; Hölderich, W. F. Industrial Application of Solid Acid–Base Catalysts. *Appl. Catal. A Gen.* **1999**, *181* (2), 399–434.

(31) Sherman, J. D. Synthetic Zeolites and Other Microporous Oxide Molecular Sieves. *Proc. Natl. Acad. Sci. U. S. A.* **1999**, *96* (7), 3471–3478.

(32) The Nobel Foundation. The Nobel Prize in Physiology or Medicine 1998 http://nobelprize.org/nobel_prizes/medicine/laureates/1998/illpres/ (accessed Mar 30, 2017).

(33) Ignarro, L. J.; Buga, G. M.; Wood, K. S.; Byrns, R. E. Endothelium-Derived Relaxing Factor Produced and Released from Artery and Vein is Nitric Oxide. *Proc. Natl. Acad. Sci. U. S. A.* **1987**, *84* (December), 9265–9269.

(34) Wheatley, P. S.; Butler, A. R.; Crane, M. S.; Fox, S.; Xiao, B.; Rossi, A. G.; Megson, I. L.; Morris, R. E. NO-Releasing Zeolites and their Antithrombotic Properties. *J. Am. Chem. Soc.* **2006**, *128* (2), 502–509.

(35) Förstermann, U.; Sessa, W. C. Nitric Oxide Synthases: Regulation and Function. *Eur. Heart J.* **2012**, *33* (7).

(36) Boës, A. K.; Xiao, B.; Megson, I. L.; Morris, R. E. Simultaneous Gas Storage and Catalytic Gas Production Using Zeolites - A New Concept for Extending Lifetime Gas Delivery. *Top. Catal.* **2009**, *52* (1–2), 35–41.

(37) Russell, S. E.; González Carballo, J. M.; Orellana-Tavra, C.; Fairen-Jimenez, D.; Morris, R. E. A Comparison of Copper and Acid Site Zeolites for the Production of Nitric Oxide for Biomedical Applications. *Dalt. Trans.* **2017**, *46* (12), 3915–3920.

(38) Cubillas, P.; Anderson, M. W. Synthesis Mechanism: Crystal Growth and Nucleation. In *Zeolites and Catalysis: Synthesis, Reactions and Applications*; Wiley-VCH Verlag GmbH & Co. KGaA: Weinheim, Germany, 2010; Vol. 1, pp 1–55.

(39) Cundy, C. S.; Cox, P. A. The Hydrothermal Synthesis of Zeolites: Precursors, Intermediates and Reaction Mechanism. *Microporous Mesoporous Mater.* **2005**, *82* (1–2), 1–78.

(40) Lok, B. M.; Cannan, T. R.; Messina, C. A. The Role of Organic Molecules in Molecular Sieve Synthesis. *Zeolites* **1983**, *3*, 282–291.

(41) Yu, J. Chapter 3 - Synthesis of Zeolites. In *Introduction to Zeolite Science and Practice*; Čejka, J., Corma, A., Bekkum, H. van, Schüth, F., Eds.; Elsevier, 2007; Vol. 168, pp 39–103.

(42) Burkett, S. L.; Davis, M. E. Mechanisms of Structure Direction in the Synthesis of Pure-Silica Zeolites. 1. Synthesis of TPA/Si-ZSM-5. *Chem. Mater.* **1995**, *7* (1), 920–928.

(43) Caratzoulas, S.; Vlachos, D. G.; Tsapatsis, M. On the Role of Tetramethylammonium Cation and Effects of Solvent Dynamics on the Stability of the Cage-Like Silicates $Si_6O_{15}^{6-}$ and $Si_8O_{20}^{8-}$ in Aqueous Solution. A Molecular Dynamics Study. *J. Am. Chem. Soc.* **2006**, *128* (2), 596–606.

(44) Flanigen, E. M.; Bennett, J. M.; Grose, R. W.; Cohen, J. P.; Patton, R. L.; Kirchner, R. M.; Smith, J. V. Silicalite, a New Hydrophobic Crystalline Silica Molecular Sieve. *Nature* **1978**, *271* (5645), 512–516.

(45) Davis, M. E.; Lobo, R. F. Zeolite and Molecular Sieve Synthesis. *Chem. Mater.* **1992**, *4* (4), 756–768.

(46) Lawton, S. L.; Rohrbaugh, W. J. The Framework Topology of ZSM-18, a Novel Zeolite Containing Rings of Three (Si,Al)-O Species. *Science* **1990**, *247* (4948), 1319–1322.

(47) Pinar, A. B.; Wright, P. A.; Gómez-Hortigüela, L.; Pérez-Pariente, J. Synthesis of Ferrierite Zeolite with Pyrrolidine as Structure Directing Agent: A Combined X-ray Diffraction and Computational Study. *Microporous Mesoporous Mater.* **2010**, *129* (1–2), 164–172.

(48) Wang, S.; Peng, Y. Natural Zeolites as Effective Adsorbents in Water and Wastewater Treatment. *Chem. Eng. J.* **2010**, *156* (1), 11–24.

(49) Gies, H.; Marker, B. The Structure-Controlling Role of Organic Templates for the Synthesis of Porosils in the Systems SiO_2/Template/H_2O. *Zeolites* **1992**, *12* (1), 42–49.

(50) Lobo, R. F.; Zones, S. I.; Davis, M. E. Structure-Direction in Zeolite Synthesis. *J. Incl. Phenom. Mol. Recognit. Chem.* **1995**, *21* (1–4), 47–78.

(51) Zones, S. I.; Nakagawa, Y.; Lee, G. S.; Chen, C. Y.; Yuen, L. T. Searching for New High Silica Zeolites Through a Synergy of Organic Templates and Novel Inorganic

Conditions. *Microporous Mesoporous Mater.* **1998**, *21* (4–6), 199–211.

(52) Guth, J. L.; Caullet, P.; Seive, A.; Patarin, J.; Delprato, F. New Mobilizing and Templating Agents in the Synthesis of Crystalline Microporous Solids. In *Guidelines for Mastering the Properties of Molecular Sieves*; Barthomeuf, D., Derouane, E. G., Hölderich, W., Eds.; Springer Science & Business Media, 2013.

(53) Kamakoti, P.; Barckholtz, T. A. Role of Germanium in the Formation of Double Four Rings in Zeolites. *J. Phys. Chem. C* **2007**, *111* (9), 3575–3583.

(54) Liu, X.; Ravon, U.; Tuel, A. Fluoride Removal from Double Four-Membered Ring (D4R) Units in As-Synthesized Ge-Containing Zeolites. *Chem. Mater.* **2011**, *23* (22), 5052–5057.

(55) Weitkamp, J.; Hunger, M. Chapter 22 - Acid and Base Catalysis on Zeolites. In *Introduction to Zeolite Science and Practice*; Čejka, J., Corma, A., Bekkum, H. van, Schüth, F., Eds.; Elsevier, 2007; Vol. 168, pp 787–835.

(56) Szostak, R. Structural Aspects. In *Molecular Sieves*; Springer Netherlands, 1998; pp 29–59.

(57) Fletcher, R. E.; Ling, S.; Slater, B. Violations of Löwenstein's Rule in Zeolites. *Chem. Sci.* **2017**, *8* (11), 7483–7491.

(58) Li, Y.; Yu, J.; Xu, R. AlPO Database http://mezeopor.jlu.edu.cn/alpo/ (accessed Apr 19, 2017).

(59) Sierra de Saldarriaga, L.; Saldarriaga, C.; Davis, M. E. Investigations into the Nature of a Silicoaluminophosphate with the Faujasite Structure. *J. Am. Chem. Soc.* **1987**, *109* (9), 2686–2691.

(60) Pastore, H. O.; Coluccia, S.; Marchese, L. Porous Aluminophosphates: From Molecular Sieves to Designed Acid Catalysts. *Annu. Rev. Mater. Res.* **2005**, *35* (1), 351–395.

(61) Sastre, G.; Lewis, D. W.; Catlow, C. R. A. Structure and Stability of Silica Species in SAPO Molecular Sieves. *J. Phys. Chem.* **1996**, *100* (16), 6722–6730.

(62) Strohmaier, K. G. Synthesis Approaches. In *Zeolites and Catalysis: Synthesis, Reactions and Applications*; Wiley-VCH Verlag GmbH & Co. KGaA: Weinheim, Germany, 2010; Vol. 1, pp 57–86.

(63) Kuehl, G. H. Preparation of Crystalline Silicoaluminophosphates. US Patent. 4,786,487, 1988.

(64) O'Keeffe, M.; Yaghi, O. M. Germanate zeolites: Contrasting the behavior of germanate and silicate structures built from cubic T8O20 units (T = Ge or Si). *Chem. Eur. J.* **1999**, *5* (10), 2796–2801.

(65) Qian, K.; Wang, Y.; Liang, Z.; Li, J. Germanosilicate Zeolite ITQ-44 with Extra-Large 18-Rings Synthesized by Using Commercial Quaternary Ammonium as Structure-Directing Agent. *RSC Adv.* **2015**, *5*, 63209–63214.

(66) Hernández-Rodríguez, M.; Jordá, J. L.; Rey, F.; Corma, A. Synthesis and Structure Determination of a New Microporous Zeolite with Large Cavities Connected by Small Pores. *J. Am. Chem. Soc.* **2012**, *134* (32), 13232–13235.

(67) Xu, H.; Jiang, J.; Yang, B.; Zhang, L.; He, M.; Wu, P. Post-Synthesis Treatment gives Highly Stable Siliceous Zeolites through the Isomorphous Substitution of Silicon for Germanium in Germanosilicates. *Angew. Chemie Int. Ed.* **2014**, *53* (5), 1355–1359.

(68) Shamzhy, M. V.; Eliášová, P.; Vitvarová, D.; Opanasenko, M. V.; Firth, D. S.; Morris, R. E. Post-Synthesis Stabilization of Germanosilicate Zeolites ITH, IWW, and UTL by Substitution of Ge for Al. *Chem. - A Eur. J.* **2016**, *22* (48), 17377–17386.

(69) Bhatia, S. *Zeolite Catalysis: Principles and Applications*; CRC Press, 2012.

(70) Kuperman, A.; Nadimi, S.; Oliver, S.; Ozin, G. a.; Garcés, J. M.; Olken, M. M. Non-Aqueous Synthesis of Giant Crystals of Zeolites and Molecular Sieves. *Nature* **1993**, *365* (6443), 239–242.

(71) Camblor, M. A.; Villaescusa, L. A.; Díaz-Cabañas, M. J. Synthesis of All-Silica and High-Silica Molecular Sieves in Fluoride Media. *Top. Catal.* **1999**, *9*, 59–76.

(72) Villaescusa, L. a.; Barrett, P. a.; Camblor, M. a. ITQ-7: A New Pure Silica Polymorph with a Three-Dimensional System of Large Pore Channels. *Angew. Chemie Int. Ed.* **1999**, *38* (13–14), 1997–2000.

(73) Koller, H.; Wölker, A.; Villaescusa, L. A.; Díaz-Cabañas, M. J.; Valencia, S.; Camblor, M. A. Five-Coordinate Silicon in High-Silica Zeolites. *J. Am. Chem. Soc.* **1999**, *121* (14), 3368–3376.

(74) Burton, A. W.; Zones, S. I. Chapter 5 - Organic Molecules in Zeolite Synthesis: Their

Preparation and Structure-Directing Effects. In *Studies in Surface Science and Catalysis*; Čejka, J., Corma, A., Bekkum, H. van, Schüth, F., Eds.; Elsevier, 2007; Vol. 168, pp 137–179.

(75) Morris, R. E. Ionothermal Synthesis of Zeolites and Other Porous Materials. In *Zeolites and Catalysis: Synthesis, Reactions and Applications*; Wiley-VCH Verlag GmbH & Co. KGaA: Weinheim, Germany, 2010; Vol. 1, pp 87–105.

(76) Camblor, M. A.; Corma, A.; Valencia, S. Spontaneous Nucleation and Growth of Pure Silica Zeolite-B Free of Connectivity Defects. *Chem. Commun.* **1996**, *5* (20), 2365.

(77) Parnham, E. R.; Morris, R. E. Ionothermal Synthesis of Zeolites, Metal–Organic Frameworks, and Inorganic–Organic Hybrids. *Acc. Chem. Res.* **2007**, *40* (10), 1005–1013.

(78) Pinnavaia, T. J. Intercalated Clay Catalysts. *Science* **1983**, *220* (4595), 365–371.

(79) Vaughan, D. E. W.; J, L. R.; Magee, J. S. Pillared Interlayered Clay Materials Useful as Catalysts and Sorbents. US Patent. 4,176,090, 1978.

(80) Lawton, S. L.; Fung, A. S.; Kennedy, G. J.; Alemany, L. B.; Chang, C. D.; Hatzikos, G. H.; Lissy, D. N.; Rubin, M. K.; Timken, H.-K. C.; Steuernagel, S.; et al. Zeolite MCM-49: A Three-Dimensional MCM-22 Analogue Synthesized by in Situ Crystallization. *J. Phys. Chem.* **1996**, *100* (9), 3788–3798.

(81) Marler, B.; Gies, H. Hydrous Layer Silicates as Precursors for Zeolites Obtained Through Topotactic Condensation: A Review. *Eur. J. Mineral.* **2012**, *24* (3), 405–428.

(82) Kresge, C. T.; Leonowicz, M. E.; Roth, W. J.; Vartuli, J. C. Composition of Synthetic Porous Crystalline Material, Its Synthesis and Use. US Patent. 4,954,325, 1992.

(83) Schreyeck, L.; Caullet, P.; Mougenel, J. C.; Guth, J. L.; Marler, B. PREFER: A New Layered (Alumino) Silicate Precursor of FER-Type Zeolite. *Microporous Mater.* **1996**, *6* (5–6), 259–271.

(84) Dhingra, S. S.; Kresge, C. T.; Casmer, S. G. Crystalline Molecular Sieve Composition MCM-65, its Synthesis and Use. US Patent. 6,869,587, 2005.

(85) Roth, W. J. Chapter 7 – Synthesis of Delaminated and Pillared Zeolitic Materials. In *Studies in Surface Science and Catalysis*; Čejka, J., Corma, A., Bekkum, H. van,

Schüth, F., Eds.; 2007; Vol. 168, pp 221–239.

(86) Roth, W. J.; Dorset, D. L. Expanded View of Zeolite Structures and their Variability Based on Layered Nature of 3-D Frameworks. *Microporous Mesoporous Mater.* **2011**, *142* (1), 32–36.

(87) Park, W.; Yu, D.; Na, K.; Jelfs, K. E.; Slater, B.; Sakamoto, Y.; Ryoo, R. Hierarchically Structure-Directing Effect of Multi-Ammonium Surfactants for the Generation of MFI Zeolite Nanosheets. *Chem. Mater.* **2011**, *23* (23), 5131–5137.

(88) Jung, J.; Jo, C.; Cho, K.; Ryoo, R. Zeolite Nanosheet of a Single-Pore Thickness Generated by a Zeolite-Structure-Directing Surfactant. *J. Mater. Chem.* **2012**, *22* (11), 4637–4640.

(89) Roth, W. J.; Gil, B.; Marszalek, B. Comprehensive System Integrating 3D and 2D Zeolite Structures with Recent New Types of Layered Geometries. *Catal. Today* **2014**, *227*, 9–14.

(90) Kikhtyanin, O.; Chlubná, P.; Jindrová, T.; Kubička, D. Peculiar Behavior of MWW Materials in Aldol Condensation of Furfural and Acetone. *Dalton Trans.* **2014**, *43* (27), 10628–10641.

(91) Eliášová, P.; Opanasenko, M.; Wheatley, P. S.; Shamzhy, M.; Mazur, M.; Nachtigall, P.; Roth, W. J.; Morris, R. E.; Čejka, J. The ADOR Mechanism for the Synthesis of New Zeolites. *Chem. Soc. Rev.* **2015**, *44* (20), 7177–7206.

(92) Roth, W. J.; Nachtigall, P.; Morris, R. E.; Wheatley, P. S.; Seymour, V. R.; Ashbrook, S. E.; Chlubná, P.; Grajciar, L.; Položij, M.; Zukal, A.; et al. A Family of Zeolites with Controlled Pore Size Prepared Using a Top-Down Method. *Nat. Chem.* **2013**, *5* (7), 628–633.

(93) Mazur, M.; Wheatley, P. S.; Navarro, M.; Roth, W. J.; Položij, M.; Mayoral, A.; Eliášová, P.; Nachtigall, P.; Čejka, J.; Morris, R. E. Synthesis of "Unfeasible" Zeolites. *Nat. Chem.* **2015**, *8* (1), 58–62.

(94) Kasneryk, V.; Shamzhy, M.; Opanasenko, M.; Wheatley, P. S.; Morris, S. A.; Russell, S. E.; Mayoral, A.; Trachta, M.; Čejka, J.; Morris, R. E. Expansion of the ADOR Strategy for the Synthesis of Zeolites: The Synthesis of IPC-12 from Zeolite UOV. *Angew. Chemie* **2017**, *129* (15), 4388–4391.

(95) Morris, R. E.; Čejka, J. Exploiting Chemically Selective Weakness in Solids as a

Route to New Porous Materials. *Nat. Chem.* **2015**, *7* (5), 381–388.

(96) Roth, W. J.; Shvets, O. V.; Shamzhy, M.; Chlubná, P.; Kubů, M.; Nachtigall, P.; Čejka, J. Postsynthesis Transformation of Three-Dimensional Framework into a Lamellar Zeolite with Modifiable Architecture. *J. Am. Chem. Soc.* **2011**, *133* (16), 6130–6133.

(97) Chlubná, P.; Roth, W. J.; Greer, H. F.; Zhou, W.; Shvets, O.; Zukal, A.; Čejka, J.; Morris, R. E. 3D to 2D Routes to Ultrathin and Expanded Zeolitic Materials. *Chem. Mater.* **2013**, *25* (4), 542–547.

(98) Ikeda, T.; Inagaki, S.; Hanaoka, T.; Kubota, Y. Investigation of Si Atom Migration in the Framework of MSE-Type Zeolite YNU-2. *J. Phys. Chem. C* **2010**, *114* (46), 19641–19648.

(99) Wheatley, P. S.; Chlubná-Eliášová, P.; Greer, H.; Zhou, W.; Seymour, V. R.; Dawson, D. M.; Ashbrook, S. E.; Pinar, A. B.; McCusker, L. B.; Opanasenko, M.; et al. Zeolites with Continuously Tuneable Porosity. *Angew. Chemie - Int. Ed.* **2014**, *53* (48), 13210–13214.

(100) Morris, S. A.; Bignami, G. P. M.; Tian, Y.; Navarro, M.; Firth, D. S.; Čejka, J.; Wheatley, P. S.; Dawson, D. M.; Slawinski, W. A.; Wragg, D. S.; et al. In Situ Solid-State NMR and XRD Studies of the ADOR Process and the Unusual Structure of Zeolite IPC-6. *Nat. Chem.* **2017**, *9*, 1012–1018.

(101) Mazur, M.; Chlubná-Eliášová, P.; Roth, W. J.; Čejka, J. Intercalation Chemistry of Layered Zeolite Precursor IPC-1P. *Catal. Today* **2014**, *227*, 37–44.

(102) Andrews, S. J.; Papiz, M. Z.; McMeeking, R.; Blake, A. J.; Lowe, B. M.; Franklin, K. R.; Helliwell, J. R.; Harding, M. M. Piperazine Silicate (EU 19): The Structure of a Very Small Crystal Determined with Synchrotron Radiation. *Acta Crystallogr. Sect. B* **1988**, *44* (1), 73–77.

(103) Marler, B.; Wang, Y.; Song, J.; Gies, H. Topotactic Condensation of Layer Silicates with Ferrierite-Type Layers Forming Porous Tectosilicates. *Dalt. Trans.* **2014**, *43* (27), 10396–10416.

(104) Wu, P.; Ruan, J.; Wang, L.; Wu, L.; Wang, Y.; Liu, Y.; Fan, W.; He, M.; Terasaki, O.; Tatsumi, T. Methodology for Synthesizing Crystalline Metallosilicates with Expanded Pore Windows Through Molecular Alkoxysilylation of Zeolitic Lamellar Precursors. *J. Am. Chem. Soc.* **2008**, *130* (26), 8178–8187.

(105) Shamzhy, M.; Opanasenko, M.; Tian, Y.; Konysheva, K.; Shvets, O.; Morris, R. E.; Heyrovskynstitute, J.; Pisarzhevskiy, L. Germanosilicate Precursors of ADORable Zeolites Obtained by Disassembly of ITH, ITR, and IWR Zeolites. *Chem. Mater.* **2014**, *26* (19), 5789–5798.

(106) Chlubná-Eliášová, P.; Tian, Y.; Pinar, A. B.; Kubů, M.; Čejka, J.; Morris, R. E. The Assembly-Disassembly-Organization-Reassembly Mechanism for 3D-2D-3D Transformation of Germanosilicate IWW Zeolite. *Angew. Chemie* **2014**, *126* (27), 7168–7172.

(107) Blatov, V. A.; Ilyushin, G. D.; Proserpio, D. M. The Zeolite Conundrum: Why are There so Many Hypothetical Zeolites and so Few Observed? A Possible Answer from the Zeolite-Type Frameworks Perceived as Packings of Tiles. *Chem. Mater.* **2013**, *25* (3), 412–424.

(108) Pophale, R.; Cheeseman, P. A.; Deem, M. W. A Database of New Zeolite-like Materials. *Phys. Chem. Chem. Phys.* **2011**, *13* (27), 12407–12412.

(109) Akporiaye, D. E.; Price, G. D. Systematic Enumeration of Zeolite Frameworks. *Zeolites* **1989**, *9* (1), 23–32.

(110) Ennaert, T.; Van Aelst, J.; Dijkmans, J.; De Clercq, R.; Schutyser, W.; Dusselier, M.; Verboekend, D.; Sels, B. F. Potential and Challenges of Zeolite Chemistry in the Catalytic Conversion of Biomass. *Chem. Soc. Rev.* **2016**, *45* (3), 584–611.

(111) Li, X.; Deem, M. W. Why Zeolites Have So Few Seven-Membered Rings. *J. Phys. Chem. C* **2014**, *118* (29), 15835–15839.

(112) Earl, D. J.; Deem, M. W. Toward a Database of Hypothetical Zeolite Structures. *Ind. Eng. Chem. Res.* **2006**, *45* (16), 5449–5454.

(113) Foster, M. D.; Simperler, A.; Bell, R. G.; Friedrichs, O. D.; Paz, F. A. A.; Klinowski, J. Chemically Feasible Hypothetical Crystalline Networks. *Nat Mater* **2004**, *3* (4), 234–238.

(114) Li, Y.; Yu, J.; Xu, R. Criteria for Zeolite Frameworks Realizable for Target Synthesis. *Angew. Chemie - Int. Ed.* **2013**, *52* (6), 1673–1677.

2 Aims

This thesis aims to investigate possible areas to expand the application of the ADOR process:

Using the ADOR process to incorporate Al and P in between the silicate layers of an already known ADORable zeolite.

Evaluating the suitability of other already known germanosilicates to undergo the ADOR process.

Using new organic SDAs to synthesise new germanosilicate zeolites.

Evaluate the suitability of these new germanosilicates to undergo the ADOR process.

3 Experimental Methods

3.1 Synthetic Methods

3.1.1 Hydrothermal Synthesis

Zeolites are found in nature as the metastable product of silica condensation under high temperatures and intense pressures.[1] In the lab, zeolites are produced under milder conditions using initial sources of silica, aluminium and other metals with an alkali hydroxide solution to make a reaction mixture. This mixture is the placed in a Teflon liner, that is then sealed in a steel autoclave (Figure 3.1) and heated to 100-200 °C. This creates an autogenous pressure and the zeolite is crystallised over several days.[2]

Figure 3.1 Shows a standard autoclave used in hydrothermal synthesis (1) assembled by placing the PTFE liner and lid (3 and 4) into the metal jacket (2), then placing the frangible metal discs (9), inner disc (8),spring (7) and outer disc (6) on top before then screwing the cap (5) to create the closed system required for hydrothermal synthesis.

As discussed in the Chapter 1 this approach was first used by Barrer and Milton in the late 1940s to synthesise zeolites A, X and P.[3,4] Since then the field has expanded with the use of quaternary ammonium cations, the use of fluoride and the addition of new elements.[2] The use of hydrothermal synthesis unlike direct solid state synthesis allows for the formation of products with high purity, crystallinity with low energy consumption, and reduced air and liquid waste pollution.[5]

Hydrothermal synthesis allows access to metastable zeolite phases as the system has a thermodynamic trough, which is not the ground state. Hydrothermal synthesis allows access to these troughs as the bond types that occur in zeolites, are like those present in their precursor oxides. This means that there is no real change in enthalpy with the formation of a zeolite framework, and this combined with a small free energy gain for most zeolites, leaves their formation within the kinetic realm.[6]

Even though the synthesis of zeolite seems relatively simple it is still hard to have full control and predictability. There is a fine balance between many different processes solution, precipitation, polymerisation and nucleation and crystallisation. Each is dependent on different internal and external factors, including batch composition, alkalinity, water inorganic cation presence, temperature, ageing, seeding, stirring.[2]

Most samples were produced with the use of hydrothermal synthesis with the use of different sized General-Purpose Acid Digestion Vessel Parr steel autoclaves with Teflon liners. Three Carbolit High-Temperature Laboratory Oven, model PF60, were used to induce hydrothermal conditions over a range of days from 0 - 30 and temperatures from 100 – 200 °C.

3.1.2 Low Water Synthesis

It is well documented that the amount of water can play a key role in zeolite formation.[7] Firstly, an increase in water tends to lead to a dilution of the reactants and so lower supersaturation, slower nucleation and leads to greater crystal growth. It has been shown that under F^- conditions the amount of water is even more significant.[8] As the water content of the reaction reaches reagent rather than solvent level, the phase selectivity becomes even more pronounced, as low density phases become more favoured.[9]

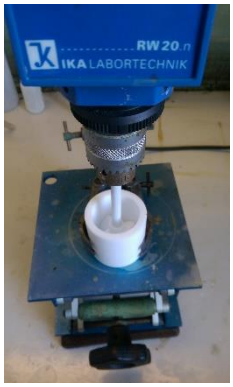

Figure 3.2 Shows the overhead motor with the stirrer attachment and the tight-fitting Teflon cup held in place by a clamp.

Recent advances in hydrothermal synthesis have used this knowledge to afford new low density zeolite frameworks with extra-large pores.[10–14] Unfortunately, the small amount of water requires a modification to the standard experimental procedure, as the gels become too thick to be mixed in the Teflon liner with a magnetic flea. For this purpose, a tight-fitting Teflon vessel was made for an overhead stirrer (Figure 3.2). This simple set-up allowed for synthesis gels to be stirred while the water content was lowered to the correct levels. This also allowed for safe addition and stirring of hydrofluoric acid to form the final

homogeneous gel, that was subsequently placed in a Teflon lined autoclave, sealed, and heated in the oven. All the low water syntheses were performed using this method.

3.2 X-Ray Diffraction

3.2.1 Crystallography

3.2.1.1 The Unit Cell

A crystal is made up of many molecules, atoms or ions arranged in an ordered repetitive fashion in all directions. The simplest repeating unit of the structure is defined as the unit cell and is repeated throughout the crystal by purely translational symmetry to form the lattice. The lattice is therefore an array of points equivalent by translational symmetry, called lattice points. This means that any atom placed on a lattice point is identical to any other placed on another lattice point. The unit cell can be selected to include all these lattice points and so contains all the symmetry elements of the structure.

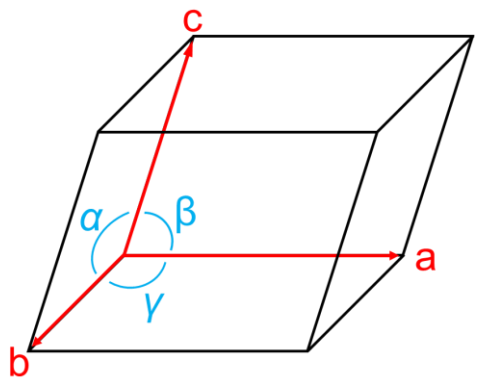

Figure 3.3 a schematic representation of a unit cell and its parameters.

The basic unit cell in three dimensions is a parallelepiped with side lengths and angles defined by 6 lattice parameters (Figure 3.3) a, b, c (corresponding to the vectors between lattice points) and *a*, *β*, *γ* (where *a* is the angle between the b- and c-axes *etc.*). The unit cell is defined based on the positions of the lattice points in the parallelepiped, in a primitive cell (*P*) there is one lattice point per unit cell, with an eighth at each corner. Other unit cells contain more than one lattice point per unit cell and include body centred (*I*), face centred (*F*) and base centred (*C*). Unlike the primitive unit cell these last three have additional lattice points, that result from translational symmetry within the unit cell. The lattice type describes the purely translational symmetry or periodicity of the structure and does not provide definitive information on atoms or molecules in the unit cell.[15–17]

3.2.1.2 Point and Space Groups

The symmetry elements of a single molecule all pass through one point and the various combinations of rotation and reflection symmetry elements gives rise to 7 crystal systems or 32 point groups. These crystal systems each possess characteristic symmetries and so place restrictions on the unit cell parameters. The combination of the crystal systems, and their restrictions, with the unit cells centring leads to the 14 Bravais lattices, as different combinations can in fact lead to equivalent lattices (Table 3.1). The Bravais lattice helps to describe the translational symmetry of the lattice.

Table 3.1 Shows the seven crystal systems, their essential symmetries and unit cell restrictions, with the 14 corresponding Bravais lattices available.

Crystal System	Essential Symmetry	Restrictions on unit cell	Bravais Lattices
Triclinic	None	None	*P*
Monoclinic	One twofold rotation and/or mirror	$\alpha = \gamma = 90°$	*P, C*
Orthorhombic	Three twofold rotations and/or mirrors	$\alpha = \beta = \gamma = 90°$	*P, I, F, C*
Tetragonal	One fourfold rotation	$a = b$; $\alpha = \beta = \gamma = 90°$	*P, I*
Trigonal	One threefold rotation	$a = b$; $\alpha = \beta = 90°$ $\gamma = 120°$	*P*
Hexagonal	One sixfold rotation	$a = b$; $\alpha = \beta = 90°$; $\gamma = 120$	*P*
Cubic	Four threefold rotation axes	$a = b = c$; $\alpha = \beta = \gamma = 90°$	*P, I, F*

In a crystal, symmetry elements do not all pass through one point, but they are regularly arranged in space in accordance with the lattice translation symmetry. This combination of translational symmetry (Bravais lattice) with the point group symmetry results in the 230 space groups. By knowing the space group and so all the symmetry operations within a crystal, it is possible to fully describe the crystal structure from the smallest unique part of the structure, or asymmetric unit. The atoms in the asymmetric unit cell are subjected to the symmetry elements of the point group to produce the unit cell and then the translational symmetry of the space group is used to obtain the whole crystal structure.[15–17]

3.2.2 Theory of X-Ray Diffraction

3.2.2.1 Introduction

The structure of a zeolite determines much of its chemistry and therefore its applications. These are closely linked to the long-range crystalline architecture. To fully understand this long-range ordering a diffraction wavelength is required that is of the same order of magnitude as the distances between atoms in the structure (around 0.1-0.2 nm). X-rays are most suited for this and are by far the most common radiation used for structure determination (though electron and neutron radiation are also used).[18]

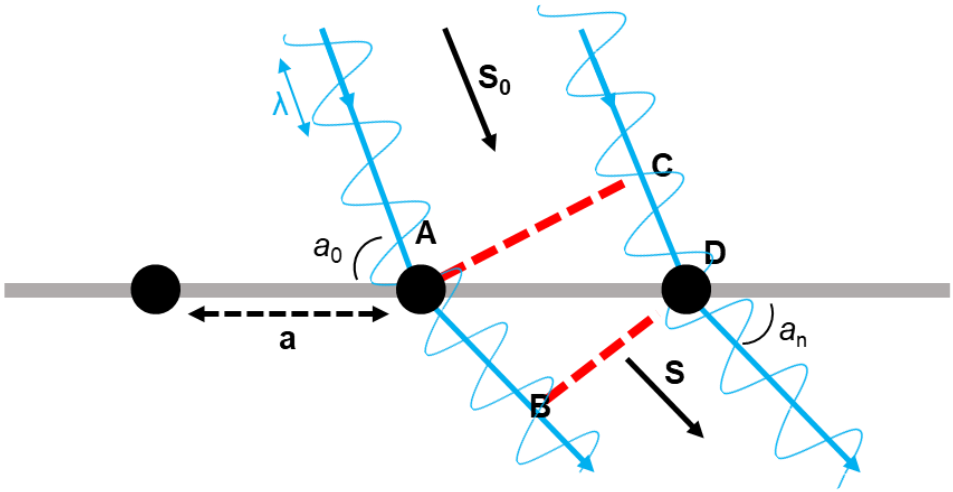

Figure 3.4 Shows a schematic representation of the Laue equation where lines AB and CD indicate the distance required to be an integral number of wavelength long for the diffraction interaction to be constructive and observed.

In 1912 Max von Laue was the first to discover the process of X-ray diffraction and theorised about conditions for diffraction to take place. In the case of a single row of ordered atoms regularly spaced by a distance (a) and scatter the incoming radiation with a wavelength (λ) (Figure 3.4). These scattered waves can interact with each other to produce either constructive of destructive interference. The path difference of the scattered rays at points A and D is AB-CD. For constructive interference to occur between the waves, the waves must be in phase and the path difference must be equal to a whole number of wavelengths. This leads to the Laue equation (Equation 3.1), where a_0 is the angle of incidence and a_n is the angle of scattering, h corresponds to an integer.[17,19]

$$\text{path difference} = a\cos a_n - a\cos a_0 = h\lambda \qquad (Equation\ 3.1)$$

This result is valid for any scattered ray that makes an angle a_n with the unit cell axis. The Laue condition is then consistent with a cone of scattered rays centred about the a axis. If written with respect to vectors the a axis then becomes $\vec{a}$ vector. The vector running

parallel to the incoming ray is $\vec{s}_0$ and that running parallel to the scattered ray is $\vec{s}$. This results in Equation 3.2 which can be rearranged using the scattering vector S defined as $\frac{1}{\lambda}(\vec{s} - \vec{s}_0)$ as seen in Equation 3.3:

$$\vec{a} \cdot \vec{s} - \vec{a} \cdot \vec{s}_0 = h\lambda \qquad (Equation\ 3.2)$$

$$\vec{a} \cdot \frac{(\vec{s} - \vec{s}_0)}{\lambda} = \vec{a} \cdot S = h \qquad (Equation\ 3.3)$$

As many crystals are a three-dimensional lattice there are three separate equations:

$$\vec{a} \cdot S = h \qquad (Equation\ 3.4)$$

$$\vec{b} \cdot S = k \qquad (Equation\ 3.5)$$

$$\vec{c} \cdot S = l \qquad (Equation\ 3.6)$$

Where h, k and l correspond to integer values. This means that for a diffraction intensity to be in phase these three equations must be satisfied simultaneously (Equation 3.7). This means that the new set of lattice vectors are related constructively to their previous ones so that $\vec{a}^* \cdot \vec{a} = 1$ and $\vec{a}^* \cdot \vec{b} = 0$ this mean that the allowed values of S form a reciprocal lattice.

$$S = h\vec{a}^* + k\vec{b}^* + \vec{l}c^* \qquad (Equation\ 3.7)$$

These Laue conditions are difficult to use and the easier method derived by Bragg soon after has become the universal basis for X-ray diffraction geometry (Figure 3.5).[17]

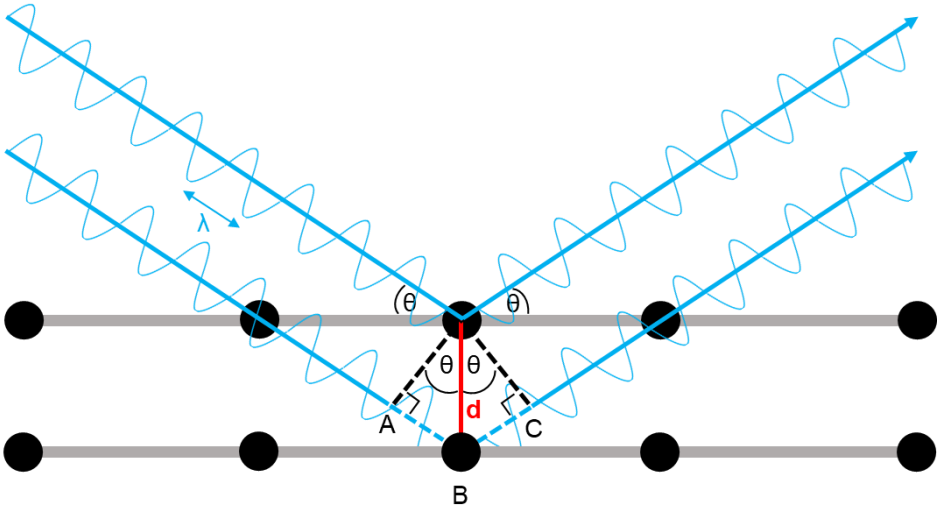

Figure 3.5 Shows a schematic representation of Bragg's Law

Bragg showed that every diffracted beam that can be produced by appropriate orientation of a crystal in an X-ray beam can be considered as though it were a reflection from sets of parallel planes passing through lattice points (or planes), like light reflecting off a mirror (Figure 3.5). This means that the angles of incidence and reflection must be equal and that the incoming and outgoing beams and the normal to the reflecting planes must themselves all lie in one plane. The path difference must then be an integer number of wavelengths given by AB+BC = $d$sinθ + $d$sinθ leading to Bragg's Law (Equation 3.8).

$$2d_{hkl}\sin\theta = n\lambda \qquad (Equation\ 3.8)$$

The plane of this reflection is defined by three integers to specify its orientation with respect to the three unit cell edges, called a Miller plane, these indices correspond to three values *h, k* and *l*. The distance between successive planes is determined by the lattice geometry and so is a function of the unit cell parameters.[15–17,19]

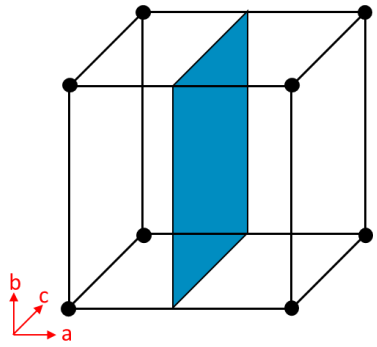

Figure 3.6 Shows a schematic representation of the (200) miller plane which intersects the unit cell halfway along the a axis, and at the origin of the b and c axes.

Miller plane indices correspond to fractional coordinates along the axes set by the unit cell. For example, the (200) plane would cut the a axis at ½, while running parallel to the b and c axes and bisecting the unit cell at ½ a (Figure 3.6). By drawing the (200) plane in every unit cell of the crystal, then an infinite number of planes is formed, separated by the distance d_{200}.If atoms reside close to or on these planes in a repetitive fashion, then the incoming X-rays are 'reflected' off this group of planes and a diffraction spot is observed at the scattering angle 2θ.[15–17,19]

3.2.2.2 Single Crystal X-Ray Diffraction

Single crystal X-ray diffraction is one of the best methods for determination of a crystal structure. By rotating a single crystal in the X-ray beam and recording the pattern of spots and their intensities it is possible to gain insight into the structure of the crystal (Figure 3.7). From a diffraction pattern it is possible to discern three key properties:[17]

- The pattern will have a specific geometry, which is related to the lattice and unit cell geometry of the crystal structure, and can be used to determine the repeat distance (and direction) between molecules.
- The pattern has symmetry not just in the spatial arrangement of spots but also their intensity as spots that lie in symmetry-related positions will have similar intensities. This symmetry is closely related to the symmetry of the unit cell of the crystal structure.
- Apart from the symmetry there is no apparent relationship between the intensities of the individual spots. These intensities hold the information for determining positions of atoms in the unit cell as the relative atomic positions, through their combination of their individual interactions with the X-rays, that generate the different amplitudes for the different directions of scattering.

By measuring the geometry and symmetry of the scattering pattern it is therefore possible to determine the unit cell geometry and symmetry. Then by measuring the individual intensities it is possible to determine the full molecular structure.

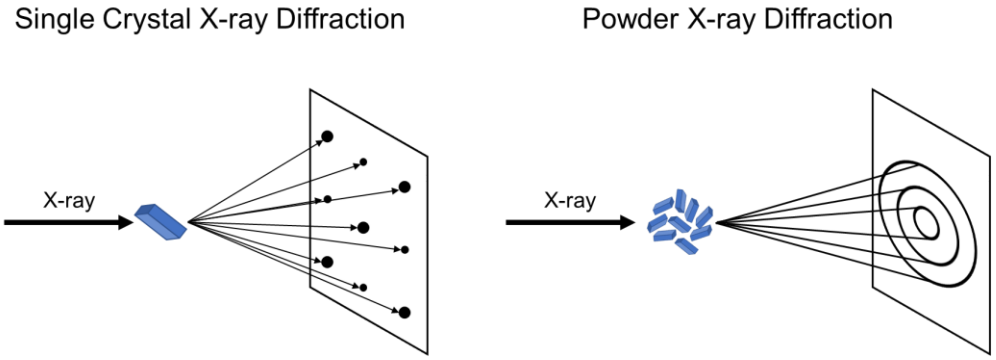

Figure 3.7 Shows a comparison between the single crystal and powder X-ray diffraction. Showing the spots created when X-rays interact with a single large crystal and the rings of intensity that are generated upon interacting with a material with multiple crystal in random orientations.

3.2.2.3 Powder X-Ray Diffraction

Single crystal X-ray analysis is an incredibly powerful tool as it gives a diffraction pattern with discrete diffracted beam, in a definite direction relative to the orientation of the crystal and the incident beam. The diffraction conditions are severe and so the single crystal is rotated to generate the whole pattern. However, as is clear from the title it requires a single, well-formed crystal of a large enough size to be selected, mounted, and diffracted. In the case of zeolites, a large majority of the crystals are too small to analyse efficiently. This is because if more than one single crystal is present, then the X-rays simultaneously irradiate different orientations. This results in two separate diffraction

patterns being superimposed on each other and means that as the sample is rotated different reflections for both crystals will be generated. However, while the direction of the diffracted beam will vary the Bragg intensities will be the same in each crystal. This results in a powder pattern where the corresponding reflections appears as identical spots on a circle. As the number of crystals increases, for example a microcrystalline powder sample, then the diffraction pattern appears as set of circles (Figure 3.7). Each circle represents a reflection, where the radii is dictated by the Bragg equation and related to the unit cell geometry, the intensity is closely related to those that would be produced by a single crystal. For ease of analysis these circles are then transformed to into a 2D plot by taking a cross-section of the circles, where the *x*- and y-axes correspond to the 2θ angle and the intensity respectively.[16,17,19]

3.2.2.3.1 Phase Identification

Powder X-ray Diffraction has two main applications phase identification and Rietveld refinement. The peaks in a PXRD pattern contain the same information concerning unit cell parameters as would be observed in single crystal. This means that a PXRD pattern can be considered as a 'fingerprint' to identify a material. By comparing the PXRD pattern against a known database it is possible to determine the structure and the purity of the sample. This aids in the identification of already known materials, whether they have been correctly synthesised, or ensuring that data gathered on a new sample during single crystal analysis is representative of the entire sample. The IZA website contains simulated PXRD patterns for all the currently known unique frameworks.[16,20]

3.2.2.3.2 Rietveld Refinement

Determining a new structure just from a PXRD pattern is more complicated, than single crystal analysis, due to overlapping peaks. However, determining the structure is made easier when a starting model for the proposed structure is known, this method is known as Rietveld refinement.[21,22]

The parameters are refined against each individual intensity to minimise the residual R_{wp} using a least squares method (Equation 3.9), where y_{io} and y_{ic} are the observed and calculated intensities at the i^{th} step and $w_i = 1/y_{io}$ is set to be equal to a suitable weighting.[18]

$$R_{wp} = \sum w_i |y_{io} - y_{ic}|^2 \qquad Equation\ 3.9$$

Using the least squares method, the difference between y_{io} and y_{ic} is minimised. This is done by firstly considering factors like the diffractor zero-point, background, and peak shape. Once a reasonable model is established, then other parameters are refined including the unit cell, coordinates and site occupancies. It is possible to simply refine only the profile parameters, to obtain accurate lattice parameters, and achieving a 'structureless fit', known as a Le Bail fit.[23]

The quality of a refined model is quantified using the weighted profile or R_{wp} (Equation 3.10) and the expected profile R_e (Equation 3.11), where N is the number of profile points and P is the number of parameters.

$$R_{wp} = \sqrt{\frac{\sum w_i(y_{io} - y_{ic})^2}{\sum w_i y_{io}^2}} \qquad Equation\ 3.10$$

$$R_{exp} = \sqrt{\frac{N - P}{\sum w_i {y_{io}}^2}} \qquad Equation\ 3.11$$

The quality or goodness of the fit is given for the data by comparing the R_{exp} and R_{wp} using Equation 3.12. A good refinement is typified by a χ^2 value close to 1. As R_{wp} approaches R_{exp}, and the χ^2 value moves closer to 1, this indicates that the model fits well with the observed data.

$$\chi^2 = \frac{R_{wp}}{R_{exp}} \qquad Equation\ 3.12$$

Monitoring the many parameters can often be less intuitive and misleading. During refinement, a plot of observed vs calculated profiles and their difference is used. This allows for problems to be spotted more easily.[24]

3.2.3 Sources for X-Ray Powder Diffraction

3.2.3.1 Laboratory Sources

The standard source of X-rays in the laboratory is an X-ray tube. This involves an evacuated enclosure of glass and a metal. Electrons are produced by passing of an electric current through a wire filament. These electrons are then accelerated to a high velocity by an electrical potential and then abruptly stopped with a water-cooled metal block. The majority of this kinetic energy is then released as wasted heat, but a small portion generates X-rays from interacting with the metal atoms. This interaction involves the

ejection of a core orbital electron from the metal atom, which is then replaced by an electron from a higher energy orbital dropping down. The difference in energy is then emitted as electromagnetic radiation. As there are several different transitions the most intense is selected and the other emissions suppressed using a monochromator crystal (typically graphite).[16,17]

3.2.3.2 Synchrotron Sources

Laboratory source X-ray generation is a relatively cheap and efficient way to get relatively good data. However, the production of more X-rays results in the generation of a large amount of heat, therefore laboratory sources are limited if researchers want more intense X-rays and better data, particularly for Rietveld refinement. The synchrotron provides incredibly good data for such purposes.

In a synchrotron, the electrons are generated by an electron gun, accelerated close to the speed of light by an accelerator, transferred to a booster ring, to increase their energy, and then transferred to the outer storage ring (Figure 3.8). The outer storage ring can be described as a large ring (usually hundreds of metres in diameter) consisting of a series of straight sections separating electric and/or magnetic fields.

As the electrons travel around the ring and are deflected by the magnets they emit electromagnetic radiation at a tangent to the electrons' orbit. The radiation emitted is channelled down beamlines as a continuous spectrum of electromagnetic radiation that is then tuned/monochromated for the desired experiment. The intensity of the radiation produced can be increased with the use of insertion devices. These devices force the electrons to do a 'wiggling' motion, this increases the amount of radiation emitted as radiation is released at each bend in the 'wiggle'. These individual emissions superimpose on each other increasing the intensity of the radiation emitted at each magnet compared to the standard bending magnets.

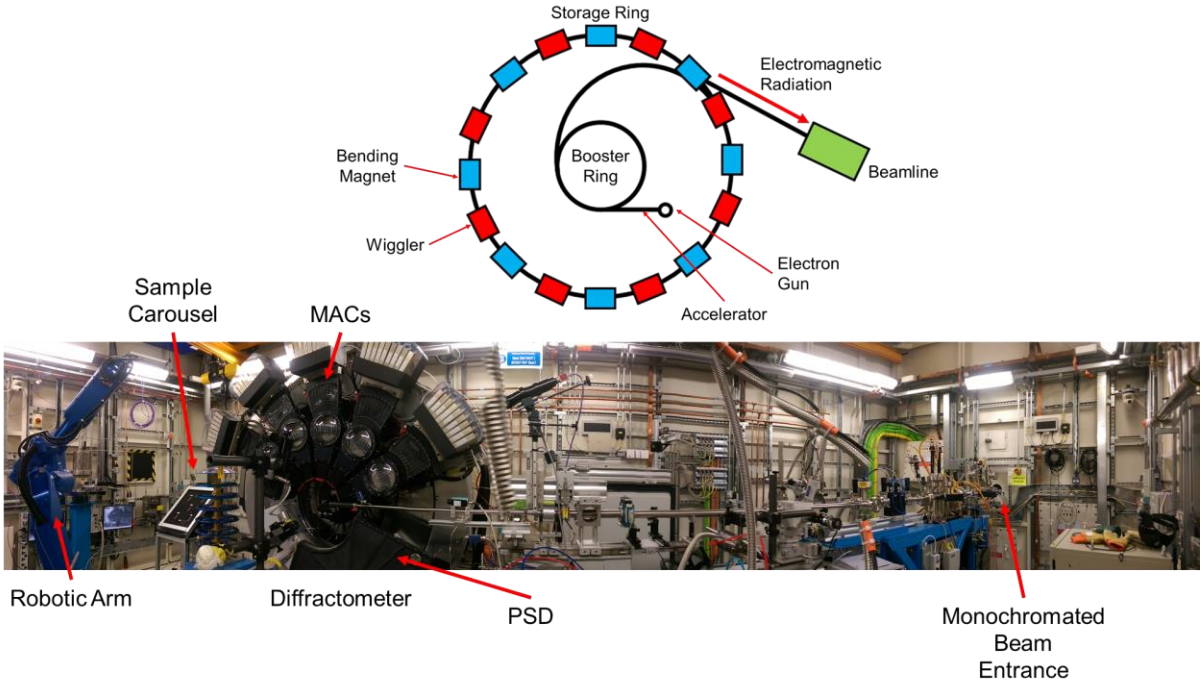

Figure 3.8 Shows a schematic representation of a synchrotron (top) and a photo from inside of the experimental hutch from beamline I11 at the Diamond Light Source

The production of such high intensity X-rays allows for single crystal analysis of smaller crystals and the production of higher quality powder X-ray diffraction patterns for refinement, that is impossible with laboratory grade X-ray sources.[17,25]

3.2.3.2.1 Beamline I11

Before entering the experimental hutch on Beamline I11 the high-energy X-rays (15 KeV) are trimmed using primary slits, then monochromated with two liquid cooled Si(111) crystals. The beam then passes through a set of double bounce harmonic rejection mirrors and two sets of additional monochromating slits.

The beam enters the hutch and passes along the beam pipe the interaction with the sample is then collected by the diffractometer (Figure 3.8), which has 3 coaxial, high precision rotary stages (θ, 2θ and δ). The MAC detectors (high resolution) are mounted on the 2θ circle and the PSD (high speed) is mounted on the δ circle. Each of the 5 MAC detectors consists of 9 Si crystals and allows for a full 2θ scan of 3-150° with 40° of motion, allowing for overlap between the detectors, allowing for quick and good quality data aquisition.[26]

3.2.3.3 Equipment Used for X-Ray Diffraction

Laboratory powder X-ray diffraction measurements were carried out using either a PANalytical Empyrean or a STOE STADIP diffractometer both using monochromated Cu $K\alpha_1$ radiation.

The PANalytical Empyrean diffractometers are operated in capillary Debye-Scherrer mode with data collected at room temperature. A sample is placed in a glass capillary and spun while the detector moves across a range of 2θ values stopping at specific intervals to collect data for a set amount of time.

The STOE diffractometers operate in reflection, Bragg Brentano, θ-2θ mode with data collected at room temperature. A sample is placed in a sample holder that is then placed on a moveable platform. The sample is then rotated as the detector moves across a range of 2θ values stopping at specific intervals to collect data for a set amount of time.

Powder X-ray diffraction measurements were carried out at beamline I11 at the Diamond Light Source, Oxfordshire (Figure 3.8).[27] Some limited single crystal analysis was conducted at beamline I19 at the Diamond Light Source, Oxfordshire.

3.3 Adsorption Analysis

3.3.1 Introduction

Because of the pores and channels present in zeolites their potential surface area is very large. When gases enter the pores of the zeolite they can then bind to the internal surface of the zeolite (adsorbed). Adsorption can happen in two ways: physical and chemical adsorption. Physical adsorption (or physisorption) is weaker than chemical adsorption (chemisorption) as it is due to induced or permanent dipoles, and is only observed at low temperatures, with reduced capacity at higher temperatures. This tends to mean that physisorption tends to be reversible on the decrease in partial pressure.

3.3.1.1 Adsorption Isotherms

Most adsorption properties are reported as adsorption isotherms, where the experiment is carried out using an adsorption gas (like N_2), while maintained at a constant temperature (usually 77.4 K). The adsorption isotherm therefore represents the totality of equilibrium states for pressures from 0 to saturation vapour pressure of the adsorbate. The isotherm is usually displayed, according to IUPAC recommendations, as the amount adsorbed per gram of adsorbent as a function of the equilibrium pressure. If the experiment occurs above the triple point of the adsorption gas, then it is plotted as a

function of the relative equilibrium pressure (p/p^0), where p^0 is the saturation vapor pressure of the adsorption gas. Isotherms can be split into six characteristic isotherm types, classified by IUPAC.[28]

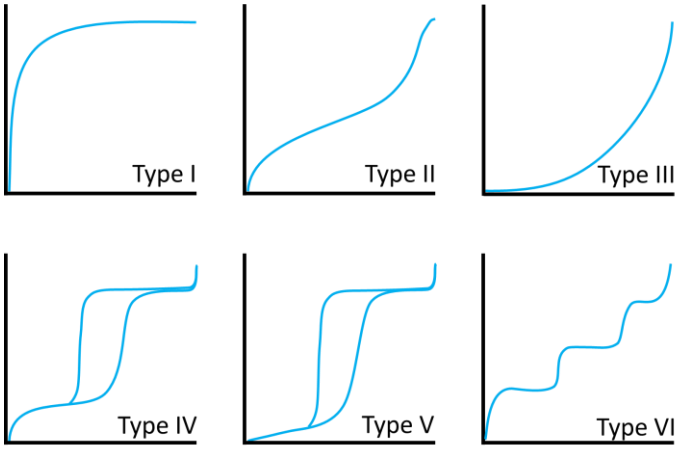

Figure 3.9 Shows examples of the 6 characteristic isotherms that can be observed, where the x-axis is pressure and the y-axis is amount of gas adsorbed.

The shape of the isotherm (Figure 3.9) correlates to the structure and so can imply some important properties of the structure. Zeolites, like most microporous materials, exhibit a Type I isotherm, where the isotherm shows an initial large adsorption step at low partial pressures followed by a plateau. This corresponds to the gas molecules adsorbing in a monolayer fashion onto the inner walls of the zeolite due to the greater affinity of the gas for the zeolite walls. This monolayer of gas molecules fills the micropores and the framework becomes saturated resulting in the plateau that is observed. A further increase in uptake is sometimes observed when, at high partial pressures, the probe gas begins to condense.

Type II, Type III, and Type VI isotherms are indicative of nonporous or macroporous materials. Type II isotherms show a similar profile to Type I isotherms except there is a gradual increase in the adsorption amount instead of a plateau as the gas can uptake beyond the monolayer adsorption. Type III isotherms indicate a formation of multilayers of adsorbate but the initial monolayer formation step is missing, due to a strong adsorbate-adsorbate interaction. Type VI isotherms show a step-wise profile, because of the adsorption of distinct monolayers of gas and requires a material with a very uniform surface area and adsorbent sites.

Type IV and Type V isotherms are related to Type II and Type III isotherms respectively, but show a slight variation as Type IV and V isotherms show a finite number of layers of gas molecules adsorbed onto the material and so their adsorption terminates near to

relative pressure of unity. Type IV and V isotherms also show a difference in their adsorption and desorption behaviour, known as hysteresis loops, due to the capillary condensation typically associated with mesoporosity.[29]

3.3.1.2 Determining Porosity

There are many theories to explain the adsorption behaviour observed that can be used to determine the surface area and porosity of materials from their isotherms. The Langmuir theory assumes that the gas molecules do not interact with each other and that they adsorb in a monolayer on an energetically identical surface. However, the most widely used theory is Brunauer-Emmett-Teller (BET theory) and is derived from the Langmuir theory.[30,31] The main difference is that BET considers the multi-layered adsorption of gas molecules. The main assumption is that the binding energy between layers of gas molecules is about the same as that between the gas molecules and the surface and that a lower monolayer does not need to be completed before the formation of an upper layer. This results in Equation 3.13:

$$\frac{p/p^0}{n^a(1-p/p^0)} = \frac{1}{n_m^a C} + \left[\frac{C-1}{n_m^a C}\right]\left(\frac{p}{p_0}\right) \qquad (Equation\ 3.13)$$

Where p and p_0 are the equilibrium and saturation pressure of adsorbates at the temperature of adsorption, n_m^a is the quantity adsorbed at the statistical monolayer and C is the BET constant related to the energy of adsorption.

By plotting $\frac{p/p^0}{n^a(1-p/p^0)}$ against $\left(\frac{p}{p_0}\right)$ and looking at the linear region below $\left(\frac{p}{p_0}\right) = 0.3$ it is possible to determine C and n_m^a from the slope $\left[\frac{C-1}{n_m^a C}\right]$ and the y-intercept of the line $(\frac{1}{n_m^a C})$. The monolayer capacity n_m^a can be used to calculate the specific BET surface area of a solid by taking into account the equivalent surface area σ_m that the probe molecule takes up in the monolayer, using the Equation 3.14:

$$a_{BET} = \frac{A}{m^s} = \left(\frac{n_m^a}{m^s}\right) N_A \sigma_m \qquad (Equation\ 3.14)$$

Where N_A is Avogadro's number. This method works well for non-porous and mesoporous materials where the linear region is found between $\left(\frac{p}{p_0}\right)$=0.05 and 0.35, however for microporous solids this linear region occurs typically below 0.05.[28]

This means that the application of BET to microporous materials, while convenient, is also considered rather flawed as it provides a surface area measurement that only works in a

comparative sense, rather than the real surface area. To increase the reproducibility Rouquerol proposed the use of several criteria to better the selection of an appropriate linear region.[32]

The Rouquerol criteria, as in BET, requires the *C* value to be positive. In addition, the term $n^a(p^0 - p)$ should increase with increasing $\frac{p}{p_0}$ for the data selected. The BET treatment can then be validated by ensuring that the relative pressure at which the monolayer capacity n_m^a is found within the data that was used to fit the BET parameters. Finally the term $1\sqrt{C} + 1$ is used to provide further confirmation as its value should be close to the relative pressure calculated from the BET at the monolayer capacity.[29]

N_2 Adsorption Analysis were conducted on a Micromeritics ASAP 2020 surface area and porosity analyser at -196 ˚C.

3.4 TGA

Most zeolites crystallise with the organic SDA trapped in the pores, calcination then removes the volatile organic SDA. An important measurement is to ascertain the difference between the weight of as-synthesised versus calcined samples. The as-made sample is placed in an inert crucible and heated under a specified atmosphere. As the temperature increases a microbalance measures the weight loss of the sample. With respect to zeolites, weight losses are typically observed first from the loss of water from the pores and then from decomposition of the SDA and its loss from then pores.[33]

The TGA experiments were measured on a Netzsch TG 209 instrument in air. The samples were heated in an alumina crucible at a heating ramp rate of 10 °C/min.

3.5 Electron Microscopy

3.5.1.1 SEM

Scanning electron microscopy differs from conventional microscopy in its use of a focused beam of high-energy electrons instead of a conventional light source to generate a variety of signals at the surface of solid specimens instead of penetrating through the sample. These signals from interactions between the sample and the electron beam can then be used to reveal information about the sample including: external morphology, chemical composition, crystalline structure, and orientation of materials making up the sample.

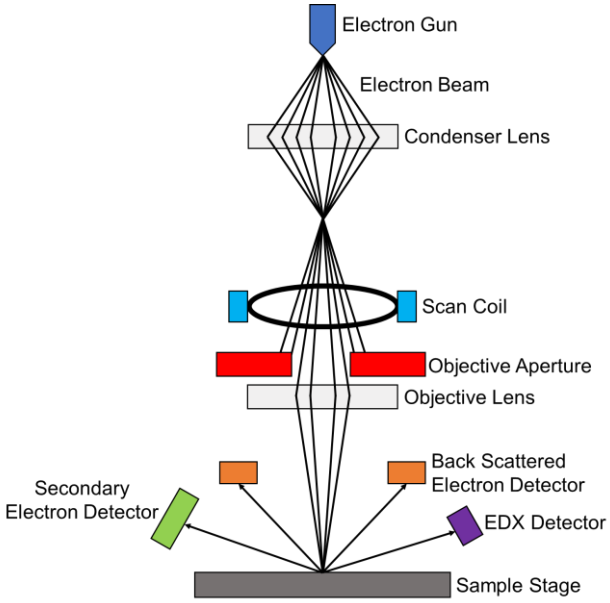

Figure 3.10 Shows a schematic representation of a scanning electron microscope setup with the electron beam shown

In a scanning electron microscope, the flow of electrons produced by an electron gun under vacuum are accelerated down towards the sample (Figure 3.10). Electromagnetic fields, lenses and apertures act on the beam to produce a monochromatic, focussed beam of a specific 'spot size' on the sample. Once the beam reaches the sample the interaction between the electrons and the sample produces a variety of signals, that are detected and used to form an image.[34,35] Of the signals produced the most interesting are secondary electrons and backscattered electrons, which are collected by the detector to produce an image and collect information about the surface of the sample that has come into contact with the electron beam.

Secondary electrons occur from the inelastic scattering interaction of the primary electron beam with the outer valence electrons of the specimen atoms. This leads to the ejecting of the electron and the excitation of the atom. After several collisions, the low energy electron may then be able to escape from the surface if enough energy remains. The energy required to escape the sample surface means that secondary electrons tend to originate from a few nanometres from the sample surface.[36] Another issue associated with secondary electrons is the prevalence of charging, which is produced by the build-up of electrons in the sample and their uncontrolled discharge, this often leads to the loss of resolution and the build-up of bright spots. The effect of charging can be reduced with the use of lower currents, to prevent the build-up of electrons, and the use of a conducting gold-coating, so that developed charges are passed to the ground.[37]

Backscattered electrons occur from the elastic scattering of the primary beam electrons by positive nuclei of the sample atoms towards the detector. These elastic scattering electrons have a higher energy as they are simply reflected out of the specimen. This is particularly useful for imaging as these higher energy electrons originate from deeper within the sample and, as heavier elements back scatter electrons more strongly, better contrast between areas of different chemical compositions can be produced.[36]

3.5.1.2 STEM

Scanning electron microscopy (SEM) uses a focused beam in a raster pattern to scan the sample while transmission electron microscopy (TEM) is more like an optical microscope in that a very thin sample is flooded with electron beams and an image is produced from the effect of the sample on the transmitted electrons.[38]

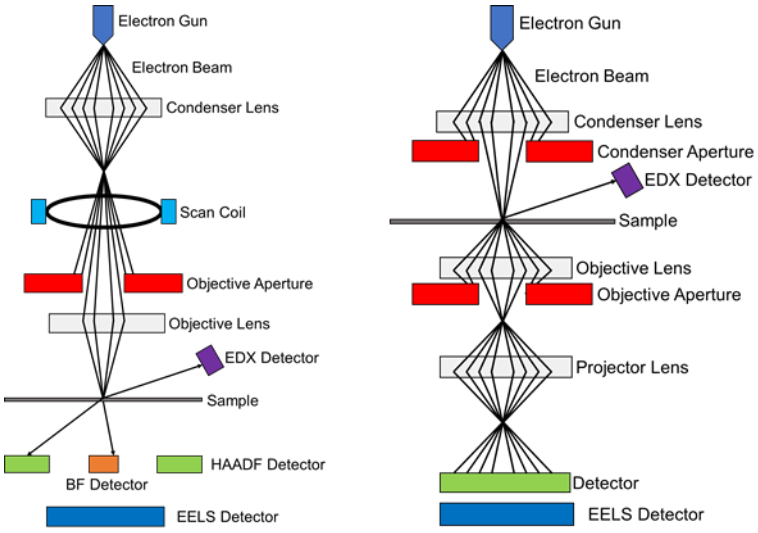

Figure 3.11 Shows a schematic representation of a scanning transmission electron microscope (left) and a transmission electron microscope (right) for comparison.

Scanning transmission electron microscopy (STEM) combines both principles as it requires a very thin sample and scans the sample with a finely focused beam of electrons in a raster pattern. The STEM is then able to collect information on the electrons that are transmitted through the sample and on those that are produced from the interaction with the sample. This gives STEM some incredible advantages, as it uses a smaller electron beam and working distances than SEM it can produce much higher resolution images (better than 0.1 nm). STEM is also, unlike TEM, able to analyse all the additional signals produced from the interaction of the beam with the sample and thanks to the raster pattern correlate those spatially in the sample providing more in-depth knowledge of the sample.

The interaction of the beam with the sample produces a variety of signals that can be analysed. Electrons that leave the sample at low angles with respect to the incident beam, due to inelastic scattering, are known as bright field signals (BF) and provide an image in a similar way to the electrons in TEM. Electrons that leave the sample at relatively high angles, due to elastic scattering, are referred to as high angle annular dark field (HAADF) signals. These are scattered electrons, with an intensity dependent on the thickness of the sample, and so help to produce an image with better resolution and contrast than with just BF. Transmitted electrons that lose a measurable amount of energy lead to electron energy loss spectroscopy (EELS). This can provide information about the interacting atoms, including elemental identity, chemical bonding, and surface properties. It is also possible to generate X-rays for EDX analysis.[38]

3.5.1.3 EDX

The collision of the primary electron beam with core electrons of an atom can result in their ejection from the atom. This produces a vacancy in the inner orbital and the atom moves to an excited state. This causes the relaxation of a higher energy electron, from an outer orbital, to fill this vacancy. The difference in energy results in the emission of an X-ray photon of a specific wavelength related to the energy gap between these orbitals. The quantisation of electron energy levels means that atoms produce X-rays characteristic of their energy gaps and so differ from element to element. By collecting and identifying the characteristic X-rays emitted and their relative quantities, by a sample, it is possible to determine the chemical composition of the sample.[35]

3.5.1.4 Equipment Used for SEM and EDX

The SEM images were recorded using a Jeol JSM-5600 scanning electron microscope with a tungsten filament electron gun. The operating voltage ranged between 5 and 25 kV. Samples were coated with gold, using a Quorom Q150R ES, to reduce the effect of charging on the sample. EDX analysis was carried out with an Oxford Inca Energy system on the same SEM instrument using a higher operating voltage of 25 kV.

3.5.1.5 Equipment Used for STEM

STEM images were provided by Dr Alvaro Mayoral from the Nanoscience Institute of Aragon, Advanced Microscopy Laboratory. The measurements were performed using an X-FEG TITAN FEI 60-300 transmission electron microscope operated at 300 kV. The column was fitted with a CEOS spherical aberration corrector for the electron probe which was aligned using a gold standard sample prior to every experiment, assuring a nominal

point resolution of 0.8Å. The microscope also incorporated a Gatan Tridiem energy filter, an EDAX EDS and a Fischione HAADF detector. The half-angle employed was 17.5 mrad.

3.6 Nuclear Magnetic Resonance Spectroscopy

3.6.1 Introduction

3.6.1.1 Origin of NMR Signal

Atomic nuclei have an intrinsic spin quantum number (I) that depends on the number of protons and neutrons in its nucleus. The spin angular momentum vector quantity, $\boldsymbol{I}$, is quantised:

$$\boldsymbol{I_z} = m\hbar \qquad (Equation\ 3.15)$$

Where the magnetic quantum number (m) takes values +I and -I in integer steps, leading to 2I+1 degenerate spin states. In the case of ^{1}H, which has a value of I = ½ and so has two spin states so $\boldsymbol{I} = \pm\frac{1}{2}\hbar$.

Nuclei with $I > 0$ possess a magnetic dipole moment ($\boldsymbol{\mu}$) that is directly proportional to $\boldsymbol{I}$ (Equation 3.16), where γ is the gyromagnetic ratio constant, which is unique to each nuclei type.

$$\boldsymbol{\mu} = \gamma\hbar \qquad (Equation\ 3.16)$$

This leads to the quantisation of $\boldsymbol{I}$ and $\boldsymbol{\mu}$. These discrete values are energetically degenerate in the absence of an external magnetic field. However, in the presence of an external magnet (B_0) this degeneracy is removed, and two discrete levels are formed (Figure 3.12). The energy between the levels is shown in Equation 3.17:

$$\Delta E = -\boldsymbol{\mu B} \qquad (Equation\ 3.17)$$

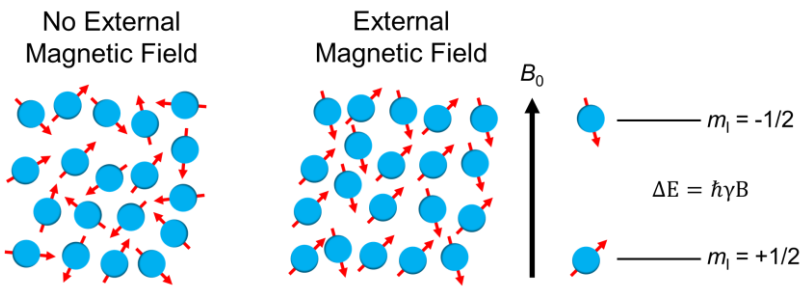

Figure 3.12 Shows the impact of no external magnetic field (left) and an external magnetic field (right) on the nuclear magnetic moments. With no external magnetic field all orientations of the nuclear magnetic moment are degenerate. With an external magnetic field (B_0) the nuclear spins will align, removing the degeneracy of the energy levels through the Zeeman interaction. An example is shown for a I = ½ nuclei where the degenerate spin states split into 2I+1 spins states with an energy $m\hbar\gamma B$.

In the presence of a strong field, in the z axis, the quantisation axis coincides with the field direction.

$$\Delta E = -\mu_z B \qquad (Equation\ 3.18)$$

Where B is the strength of the field and μ_z is the projection of the magnetic moment ($\boldsymbol{\mu}$) onto $\boldsymbol{B}$. These equations can be combined to give the field-induced splitting of the nuclear energy levels or the Zeeman interaction, the Zeeman energy of state is given by:

$$E = -m\hbar\gamma B \qquad (equation\ 3.19)$$

This means that the energy of the nucleus is shifted by an amount proportional to the magnetic field strength (B), gyromagnetic ratio (γ) and the z component of the angular momentum (m).[39] The 2I+1 states are equally spaced with an energy gap of $\hbar\gamma B$. The selection rules for NMR state that only transitions with $\Delta m = \pm 1$ are observed. This means that the resonance condition ($\Delta E = h\nu$) is given by:

$$\Delta E = h\nu = \hbar\gamma B$$
$$\nu = \frac{\gamma B}{2\pi} \qquad (Equation\ 3.20)$$

Where (ν) is the frequency of the electromagnetic radiation. All $2I$ allowed transitions for a spin I nucleus have the same energy. The magnetic moment experienced by a nucleus in a molecule is slightly different from the external magnetic. This effect is used to characterise specific chemical environment and is known as chemical shift (Section 3.6.1.2).

When placed in a magnetic field a collection of magnetic nuclei will spread themselves amongst the available $2I + 1$ energy levels according to the Boltzmann distribution. The ratio of the populations is:

$$\frac{n_{upper}}{n_{lower}} = e^{-\frac{\Delta E}{kT}} \qquad (Equation\ 3.21)$$

The energy required to reorientate spins becomes dwarfed by the thermal energy Kt, leading to little tendency for the spins to become ordered in the lower energy level. This simplifies Equation 3.21 to:

$$\frac{n_{lower} - n_{upper}}{n_{lower} + n_{upper}} = \frac{\Delta E}{2kT} \qquad (Equation\ 3.22)$$

As spectroscopy relies on the excitation of nuclei *etc.* from lower energy levels to higher energy levels with the same probability as it is to induce the reverse. This means the

intensity of signal is dependent on the difference in the two population levels. In the case of NMR, the upward transition outnumbers the reverse by 10^4 – 10^6 this means that NMR signals are generally weaker than other spectroscopic methods. To maximise the signal strength, it is therefore necessary to maximise the ΔE with the use of strong magnets or nuclei with a high γ.[39,40]

3.6.1.2 Origin of Chemical Shift

The magnetic moment of a nucleus in a molecule changes depending on its chemical environment as the circulation of electrons around the nuclei produces a local magnetic field (B'). B' can oppose or augment the external magnetic field (B_0) and changes the effective magnetic field experienced by the nucleus B_{eff}, this is known as chemical shielding:

$$B_{eff} = B_0 - B' = B_0(1 - \sigma) \qquad (Equation\ 3.23)$$

Where the shielding constant (σ) is a field-independent shielding constant and is related to the chemical environment of the nucleus. This indicates that nuclei of the same type but in different bonding situations would be excited by a different frequency and so the resonance frequency (Equation 3.24) of a nucleus becomes characteristic of its environment and can defined as:

$$v = \frac{\gamma B_0(1 - \sigma)}{2\pi} \qquad (Equation\ 3.24)$$

In practice the shielding constant is a cumbersome way to measure chemical shift, so chemical shifts are defined by the difference in resonance frequencies between the nucleus of interest and a reference (Equation 3.25). In practice this usually involves putting a small amount of reference compound in with the sample. For ^{1}H and ^{13}C the reference compound used is tetramethylsilane.

$$\delta = 10^6 \frac{(v - v_{ref})}{v_{ref}} \qquad (Equation\ 3.25)$$

3.6.1.3 Anisotropic Interactions

Anisotropic interactions play a key role in the chemical shifts observed in an NMR spectrum and occur due to chemical shielding, dipolar, J-coupling and quadrupolar interactions. Electron distribution around a nucleus is not perfectly spherical and so this means the constants σ and δ should not be used and instead described as a vector, **σ** and therefore the shift as **δ**. This means that the observed chemical shift δ can be described as:

$$\delta = \delta_{11} \sin^2 \theta \cos^2 \Phi + \delta_{22} \sin^2 \theta \sin^2 \Phi + \delta_{33} \cos^2 \theta \qquad (Equation\ 3.26)$$

Where δ_{ll}, δ_{22} and δ_{33} describe the three principle components of $\boldsymbol{\delta}$ when expressed in its principal axis system. The angles θ and Φ describe the orientation of the vector in relation to the external magnetic field B_0. By rewriting Equations 3.26 as:

$$\delta = \delta_{iso} + \left(\frac{\Delta}{2}\right)[(3\cos^2 \theta - 1) + \eta(\sin^2 \theta \cos 2\Phi)] \qquad (Equation\ 3.27)$$

This indicates that the chemical shift δ is because of an orientation dependent (anisotropic) and an orientation independent term (isotropic). The $\delta_{iso,}$ or isotropic component, is given by the average of three principle components $((\delta_{11} + \delta_{22} + \delta_{33})/3)$, while $\Delta = \delta_{33} - \delta_{iso}$ and $\eta = (\delta_{22} - \delta_{11})/\Delta$ describe the magnitude and asymmetry of the shielding vector respectively.[39]

3.6.1.4 Internuclear Interactions

The position of the peak in an NMR spectrum is also dependent on the interactions between nuclei. Every nucleus with a non-zero spin quantum number has a magnetic dipole and so behaves like a small bar magnet. When two spins are close to each other they experience each other's magnetic field, this leads to a slightly different effective magnetic field that depends on the orientation of both nuclei's magnetic dipole moments. This dipole-dipole interaction is dependent on the spin-spin distance and the gyromagnetic moment ratios of the coupled spins and is given by the dipole-dipole coupling constant:

$$\omega_D = -\left(\frac{\mu_0}{4\pi}\right)\frac{\hbar \gamma_A \gamma_X}{r_{AX}^3} 1/2(3\cos^2 \theta - 1) \qquad (Equaiton\ 3.28)$$

Where r^3_{AX} is the internuclear distance between spins A and X, θ is the angle between the internuclear vector and the external magnetic field B_0.[39,40]

3.6.2 Solution-State NMR

Typically, NMR for the analysis of organic molecules uses solution state NMR where the sample is dissolved in a deuterated solvent. Molecules in a liquid tumble rapidly and consequently the axis and speed of rotation also change rapidly. This Brownian motion means that the anisotropic interactions are averaged out leaving just the isotropic value δ_{iso}. This means that solution state NMR does not suffer from line broadening. J-coupling caused by indirect dipole-coupling, through the electrons, which has a much smaller magnitude than direct dipole-coupling, can be observed.[40]

3.6.2.1 Instruments Used for Solution-State NMR

^{1}H and ^{13}C solution state NMR were carried out on either a Bruker Avance AVII 400 or Bruker AV 400. Compounds were dissolved in deuterated water or chloroform containing tetramethylsilane (TMS) as a reference.

3.6.3 Solid-State NMR

Unlike the organic SDAs analysed with solution state NMR, zeolites and other inorganic solids cannot be dissolved in a deuterated solvent for analysis. This leads to a specific set of problems in the characterisation of solids by NMR.

As zeolites are analysed in the solid-state there is no rapid tumbling of molecules. In a solid the nuclei are held in place and every nucleus has a neighbour, which they have a dipolar coupling interaction with and each interaction will have different orientations and distances. This means that direct dipolar interactions play a greater role in the NMR spectra as the constant ω_D is dependent on the orientation and distance. This infinite number of dipolar interactions leads to a Gaussian type line broadening of the NMR peak. The width and shape of the line are determined primarily by Δ and η, providing information about the local structure and symmetry.[41]

This broad signal, that is removed by the rapid tumbling of molecules in solution, is not possible in a solid. This means that to decrease this broadening effect, solid-state NMR uses Magic Angle Spinning (MAS). Where the sample is placed in a ZrO_2 holder or 'rotor' and spun at an angle of 54.74 ° θ with respect to the direction of the external magnetic field (Figure 3.13).

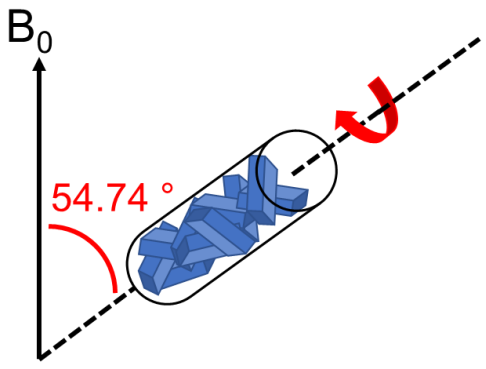

Figure 3.13 Shows a schematic representation of a sample spun at the magic angle in relation to the external magnetic field.

By spinning at this precise angle, the $(3\cos^2\theta - 1)$ factor becomes 0 and so the anisotropic interaction angular dependency is removed. This leads to less line broadening caused by the dipolar coupling and so a sharper NMR peak. The rotation speed of the rotor

can be varied, and this rotation speed is increased in relation to the magnitude of the anisotropic interactions, so that they can be efficiently removed. Without this the line shape is broken into a series of 'spinning side-bands' separated by integer multiples of the spinning rate vR from the isotropic peak.[39]

Another issue for solid-state NMR, with respect to zeolites, is that the nuclei typically of interest have relatively low abundance, this is particularly the case for ^{29}Si, which has a natural abundance of about 4 %. This means that solid-state MAS NMR runs on zeolite samples require far more time than typically seen for solution state NMR or for solid-state MAS NMR of more abundant nuclei like ^{27}Al and ^{31}P.[39]

3.6.3.1 Experiments for Solid-State NMR

3.6.3.1.1 Single Pulse NMR

Single pulse NMR experiments are the simplest form of analysis and involve a 90 ° pulse being applied to the sample and the resultant signal subsequently recorded (Figure 3.14). To allow time for relaxation before another pulse a waiting period of 5 T_2 is used before each repetition.

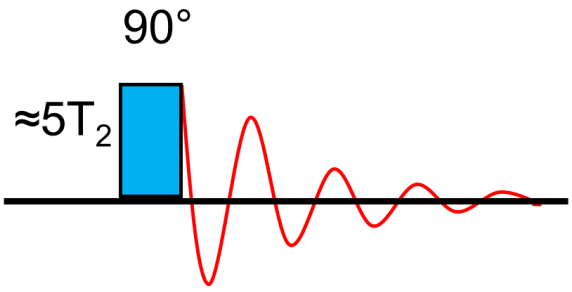

Figure 3.14 Shows a typical single-pulse NMR experiment, where the initial 90 ° pulse (blue) is applied and the signal (red) recorded.

^{29}Si single pulse experiments were carried out at 9.4 T field using radiofrequency field strength between 71-83 kHz, octakis(trimethylsiloxy)silsequioxane as the reference compound, with relaxation intervals of 120 s. [39,41,42]

3.6.3.1.2 Cross-Polarisation Experiments

Cross-polarisation experiments aim to increase the sensitivity of MAS NMR to certain spins, this is particularly helpful for zeolites and their ^{29}Si NMR analysis. Its low natural abundance of around 4.7 % leads to a low signal-to-noise ratio. ^{29}Si nuclei also require longer relaxation times between pulses due to the absence of relaxation stimulating strong homonuclear dipolar interactions. Cross-polarisation experiments use the transfer of magnetisation to overcome both these issues (Figure 3.15).

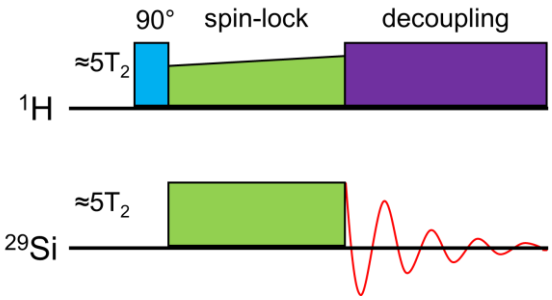

Figure 3.15 Shows a schematic representation of the pulse sequence used for a cross-polarisation experiment involving ^{1}H and ^{29}Si. Showing the initial pulse on ^{1}H (blue), followed by the ramped pulse during spin=locking (green) and the decoupling applied (purple) while the signal (red) for ^{29}Si is measured.

This technique involves the creation of magnetisation by a 90 ° pulse on ^{1}H nuclei, this magnetisation is then transferred to the ^{29}Si nuclei during 'contact time'. This involves the use of low-power pulses applied to both spins to 'lock' the magnetisation along a particular direction while transfer takes place. The spin-lock time is chosen to maximise the transferred signal intensity, which depends on the transfer rate and the relaxation times of each spin. After this contact time the ^{29}Si signal is acquired through decoupling of the ^{1}H.[39,42]

The magnetisation is transferred from highly-abundant and high γ ^{1}H nuclei to the less abundant ^{29}Si and leads to a gain in signal related to the ratio of γ_H/γ_{Si}. This also allows the experiment to be repeated more frequently due to this increase in abundance of ^{1}H nuclei and its higher γ. The use of cross-polarisation does not just increase signal strength but also gives vital structural information as this gives an indication of the proximity of these two nuclei, making such experiments particularly useful for seeing Silanol groups.

3.6.3.1.3 2D Correlation Experiments

Two-Dimensional experiments can be used to get an even better understanding of the nature of chemical bonding in the solid, using interactions between nuclei of different spins.

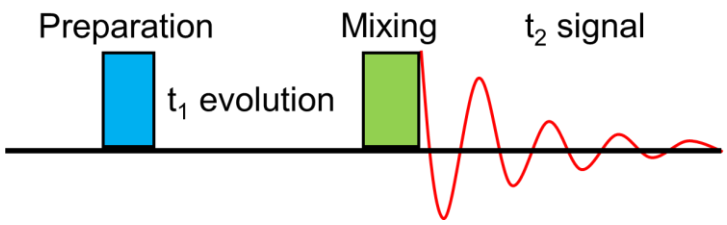

Figure 3.16 Shows a schematic representation of the pulse sequence used for a 2D correlation experiment. Showing the initial preparation step, where magnetisation is created (blue). This magnetisation is allowed to evolve before a second pulse is applied in a mixing step (green). The t_2 signal produced can then be recorded, whose amplitude is related to the t_1 evolution time and the proximity of the two nuclei.

This involves several steps to produce a signal (Figure 3.16). First magnetisation is created in a preparation step, using a single or combination of pulses, this magnetisation evolves over time (t_1). After this period a second pulse or a combination of pulses is applied in a mixing step. This causes the transfer of magnetisation from one spin to the other, which is then followed by the acquiring of the signal produced during the t_2 stage. This means that the amplitude of t_2 can be correlated to the evolution in t_1 indicating how close the nuclei are in space. By performing a double Fourier transformation of the data this leads to a 2D spectrum showing between which spins the magnetisation was transferred to. Correlation experiments can be between the same nuclei or two different nuclei, which requires the application of different pulses. The experiments can be designed to show the magnetisation transferred either through J-coupling or through-space dipolar interactions. If a cross peak is observed this indicates that the two spins are connected by covalent bonds or close in space.[39,41]

3.6.3.2 Instruments Used for Solid-State NMR

Solid-state NMR experiments in this thesis were conducted using a Bruker Avance III spectrometer equipped with either a 9.4 T superconducting magnet (^{1}H Larmor frequency of 400.13 MHz) or a wide-bore 14.1 T magnet (^{1}H Larmor frequency of 600 MHz). the samples were packed into standard ZrO_2 rotors and rotated at the magic angle at different rates (from 10-14 kHz).

3.7 NO Production

NO production of the copper and acid site zeolites was monitored using a Sievers 280i Nitric Oxide Analyser (NOA). A supply of nitrogen and oxygen is connected to the analyser, with the nitrogen gas passing through the vial containing the sample to be analysed. Ozone is generated in the analyser from the oxygen supply. The reaction of NO, produced from the zeolite, with the ozone, results in the formation of excited nitrogen dioxide, that relaxes releasing a photon, that is measured by a photo multiplier. This

means the more photon detected is proportional to the amount of NO produced by the zeolite.

3.8 References

(1) Colella, C. Chapter 27 - Natural Zeolites and Environment. In *Introduction to Zeolite Science and Practice*; Čejka, J., Corma, A., Bekkum, H. van, Schüth, F., Eds.; Elsevier, 2007; Vol. 168, pp 999–1035.

(2) Yu, J. Chapter 3 - Synthesis of Zeolites. In *Introduction to Zeolite Science and Practice*; Čejka, J., Corma, A., Bekkum, H. van, Schüth, F., Eds.; Elsevier, 2007; Vol. 168, pp 39–103.

(3) Barrer, R. M. Synthesis of a Zeolitic Mineral with Chabazite-like Sorptive Properties. *J. Chem. Soc.* **1948**, 127–132.

(4) Milton, R. M. Molecular Sieve Adsorbents. US Patent. 2,882,244, 1959.

(5) Morris, R. E. Ionothermal Synthesis of Zeolites and Other Porous Materials. In *Zeolites and Catalysis: Synthesis, Reactions and Applications*; Wiley-VCH Verlag GmbH & Co. KGaA: Weinheim, Germany, 2010; Vol. 1, pp 87–105.

(6) Cundy, C. S.; Cox, P. A. The Hydrothermal Synthesis of Zeolites: Precursors, Intermediates and Reaction Mechanism. *Microporous Mesoporous Mater.* **2005**, *82* (1–2), 1–78.

(7) Strohmaier, K. G. Synthesis Approaches. In *Zeolites and Catalysis: Synthesis, Reactions and Applications*; Wiley-VCH Verlag GmbH & Co. KGaA: Weinheim, Germany, 2010; Vol. 1, pp 57–86.

(8) Burton, A. W.; Zones, S. I. Chapter 5 - Organic Molecules in Zeolite Synthesis: Their Preparation and Structure-Directing Effects. In *Studies in Surface Science and Catalysis*; Čejka, J., Corma, A., Bekkum, H. van, Schüth, F., Eds.; Elsevier, 2007; Vol. 168, pp 137–179.

(9) Camblor, M. A.; Villaescusa, L. A.; Díaz-Cabañas, M. J. Synthesis of All-Silica and High-Silica Molecular Sieves in Fluoride Media. *Top. Catal.* **1999**, *9*, 59–76.

(10) Jiang, J.; Jorda, J. L.; Yu, J.; Baumes, L.; Mugnaioli, E.; Diaz-Cabanas, M. J.; Kolb, U.; Corma, A. Synthesis and Structure Determination of the Hierarchical Meso-Microporous Zeolite ITQ-43. *Science* **2011**, *333* (6046), 1131–1134.

(11) Sun, J.; Bonneau, C.; Cantín, Á.; Corma, A.; Díaz-Cabañas, M. J.; Moliner, M.; Zhang, D.; Li, M.; Zou, X. The ITQ-37 Mesoporous Chiral Zeolite. *Nature* **2009**, *458* (7242), 1154–1157.

(12) Corma, A.; Díaz-Cabañas, M. J.; Jiang, J.; Afeworki, M.; Dorset, D. L.; Soled, S. L.; Strohmaier, K. G. Extra-Large Pore Zeolite (ITQ-40) with the Lowest Framework Density Containing Double Four- and Double Three-Rings. *Proc. Natl. Acad. Sci. U. S. A.* **2010**, *107* (32), 13997–14002.

(13) Jiang, J.; Yun, Y.; Zou, X.; Jorda, J. L.; Corma, A. ITQ-54: A Multi-Dimensional Extra-Large Pore Zeolite with 20 x 14 x 12-Ring Channels. *Chem. Sci.* **2015**, *6* (1), 480–485.

(14) Qian, K.; Wang, Y.; Liang, Z.; Li, J. Germanosilicate Zeolite ITQ-44 with Extra-Large 18-Rings Synthesized by Using Commercial Quaternary Ammonium as Structure-

Directing Agent. *RSC Adv.* **2015**, *5*, 63209–63214.

(15) Clegg, W. *Crystal Structure Determination*; Oxford University Press, 1998.

(16) Weller, M. T. *Inorganic Materials Chemistry*; Oxford University Press, 2011.

(17) Clegg, W. *X-ray Crystallography*, 2nd ed.; Oxford University Press: Oxford, 2015.

(18) Morris, R. E.; Wheatley, P. S. Chapter 11 - Diffraction Techniques Applied to Zeolites. In *Introduction to Zeolite Science and Practice*; Čejka, J., Corma, A., Bekkum, H. van, Schüth, F., Eds.; Elsevier, 2007; Vol. 168, pp 375–401.

(19) Hammond, C. *The Basics of Crystallography and Diffraction*; Oxford University Press, 2005.

(20) McCusker, L. B.; Baerlocher, C. Chapter 2 - Zeolite Structures. In *Introduction to Zeolite Science and Practice*; Čejka, J., Corma, A., Bekkum, H. van, Schüth, F., Eds.; Elsevier, 2007; Vol. 168, pp 13–37.

(21) Rietveld, H. M. Line Profiles of Neutron Powder-Diffraction Peaks for Structure Refinement. *Acta Crystallogr.* **1967**, *22* (1), 151–152.

(22) David, W. I. F.; Shankland, K.; McCusker, L. B.; Bärlocher, C. *Structure Determination from Powder Diffraction Data*; David, W. I. F., Shankland, K., McCusker, L. B., Bärlocher, C., Eds.; Oxford University Press: Oxford, 2006.

(23) Le Bail, A. Whole Powder Pattern Decomposition Methods and Applications: A Retrospection. *Powder Diffr.* **2005**, *20* (4), 316–326.

(24) Young, R. A. *The Rietveld Method*; International Union of Crystallograhy, 1993.

(25) Willmott, P. *An Introduction to Synchrotron Radiation: Techniques and Applications*; Wiley, 2011.

(26) Adamson, P.; Lennie, A.; Murray, C.; Parker, J.; Potter, J.; Tang, C.; Thompson, S.; Yuan, F. *Beamline I11 User Manual*, 1.7.9.; Diamond Science Division, 2015.

(27) Diamond Light Source. How Diamond Works http://www.diamond.ac.uk/Home/About/How-Diamond-Works.html# (accessed Apr 25, 2017).

(28) Sing, K. S. W. Reporting Physisorption Data for Gas/Solid Systems with Special Reference to the Determination of Surface Area and Porosity. *Pure Appl. Chem.* **1982**, *54* (11), 2201–2218.

(29) Llewellyn, P. L.; Maurin, G. Chapter 17 - Gas Adsorption in Zeolites and Related Materials. In *Introduction to Zeolite Science and Practice*; Čejka, J., Corma, A., Bekkum, H. van, Schüth, F., Eds.; Elsevier, 2007; Vol. 168, pp 555–610.

(30) Brunauer, S.; Emmett, P. H.; Teller, E. Adsorption of Gases in Multimolecular Layers. *J. Am. Chem. Soc.* **1938**, *60* (2), 309–319.

(31) Langmuir, I. Chemical Reactions at Low Pressures. *J. Am. Chem. Soc.* **1915**, *37* (5), 1139–1167.

(32) Rouquerol, J.; Llewellyn, P.; Rouquerol, F. Is the BET Equation Applicable to Microporous Adsorbents? In *Studies in Surface Science and Catalysis*; Llewellyn, P., Rodriquez-Reinoso, F., Rouquerol, J., Seaton, N., Eds.; 2007; Vol. 160, pp 49–56.

(33) Coats, A. W.; Redfern, J. P. Thermogravimetric Analysis. A Review. *Analyst* **1963**, *88* (1053), 906–924.

(34) Hafner, B. Scanning Electron Microscopy (SEM). In *Electron Microscopy of Polymers*; Springer Berlin Heidelberg: Berlin, Heidelberg, 2013; pp 87–120.

(35) Goldstein, J. I.; Newbury, D. E.; Echlin, P.; Joy, D. C.; Lyman, C. E.; Lifshin, E.; Sawyer, L.; Michael, J. R. *Scanning Electron Microscopy and X-ray Microanalysis*; Springer US, 2003.

(36) Egerton, R. F. The Scanning Electron Microscope. In *Physical Principles of Electron Microscopy*; Springer US: Boston, MA, 2005; pp 125–153.

(37) Echlin, P. Sample Surface Charge Elimination. In *Handbook of Sample Preparation for Scanning Electron Microscopy and X-Ray Microanalysis*; Springer US: Boston, MA, 2009; pp 247–298.

(38) Nellist, P. D. Theory and Simulations of STEM Imaging. In *Aberration-Corrected Analytical Transmission Electron Microscopy*; Springer New York: New York, NY, 2011; pp 89–110.

(39) Ashbrook, S. E.; Dawson, D. M.; Griffin, J. M. Solid-State Nuclear Magnetic Resonance Spectroscopy. In *Local Structural Characterisation*; John Wiley & Sons, Ltd, 2013; pp 1–88.

(40) Hore, P. J. *Nuclear Magnetic Resonance*; Oxford University Press, 1995.

(41) Gedeon, A.; Fernandez, C. Chapter 12 - Solid-State NMR Spectroscopy in Zeolite Science. In *Introduction to Zeolite Science and Practice*; Čejka, J., Corma, A., Bekkum, H. van, Schüth, F., Eds.; Elsevier, 2007; Vol. 168, pp 403–434.

(42) Fyfe, C. A. *Solid state NMR for chemists*; C.F.C. Press, 1983.

4 Formation of a Zeolite-AlPO Hybrid Using the ADOR Process

4.1 Aim

This chapter will discuss the previous research and the recent history of incorporating Al, P and Si into the same framework and the issues surrounding their formation using hydrothermal synthesis, including the prevalence to avoid Si-O-P bonds. The advantages of the ADOR process in forming other energetically unfavourable structures, through a step-wise irreversible process will be discussed. Investigations will then be conducted into the use of the ADOR process to incorporate Al and P in between the IPC-1P layers of the dissembled germanosilicate **UTL**, thereby creating a Zeolite-AlPO hybrid material like IPC-2 with distinct AlPO and silicate zones in the framework. This material will then be characterised through chemical and spectroscopic analysis.

4.2 Introduction

4.2.1 Zeotypes

Zeotypes include a family of materials whose structure is based on that of zeolites but consist of elements atypical of aluminosilicate zeolites. Examples of these materials include AlPOs and SAPOs (aluminophosphates and silicoaluminophosphates respectively). Aluminophosphates were first described by Flanigen *et al*. in the early 1980s.[1] AlPOs have a similar framework structure to traditional zeolites, with tetrahedral AlO_4^- and PO_4^+ units bound together through corner sharing oxygens. The need for charge balancing leads to the formation of a zeolite framework with a 1:1 ratio of Al to P, with a preferential formation of even-numbered rings.[2] Consequently the frameworks of AlPOs are neutral and do not require cations or anions to compensate for any framework charge. This leads to AlPOs having no Brønsted acidity and somewhat limited catalytic activity.[3] There are over 50 phosphate-containing structures recognised by the IZA, some of which are not known in their aluminosilicate zeolite analogue forms.[4] SAPOs consist of Al, P and Si tetrahedra together in the same framework imparting the properties of both zeolites and AlPOs on the same framework. The structures are typically described as an AlPO framework with Si substituted into Al and P sites.[3]

4.2.2 Formation of Si-O-P Bonds

The early days of zeolite research saw great interest in investigations into the inclusion of other elements like phosphorus into the zeolite framework structures. Flanigen *et al.* reported the incorporation of phosphorus into the zeolite framework using similar conditions as those used for the hydrothermal synthesis of zeolites.[5,6] However such claims were controversial and refuted by the other leading figures of the zeolite research community Barrer and Kuehl. Both argued that the presence of phosphorus, in the zeolitic materials synthesised by Flanigen, was simply a result of the intercalation of phosphate ions within the zeolite cavities and not of the incorporation of tetrahedral phosphorus into the framework structure.[7–9]

The formation of the first SAPOs in the 1980s was the first instance of Si and P being present in the same framework structure.[10] Yet the successful inclusion of Si and P into the same framework did not result in the formation of Si-O-P bonds.[11] The substitution of Si into the framework is shown to avoid the formation of unfavourable bonds like P-O-P, P-O-Si, and Al-O-Al. Si is therefore only incorporated into the SAPO structure in two ways: either into a hypothetical P site, or into a hypothetical Al and P site. A combination of these two substitutions is seen in the formation of Si islands in SAPOs (Figure 4.1). [3,12]

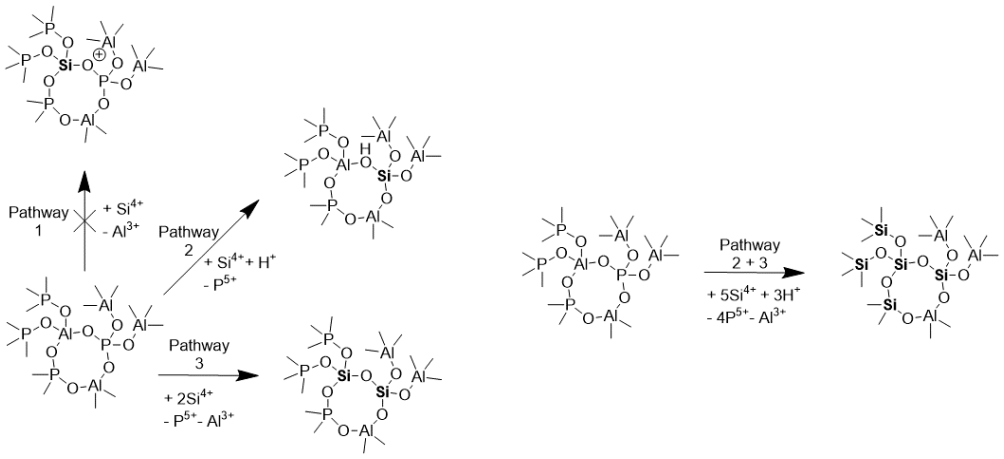

Figure 4.1 Shows a schematic representation of the incorporation of Si into the AlPO framework to form a SAPO; avoiding the formation of Si-O-P bonds. 3 different pathways are possible (left). Pathway 1 involves the substitution of Al by Si; this is disallowed as it involves the formation of the energetically unfavourable Si-O-P bonds. Pathway 2 involves the insertion of Si into a P site, leading to the formation of a negatively charged framework that is balanced by protons attached to bridging oxygens. Pathway 3 involves the double substitution of neighbouring P and Al sites by Si. The combination of pathways 2 and 3 (right) results in the formation of islands of Si as the surrounding P sites are replaced with Si, resulting in a total substitution of 5Si for 4P and 1Al. The positions that underwent substitution are highlighted in bold.

Further research has also resulted in similar conclusions, showing that SAPOs are able to avoid the formation of these energetically unfavourable Si-O-P bonds.[13–16] The different conditions required for the synthesis of AlPOs and zeolites makes them mutually exclusive

adding further complication to the formation of a framework containing Si, P and Al. A typical synthesis for AlPOs is favoured using a low to neutral pH. AlPO formation is disrupted when the pH is above 10 or below 3, due to solubilisation of the materials and dense phase formation/deformation due to Al coordination expansion under those respective conditions.[12,17] In comparison zeolites are favoured by alkaline conditions to promote the deprotonation and solubilisation of silica. Attempts to synthesise zeolites at lower pH tends to lead to the formation of dense phases.[18] It seems that using the traditional hydrothermal or bottom-up synthesis methods is unsuited for the formation of a framework with Si, P and Al, due to the impossibility of accommodating these mutually exclusive requirements. Although frameworks containing Si, Al and P do exist (SAPOs) there are some limitations regarding controlling the location of silicon in the framework and, as mentioned previously, the system will actively avoid the formation of Si-O-P bonds.

The inability to form these energetically unfavourable structures is reminiscent of the challenges faced by zeolite researchers in the formation of 'unfeasible' zeolites. It is possible that, like 'unfeasible' zeolites, the formation of these structures is hampered by the techniques used in their synthesis. The use of hydrothermal synthesis allows for the easy making and breaking of bonds. This allows the system to avoid the more energetically unfavourable bonding situations, whether it's the formation of Si-O-P bonds or the formation of seven-member rings.[19–21]

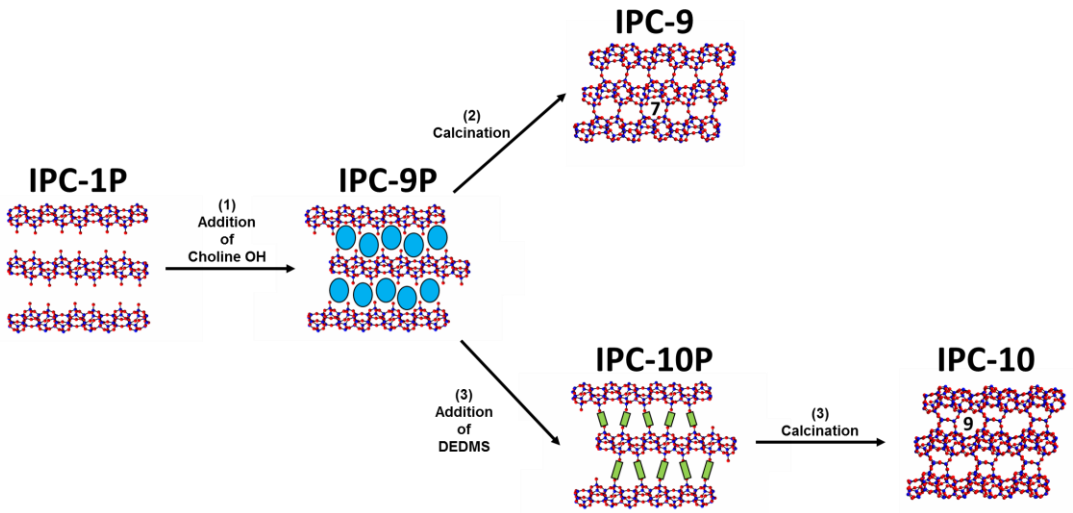

Figure 4.2 Shows a schematic representation of the formation of the 'unfeasible' zeolites IPC-9 and IPC-10. 1) After disassembly of UTL to form IPC-1P the addition of choline cation (blue circle) causes the layers to shift with respect to each other. The layers can then be reassembled in two ways. 2) Direct calcination to form IPC-9 (top). 3) Intercalation of the covalent bonding agent DEDMS (green rectangles) followed by calcination to form IPC-10 (bottom). The shift in the layers by the choline allows for the formation of 7 rings in IPC-9 and 9 rings in IPC-10 (highlighted). Ge *d4r* T-atoms in black, Si T-atoms in blue and O in red.

The use of the ADOR process has already yielded the successful formation of 'unfeasible' zeolites IPC-9 and IPC-10, whose frameworks contain 7- and 9-ring channels respectively (Figure 4.2).[21] The key to the success of the ADOR process is the use of the irreversible reassembly step, which involves the condensation of the layers by calcination.[22] This means that, unlike traditional hydrothermal synthesis, the ADOR process has the potential to accommodate the requirements for the formation of zeolites and AlPOs through a step-wise manner; while the irreversibility of these steps could prevent the system from avoiding energetically unfavourable situations like Si-O-P bonds. It was therefore hoped that by using the ADOR process it would be possible to organise the incorporation of aluminium and phosphorus into the IPC-1P structure and then force the formation of Si-O-P bonds through the reassembly step (Figure 4.3).

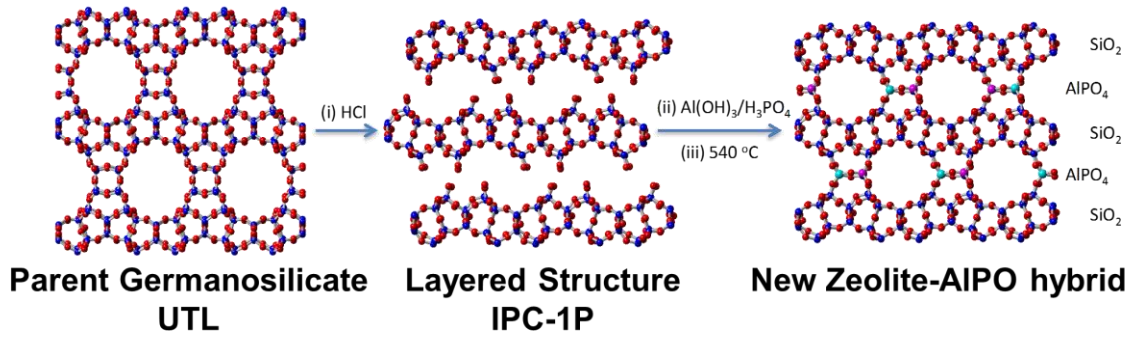

Figure 4.3 Shows a schematic of the use of the ADOR process to dissemble UTL and then incorporate AlPO zones between the silicate layers to form a zeolite-AlPO hybrid (highlighted). Si/Ge atoms are represented with blue atoms, oxygens with red, phosphorus with pink and aluminium with turquoise.

This organisation and reassembly process would not only lead to the formation of high energy structures through an irreversible step-wise process, but will also provide an avenue to direct the location of Al, P, and Si. The disassembly of the germanosilicate to form silicate layers followed by the incorporation of Al and P between these layers will result in the formation of discrete zones of AlPO and silicate layers.

4.3 Experimental

4.3.1 Synthesis of UTL

The synthesis of **UTL** was carried out according to the procedure reported by Paillaud *et al.* and Shamzhy *et al.*[23,24] Germanium dioxide (1.35 g, 12.90 mmol) was added to a solution of (6R,10S)-6,10-dimethyl-5-azaspiro[4.5]decan-5-ium hydroxide (30 mL, 12 mmol) in a Teflon liner and stirred until homogeneous. Fumed silica (1.56 g, 25.97 mmol) was added to the solution and stirred until homogeneous. The synthesis gel weight was checked, and water added to reach the required molar ratio. The pH of the solution was then checked

and 12 M HCl added dropwise to reach a pH of ~11. The synthesis was then placed in a steel-lined autoclave and heated at 175 °C for 10 days. The resultant product was then filtered, washed with distilled water, and then allowed to dry overnight.

4.3.2 Formation of IPC-1P

The formation of IPC-1P was carried out according to the procedure reported by Roth *et al.*[25] In an example synthesis Ge-**UTL** (1.00 g) was placed in a stirring solution of 0.1 M HCl (100 mL) and heated at 95 °C for 16 hours. The resultant product was then filtered and washed with additional water and dried overnight (yield = 0.86 g).

4.3.3 Investigations into the Formation of the Zeolite-AlPO Hybrid

Investigations into the incorporation of Al and P into the IPC-1P structure were conducted based on a similar procedure to form the IPC-2 structure from IPC-1P.[25] IPC-1P was placed into a solution containing the source of aluminium and phosphorus. These were stirred for 30 mins and then the Teflon liner placed in a steel-lined autoclave and heated for 16 hours at 150 – 175 °C. The resultant product was then taken out, filtered, washed with water, and dried overnight. The final reassembly step took place by calcination of the product at 580 °C for 6 hours with a 1 °C/min ramp rate.

The syntheses were varied according to pH, aluminium, and fluoride source. The pH was varied by the addition of extra phosphoric acid or aluminium hydroxide until the desired pH was reached.

4.3.4 Synthesis of the Zeolite-AlPO Hybrid

IPC-1P (0.100 g) was added to a stirring solution of distilled water (10 mL) in a Teflon liner, followed by the addition of aluminium hydroxide (0.03 g, 0.038 mmol). After 30 minutes, phosphoric acid was added until the solution reached pH 5. Once complete the solution was transferred to a steel-lined autoclave and heated at 175 °C for 16 hours. The solution was then filtered with 0.01 M HCl, then water before being allowed to dry overnight. The material was then calcined at 575 °C for 6 hours with a ramp rate of 1 °C/min (yield = 0.89 g).

4.3.5 Reformation of IPC-1P

The IPC-1P material was reformed by placing the zeolite-AlPO hybrid (0.50 g) with HCl (2 M, 10 mL) followed by heating at 95 °C for 16 hours. The resultant solid was then filtered, washed with water, and then dried overnight (yield = 0.34 g).

4.3.6 Synthesis of ^{29}Si-Enriched Zeolite-AlPO Hybrid

Germanium dioxide (0.609 g, 5.82 mmol) was added to a solution of (6R,10S)-6,10-dimethyl-5-azaspiro[4.5]decan-5-ium hydroxide (10 mL, 5.85 mmol) in a Teflon liner and stirred until homogeneous. A combination of normal TEOS (2.04 g, 9.79 mmol) and ^{29}Si-enriched TEOS (0.386 g, 1.85 mmol) was then added and the solution stirred overnight to ensure hydrolysis of the TEOS. The synthesis gel weight was checked, and water added to reach the required molar ratio. The pH of the solution was then checked and 12 M HCl added to reach a pH of ~11. The synthesis was then placed in a steel-lined autoclave and heated at 175 °C for 10 days. The resultant product was then filtered, washed with distilled water, and then allowed to dry overnight.

The formation of the zeolite-AlPO hybrid followed the same procedure as for the unenriched sample.

4.4 Results and Discussion

4.4.1 Formation of UTL and IPC-1P

4.4.1.1 Formation of UTL

The first procedure was to simply repeat the process that was reported by Roth *et al.*[25] The assembly of Ge-**UTL** was analysed by PXRD to show that the material had indeed been synthesised correctly (Figure 4.4).

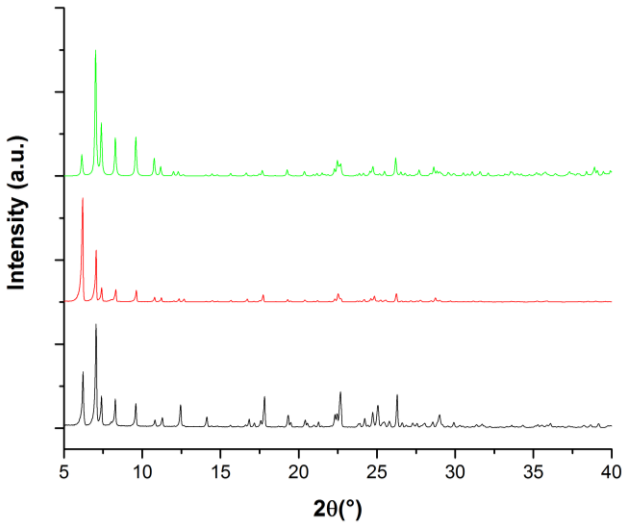

Figure 4.4 Shows the PXRD patterns for the standard Ge-UTL (green) compared to the synthesised Ge-UTL before (black) and after calcination (red) showing the correlation of the material to the PXRD pattern previously reported.

The PXRD pattern of the Ge-**UTL** was shown to match the expected PXRD pattern of the **UTL** framework. Even after calcination the material retained the key peaks associated with the PXRD pattern of **UTL** including the 200 peak at 6.14 ° 2θ.

SEM and EDX analysis of this material showed the characteristic crystal morphology associated with **UTL** (Figure 4.5).

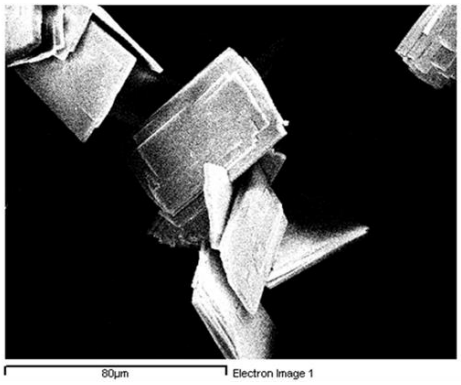

Elemental Analysis (Atomic Percent)

Spectrum	O	Si	Ge	Total
1	70.91	24.04	5.05	100
2	69.53	23.48	6.99	100
3	71.79	23.17	5.04	100
Average	70.74	23.56	5.69	

Figure 4.5 Shows the SEM and EDX analysis of the Ge-UTL confirming the rectangular platelet crystal morphology and Si/Ge ratio (4.14) typically associated with Ge-UTL.

The SEM images confirmed the crystals obtained were comparable to those reported previously.[23] The crystals showed the typical rectangular platelet-like morphology associated with **UTL**, while EDX analysis indicated the crystals had a Si/Ge ratio of 4.14, which is comparable to that used in the ADOR process reported by Roth *et al.*[25]

4.4.1.2 Disassembly of UTL

The disassembly of the product to form IPC-1P was also conducted using similar conditions reported by Roth *et al*.[25] Treatment of the germanosilicate **UTL** with 0.1 M HCl resulted in a dramatic change in the PXRD pattern, typically associated with disassembly of the Ge-**UTL** to form a layered material (Figure 4.6).

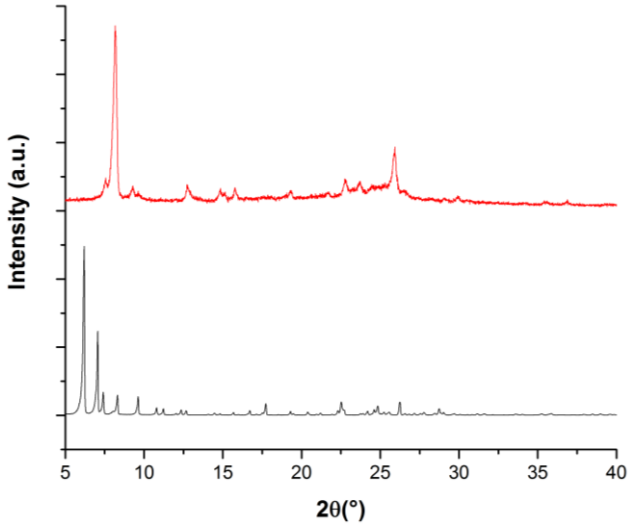

Figure 4.6 Shows the PXRD pattern of Ge-UTL before (black) and after hydrolysis (red), clearly showing the successful disassembly of the *d4r* and the formation of a layered material IPC-1P.

The PXRD pattern was dominated by a single peak at 8.18 ° 2θ, associated with the movement of the (200) interlayer reflection. The movement of this peak from the higher 2 θ angle of 6.14 ° is associated with the removal of the Ge-dominated *d4r* and the subsequent collapse of the layers together resulting in a lower *d*-spacing. In addition, some of the key peaks that dominated the initial Ge-**UTL** PXRD pattern were either severely reduced in intensity or were completely lost, this is primarily due to loss of ordering of the layers in the [200] direction. Many of these peaks were lost as they corresponded to reflections with *h* values greater than 0. Other peaks were also unaffected including peaks at 7.59 ° and 12.8 ° 2θ. These are associated with the (001) and (020) reflections respectively. Such reflections remain preserved as they are unaffected by the increase in disorder of the stacking of the layers in the [100] direction as their *h* values are 0.

The SEM and EDX analysis also showed a significant change in chemical properties of the resulting crystals (Figure 4.7).

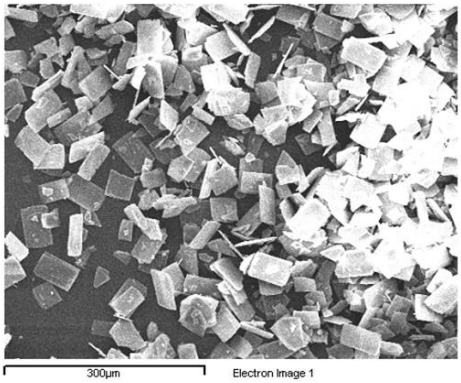

Elemental Analysis (Atomic Percent)				
Spectrum	O	Si	Ge	Total
1	72.73	26.70	0.57	100
2	73.01	26.22	0.77	100
3	72.70	26.85	0.45	100
Average	72.81	26.59	0.60	

Figure 4.7 Shows the SEM and EDX analysis of the UTL layers after treatment with 0.1 M HCl showing the preservation of the crystal morphology and the higher Si/Ge ratio (44.32) associated with the successfully disassembled IPC-1P material.

The SEM images confirmed the preservation of the rectangular crystal morphology while also showing a substantial increase in the Si/Ge ratio from 4.14 to 44.32. Such results are typical for a successful disassembly process. This confirmed that the Ge has been selectively removed from the structure, leading to selective removal of the interlayer Ge-dominated *d4r*, producing a layered material known as IPC-1P and did not lead to complete fragmentation of the layers.[26]

4.4.2 Investigating the Incorporation of Al and P

With the successful formation of the IPC-1P structure investigations into the incorporation of Al and P into the layered material were of interest. Investigations included changing the aluminium source, using the addition of fluoride, varying the pH, and changing the temperature.

4.4.2.1 Varying the pH

Due to the impact of the pH of a solution on the formation of AlPOs and the inherent instability of AlPOs and zeolites to different ranges of pH, it was important to investigate the impact of pH on the incorporation of Al and P. To this end an initial amount of $Al(OH)_3$ and H_3PO_4 was added and then the pH was varied by either the addition of extra acid or base. The resultant PXRDs of the materials confirmed the impact of the pH on the layers was varied (Figure 4.8).

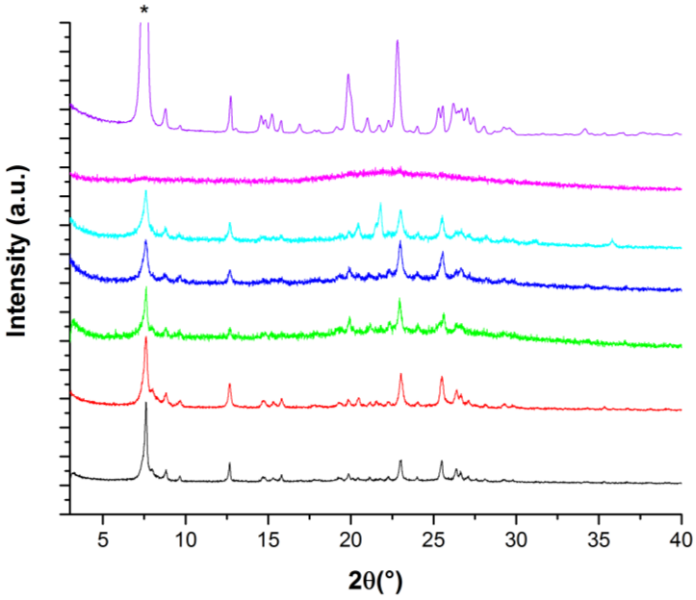

Figure 4.8 Shows the PXRD patterns for the materials obtained after the attempted incorporation of aluminium and phosphorus with increasing pH (pH 1, 3, 5, 7, 9 and 11 from black to pink respectively). A sample of IPC-1P after incorporation of DEDMS is also shown for comparison (purple). The large peak at 7.59 ° 2θ (*) is cut off to allow for better comparison with the other PXRD patterns.

The resultant PXRD patterns showed that the highest pH of 11 (pink) led to complete destruction of the layers. Such behaviour is typically seen for zeolites due to the solubilisation of silica under highly alkaline conditions. Another trend was that as the pH of the solution decreased the crystallinity of the sample increased. The materials synthesised at pH 1 and pH 3 (black and red respectively) showed the greatest crystallinity in the PXRD pattern compared to the other samples. This is perhaps to be expected as a greater acid strength is already known to help with removal and rearrangement of silica species to form *s4r* between the layers to aid in the formation of a more crystalline sample.[25,27] Although the samples synthesised at pH 5, 7 and 9 still showed enough crystallinity to be comparable with a sample typically associated with the IPC-1P material after the incorporation of DEDMS (IPC-2P). SEM and EDX analysis of the samples showed that while all these samples seemed similar by PXRD, there was a significant difference in the morphology and chemical properties of the samples (Figure 4.9).

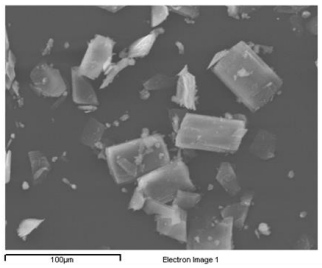

Elemental Analysis (Atomic Percent)					
Spectrum	O	Al	Si	P	Total
1	70.54	-0.14	29.70	-0.10	100
2	72.72	-0.08	27.41	-0.36	100
3	69.62	0.02	30.61	-0.25	100
Average	70.96	-0.07	29.24	-0.24	

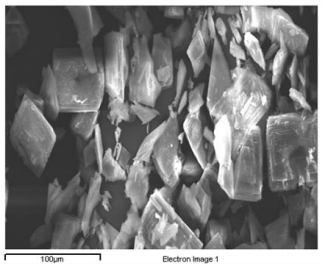

Elemental Analysis (Atomic Percent)					
Spectrum	O	Al	Si	P	Total
1	70.76	0.10	29.39	-0.25	100
2	73.59	-0.22	27.10	-0.47	100
3	56.92	-0.06	43.10	0.04	100
Average	67.09	-0.06	33.20	-0.23	

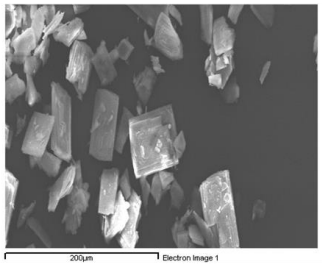

Elemental Analysis (Atomic Percent)					
Spectrum	O	Al	Si	P	Total
1	72.62	2.05	23.90	1.43	100
2	73.54	2.36	22.44	1.66	100
3	73.01	2.33	23.28	1.37	100
Average	73.06	2.25	23.21	1.49	

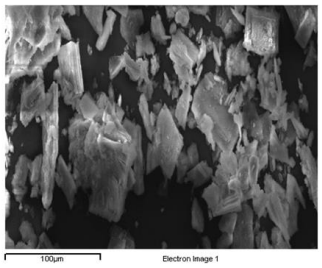

Elemental Analysis (Atomic Percent)					
Spectrum	O	Al	Si	P	Total
1	57.62	4.71	36.16	1.5	100
2	70.53	6.57	16.65	6.25	100
3	41.12	3.24	54.15	1.49	100
Average	56.42	4.84	35.65	3.08	

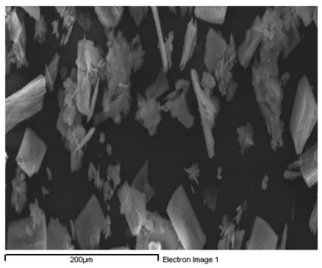

Elemental Analysis (Atomic Percent)					
Spectrum	O	Al	Si	P	Total
1	67.43	11.14	8.88	12.55	100
2	60.95	2.83	32.84	3.37	100
3	69.24	1.77	27.42	1.57	100
Average	65.87	5.25	23.05	5.83	

Figure 4.9 Shows the SEM and EDX analysis of samples after the attempted incorporation of Al and P at (from top to bottom) pH 1, pH 3, pH 5, pH 7 and pH 9.

All the SEM and EDX images of the samples showed the presence of crystals typical for **UTL** and her daughter zeolites; the morphology of the crystals was rectangular and platelet-like, with some showing more degradation. Crystals produced from syntheses at higher pH (pH 7 and pH 9) showed a rather more irregular crystal morphology, most likely from the formation of some additional non-crystalline material that was not observed in the PXRD pattern. The EDX analysis of these materials suggested that this additional material consisted of predominantly Al and P species. The presence of such species is

perhaps because of the slightly raised pH levels interfering with the formation of AlPO species; typically AlPOs are formed in conditions up to pH 6.[12,17] In comparison the syntheses conducted at pH 1 and pH 3 showed a material that was far more crystalline, although the images seemed to indicate the presence of a denser species. Typically, a lower pH is associated with the formation of denser phase AlPOs. This is perhaps hinted at, particularly in the pH 1 material, by the presence of small sphere-like species. The somewhat limited synthesis time of 16 hours may have prevented this species from becoming the dominant proportion of species in the material, explaining the lack of observable peaks in the PXRD patterns associated with such dense species. These dense phases however did not seem to impact on the EDX results. Both syntheses conducted at pH 1 and pH 3 showed a distinct lack of observable Al and P, suggesting that this dense material may not be the result of any AlPO-like species but rather some sort of silicate species. In comparison to all the other syntheses, the synthesis conducted at pH 5 seemed to show the greatest promise for the incorporation of Al and P in between the layers of the IPC-1P material. The crystals showed the typical rectangular platelet-like morphology associated with **UTL** with the limited presence of additional phases. In addition, EDX analysis of the material showed the presence of Al and P species with a Si/Al ratio of 10.31 and a Si/P ratio of 15.57 respectively. This is perhaps of interest as the combined Si/Al+P ratio of 6.21 is comparable to that seen for the Si/Ge ratio of the previous material of 4.14, with the slight increase in Si content owing to the formation of *s4r* interlayer connections instead of the original *d4r* in the Ge-**UTL**. Such results indicated that the pH of the synthesis had a profound impact on the incorporation of Al and P. It was clear that such a procedure was favoured by conditions where the pH was like that typically used for the traditional synthesis of AlPO materials. The step-wise ADOR process seems to help overcome the mutually exclusive pH requirements for the formation of both zeolites and AlPOs by allowing for both to be accommodated for in different steps.

4.4.2.2 Changing the Source of Aluminium

With the impact of pH on the successful incorporation of Al and P in between the layers, another important factor that was of interest was the impact of different aluminium sources on the resultant material. Analysis of the materials showed that varying the source of aluminium had a dramatic impact on the PXRD patterns of the resultant materials even though all syntheses were conducted at pH 5 (Figure 4.10).

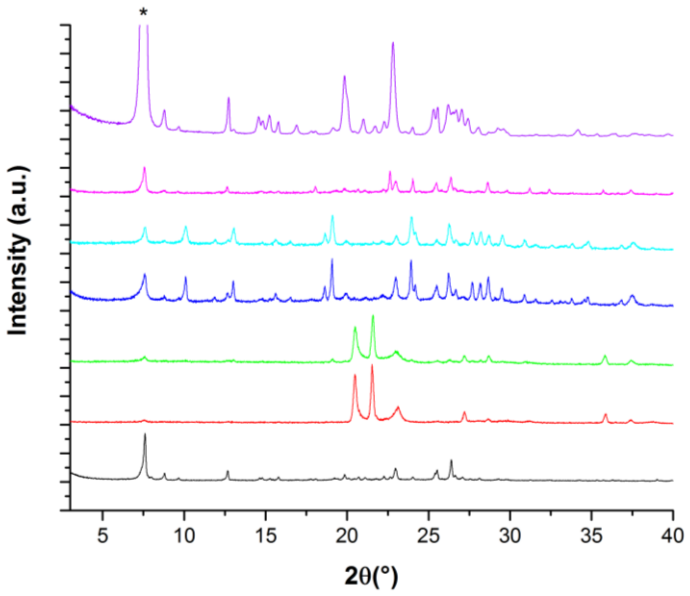

Figure 4.10 Shows the PXRD patterns for the materials obtained after the attempted incorporation of aluminium and phosphorus using different sources of aluminium including: $Al(OH)_3$ (black), $Al(NO_3)_3$ (red), $AlCl_3$ (green), $AlCl_3.6H_2O$ (blue), aluminium sec-butoxide (cyan) and aluminium isopropoxide (pink). A sample of IPC-1P after incorporation of DEDMS is also shown for comparison (purple). The large peak at 7.59 ° 2θ (*) is cut off to allow for better comparison with the other PXRD patterns.

The PXRD patterns of the resultant materials indicated that when aluminium nitrate and aluminium chloride were used, a new dense phase was formed and dominated the material, so that the peak at 7.62 ° 2θ, associated with the interlayer reflection of the IPC-1P material, was almost completely lost. The PXRD pattern was dominated by three peaks between 20 and 23 ° 2θ, the presence of this new dense phase is perhaps because of the higher reactivity associated with these aluminium sources. In comparison both aluminium chloride hydrate and aluminium sec-butoxide indicated the presence of an additional material, with peaks at 10 and 13 ° 2θ. However, the peaks originating from the material did not completely dominate the PXRD pattern. This is perhaps due to the lower reactivity of these aluminium sources in comparison to aluminium chloride and aluminium nitrate, resulting in a lower proportion of the AlPO in the recovered material. The only aluminium source that resulted in a PXRD pattern like that obtained for to $Al(OH)_3$ was aluminium isopropoxide, this is most likely because of the similarly low reactivity of this species, which prevented the formation of additional phases according to the PXRD patterns.

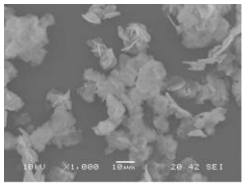

Elemental Analysis (Atomic Percent)

Spectrum	O	Al	Si	P	Total
1	74.45	1.22	21.84	2.49	100
2	76.28	0.94	21.81	0.97	100
3	69.76	1.98	26.72	1.54	100
Average	73.50	1.38	23.46	1.67	

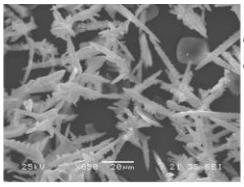

Elemental Analysis (Atomic Percent)o

Spectrum	O	Al	Si	P	Total
1	73.73	11.52	2.13	12.62	100
2	73.5	12.44	0.74	13.32	100
3	68.44	13.57	1.93	16.06	100
Average	68.44	13.57	1.93	16.06	

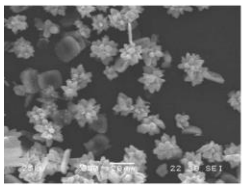

Elemental Analysis (Atomic Percent)

Spectrum	O	Al	Si	P	Total
1	75.57	9.86	4.02	10.54	100
2	67.64	2.44	27.49	2.43	100
3	65.41	9.33	12.89	12.37	100
Average	66.53	5.89	20.19	7.40	

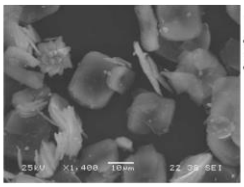

Elemental Analysis (Atomic Percent)

Spectrum	O	Al	Si	P	Total
1	76.77	1.63	19.64	1.97	100
2	61.59	1.37	34.57	2.47	100
3	72.78	11.99	1.91	13.32	100
Average	70.38	5.00	18.71	5.92	

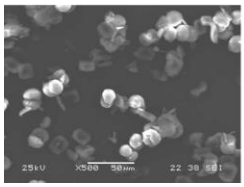

Elemental Analysis (Atomic Percent)

Spectrum	O	Al	Si	P	Total
1	75.87	7.15	8.33	8.65	100
2	74.25	1.28	23.88	0.59	100
3	62.34	15.48	1.55	20.64	100
Average	70.82	7.97	11.25	9.96	

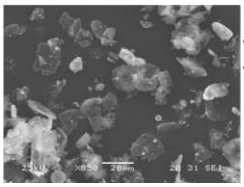

Elemental Analysis (Atomic Percent)

Spectrum	O	Al	Si	P	Total
1	79.34	3.34	11.32	3.16	2.83
2	76.86	0.67	15.30	0.10	7.07
3	79.06	3.61	10.00	4.33	3.01
Average	78.42	2.54	12.21	2.53	

Figure 4.11 Shows the SEM and EDX analysis of samples after the attempted incorporation of Al and P using different sources of aluminium including: $Al(OH)_3$ (top left), $Al(NO_3)_3$ (top right), $AlCl_3$ (middle left), $AlCl_3.6H_2O$ (middle right), aluminium sec-butoxide (bottom left) and aluminium isopropoxide (bottom right).

SEM and EDX analysis of the materials highlighted the staggering difference between the resultant materials just by alteration of the source of aluminium (Figure 4.11). The SEM images of the materials made using aluminium nitrate and aluminium chloride confirmed that the dominant phase was not the **UTL**-like crystals, but an additional phase consisting of primarily P and Al. These crystals were needle like with the synthesis using aluminium chloride showing more intergrowth between the needles. This confirmed that these additional, more reactive, aluminium sources had resulted in the formation of a dominant phase of dense aluminophosphate material. The lower reactivity of the aluminium chloride hydrate and the aluminium sec-butoxide was also highlighted with both showing an additional phase with the **UTL**-like crystals, which did not completely dominate the material. One interesting behaviour of the additional phases was the slightly different crystal morphologies. The AlPO formed using aluminium chloride hydrate seemed to show similar morphology like that obtained for aluminium chloride, with the morphology ranging between clusters of needle intergrowths and more elongated spherical crystals. In comparison, the AlPO material obtained when using aluminium sec-butoxide showed a spherical crystal morphology. It is perhaps to be noted that this subtle change in morphology could be due to the additional butanol present in the synthesis, caused by the hydrolysis of the aluminium *sec*-butoxide, as alcohol is well known to have an impact on the crystal morphology by effecting the growth kinetics.[28] The SEM and EDX analysis of the materials formed with the use of aluminium isopropoxide was shown to also contain some additional material that was not noticed in the original PXRD pattern. It is likely

that this additional non-crystalline phase was a result of the presence of additional isopropanol from the aluminium isopropoxide that impacted on the crystal growth of the additional AlPO phase. Such results showed that the ideal aluminium source was therefore the original $Al(OH)_3$ due to a combination of its lower reactivity and the lack of additional components that could interfere with the synthesis (such as alcohols).

4.4.2.3 Using HF

Another variation in the synthesis conditions was the use of additional fluoride to promote the formation of a more crystalline material. Two sources of fluoride were used, NH_4F and HF, that have been previously used to form more crystalline zeolite frameworks[29,30]. PXRD analysis of the resultant materials showed some unfavourable comparisons to the standard synthesis attempted without the presence of fluoride (Figure 4.12).

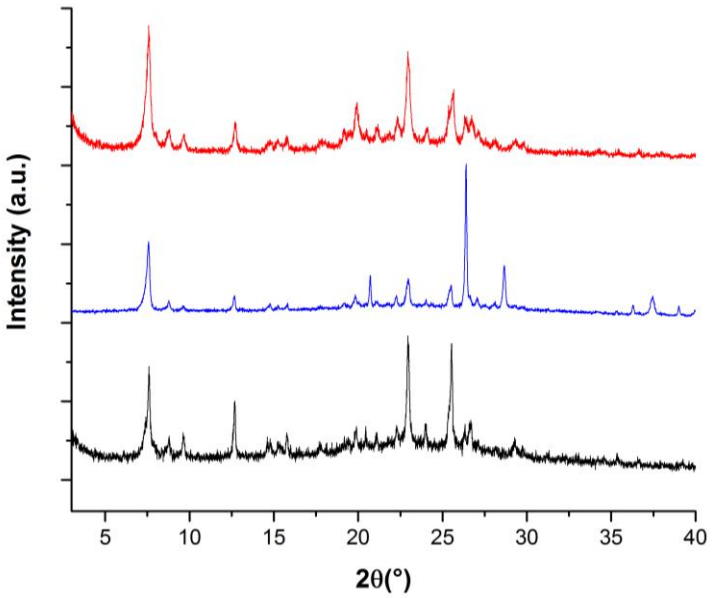

Figure 4.12 Shows the PXRD patterns for the materials obtained after the attempted incorporation of aluminium and phosphorus with the use of a fluoride source; with HF(black), with NH_4F (blue) and standard without HF (red).

The PXRD pattern obtained for the incorporation of Al and P in the presence of HF compared favourably to the PXRD pattern of the material made without the presence of HF. However, the presence of NH_4F resulted in a PXRD pattern that was dominated by an additional peak at 26.4 ° 2θ. This clearly indicated that the use of NH_4F seemed to result in the formation of an additional phase although it is unclear what this species is. SEM and EDX analysis confirmed the results seen by PXRD (Figure 4.13).

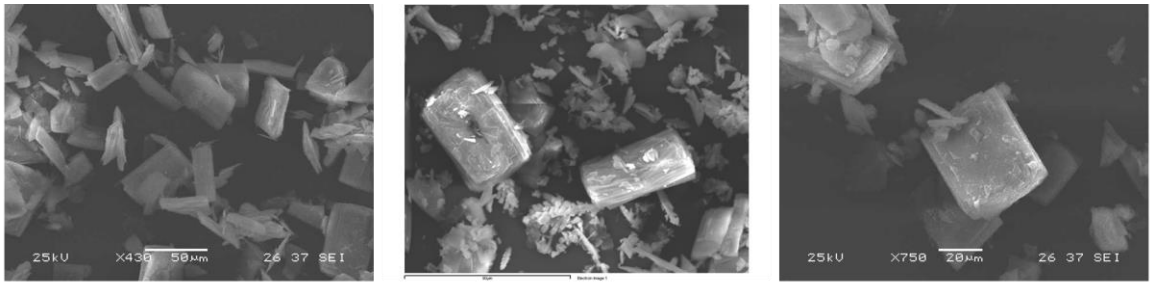

Elemental Analysis (Atomic Percent)

Spectrum	O	Al	Si	P	Total
1	80.76	-0.35	20.11	-0.52	100
2	82.72	-0.29	18.00	-0.43	100
3	79.42	-0.60	21.31	-0.13	100
Average	80.97	-0.41	19.81	-0.36	

Elemental Analysis (Atomic Percent)

Spectrum	O	Al	Si	P	Total
1	69.84	1.17	28.00	0.99	100
2	77.31	1.15	20.63	0.91	100
3	71.13	3.41	20.62	4.83	100
Average	72.76	1.91	23.08	2.24	

Elemental Analysis (Atomic Percent)

Spectrum	O	Al	Si	P	Total
1	67.77	2.70	25.76	3.77	100
2	76.35	1.13	20.07	2.45	100
3	76.44	1.77	19.97	1.82	100
Average	73.52	1.87	21.93	2.68	

Figure 4.13 Shows the SEM and EDX analysis of samples after the attempted incorporation of Al and P using additional sources of fluoride including: HF (left), NH_4F (middle), and without (right).

All the materials were dominated by the presence of the rectangular platelet-like crystals associated with **UTL** and its daughter zeolites. However, in comparison to the incorporation of Al and P without HF, the presence of HF did not result in the successful incorporation of Al or P into the material. It is possible that the presence of additional HF simply resulted in the promotion of the rearrangement process, whereby Si species are transferred to form the *s4r* rather than incorporating the Al or P species. This is most likely as a result of the increased acidity brought about by the HF and the increased solubility of the Si species in the presence of fluoride.[31] The presence of NH_4F showed, as suspected, an additional aluminophosphate dense phase, perhaps as the ammonium cation or ammonia (from the breakdown of the NH_4F) acted as a templating agent to form this additional phase. These results clearly showed that the use of fluoride to aid in the crystallinity of the samples prepared was not successful, due to the increased acidity/solubilisation power of fluoride or due to the presence of additional cations that promoted the formation of an additional undesired phase.

4.4.3 Synthesis and Characterisation of the Zeolite-AlPO hybrid

With the factors effecting the synthesis of this zeolite-AlPO hybrid investigated an ideal synthesis procedure was fashioned. PXRD analysis of the resultant material after calcination of the organised layers showed a similar pattern to that previously seen for the IPC-2 material (Figure 4.14).

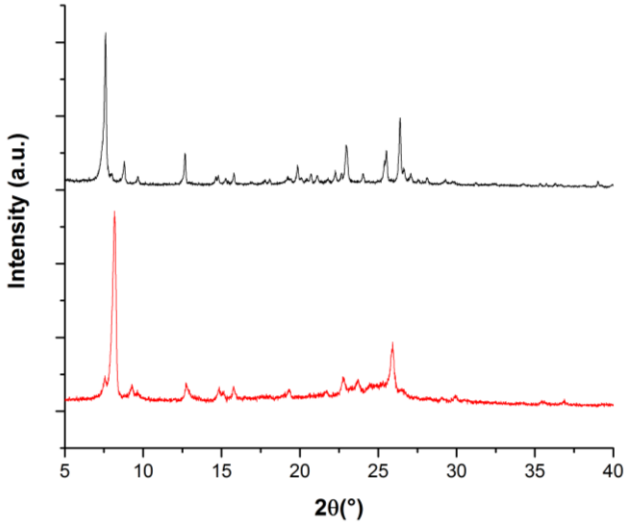

Figure 4.14 Shows the PXRD patterns for the materials obtained before (red) and after the incorporation of aluminium and phosphorus followed by calcination (black).

The PXRD pattern for the calcined material compared favourably with that obtained for previous sample of IPC-2, where the layers are connected by *s4r* linkages. The pattern was dominated by the 200 peak at 7.60 ° 2θ, which is at a slightly higher 2θ angle compared to the hydrolysed material as the interlayer *d*-spacing is increased with the incorporation of *s4r* interlayer linkages. The PXRD pattern also showed the characteristic peaks at 8.80 °, 9.68 ° and 12.68 ° 2θ corresponding to the $(\bar{1}10)$, $(1\bar{1}1)$ and (110) reflections. The presence of such peaks confirmed the formation of well-ordered layers during the reassembly of the IPC-1P layers to a IPC-2-like structure. As disorder in the direction of the stacking of the layers in the [200] direction would lead to all those reflections with *h* values higher than 0 being severely reduced in intensity.[25]

To ascertain the chemical nature of this material a single crystal was isolated for analysis by SEM and EDX (Figure 4.15), unfortunately the material was not able to be analysed by single crystal X-ray diffraction, despite their relatively large size, as they did not diffract well. This has been previously noticed for other daughter zeolites of **UTL** within the group and is not necessarily an indicator of any specific issue relating to the zeolite-AlPO hybrid material.

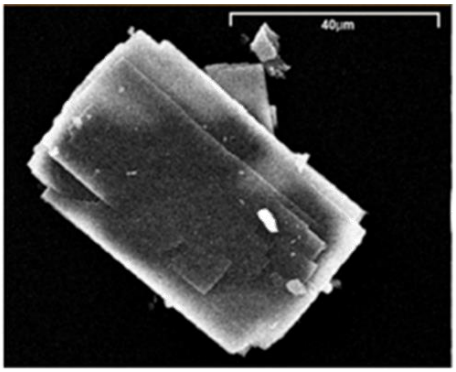

Elemental Analysis (Atomic Percent)					
Spectrum	O	Al	Si	P	Total
1	72.52	2.44	21.86	3.18	100
2	73.46	2.32	21.75	2.47	100
3	66.36	2.21	28.63	2.8	100
4	66.71	2.13	28.55	2.61	100
Average	69.76	2.28	25.20	2.77	

Figure 4.15 Shows the SEM and EDX analysis of samples after the incorporation of Al and P.

The material showed the typical rectangular platelet-like crystals associated with **UTL** and its daughter zeolites. This material showed a typical Si/Al ratio of 9.09 and a Si/P ratio of 11.05, which combined gave a Si/Al+P ratio of 4.99. This value was once again close to the value of the original Si/Ge ratio of Ge-**UTL** (4.14), with a slight increase due to the reduced size of the interlayer linkages from *d4r* to *s4r*. Although it should be noted that such results cannot be regarded as exact due to the nature of EDX, however it is still of interest that the Si/Ge and Si/Al+P ratios were similar.

4.4.3.1 Reformation of the IPC-1P Material

With the successful formation of this material and the confirmation of the incorporation of Al and P in between the layers it was decided to investigate the relative stability of this material. The zeolite-AlPO hybrid was placed in 2 M HCl acid and heated at 95 ° for 16 hours and then analysed by PXRD to see the impact of these acidic conditions on the material (Figure 4.16).

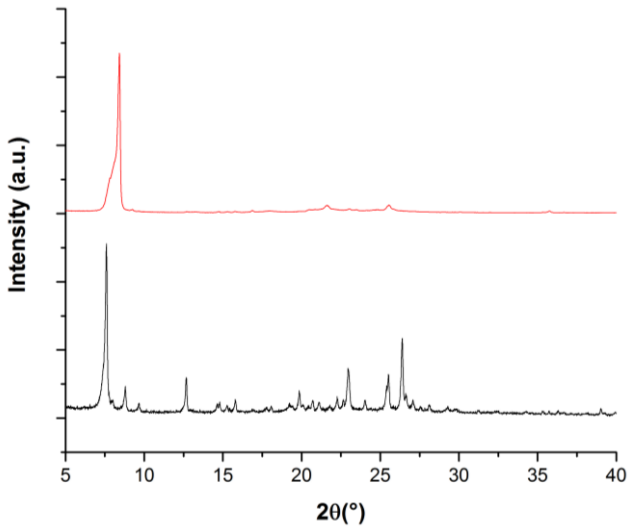

Figure 4.16 Shows the PXRD patterns for the materials obtained before (black) and after treatment of the zeolite-AlPO hybrid with acid at elevated temperature (red). Clearly indicating the reformation of a layered material.

The resultant material showed a very clear change compared to the IPC-2-like PXRD pattern of the original material and bore a strong resemblance to the PXRD pattern associated with the IPC-1P structure.[22,25,32] The pattern was dominated by a single peak at 8.42 ° 2θ instead of the 200 peak at 7.78 ° 2θ in the original zeolite-AlPO hybrid material. This indicated a movement of the interlayer reflection to a smaller d-spacing and suggested that the layers had collapsed together, most likely because of the removal of the unstable interlayer AlPO-like linkages between the layers.

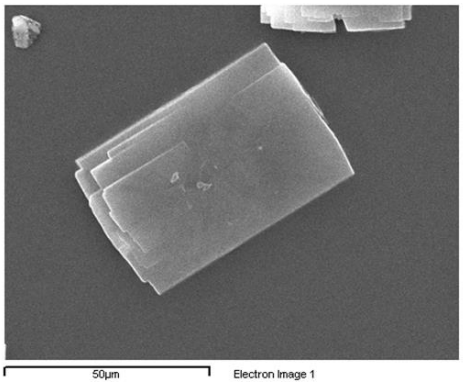

Elemental Analysis (Atomic Percent)

Spectrum	O	Al	Si	P	Total
1	74.99	-0.05	25.13	-0.07	100
2	75.37	-0.03	24.74	-0.08	100
3	75.39	-0.01	24.71	-0.09	100
4	76.18	-0.12	24.07	-0.13	100
Average	75.48	-0.05	24.66	-0.09	

Figure 4.17 Shows the SEM and EDX analysis of sample after the zeolite-AlPO hybrid has been placed in contact with 2 M HCl, at 95 °C for 18 hrs.

SEM and EDX analysis of this material (Figure 4.17) established that the removal of the Al and P species from the zeolite-AlPO material had occurred and that the layered IPC-1P material had been reformed. The SEM images confirmed preservation of the crystal morphology associated with **UTL** and her daughter zeolites, while EDX analysis confirmed the complete removal of all Al and P species.

These results added further credence to the idea that a zeolite-AlPO hybrid material had been formed, and that this material was highly unstable to even relatively moderate conditions. The original layered material IPC-1P could be reformed using conditions that were like those used for the removal of Ge from the germanosilicate **UTL**. In the presence of weak acid and elevated temperatures the IPC-1P material was reformed with the presence of Al and P species from the original zeolite-AlPO hybrid material completely lost. This seems to confirm the relative instability of this species, most likely due to the presence of Si-O-P bonds caused by the formation of AlPO *s4r* linkages between the silicate layers.

4.4.3.2 MAS NMR Characterisation

While this initial chemical test strongly indicated the presence of an AlPO like species between the IPC-1P layers. The exact nature of this material needed to be confirmed with the most valuable technique being solid-state MAS NMR.

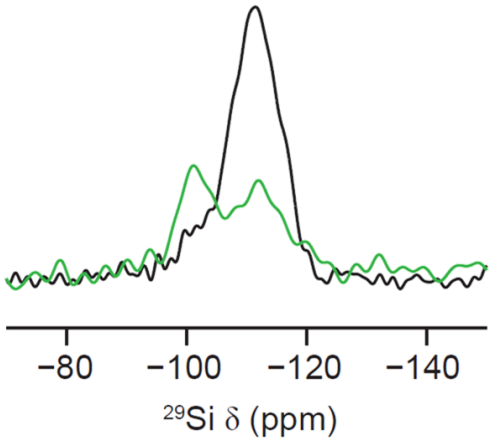

Figure 4.18 Shows the ^{29}Si MAS NMR spectra (black) and {^{1}H} ^{29}Si cross-polarisation MAS NMR (green) of the zeolite-AlPO hybrid. The initial material is dominated by the Q^4 sites, with the small number of Q^3 sites being highlighted by the cross-polarisation experiment. This suggests that the material may have successfully reassembled with some disorder in the structure, leaving some $(O_3SiO)_3Si$-OH sites.

The ^{29}Si MAS NMR spectrum (Figure 4.18) showed a dominant peak at -110 ppm with a shoulder at about -105 ppm. These two peaks corresponded to the presence of Q^4 and Q^3 sites respectively in the obtained material. The presence of Q^3 sites indicated the existence of Si species that were not connected to four other Si atoms by bridging oxygens. The {^{1}H} ^{29}Si cross-polarisation MAS NMR also showed some interesting results with the enhancement of the Q^3 sites by this technique being relatively weak. This indicated that the most likely species responsible for these Q^3 sites, were not $(O_3SiO)_3Si$-OH but rather $(O_3SiO)_3Si$-O-(Al or P). This gave the first indications that a zeolite-AlPO hybrid had been formed by the successful reconnection of the IPC-1P layers and that this material included the presence of some new Si environments that were not associated with tetrahedral Si connected to only other Si atoms.

^{27}Al MAS NMR of the material also showed promising results with the spectrum being dominated by a single peak at 40 ppm (Figure 4.19).

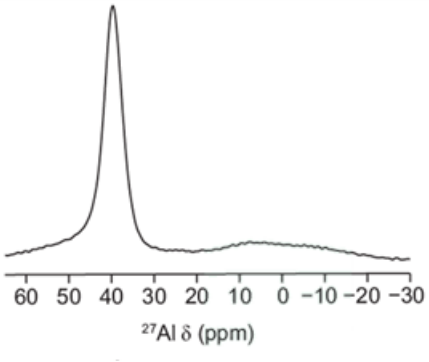

Figure 4.19 Shows the ^{27}Al MAS NMR spectrum of the zeolite-AlPO hybrid. The material shows a sharp peak at 40 ppm typically associated with Al tetrahedra. There is also a peak at ~0 ppm possibly associated with some additional material.

This peak at 40 ppm is characteristic of tetrahedral Al species.[33] Indicating that the material contained tetrahedral Al and that the Al species was not present as its 6-coordinate species and so indicating the presence of an AlPO like species in this material. The MAS NMR also showed a smaller and broader peak centring at 0 ppm, though it is not clear to what the species responsible for this peak was. The ^{31}P MAS NMR of the material also showed similar results to that already seen in the ^{27}Al MAS NMR (Figure 4.20).

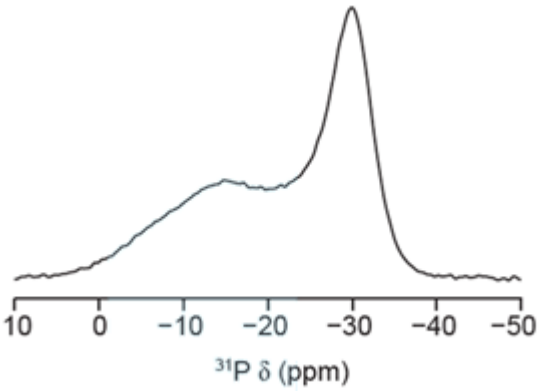

Figure 4.20 Shows the ^{31}P MAS NMR spectrum of the zeolite-AlPO hybrid. The material shows a sharp peak at -30 ppm typically associated with P tetrahedra. There is also a peak at approximately -15 ppm possibly associated with some additional material.

The ^{31}P MAS NMR spectrum was dominated by a peak at -30 ppm, corresponding to a phosphorus environment associated with tetrahedral P.[33] Indicating once again the presence of an AlPO like species in the material. There was also a larger broad peak at -13 ppm, although the nature of this species of P was not possible to ascertain. These results from the MAS NMR gave strong indications of the presence of both tetrahedral P and Al species, typically associated with the formation of AlPO.

To confirm that these species were indeed bonded to each other a 2D correlation experiment was conducted between ^{27}Al and ^{31}P species (Figure 4.21). Such correlation experiments are easier to conduct, due to the NMR active isotopes of Al and P making-up the majority of the isotopes present, therefore making the signals strong enough for 2D experiments.

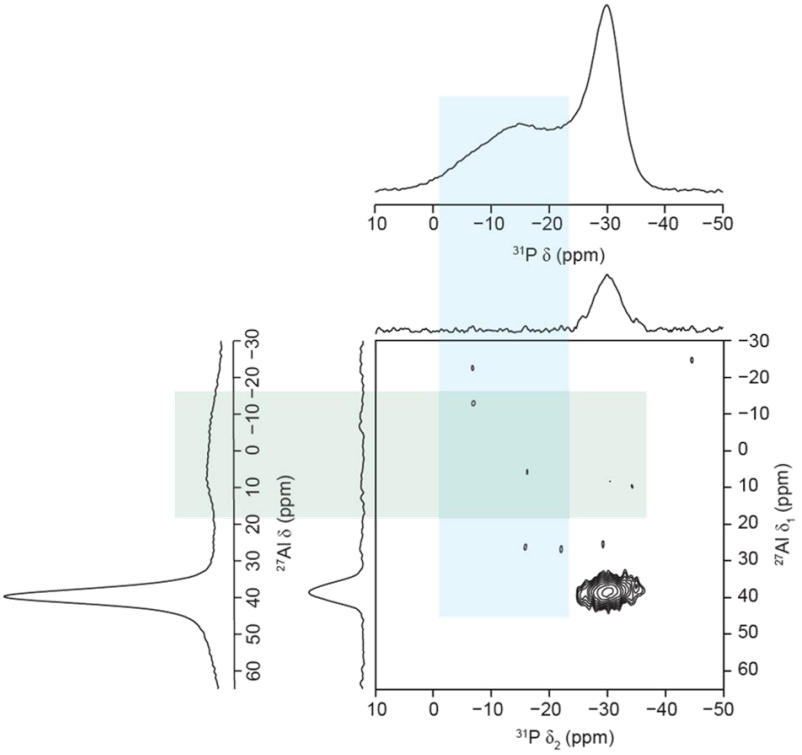

Figure 4.21 Shows the 2D correlation experiment between the ^{27}Al and ^{31}P MAS NMR spectra of the zeolite-AlPO hybrid. The material shows a strong correlation between the peaks associated with tetrahedral Al and P (40 ppm and -30 ppm respectively) suggesting that both environments are close together in space (bonding). The spectra also showed no correlation between the two additional phases seen in the original Al and P spectra (0 ppm and -20 ppm respectively) indicating that this material is not involved in the zeolite-AlPO hybrid material.

This correlation experiment confirmed the full nature of these Al and P species. The spectrum showed a large correlation between the tetrahedral Al and P species (40 ppm and -30 ppm respectively). Such a strong correlation indicated that these two species were close in space to each other and therefore most likely bonding. The correlation experiment also highlighted some important features of the two broader peaks seen at 0 and -15 ppm in the ^{27}Al and ^{31}P MAS NMR respectively. Both showed no correlation with the tetrahedral Al and P species or with each other, confirming that these additional peaks played no role in the zeolite-AlPO hybrid material and were most likely some sort of additional impurity that was previously not observed in the PXRD or SEM analysis.

The MAS NMR data confirmed the nature of the species present in the zeolite-AlPO hybrid material. The data clearly showed that the Al and P species present were

tetrahedral and close together or bonding, while the Si species confirmed the presence of Q^3 sites in addition to the Q^4. The presence of these Q^3 sites and the rather weak enhancement of these sites by cross-polarisation suggested that these Si Q^3 sites were because of Si species connected to other species (like Al and P) and not because of remaining silanols. These results indicated the presence of Al and P species in the material, most likely between the now fully reassembled silicate layers. The ^{27}Al and ^{31}P MAS NMR confirmed the presence of both tetrahedral Al and P species in the material and that these species were close to each other in space, or bonding, indicating that there was a AlPO-like species between the layers. The analysis also highlighted the presence of some additional species, however this material did not seem to interreact with any of the zeolite-AlPO hybrid species.

While these results were promising the most conclusive evidence would be a ^{29}Si and ^{31}P correlation experiment. This would show that Si and P species were close enough in space to be bonding and prove the formation of the energetically unfavourable Si-O-P bonds. However, such attempts were impossible on this sample. This was due to a combination factors including: the reduced signal inherent in MAS NMR, the reduced resolution inherent in correlation experiments and reduced signal strength for ^{29}Si due to the relatively low natural abundance (4.68 %). These factors would mean that such an experiment could not be conducted without using months of machine time. The only way to overcome such issues would be to try and synthesise an enriched **UTL** sample to increase the number of ^{29}Si atoms in the sample and increase the strength of the ^{29}Si signal.

4.4.4 Synthesis and Characterisation of the Zeolite-AlPO Hybrid Material with ^{29}Si

To increase the relative abundance of ^{29}Si in the zeolite-AlPO hybrid sample the most plausible method would be to increase its relative abundance in the original Ge-**UTL**. This was done by using ^{29}Si-enriched TEOS to synthesise Ge-**UTL** (Section 4.3.6), followed by the disassembly and incorporation of Al and P using the same procedure as previously reported, but with this enriched sample. The final material was then confirmed using PXRD analysis (Figure 4.22).

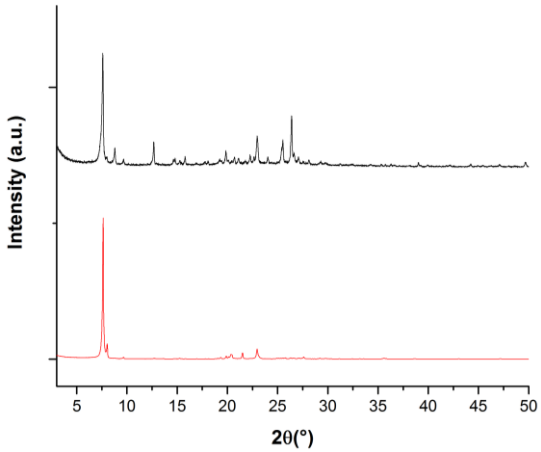

Figure 4.22 Shows the PXRD for the enriched zeolite-AlPO hybrid (red) compared with the non-enriched sample (black), the material seemed to show a similar dominant peak relating to the (200) reflection. But showed less intensity with regards to the other peaks.

A comparison of the two PXRD patterns indicated the similarity between the unenriched- and enriched-samples and the formation of the ^{29}Si-enriched zeolite-AlPO hybrid. There were signs of a high degree of preferential orientation, which lead to the dominance of the 200 peak. The similarity of the enriched- and unenriched-samples was also confirmed in the SEM and EDX analysis (Figure 4.23).

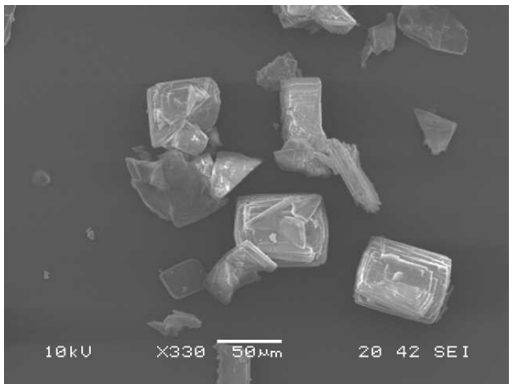

Elemental Analysis (Atomic Percent)

Spectrum	O	Al	Si	P	Ge	Total
1	65.05	2.34	29.47	3.13	0.01	100
2	67.69	2.55	27.90	1.88	-0.02	100
3	53.76	5.97	34.93	5.33	0.01	100
Average	62.17	3.62	30.77	3.45	0.00	

Figure 4.23 Shows the SEM and EDX analysis of enriched samples after the incorporation of Al and P, confirming results that had already been established with the unenriched samples.

The analysis of the ^{29}Si-enriched material confirmed the incorporation of Al and P into the enriched material. Both materials showed a similar Si/Al and Si/P ratios; the enriched material had a Si/Al ratio of 8.5, compared to 9.09 for the unenriched material, and a Si/P ratio of 8.92 compared to 11.05 for the unenriched sample.

With the confirmation of the formation of the ^{29}Si-enriched material ^{29}Si MAS NMR and ^{31}P MAS NMR analysis was carried out on the sample (Figure 4.24).

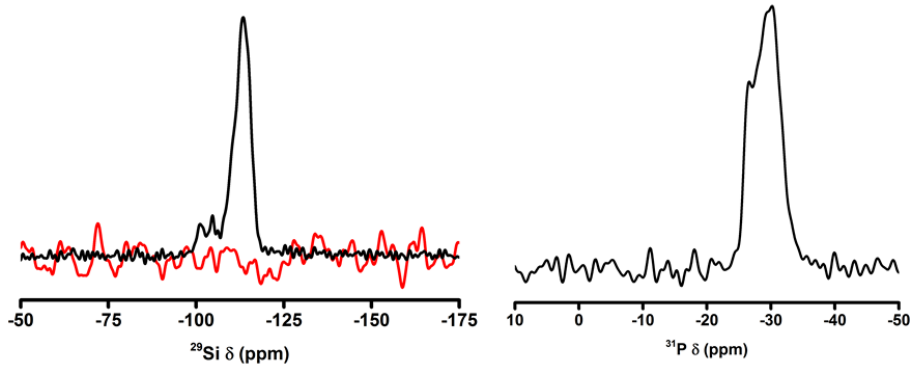

Figure 4.24 Shows the ^{29}Si MAS NMR spectra (black) and {^{1}H} ^{29}Si cross-polarisation MAS NMR (red) of the zeolite-AlPO hybrid from the ^{29}Si enriched Ge-UTL (left). The material is dominated by the Q^4 sites, with a shoulder relating to the small number of Q^3 sites that are not highlighted by the cross-polarisation experiment, indicating the presence of Q^3 sites that are not originating from silanols. Also shown is the ^{31}P MAS NMR spectrum of the zeolite-AlPO hybrid (right). The material shows a sharp peak at -30 ppm typically associated with P tetrahedra.

Both MAS NMR spectra showed similar results to those obtained for the unenriched samples. The ^{29}Si MAS NMR and cross-polarisation experiments showed a peak at -110 ppm with a shoulder at -105 ppm, indicating the presence of a large number of Q^4 Si sites with some Q^3 Si sites. The lack of enhancement by cross-polarisation also indicated that these Q^3 sites were mainly caused not by the presence of silanol groups but by bonding to other T-atoms that were not Si by bridging oxygens. The ^{31}P MAS NMR also confirmed the presence of tetrahedral P sites in the materials with a peak focussing around -30 ppm.

With the successful collection of ^{29}Si and ^{31}P MAS NMR data the correlation experiment between the Si and P species was conducted (Figure 4.25).

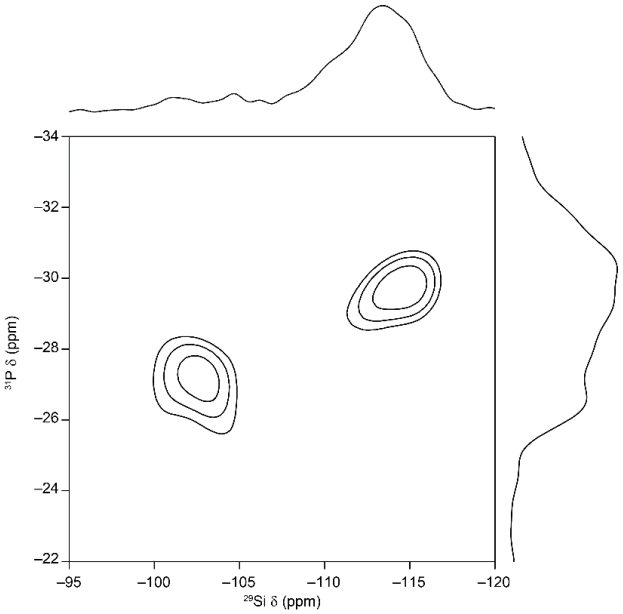

Figure 4.25 Shows the correlation experiment conducted between Si and Al species. The spectra showed some promising results however the weakness of signals in the correlation showed that the enrichment had not been enough to obtain a better correlation experiment.

The results indicated some promise, with a correlation shown between the Si environment at -115 ppm and the P environment at -30 ppm. This could indicate that these Si and P species were therefore close to each other. However, this peak was not distinct enough from the background to be considered significant enough to provide conclusive proof of the formation of such bonds. The enrichment had not resulted in enough of an increase in active ^{29}Si isotopes being present in the final material to increase the strength of signal to the degree required for 2D correlation experiments between ^{29}Si and ^{31}P to prove the presence of Si-O-P bonds in this zeolite-AlPO hybrid material.

4.5 Conclusions

This chapter discussed the difficulties surrounding the formation of a material containing Si, P, and Al. Although some progress has been made with the formation of SAPOs these materials have been able to avoid the formation of energetically unfavourable Si-O-P bonds, as hydrothermal synthesis allows for the easy making and breaking of bonds. The use of hydrothermal synthesis for these materials also results in a relatively uncontrolled distribution of Si species in the SAPO framework. Furthermore, the ideal conditions required for the synthesis of zeolites and AlPOs were shown to be mutually exclusive with the formation of one requiring very different conditions to the other.

The ADOR process was discussed as a potential mechanism for confronting these difficulties; the multiple and irreversible steps would help confront these mutually exclusive processes and the weaknesses of hydrothermal synthesis. The ADOR process allowed for the formation of a zeolite product under its ideal conditions, followed by its disassembly to form a layered material IPC-1P. These layers could then be organised to incorporate Al and P between them using conditions suitable for the incorporation of these species between the silicate layers. The final irreversible reassembly step could then be used to form AlPO like linkages between the silicate layers resulting in a zeolite-AlPO hybrid material. The inability for the system to make and break bonds during the reassembly step therefore forced the formation of energetically unfavourable Si-O-P bonds.

The incorporation of Al and P in between the IPC-1P layers was investigated while varying pH, aluminium source, and the presence of fluoride species. It was found that a pH similar to that used for the synthesis of AlPOs favoured the incorporation of Al and P species in between the layers, with pH above or below this resulted in limited Al or P being present or the degradation of the material. The aluminium source played a significant role in the

materials formed with the formation of the zeolite-AlPO hybrid favoured by sources with limited reactivity, while those sources with higher reactivity resulted in the formation of dense AlPO impurities. The presence of ammonium fluoride resulted in the formation of an additional AlPO impurity, due to the presence of ammonium cations that could act as SDAs. The presence of fluoride from HF resulted in no incorporation of Al and P and instead seemed to result in the formation of pure Si IPC-2, most likely due to the increased solubilisation of Si by fluoride.

The successful formation of the zeolite-AlPO hybrid materials was confirmed by PXRD with the pattern of the material matching very closely with the typical PXRD pattern seen for the IPC-2 material, where the layers are connected by *s4r* linkages. SEM and EDX analysis of the crystals also showed the removal of Ge and the presence of Al and P in the material at a similar level to the amount of Ge removed from the original germanosilicate. MAS NMR confirmed the dominance of the Si Q^4 sites associated with the fully reconnected 3D framework, but also showed some Q^3 that were not enhanced by cross-polarisation, indicating that these Q^3 Si species were in fact close to other T-atom species, like Al and P. The MAS NMR spectra for ^{27}Al and ^{31}P also showed the presence of both species as tetrahedra in the material and that both species were close to each other in space, indicative of bonding. Possibly the most conclusive evidence was perhaps the instability of the material to relatively weak acid and elevated temperatures. Using conditions typical for the disassembly step it was possible to reclaim the layered IPC-1P material, which would have been impossible if the interlayer linkages formed in the IPC-2 like structure were made of silicon. To prove the formation of Si-O-P bonds in the material, enrichment of the original parent germanosilicate with ^{29}Si TEOS was attempted, as the relative abundance of ^{29}Si is too small for 2D correlation experiments. The enriched material was shown to have similar structural and chemical properties to the unenriched material according to analysis by PXRD, SEM and EDX. However, the enrichment of the material, while it did lead to an increase in the NMR signal seen in the ^{29}Si MAS NMR, did not result in enough signal for the ^{29}Si and ^{31}P correlation experiment. Although some hints of a correlation were seen between the Si and P species, the strength of the signal was not enough to conclusively prove the presence of these species by NMR.

4.6 Future Work

Future work should look at the synthesis of the material with an even greater amount of ^{29}Si-enriched TEOS to increase the strength of the signal and get better correlation data.

While research has already shown the potential of germanosilicates to incorporate aluminium by the ADOR process, further research should also be considered for the incorporation of other species in between the layers such as tin, cobalt and titanium. The presence of additional metal species in large-pore silicate zeolites is highly desired and would be of immense interest, particularly for catalysis. The properties of such materials and their behaviour in comparison to traditional zeolites would also be of interest.

4.7 References

(1) Wilson, S. T.; Lok, B. M.; Messina, C. A.; Cannan, T. R.; Flanigen, E. M. Aluminophosphate Molecular Sieves: A New Class of Microporous Crystalline Inorganic Solids. *J. Am. Chem. Soc.* **1982**, *104* (4), 1146–1147.

(2) McCusker, L. B.; Baerlocher, C. Chapter 2 - Zeolite Structures. In *Introduction to Zeolite Science and Practice*; Čejka, J., Corma, A., Bekkum, H. van, Schüth, F., Eds.; Elsevier, 2007; Vol. 168, pp 13–37.

(3) Sastre, G.; Lewis, D. W.; Catlow, C. R. A. Structure and Stability of Silica Species in SAPO Molecular Sieves. *J. Phys. Chem.* **1996**, *100* (16), 6722–6730.

(4) Li, Y.; Yu, J.; Xu, R. AlPO Database http://mezeopor.jlu.edu.cn/alpo/ (accessed Apr 19, 2017).

(5) Flanigen, E. M.; Grose, R. W. Phosphorus Substitution in Zeolite Frameworks. In *Molecular Sieve Zeolites-I*; Advances in Chemistry; American Chemical Society, 1974; Vol. 101, pp 6–76.

(6) Flanigen, E. M.; Khatami, H.; Szymanski, H. A. Infrared Structural Studies of Zeolite Frameworks. *Advan. Chem. Ser.* **1971**, *101*, 201–229.

(7) Barrer, R. M.; Marshall, D. J. 1218. Chemistry of Soil Minerals. Part I. Hydrothermal Crystallisation of Some Alkaline Al_2O_3-SiO_2-P_2O_5 Compositions. *J. Chem. Soc.* **1965**, 6616–6621.

(8) Barrer, R. M.; Marshall, D. J. 1219. Chemistry of Soil minerals. Part II. Reactions of Phosphates with Kaolin and Faujasite. *J. Chem. Soc.* **1965**, 6621.

(9) Kuehl, G. H. Influence of Phosphate and Other Complexing Agents on the Crystallisation of Zeolites. In *Molecular Sieves: Papers Read at the Conference Held at the School of Pharmacy, (University of London), Brunswick Square, London, WC1*; S.C.I. monograph; Society of Chemical Industry, 1968; pp 85–91.

(10) Kuehl, G. H. Preparation of Crystalline Silicoaluminophosphates. US Patent. 4,786,487, 1988.

(11) Flanigen, E. M.; Patton, R. L.; Wilson, S. T. Structural, Synthetic and Physicochemical Concepts in Aluminophosphate-Based Molecular Sieves; 1988; pp 13–27.

(12) Pastore, H. O.; Coluccia, S.; Marchese, L. Porous Aluminophosphates: From Molecular Sieves to Designed Acid Catalysts. *Annu. Rev. Mater. Res.* **2005**, *35* (1), 351–395.

(13) Fjermestad, T.; Svelle, S.; Swang, O. Mechanism of Si Island Formation in SAPO-34. *J. Phys. Chem. C* **2015**, *119* (4), 2086–2095.

(14) Sastre, G.; Lewis, D. W.; Richard, C.; Catlow, A. Modeling of Silicon Substitution in SAPO-5 and SAPO-34 Molecular Sieves. *J. Phys. Chem. B* **1997**, *101* (27), 5249–5262.

(15) Blackwell, C. S.; Patton, R. L. Solid-State NMR of Silicoaluminophosphate Molecular Sieves and Aluminophosphate Materials. *J. Phys. Chem.* **1988**, *92* (13), 3965–3970.

(16) Tan, J.; Liu, Z.; Bao, X.; Liu, X.; Han, X.; He, C.; Zhai, R. Crystallization and Si Incorporation Mechanisms of SAPO-34. *Microporous Mesoporous Mater.* **2002**, *53* (1–3), 97–108.

(17) Ren, X.; Komarneni, S.; Roy, D. M. The Role of Gel Chemistry in Synthesis of Aluminophosphate Molecular Sieves. *Zeolites* **1991**, *11* (2), 142–148.

(18) Yu, J. Chapter 3 - Synthesis of Zeolites. In *Introduction to Zeolite Science and Practice*; Čejka, J., Corma, A., Bekkum, H. van, Schüth, F., Eds.; Elsevier, 2007; Vol. 168, pp 39–103.

(19) Li, X.; Deem, M. W. Why Zeolites Have So Few Seven-Membered Rings. *J. Phys. Chem. C* **2014**, *118* (29), 15835–15839.

(20) Blatov, V. A.; Ilyushin, G. D.; Proserpio, D. M. The Zeolite Conundrum: Why are There so Many Hypothetical Zeolites and so Few Observed? A Possible Answer from the Zeolite-Type Frameworks Perceived as Packings of Tiles. *Chem. Mater.* **2013**, *25* (3), 412–424.

(21) Mazur, M.; Wheatley, P. S.; Navarro, M.; Roth, W. J.; Položij, M.; Mayoral, A.;

Eliášová, P.; Nachtigall, P.; Čejka, J.; Morris, R. E. Synthesis of "Unfeasible" Zeolites. *Nat. Chem.* **2015**, *8* (1), 58–62.

(22) Eliášová, P.; Opanasenko, M.; Wheatley, P. S.; Shamzhy, M.; Mazur, M.; Nachtigall, P.; Roth, W. J.; Morris, R. E.; Čejka, J. The ADOR Mechanism for the Synthesis of New Zeolites. *Chem. Soc. Rev.* **2015**, *44* (20), 7177–7206.

(23) Paillaud, J.-L.; Harbuzaru, B.; Patarin, J.; Bats, N. Extra-Large-Pore Zeolites with Two-Dimensional Channels Formed by 14 and 12 Rings. *Science* **2004**, *304* (5673), 990–992.

(24) Shamzhy, M. V; Shvets, O. V; Opanasenko, M. V; Yaremov, P. S.; Sarkisyan, L. G.; Chlubná, P.; Zukal, A.; Marthala, V. R.; Hartmann, M.; Čejka, J. Synthesis of Isomorphously Substituted Extra-Large Pore UTL Zeolites. *J. Mater. Chem.* **2012**, *22* (31), 15793.

(25) Roth, W. J.; Nachtigall, P.; Morris, R. E.; Wheatley, P. S.; Seymour, V. R.; Ashbrook, S. E.; Chlubná, P.; Grajciar, L.; Položij, M.; Zukal, A.; et al. A Family of Zeolites with Controlled Pore Size Prepared Using a Top-Down Method. *Nat. Chem.* **2013**, *5* (7), 628–633.

(26) Roth, W. J.; Shvets, O. V.; Shamzhy, M.; Chlubná, P.; Kubů, M.; Nachtigall, P.; Čejka, J. Postsynthesis Transformation of Three-Dimensional Framework into a Lamellar Zeolite with Modifiable Architecture. *J. Am. Chem. Soc.* **2011**, *133* (16), 6130–6133.

(27) Morris, S. A.; Bignami, G. P. M.; Tian, Y.; Navarro, M.; Firth, D. S.; Čejka, J.; Wheatley, P. S.; Dawson, D. M.; Slawinski, W. A.; Wragg, D. S.; et al. In Situ Solid-State NMR and XRD Studies of the ADOR Process and the Unusual Structure of Zeolite IPC-6. *Nat. Chem.* **2017**, *9*, 1012–1018.

(28) Cheng, C.-H.; Shantz, D. F. Silicalite-1: Growth from Clear Solution: Effect of Alcohol Identity and Content on Growth Kinetics. *J. Phys. Chem. B* **2005**, *109* (41), 19116–19125.

(29) Chen, F.-J.; Xu, Y.; Du, H.-B. An Extra-Large-Pore Zeolite with Intersecting 18-, 12-, and 10-Membered Ring Channels. *Angew. Chemie Int. Ed.* **2014**, *53* (36), 9592–9596.

(30) Qian, K.; Wang, Y.; Liang, Z.; Li, J. Germanosilicate Zeolite ITQ-44 with Extra-Large 18-Rings Synthesized by Using Commercial Quaternary Ammonium as Structure-

Directing Agent. *RSC Adv.* **2015**, *5*, 63209–63214.

(31) Zones, S. I.; Hwang, S. J.; Elomari, S.; Ogino, I.; Davis, M. E.; Burton, A. W. The Fluoride-Based Route to All-Silica Molecular Sieves; a Strategy for Synthesis of New Materials Based upon Close-Packing of Guest-Host Products. *Comptes Rendus Chim.* **2005**, *8* (3–4), 267–282.

(32) Mazur, M.; Chlubná-Eliášová, P.; Roth, W. J.; Čejka, J. Intercalation Chemistry of Layered Zeolite Precursor IPC-1P. *Catal. Today* **2014**, *227*, 37–44.

(33) Wang, X.; Dai, W.; Wu, G.; Li, L.; Guan, N.; Hunger, M. Verifying the Dominant Catalytic Cycle of the Methanol-to-Hydrocarbon Conversion Over SAPO-41. *Catal. Sci. Technol.* **2014**, *4* (3), 688–696.

5 Attempts to Expand the ADOR Process to Other Germanosilicates

5.1 Aim

This chapter will discuss the attempts to expand the use the application of the ADOR process, by applying it to other already known germanosilicates. This will firstly include discussion of the factors involved in the selection of materials, their syntheses and any issues that were encountered. The results from the application of the ADOR process will be discussed and any inferences as to the possibility of expanding the ADOR process.

5.2 Introduction

5.2.1 The ADOR Process

As discussed in the introduction the ADOR process has played a large role in expanding the horizons of zeolite synthesis. The ability to convert a 3D zeolite framework to a 2D layered material, manipulate those layers, and then reconnect them to form a new 3D zeolite framework (Figure 5.1); has led to the synthesis of many new materials unattainable by traditional zeolite synthesis techniques.[1–4]

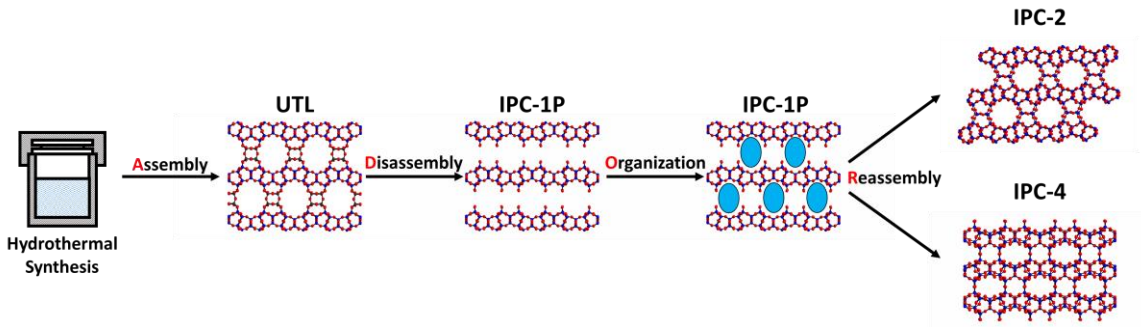

Figure 5.1 Shows a schematic representation of the ADOR process applied to UTL. First the assembly of the original parent germanosilicate through traditional hydrothermal synthesis. Second the disassembly of that germanosilicate into a layered silicate material by the selective removal of the Ge-dominated *d4r*. Third the organisation of the material with the use of intercalating agents. Finally, the irreversible reassembly of that material to form a new 3D framework.

Since the first successes of the ADOR process with **UTL**,[2] the drive has been to apply the ADOR process to other germanosilicates and thereby prove that the process is a more general approach rather than highly specialised. The ADOR process has now been applied to other known germanosilicates **UOV** and **IWW** with some success (producing IPC-5 and IPC-12 respectively).[3,4] However, with 232 unique frameworks on the IZA database,[5] it is

clear that there are still many other frameworks, whose ability to undergo the ADOR process needs to be probed.

The ADOR process consists of four key steps: Assembly, disassembly, organisation and reassembly. These steps have individual characteristics that put different requirements on the material for their successful implementation. Fulfilment of each of the requirements at each step is wholly dependent on the chemical and framework properties of the parent germanosilicate. Based on previous research a 'wish list' of chemical and framework properties can be inferred and then applied as selection criteria to single out frameworks that may be suitable candidates for the ADOR process.

5.2.2 The 'Wish List'

5.2.2.1 Ge-Dominated *d4r* Units

It has been shown that Ge-dominated double four rings (*d4r*) are an excellent target for linking these silicate layers together for two reasons. Firstly, the larger size of germanium compared to silicon means that it preferentially occupies *d4r* units, due to their ability to handle the high strain from the low angles present in such units.[6] This often leads to silica-rich layers linked by germanium rich *d4r* units. Secondly, O-Ge-O bonds in zeolites are much more hydrolytically sensitive than their O-Si-O counterparts, this allows for the preferential removal of Ge from the zeolite and thus the destruction of the *d4r* units linking the silicate layers together.

5.2.2.2 These *d4r* Units Need to be Monodirectional

If these germanium-dominated *d4r* units are not monodirectional, then this leads to the fragmentation of the zeolite as there are no clearly defined silicate layers and so during the disassembly process the whole zeolite is broken apart instead of forming layers.

5.2.2.3 These Units Should be Between Stable Silicate Layers

The silicate layers left behind after hydrolysis need to be stable to the conditions required during the ADOR process. The stability of these layers is increased if they are dense. Should the silicate layers contain large pores within them then the stability of the silicate layers is compromised. As this leaves the layer weak to attack from the molecules used in the ADOR process.

5.2.2.4 Need Large Pores Near to the *d4r* Units

Large pores close to the *d4r* units is key to provide a point of access for the ADOR process. Should the *d4r* units be blocked then their removal during the disassembly step will be severely hindered and the zeolite will either not be disassembled or if the germanium is

removed there can be a large build-up of by-products. This would then also hinder the subsequent organisation and reassembly steps, thus making the likelihood of producing a highly order daughter zeolite extremely unlikely.

ABW	ACO	AEI	AEL	AEN	AET	AFG	AFI	AFN	AFO	AFR	AFS
AFT	AFV	AFX	AFY	AHT	ANA	APC	APD	AST	ASV	ATN	ATO
ATS	ATT	ATV	AVL	AWO	AWW	BCT	*BEA	BEC	BIK	BOF	BOG
BOZ	BPH	BRE	BSV	CAN	CAS	CDO	CFI	CGF	CGS	CHA	-CHI
-CLO	CON	CSV	CZP	DAC	DDR	DFO	DFT	DOH	DON	EAB	EDI
EEI	EMT	EON	EPI	ERI	ESV	ETL	ETR	EUO	*-EWT	EZT	FAR
FAU	FER	FRA	GIS	GIU	GME	GON	GOO	HEU	IFO	IFR	-IFU
IFW	IFY	IHW	IMF	IRN	IRR	-IRY	ISV	ITE	ITG	ITH	*-ITN
ITR	ITT	-ITV	ITW	IWR	IWS	IWV	IWW	JBW	JNT	JOZ	JRY
JSN	JSR	JST	JSW	KFI	LAU	LEV	LIO	-LIT	LOS	LOV	LTA
LTF	LTJ	LTL	LTN	MAR	MAZ	MEI	MEL	MEP	MER	MFI	MFS
MON	MOR	MOZ	*MRE	MSE	MSO	MTF	MTN	MTT	MTW	MVY	MWF
MWW	NAB	NAT	NES	NON	NPO	NPT	NSI	OBW	OFF	OKO	OSI
OSO	OWE	-PAR	PAU	PCR	PHI	PON	POS	PSI	PUN	RHO	-RON
RRO	RSN	RTE	RTH	RUT	RWR	RWY	SAF	SAO	SAS	SAT	SAV
SBE	SBN	SBS	SBT	SEW	SFE	SFF	SFG	SFH	SFN	SFO	SFS
*SFV	SFW	SGT	SIV	SOD	SOF	SOS	SSF	*-SSO	SSY	STF	STI
*STO	STT	STW	-SVR	SVV	SZR	TER	THO	TOL	TON	TSC	TUN
UEI	UFI	UOS	UOV	UOZ	USI	UTL	UWY	VET	VFI	VNI	VSV
WEI	-WEN	YUG	ZON								

Figure 5.2 Shows the 232 unique zeolite framework structures after the application of the selection criteria for the ADOR process. Frameworks highlighted are ruled out due to: not containing *d4r* (red), not containing Ge-dominated *d4r* (green) and not containing stable silicate layers (blue). Those 12 left over (white) are deemed to satisfy the selection criteria.

By applying these loose selection criteria to the currently known frameworks in the IZA database only 12 of 232 unique frameworks are left that may be able to undergo the ADOR process (Figure 5.2). Of these 12 frameworks 3 have already been researched with varying degrees of success (**IWW**, **UOV** and **UTL**).[2–4]

The loose application of these selection criteria produced several possible candidates with varying degrees of plausibility including: NUD-1 (as yet no 3-letter code assigned), ITQ-33 (**ITT**), ITQ-38 (**ITG**), IM-20 (**UWY**).[7–10]

5.3 Application of the ADOR Process on NUD-1

5.3.1 Introduction

The synthesis of NUD-1 was first published by Chen *et al.* in 2014 and has yet to be assigned a 3-letter code by the IZA.[7] The germanosilicate framework contains a 3-dimensional channel system of 18-, 12- and 10-ring channels. NUD-1 was of interest as it was the first framework to have *s3r*, *d3r* and *d4r* coexisting in the same framework structure. The material can be viewed as a hybrid material between the ITQ-33 and ITQ-44 materials.[8,11] All three can be built from the same trigonal bipyramid cage-like SBU constructed of 2 *s3r*, 3 *s4r* and 9 *s6r*. These SBUs are then connected by *d4r* to form a layer

and then these layers are connected by alternating *s3r* and *d3r* to form the NUD-1 structure (Figure 5.3).

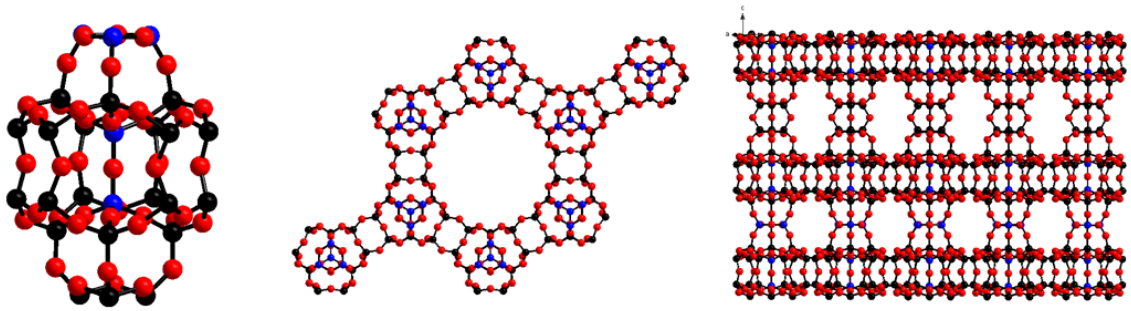

Figure 5.3 Shows the trigonal bipyramid SBU used to construct NUD-1 (left), the formation of the NUD-1 layers by connecting the *s4r* of these SBUs with bridging oxygens to form *d4r* (middle), and the formation of the 3D framework by connecting these layers through the top and bottom *s3r* by bridging oxygens to form *d3r* between layers or by sharing the same *s3r* to form *s3r* between the layers. T-atoms are shown in blue and black, O atoms are shown in red.

NUD-1 does not fulfil the idealised 'wish list' previously set out in the introduction as it contains *d4r* within the layers of the framework and these layers are penetrated by large channel systems. There are several other issues that NUD-1 has, which make it a non-ideal ADORable zeolite. Firstly, the germanium content of the zeolite is extremely high with a Si/Ge ratio of 1.05. Also, the Ge is distributed around several sites in the structure (Figure 5.4).

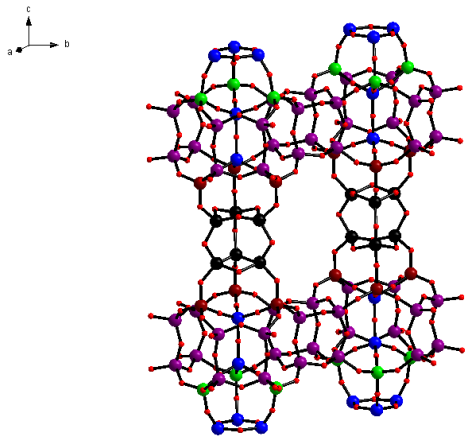

Figure 5.4 Shows the NUD-1 unit cell with the relative occupancies of the T-atoms highlighted. The Ge-dominated *d3r* T-atoms (85.9 % occupancy) are shown in black, wholly Si T-atoms are shown in blue, T-atoms with less than 10 % Ge occupancy are highlighted in green, T-atoms with 32 % occupancy are highlighted in brown, T-atoms with 60 % - 70 % Ge occupancy are highlighted in purple. This high amount and distribution of Ge in the NUD-1 structure and the general instability of the framework to the ADOR process. O atoms are in red and have been reduced in size for clarity.

This distribution of Ge throughout the structure and its high concentration in not just the *d3r* but also the *d4r* within the layers would suggest that such a structure would be unsuitable for the ADOR process. The presence of a large-pore 3-dimensional channel

system in the framework is also an indicator that NUD-1 would be a non-ideal candidate for the ADOR process as the best behaved ADORable zeolites (like **UTL**) are typified by dense silicate layers that are not penetrated by a channel system.[2] The presence of a large amount of Ge, a 3-dimensional channel system and the distribution of the Ge throughout the layers makes NUD-1 an unsuitable candidate. However, it was still of interest to see the behaviour of the germanosilicate under hydrolysis conditions, especially with the presence of these *s3r* and *d3r* that have not been seen in already known ADORable zeolite. It was also of interest to see if the behaviour of the *d3r* differed from the behaviour of the *d4r*.

5.3.2 Experimental Procedures

5.3.2.1 Synthesis of SDA

The synthesis of the SDA was performed according to the procedure previously reported by Chen *et al*.[7] 2-(bromomethyl)naphthalene (30 g, 0.135 mol) was combined with 1-methyl-1H-imidazole (10.8 mL, 0.135 mol) in THF (200 mL) and heated under reflux for 48 hours. The product, at this point a viscous gel, was then recovered after decantation, and drying under high vacuum. The bromide salt was then dissolved in water and converted to the hydroxide form with the use of ion-exchange resin.

5.3.2.2 Synthesis of NUD-1

The synthesis of NUD-1 was attempted according to the procedure already reported by Chen *et al*.[7] Germanium dioxide was combined with the SDA solution and stirred until homogeneous. TEOS was then added and the gel stirred to allow for hydrolysis of the TEOS and for the gel to reach the correct water content. Once the gel had reached the desired water content (48 %) HF solution was added, and the gel stirred for an additional hour. The final gel was weighed to ensure the correct water content was reached and then placed in a Teflon liner and steel-lined autoclave and heated at 150 °C for 14 days.

5.3.3 Results and Discussion

5.3.3.1 Synthesis of the Zeolite

Initial investigations were to repeat the syntheses of Chen *et al* and investigate the impact of increasing the Si/Ge ratio, to decrease the amount of Ge within the framework structure (Table 5.1).

Table 5.1 Shows the samples and synthesis conditions used to vary the Ge content of the NUD-1 structure.

Name	Si/Ge Ratio
NUD-Si1	1
NUD-Si2	2
NUD-Si3	3
NUD-Si4	4

The resultant PXRD patterns of the materials seemed to confirm the results reported by Chen *et al.*[7] It seemed that the NUD-1 framework was only able to form within a very narrow range of Si/Ge ratios. The synthesis gel was only able to reach a Si/Ge ratio of 2 before the resultant mixture, after being placed in the oven, tended towards a less crystalline product (Figure 5.5).

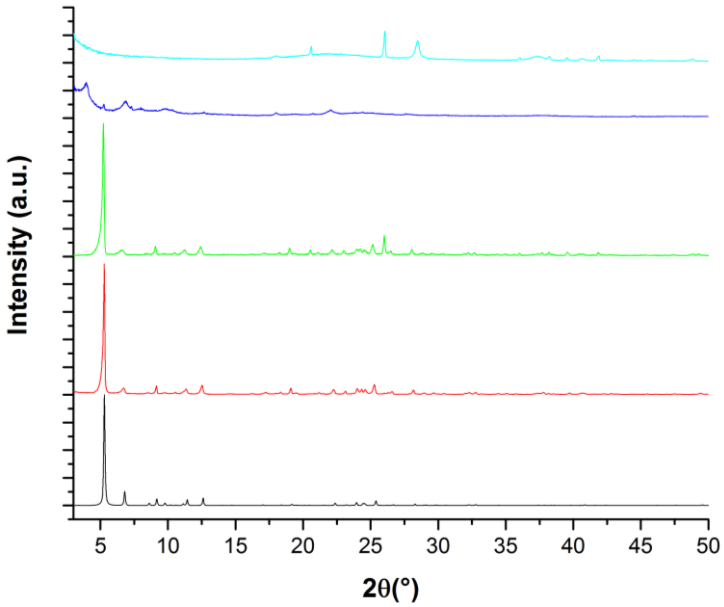

Figure 5.5 Shows the Expected PXRD pattern for NUD-1 (black) and the experimental PXRD patterns obtained for NUD-Si1 (red), NUD-Si2 (green), NUD-Si3 (blue) and NUD-Si4 (cyan). The decreasing crystallinity of the material with higher Si-content seemed to confirm that NUD-1 could only be obtained within a specific Si/Ge ratio.

Such results clearly showed that it was not possible to vary the Ge content of the NUD-1 framework. This is perhaps to be expected as the high concentration of *d4r* and *d3r* in the framework introduces lots of areas with high strain that required Ge to be present to relieve it.[12] It seems that by reducing the Ge content of the synthesis the drive for the formation of NUD-1 is lost and a material lacking in crystallinity is obtained instead. It is perhaps of interest to note the very small trace of what could be an NUD-1 peak in NUD-Si3, however this result could not be improved with repetition.

SEM and EDX analysis confirmed the formation of NUD-1 under the synthesis conditions for the formation of NUD-Si1 and NUD-Si2 (Figure 5.6).

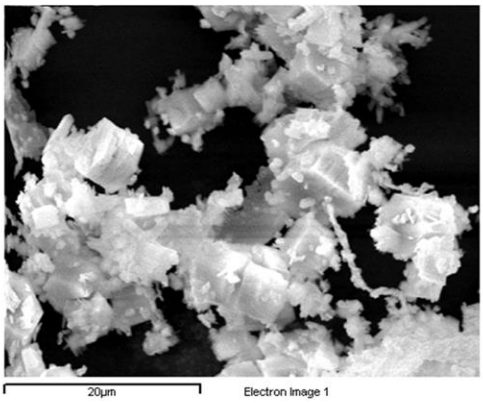

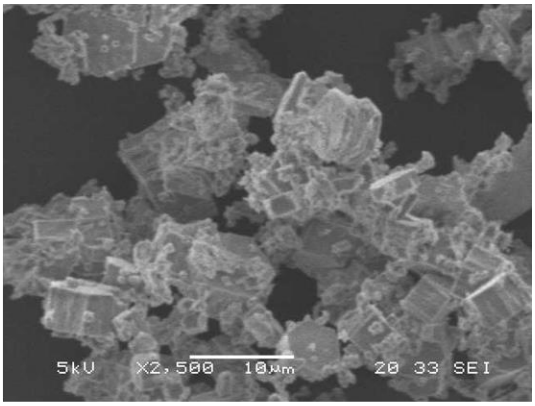

Elemental Analysis (Atomic Percent)

Spectrum	O	Si	Ge	Total
1	69.53	14.22	16.25	100
2	72.90	12.25	14.85	100
3	81.44	8.21	10.35	100
4	78.25	12.50	9.25	100
5	74.04	10.90	15.06	100
Average	75.23	11.62	13.15	

Elemental Analysis (Atomic Percent)

Spectrum	O	Si	Ge	Total
1	77.42	16.11	6.47	100
2	77.15	15.25	7.60	100
3	78.91	14.66	6.43	100
4	83.53	11.71	4.76	100
5	84.10	9.45	6.45	100
Average	80.22	13.44	6.34	

Figure 5.6 Shows then SEM and EDX analysis of NUD-Si1(left) and NUD-Si2 (right). Both showed the characteristic hexagonal morphology associated with NUD-1 and showed similar Si/Ge ratios with that expected from their respective syntheses.

SEM and EDX analysis confirmed the formation of the characteristic hexagonal NUD-1 crystal morphology. The average Si/Ge ratios of the respective crystals seemed to confirm that the NUD-Si1 and NUD-Si2 syntheses had formed NUD-1 with Si/Ge ratios (0.88 and 2.11 respectively) like the Si/Ge ratios of the initial gels. It was found that after calcination both NUD-1 materials remained intact despite the high Ge content of the framework. It was therefore decided to see the impact of hydrolysis conditions on the NUD-Si2 structure, as it contained the largest amount of Si and should be therefore more stable.

5.3.3.2 Disassembly of NUD-1

When using a standard solution of 0.1M HCl and heating the NUD-1 a dramatic change was noted in the PXRD pattern (Figure 5.7).

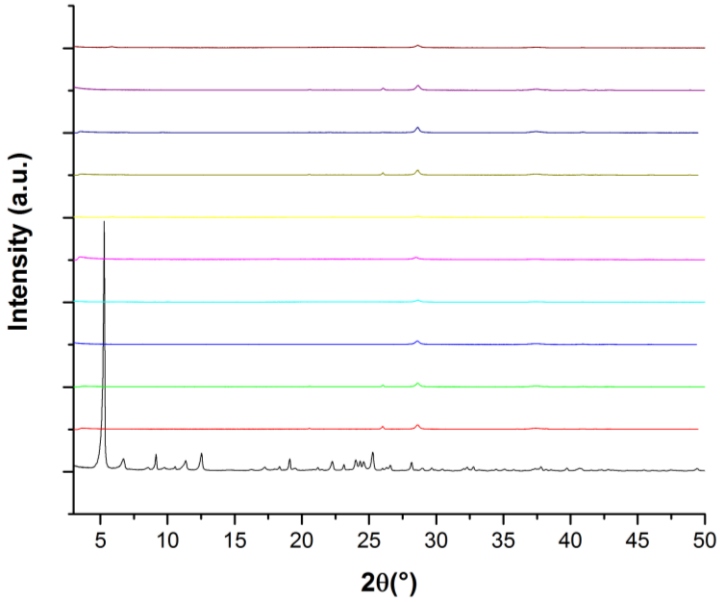

Figure 5.7 Show the PXRD pattern for NUD-Si2 before (black) and after various hydrolysis conditions including (from bottom to top): 0.1 M HCl at 95 °C for 16hrs, 0.1 M HCl at RT for 16 hrs, 12 M HCl at 50 °C for 16 hrs, 12 M HCl at RT for 16 hrs, 0.1 M HCl/EtOH at 95 °C for 16 hrs, 0.1 M HCl/EtOH at RT for 16 hrs, Ethanol at 95 °C for 16 hrs, 12 M HCl at RT for 5 mins, water at RT for 5 mins and 0.1 M HCl/EtOH at RT for 5 mins.

The results clearly showed that the NUD-1 germanosilicate structure was completely lost within a short period of time under standard hydrolysis conditions (red). Even after 5 mins at room temperature the structure was completely lost whether in 0.1 M HCl, 12 M HCl, water or in 0.1MHCl/EtOH. Even with the presence of a minimal amount of water (ethanol) and heating the resultant PXRD pattern indicated a complete loss of the structure. The Ge content of NUD-1, the concentration of *d4r*/*d3r*, and the multidirectional alignment in the framework make this framework extremely susceptible to hydrolysis conditions. It seems that the only material that could be identified in the PXRD patterns of the hydrolysed material was that associated with GeO_2 (small peak at about 27 ° 2θ). This is perhaps a further indication of the loss of the framework structure by destruction of the Ge-O-Si and Ge-O-Ge bonds.

5.3.4 Summary of Results

From the results, NUD-1 is clearly an unsuitable candidate for the ADOR process. The concentration of *d4r* and *d3r* in the structure seems to require a low Si/Ge synthesis ratio to successfully form the framework as incremental increases in the Si/Ge content of the initial gel resulted in an increasing lack of crystallinity in the material obtained. The use of the highest Si/Ge ratio sample NUD-Si2 was destroyed in a matter of minutes under hydrolysis conditions. The substantial Ge content of the structure and the presence of *d4r* and *d3r* in several directions seems to result in the complete dissolution of the structure

under even the weakest of hydrolysis conditions. It is therefore clear that NUD-1 is not a suitable candidate for the ADOR process.

5.4 Application of the ADOR Process on ITQ-33 (ITT)

5.4.1 Introduction

The failure of NUD-1 to be an ADOR candidate led to interest in the related material ITQ-33 (**ITT**). ITQ-33 was first reported by Corma *et al.* in 2006 and was given the three-letter code **ITT** in 2013.[5,8] ITT is made of the same SBU building block as NUD-1 and ITQ-44, the trigonal bipyramid cage-like SBU constructed of 2 *s3r*, 3 *s4r* and 9 *s6r*. ITQ-33, NUD-1 and ITQ-44 all form similar layers, by connecting these SBUs by *d4r*. However, where ITQ-33 differs from NUD-1 is that its framework then connects these layers with solely *s3r*, whereas the NUD-1 structure uses alternating *s3r* and *d3r* (Figure 5.8).

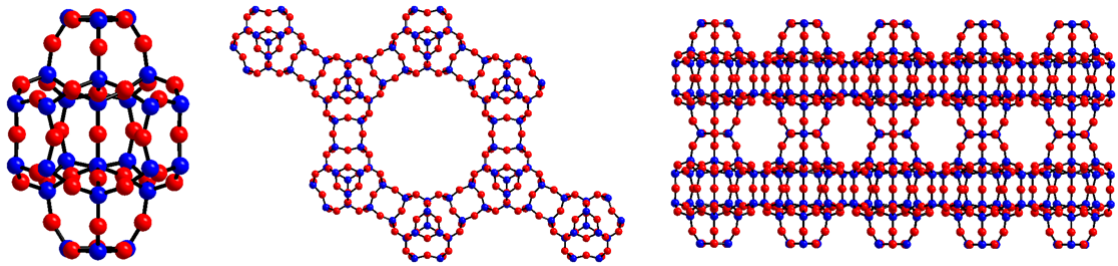

Figure 5.8 Shows the trigonal bipyramid SBU used to construct ITQ-33 (left), the formation of the ITQ-33 layers by connecting the *s4r* of these SBUs with bridging oxygens to form *d4r* (middle), and the formation of the 3D framework by connecting these layers through the top and bottom *s3r* by sharing the same *s3r* to form *s3r* between the layers, therefore differing slightly compared to the NUD-1 structure with alternating *s3r* and *d3r* between the layers. T-atoms are shown in blue and O atoms are shown in red.

This slight variation in the building scheme of **ITT** means that it has a smaller 3-dimensional channel system of 18-, 10- and 10-ring channels compared to the 3-dimensional channel system of 18-, 12- and 10-ring channels seen in NUD-1.

As already discussed with NUD-1, there are several issues with the **ITT** structure that make it a non-ideal ADORable zeolite. Firstly, the Ge content of the zeolite is extremely high with a reported Si/Ge ratio of 1.05. However, **ITT** had been has be reportedly attained with Si/Ge ratios of up to 3.6 depending on the synthesis gel.[13] Based on single crystal analysis it seems that the Ge is distributed around several sites in the structure (Figure 5.9).

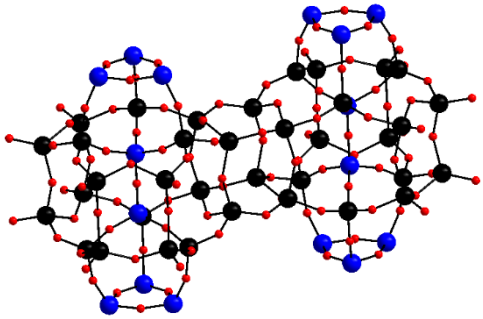

Figure 5.9 Shows the ITQ-33 unit cell with the relative occupancies of the T-atoms highlighted. The Ge-dominated T-atoms (60 % occupancy) are shown in black, wholly Si T-atoms are shown in blue. This high amount and distribution of Ge in the ITQ-33 structure and the prevalence of *d4r* increases instability of the framework to the ADOR process. O atoms are in red and have been reduced in size for clarity.

Like NUD-1, the *s3r* in ITQ-33 seem to contain wholly Si, however the distribution of Ge throughout the structure and its high concentration in not just the *d4r* but also within other atoms in the layers would suggest that such a structure would be unsuitable for the ADOR process. Further crystal structure analysis has also shown that this structure is highly disordered with the columns of SBUs shifted by half a unit cell in the *c*-direction relative to each other (Figure 5.10).[13] Such disorder would make the ADOR process even more difficult.

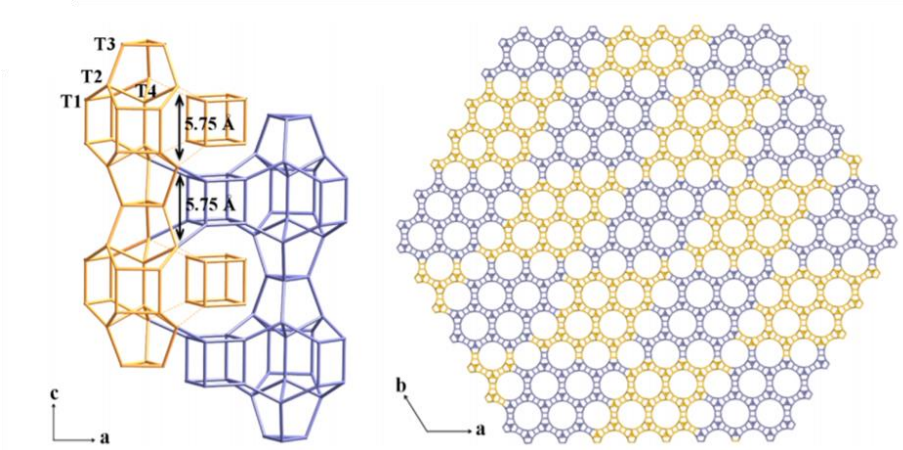

Figure 5.10 Shows the nature of the disorder in the ITQ-33 structure. Columns of SBUs are shifted by half a unit cell in the c-direction relative to each other (left) resulting in the disordered structure (right). Where yellow represents the unshifted columns of SBUs and blue represents the columns of SBUs shifted in the c-direction. The yellow *d4r* (left) represent the expected *d4r* position if the shifting of the SBU columns did not take place and no disorder was present. Taken from reference 13.

The presence of a large-pore 3-dimensional channel system in the framework is also an indicator that ITQ-33 would be a non-ideal candidate for the ADOR process as the best behaved ADORable zeolites (like **UTL**) are typified by dense silicate layers that are not penetrated by a channel system. The presence of a large amount of Ge, a 3-dimensional channel system, the distribution of the Ge throughout the layers and the presence of a

severe degree of disorder makes ITQ-33 an unsuitable candidate for the ADOR process. However, it was of interest to see if the behaviour of the ITQ-33 framework under hydrolysis conditions would differ compared to NUD-1.

5.4.2 Experimental Procedure

5.4.2.1 Synthesis of SDA

The SDA 1-butyl-3-methylimidazolium bromide (was synthesised by a previous member in the group) was converted to the hydroxide form with the use of ion-exchange resin.

5.4.2.2 Synthesis of ITQ-33

The synthesis of ITQ-33 was attempted according to the procedure already reported by Liu *et al.*[13] Germanium dioxide was placed in the stirring SDA solution, after half an hour TEOS was added and the gel stirred until homogeneous. Finally, NH_4F was added and the gel stirred until it had reached the desired water content and the final gel ratio was obtained 0.25 SDAOH: 0.5 SiO_2 : 0.5 GeO_2 : 0.05 NH_4F: 3 H_2O. The gel was then placed in a Teflon liner and steel lined autoclave and heated at 175 °C for 6 days. The Si/Ge ratio was also varied while maintaining the ratio of T atoms with the other components of the synthesis remaining constant.

5.4.3 Results and Discussion

5.4.3.1 Synthesis of the Zeolite

The synthesis of ITQ-33 (**ITT**) was conducted in a similar manner to NUD-1, whereby the Si/Ge ratio was varied, to incorporate less Ge into the structure (Table 5.2). In doing so it was hoped that the germanosilicate would be more robust under hydrolysis conditions.

Table 5.2 Shows the samples and synthesis conditions used to vary the Ge content of the ITT framework.

Name	Si/Ge Ratio
ITT-Si1	1
ITT-Si2	2
ITT-Si3	3
ITT-Si4	4

The resultant PXRD patterns of the materials seemed to follow that of NUD-1 compared to those reported by Liu *et al.*[13] It seemed that formation of **ITT** followed a similar if not even worse trend compared to that seen for the formation of the NUD-1 framework (Figure 5.11).

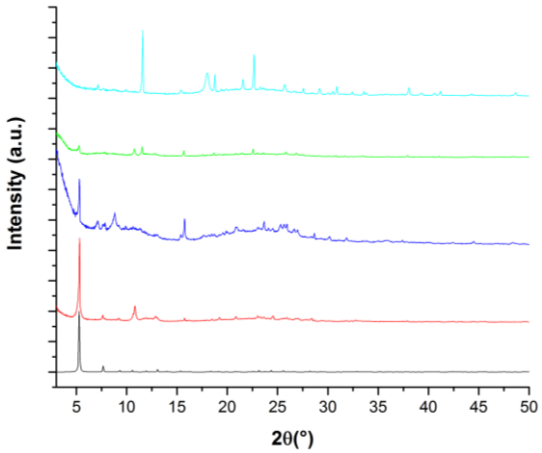

Figure 5.11 Shows the Expected PXRD pattern for ITT (black) and the experimental PXRD patterns obtained for ITT-Si1 (red), ITT-Si2 (blue), ITT-Si3 (green) and ITT-Si4 (cyan). The increasing loss of crystallinity with higher Si-content seemed to confirm that ITT could only be obtained within a specific Si/Ge ratio.

The **ITT** structure seemed to only form well at the Si/Ge ratio of 1. Even when the material was formed at higher Si/Ge ratios (Si/Ge = 2) the quality of the material was particularly substandard and would most likely be unsuitable for the ADOR process. The results of Liu *et* al. indicated that it was possible to form ITQ-33 with a Si/Ge ratio of 5. However, the quality of the material that they reported under SEM and EDX analysis was very different depending on the Si/Ge ratio used and without the PXRD patterns it is hard to discern the quality of the materials that they reported. SEM and EDX analysis (Figure 5.12) of the two samples **ITT**-Si1 and **ITT**-Si2 did seem to reflect the results seen by Liu *et* al.[13]

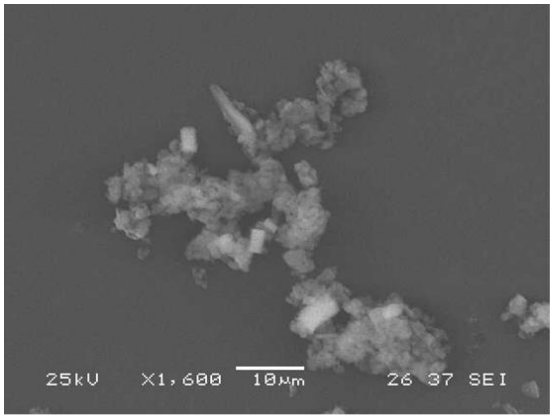

Elemental Analysis (Atomic Percent)				
Spectrum	O	Si	Ge	Total
1	77.44	10.46	12.10	100
2	78.94	9.62	11.44	100
3	81.11	10.25	8.64	100
4	82.44	9.98	7.58	100
5	76.25	12.02	11.73	100
Average	79.24	10.47	10.30	

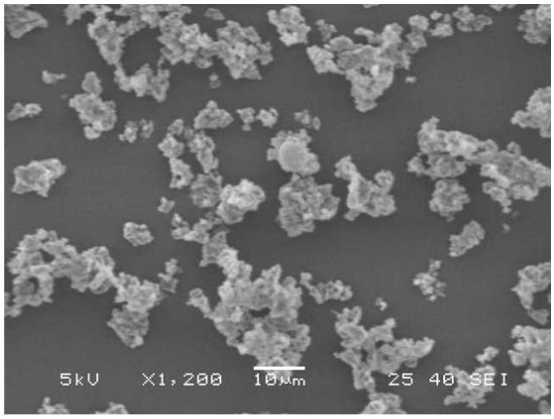

Elemental Analysis (Atomic Percent)				
Spectrum	O	Si	Ge	Total
1	74.21	16.74	9.05	100
2	77.65	14.25	8.10	100
3	82.12	10.52	7.36	100
4	69.35	19.65	11.00	100
5	77.48	15.07	7.45	100
Average	76.16	15.25	8.59	

Figure 5.12 Shows the SEM and EDX analysis for ITT-Si1 (left) and ITT-Si2 (right). Both showed Si/Ge close to the expected values. However, there was a noticeable difference in the morphology of the crystals.

Both samples seemed to show some of the characteristic hexagonal crystal morphology associated with the **ITT** structure. However, the sample **ITT**-Si2 was clearly less well formed compared with the **ITT**-Si1. It is clear that the best sample attained was for **ITT**-Si1, with the highest Ge content. Even **ITT**-Si2 with a Si/Ge ratio within the range reported by Liu *et al*, lost a significant amount of crystallinity. Such results clearly showed the limited success of changing the **ITT** Ge content by increasing the Si/Ge ratio of the synthesis. It was decided that the best sample to use for investigations into the disassembly was **ITT**-Si1 as it showed the most crystalline behaviour.

5.4.3.2 Disassembly of ITQ-33 (ITT)

By applying hydrolysis conditions on a calcined sample of **ITT**-Si1 a significant change was seen in the PXRD pattern of the material (Figure 5.13).

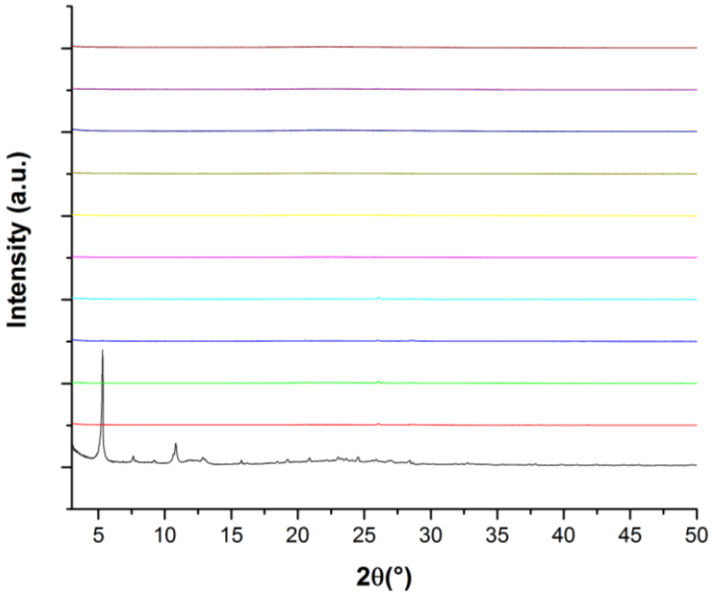

Figure 5.13 Shows the PXRD pattern for ITT-Si1 before (black) and after various hydrolysis conditions including (from bottom to top): 0.1 M HCl at 95 °C for 16hrs, 0.1 M HCl at RT for 16 hrs, 12 M HCl at 50 °C for 16 hrs, 12 M HCl at RT for 16 hrs, 0.1 M HCl/EtOH at 95 °C for 16 hrs, 0.1 M HCl/EtOH at RT for 16 hrs, Ethanol at 95 °C for 16 hrs, 12 M HCl at RT for 5 mins, water at RT for 5 mins and 0.1 M HCl/EtOH at RT for 5 mins.

The results of the hydrolysis confirmed the initial suspicions discussed earlier. Clearly the **ITT** structure was completely lost within a short period of time under standard hydrolysis conditions. Even after 5 mins at room temperature the structure was completely lost whether in 0.1 M HCl, 12 M HCl, water or 0.1MHCl/EtOH. The Ge content of **ITT**-Si1 is clearly too high. Even the lack of *d3r* in the structure was not enough to prevent the loss of the structure. The high concentration of *d4r*/*d3r* in multiple directions and the 3-dimensional channel system makes the framework extremely susceptible to any form of hydrolysis conditions and resulted in compete dissolution of the material.

5.4.4 Summary

From these results, **ITT** is clearly unsuited for the ADOR process. The concentration of *d4r* in the structure, seems to require a low Si/Ge synthesis ratio to form the framework. Attempts to decrease the Ge content lead to even those materials that had similar PXRD patterns showing decreasing uniformity in their crystal morphology when analysed by SEM. Attempts to disassemble the material **ITT**-Si1 showed the weakness of the structure to hydrolysis conditions. The increased Ge content of the structure and the presence of *d4r* in several directions seems to result in the complete dissolution of the structure under even the weakest of hydrolysis conditions. It is therefore clear that **ITT**, like NUD-1, is an unsuitable candidate for the ADOR process.

5.5 Application of the ADOR Process on ITQ-38 (ITG)

5.5.1 Introduction

The synthesis of ITQ-38 was first published by Moliner *et al.* in 2012,[10] and was assigned the official three-letter code **ITG** in 2013.[5] The germanosilicate framework contains a 3-dimensional channel system, with straight 10- and 12-ring channels along the [010] direction and zigzag 10-rings channel in the [101] and [100] direction. The material can be viewed as containing layers made of *mel*, *stf*, *mtw*, *mor*, and *bre* CBUs connected by *d4r* running in the [010] direction (Figure 5.14).

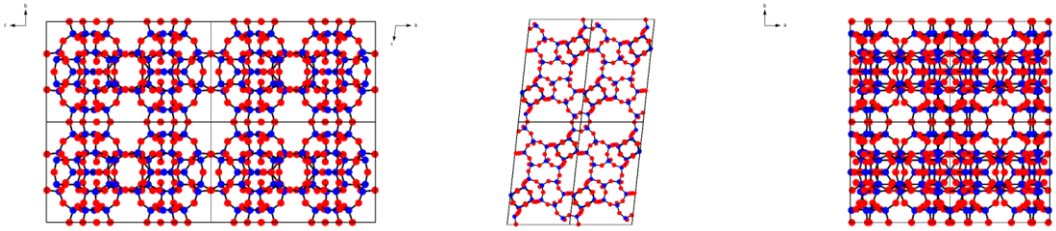

Figure 5.14 Shows the framework structure of ITG when viewed in the *a*, *b*, and *c* direction (left to right). Blue atoms represent T-atoms, red represent oxygen atoms.

ITQ-38 seems to fulfil a lot of the 'wish list' initially set out. It's a germanosilicate framework, consisting of well-defined layers connected by Ge-dominated monodirectional *d4r*. These *d4r* units are also easily accessible through the large pores present in the structure.

However, ITQ-38 has several shortcomings that may make it a non-ideal candidate for the ADOR process. The original synthesis of ITQ-38 required the use of small amounts of boron, that is then spread throughout the framework structure, in a similar fashion to aluminium. This boron is then weak to hydrolysis conditions.[14] In addition, characterisation of ITQ-38 showed that there was Ge present in the layers as well as the *d4r*, with some T-sites showing a Ge/Si occupancy of 0.1. The distribution of these Ge-occupied T-atoms in the layers is such that there is a direct link between the Ge-dominated *d4r* through the layer by these T-sites (Figure 5.15). The presence of a 3D channel system, including a channel system that penetrates through the layers, adds further instability to these layers. As the increase in surface area makes the layers more prone to attack and degradation.[15–18]

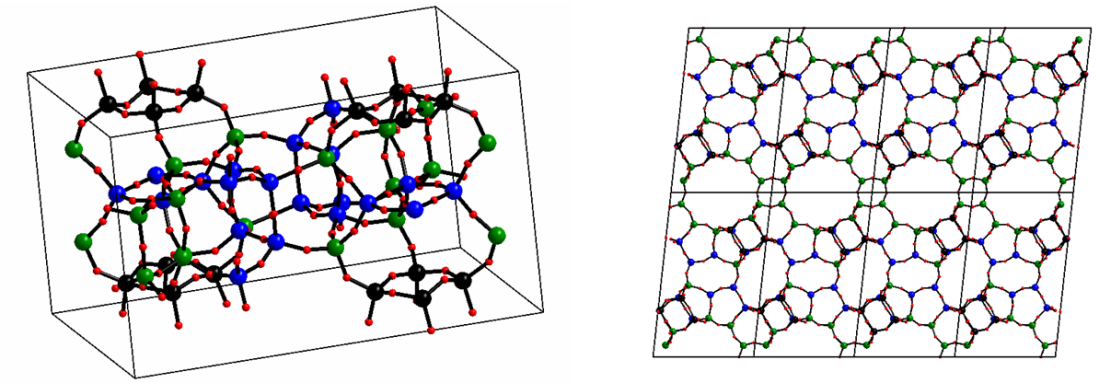

Figure 5.15 Shows the ITQ-38 unit cell (left) and the ITQ-38 structure viewed in the *b* direction (right). The relative occupancies of the T-atoms are highlighted. The Ge-dominated *d4r* T-atoms are shown in black, wholly Si T-atoms are shown in blue and T-atoms with some Ge occupancy (maximum Ge occupancy 0.1) are shown in green. This highlights the potential instability of the layers, due to the presence of Ge in the layers and the channel system that penetrates the layers.

The best behaved ADORable zeolites (like **UTL**) are typified by dense layers, without penetrating channel systems, that contain wholly silicon. The presence of a 3D channel system, the lower density of the layers, and the presence of B and Ge within them may add complications to the manipulation of the layers and the stability of the layered material later during the ADOR process. Also, the original synthesis of the organic SDA required the use of a procedure involving the release of HCN.[10] It was therefore desirable to modify the synthesis to avoid the problems associated with such a dangerous procedure.

5.5.2 Experimental Procedures

5.5.2.1 Synthesis of MPP

1-methyl-4-pyrrolidin-1-yl-piperidine (MPP) was synthesised through a modified procedure to that of Moliner *et al.*[10] Pyrrolidine (49.18 g, 0.69 mol) was placed in EtOH (300 mL), stirred and cooled with an ice bath. Then 1-methyl-4-piperidone (31.33 g, 0.27 mol) was added dropwise. 15 minutes after complete addition sodium triacetoxyborohydride (STAB) (93.68 g, 0.44 mol) was added and the reaction was left to stir at room temperature over 72 hours. Once complete, KOH was added to achieve a pH > 12, the solution was then saturated with NaCl and the product extracted with diethyl ether. This was dried over anhydrous $MgSO_4$, filtered and the solvent removed by rotary evaporation and high vacuum to yield MPP (35.76 g, 76.7 %).

5.5.2.2 Synthesis of DMPP Hydroxide

1,1-dimethyl-4-(1-methylpirrolidine-1-yl)piperidium iodide was synthesised according to the procedure reported by Dodin *et al.*[9] MPP (50 g, 0.30 mol) was dissolved in MeOH (500 mL) and placed under N_2. Methyliodide (210.86 g, 1.50 mol) was then added dropwise. The reaction was then allowed to stir at room temperature for 5 days. The white

precipitate formed was filtered and washed with MeOH and diethyl ether, then dried under vacuum to yield DMPP Iodide (125.22 g, 93 %). The iodide salt was converted to the hydroxide with the use of ion-exchange resin.

5.5.2.3 Synthesis of Zeolite ITQ-38 (ITG)

The synthesis of **ITG** was attempted using the same synthesis procedure as that reported for by Moliner *et al*.[10] for ITQ-38. Boric acid (0.049g, 0.8 mmol) was added to a stirring solution of DMPP hydroxide (19.42 mL, 10 mmol). After homogenisation germanium dioxide (0.146 g, 10 mmol) was added and the solution stirred for an additional hour. Colloidal Silica (Ludox AS-40) was then added and the solution stirred for an additional 3 hours. Once complete additional water was added to ensure a gel molar composition of 30 SiO_2: 10 GeO_2: 0.8 B: 10 SDAOH: 800 H_2O. The gel was then placed in a Teflon lined autoclave and heated at 175 °C for 15 days. The SDA containing zeolite was then calcined at 575 °C for 7 hours.

Investigations were also conducted into varying the Si/Ge content of the gel without varying the other components of the gel.

5.5.2.4 Formation of ITQ-38P

The hydrolysis of **ITG** was investigated under various conditions and with varying molarities of acid. The solid was placed in a stirring hydrolysis solution with a solid to solvent ratio of 0.1g/100ml ratio. Hydrolysis solvents included water, ethanol and HCl of various concentrations. These were then heated or left stirring at room temperature for a defined time of between 1 and 48 hrs. The resultant solid was then filtered and washed with additional water. The ideal hydrolysis conditions heated the sample in 0.1 M HCl for 1 hour.

5.5.2.5 Intercalation of ITQ-38P

5.5.2.5.1 Octylamine

ITQ-38P (0.150 g) was placed in Octylamine (15 mL), stirred at 70 °C for 3 hours and then stirred for another 16 hours at room temperature. The resultant solid was then filtered and dried to give the intercalated product (yield = 0.145 g).

5.5.2.5.2 DEDMS

ITQ-38P (0.150 g) was placed in a Teflon liner containing nitric acid (1 M, 15 mL) and DEDMS (68.9 µL,). After 10 minutes of stirring the liner was placed in a steel-lined autoclave and heated at 175 °C for 16 hours. The solid was the isolated by filtration and dried in air to give the intercalated product (yield = 0.108 g).

5.5.2.6 Reassembly of ITQ-38 After Intercalation

The intercalated ITQ-38P was calcined at 575 °C for 7 hours with a ramp rate of 1 °Cmin^{-1}.

5.5.3 Results and Discussion

5.5.3.1 Synthesis of the SDA

As mentioned previously the synthesis of the germanosilicate ITQ-38 required the organic SDA (1,1-dimethyl-4-(1-methylpirrolidine-1-yl)piperidium hydroxide or DMPP hydroxide). This was synthesised by the reaction of pyrrolidine with 1-methyl-4-piperidone to make 1-methyl-4-pyrrolidin-1-yl-piperidine (MPP) with the use of the reducing agent sodium cyanoborohydride (Scheme 5.1, Step 1). MPP is then reacted with methyl iodide to produce DMPP iodide (Step 3), which can then be converted to its hydroxide form using standard ion exchange procedures (Step 4).

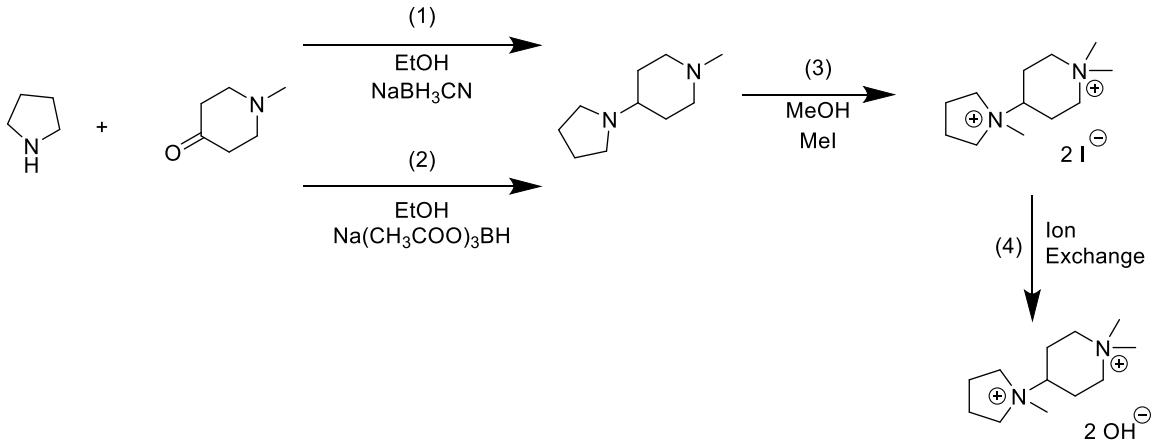

Scheme 5.1 Shows the synthesis procedure used by Dodin *et al.* to form the organic SDA 1,1-dimethyl-4-(1-methylpirrolidine-1-yl)piperidium hydroxide using steps 1, 3 and 4. Step 1 involves the release of HCN and so was avoided through a modification to produce the new scheme involving steps 2, 3 and 4.

Although the original procedure used by Moliner *et* al. can produce the required SDA,[10] the release of HCN during the procedure is highly undesirable. An alternative reducing agent, sodium triacetoxyborohydride (STAB) was proposed (Step 2). STAB is a well-known reducing agent and is commonly used instead of sodium cyanoborohydride to avoid the release of HCN. Although STAB is a milder reducing agent than sodium cyanoborohydride, is water sensitive and incompatible with methanol, the reaction conditions seem ideal for its use.

The test synthesis of MPP was conducted in a similar manner to that quoted in the experimental, but on a smaller scale (1g of 1-methyl-4-piperidone was used). The progress of the reaction was followed by TLC. Upon completion and work-up an off-white solid was

yielded (1.21 g, 81.8 %). The purity of the sample was then characterised by ^{1}H NMR (Figure 5.16).

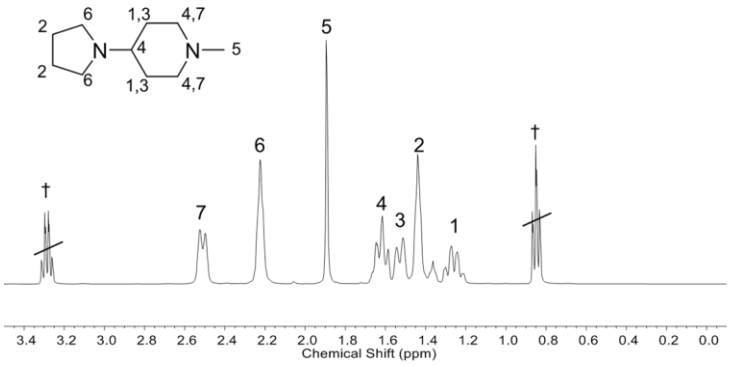

No.	Peak position (ppm)	Integration
1	1.23	2.06
2	1.41	3.70
3	1.50	1.74
4	1.59	2.89
5	1.86	3.00
6	2.19	2.19
7	2.48	2.10

Figure 5.16 Shows the ^{1}H NMR spectrum (left) of the synthesised MPP intermediate using the adapted synthesis procedure. The MPP structure is overlaid with the different environments labelled. The table (right) shows the peak position, the corresponding environment, and the integration (when peak 5 is normalises to 3.00). (†) indicates the peaks indicative of the diethyl ether impurity.

The results of the NMR showed that the adapted procedure had indeed produced the target molecule. The presence of diethyl ether was noted, but drying the sample under vacuum would easily remove such impurities. The NMR was then assigned as seen in Figure 5.16 showing the expected H environments and integration. It is noteworthy to acknowledge the different peak positions for similar H environments within the piperidine ring (positions 1,3,4 and 7). This is most likely due to the confirmation of the ring, resulting in the 2 H atoms on the same carbon experiencing different interactions and so experiencing different shifts.

With the confirmation of the successful synthesis of MPP. The experiment was reproduced on a larger scale to yield more MPP, also with a good yield and purity (Section 5.5.2.1). The next synthesis steps to form DMPP followed the same procedure as reported by Moliner *et al.*[10]

5.5.3.2 Synthesis of ITG

ITG was synthesised according to the reported synthesis procedure by Moliner *et al.*[10] This was repeated with a slightly different Si/Ge ratio to increase the amount of Ge in the parent germanosilicate and ensure the occupation of the *d4r*.

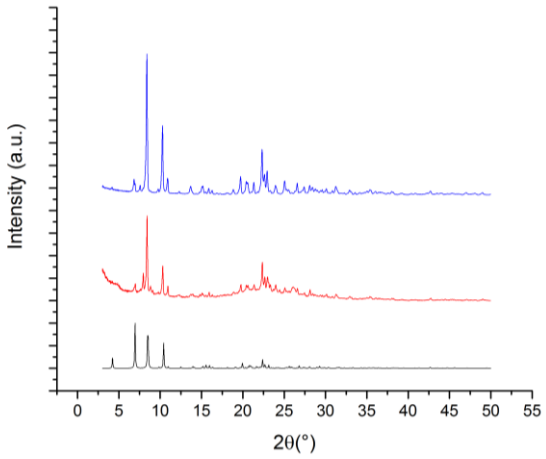

Figure 5.17 Shows the PXRD patterns of ITG (black) compared to as-synthesised ITQ-38 Si/Ge = 3 (blue) and Si/Ge =1.66 (red).

The PXRD patterns (Figure 5.17) showed a similar profile to the expected PXRD pattern for **ITG**, there was however a marked difference in intensities, most likely due to preferential orientation, which is often noted when comparing different powder patterns. It seemed that the increase in Ge content did not affect the powder pattern too much in fact it seemed that there was an increase in long range order.

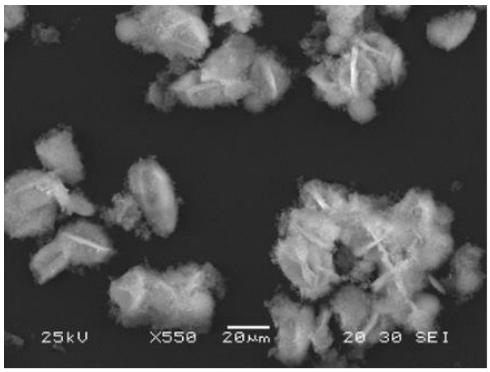

Elemental Analysis (Atomic Percent)

Spectrum	O	Si	Ge	Total
1	64.03	30.59	5.38	100
2	77.26	19.38	3.36	100
3	71.74	23.89	4.37	100
4	68.17	25.30	6.53	100
5	72.37	22.43	5.20	100
Average	70.71	24.32	4.97	

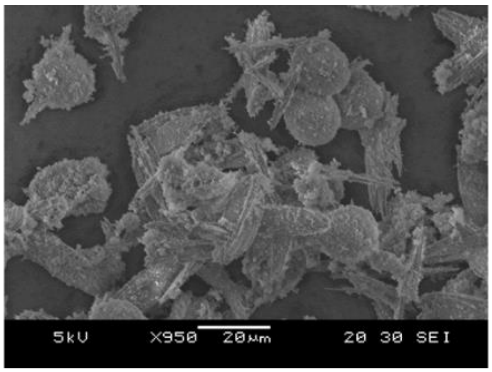

Elemental Analysis (Atomic Percent)

Spectrum	O	Si	Ge	Total
1	72.55	21.64	5.81	100
2	72.73	24.25	3.02	100
3	75.33	19.98	4.69	100
4	76.96	19.43	3.61	100
5	68.30	24.91	6.79	100
Average	73.17	22.04	4.78	

Figure 5.18 SEM and EDX analysis of samples of ITG. The crystal results of the analysis for the reported ITQ-38 synthesis showed pill-like, twinned and less defined crystals (left), while those with increased Ge content led to more defined, less twinned crystals with an additional GeO_2 phase as an impurity.

From SEM and EDX analysis (Figure 5.18) of the crystals showed that both syntheses produced similar crystal morphologies, which may have been indicated by the PXRD patterns. Both crystals showed a similar pill-like morphology. However, the crystals

produced from the ideal ITQ-38 synthesis produced less-defined crystals, whiles the increased germanium content led to a more defined crystal. In the standard synthesis, there was a prevalence of twinning. The synthesis with the increased Ge content seemed to show less twinning and a more defined crystal morphology. This perhaps was the reason for the increasing crystallinity of the PXRD pattern with the increasing Ge content of the initial synthesis gel. However, the increase in Ge content of the synthesis gel had clearly not transpired into the resultant product. As standard ITQ-38 showed a Si/Ge ratio of 4.89, while the Si/Ge = 1.666 gel lead to a Si/Ge content of 4.61. This marginal increase in the Ge content of the crystals showed that increasing the Ge content of the gel was not able to afford higher Ge-containing crystals. In addition, the higher Ge content led to the presence of a GeO_2 impurity (seen as small spheres).

The inability to increase the Ge content of the crystals shows that there is a limit for the incorporation of Ge into ITQ-38. Ge is known to preferentially locate in the *d4r,* but it seems that this does not necessarily mean that all the *d4r* T atoms are Ge. It seems that the absolute maximum amount of Ge seems to be incorporated into framework positions and any additional Ge is simply not included, forming a GeO_2 impurity. It is interesting to note that while the Si/Ge ratio in the initial gel of ITQ-38 was 3 the Si/Ge ratio in the product zeolite was about 4. Indicating that Ge is preferentially incorporated into the framework structure.

5.5.3.3 The Disassembly of ITQ-38

Treatment of ITQ-38 with 0.1 M HCl resulted in a significant change in the PXRD pattern (Figure 5.19).

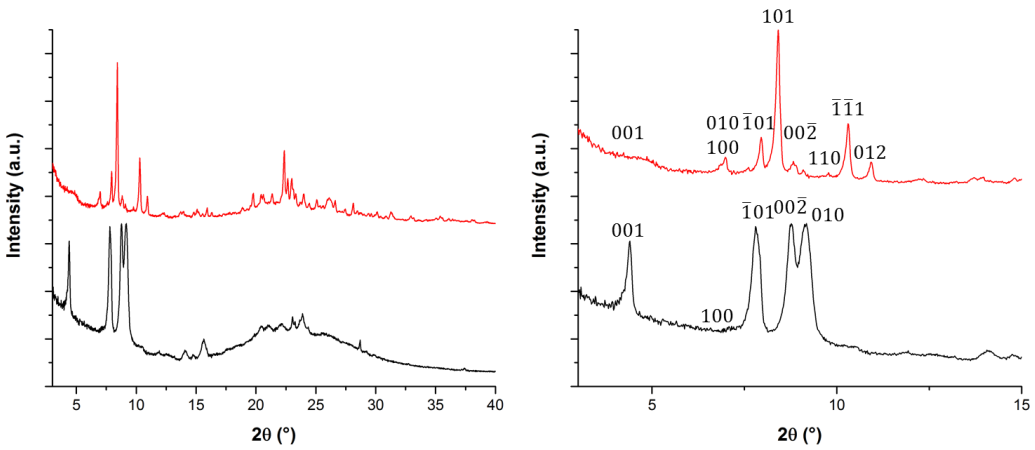

Figure 5.19 Shows the PXRD pattern of ITQ-38 before (red) and after treatment with 0.1 M HCl and heating for 1 hr (black). The difference between the powder patterns is marked by the significant change in the peaks between 3-15 ° 2θ (right) with their corresponding reflections labelled.

By indexing the peaks of the original PXRD pattern (based on the generated structure from the IZA database) for ITQ-38 and using previous trends observed for other ADORable zeolites. It was possible to predict the reflections responsible for the peaks observed in the disassembled material. In a similar fashion to that seen for other ADORable zeolites the number of observed peaks greatly decreases due to destruction of the *d4r* and the irregular ordering of the ITQ-38 layers (ITQ-38P). Four peaks dominated the PXRD pattern. First the 001 peak appears more well defined in the hydrolysed material than in the in the original sample at 4.39 ° 2θ, perhaps due to the decreased intensity of the overall diffraction pattern, resulting in the 001 peaks intensity being proportionally larger. The $(\bar{1}01)$ reflection remains intact again with greater intensity and the $(00\bar{2})$ shows a much greater intensity that seen in the original sample. Another new peak is associated with the movement of the 010 peak from 6.96 ° to 9.17 ° 2θ. This corresponds to an expected change in the interlayer distance due to the removal of the *d4r*. The change in interlayer distance therefore equalled approximately 3.1 Å, which is slightly less than the expected space occupied by a *d4r* unit, and seems to confirm the removal of the *d4r* and the subsequent collapse of the layers. Another notable change seen in the PXRD pattern of ITQ-38P is the notable absence of some of the most prominent peaks from the original ITQ-38 material. There is a complete loss of the previously observed triplet at about 10° 2θ (corresponding to the (110), $(\bar{1}\bar{1}1)$ and (012) reflections). This is a strong indication of formation of a layered material as the breakdown of the *d4r* leads to less order in the [010] direction. This is required for the reflections that have a *h* value greater than 0, and so the disorder leads to the loss of these peaks. For this reason, the less obvious absence is the 101 peak, which dominated the original ITQ-38 sample. This is notable as it would be expected to still be unaffected by the loss of order in the [010] direction. However, the loss of intensity is clear when the (101) plane is superimposed on the structure. The 101 peak corresponds to a reflection that dissects the structure, through the *d4r* rings (Figure 5.20). By destroying the *d4r* rings during the disassembly process, all the primary source of electron density in that reflection is removed and so the peak losses providence. Such conclusions seem to be furthered by the growth of the $(\bar{1}01)$ reflection, which was a minor peak in the PXRD pattern of the ITQ-38 material. The growth in intensity of the $(\bar{1}01)$ reflection indicates that the $(\bar{1}01)$ reflection is unaffected by the disassembly of ITQ-38, as it's ordering is unaffected by the movement of the layers in the [010] direction. Unlike the (101) reflection the electron density of the $(\bar{1}01)$ reflection originates from atoms in the layers, meaning that this reflection follows the typical

behaviour seen for other peaks in disassembled materials. The reflection is therefore unaffected by the removal of the *d4r* and the loss of order in the [010] direction.

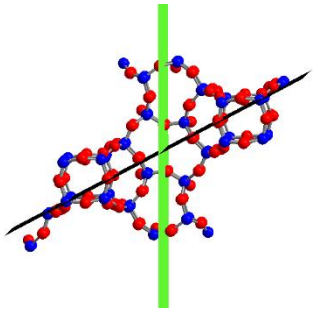

Figure 5.20 Shows a cross-section of the ITQ-38 structure when viewed in the [010] direction. From this angle, it is possible to see the (101) reflection (black) and the ($\bar{1}01$) reflection (green) and the atoms they intersect. The (101) is clearly shown intersecting the *d4r* units, while the ($\bar{1}01$) does not intersect these, but rather the atoms in the layer. This explains the reasoning for the disappearance of the 101 peak and the visibility of the $\bar{1}01$ after hydrolysis as the electron density of the former is severely reduced while the electron density of the latter is unaffected by the hydrolysis process.

SEM/EDX analysis (Figure 5.21) also showed the successful disassembly of ITQ-38. The morphology of the ITQ-38P crystals remained like the parent germanosilicate, while the EDX analysis showed that the Ge-content of the material had decreased in ITQ-38P, resulting in a Si/Ge ratio of 106.6.

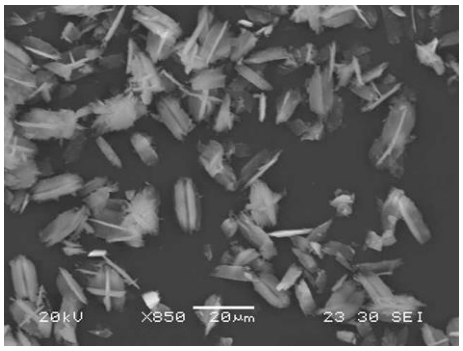

Elemental Analysis (Atomic Percent)

Spectrum	O	Si	Ge	Total
1	77.45	22.16	0.39	100
2	69.12	30.65	0.23	100
3	64.91	34.85	0.24	100
4	76.04	23.72	0.24	100
5	72.56	27.22	0.22	100
Average	72.02	27.72	0.26	

Figure 5.21 Shows the SEM and EDX analysis of disassembled ITQ-38. Showing the decrease in Ge content of the crystals and the preservation of the crystal morphology.

^{29}Si MAS NMR also confirmed the successful disassembly of ITQ-38 into a layered material (Figure 5.22).

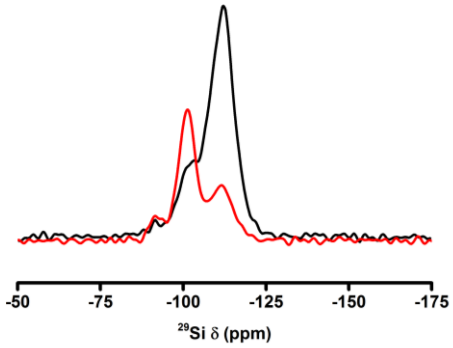

Figure 5.22 Shows the ^{29}Si MAS NMR (black) and {^{1}H} ^{29}Si cross-polarisation MAS NMR (red) spectra of ITQ-38P. Confirming the large number of Q^3 sites formed by the removal of the Ge-dominated *d4r* between the layers and the formation of large concentration of silanols in the interlayer region.

The ^{29}Si NMR showed the presence of Q^3 sites (~ -100 ppm), which was accentuated by the cross-polarisation experiment. This showed that the Si species of the material were no longer wholly bonded to 4 other T-atoms by a bridging oxygen, but was connect to 3 other T-atoms and a hydrogen atom. This is because removal of the *d4r* in between the layers leads to the formation of silanols in the interlayer region. The presence of Q^4 sites (~ -100 ppm) and the very small number of Q^2 sites seemed to confirm previous expectations about the layers. As the presence of Q^2 indicates the formation of some $Si(OH)_2$ units, due to the removal of Ge from within the layer as well as that in the *d4r*. However, the large number of Q^4 sites indicates that the amount of additional Ge in the layers was limited as most of silicon species were still connected to 4 other T-atoms. These results indicated that the ITQ-38P layers were still relatively intact after the initial hydrolysis and showed that the disassembly of ITQ-38 into a layered material was possible.

5.5.3.4 The Organisation of ITQ-38P

The first attempted organisation of the ITQ-38 involved the use of acid to replicate similar results seen for **UTL** and the formation of IPC-2 and IPC-4. Where low acidity leads to a full deintercalation of the species, while a stronger acid leads to an additional rearrangement of the silicon atoms to form *s4r* species between the layers.[19]

5.5.3.4.1 Organisation with 12M HCl

Treatment of ITQ-38 with 12 M HCl resulted in a similar initial pattern to that obtained at 0.1 M HCl, but with more disorder. This indicated that ITQ-38 could be disassembled/organised with 12 M HCl (Figure 5.23).

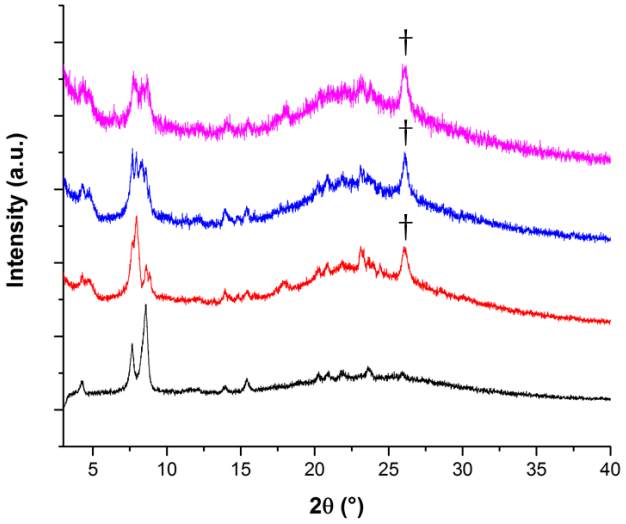

Figure 5.23 Shows the impact of 12 M HCl on ITQ-38 over time. After 1 hr (black) a similar powder pattern is seen compared with just hydrolysed sample. Increasing the time of exposure to 12 M HCl by 12 hrs (red), 24 hr (blue), 48 hr (pink) lead to an increasing loss of crystallinity instead of any reassembly process. The presence of rutile GeO_2 peak is noted (†).

However, as time was increased the PXRD patterns showed a gradual deterioration of the structure. The loss of crystallinity of the PXRD patterns gradually increased up to the 48 hrs. If **ITG** behaved in a similar way to **UTL** then it would be expected that the rearrangement would have successfully taken place with silica species forming *s4r* unit in between the layers. Yet the key peaks would be expected to move to lower *d*-spacing/higher 2θ angles as the deintercalation process is followed by rearrangement of silicon to form *s4r* connection between the layers. The patterns seemed to indicate the initiation of the rearrangements process, however this process is overshadowed by the material's increasing loss of crystallinity over time. Such conclusions were also confirmed by the increasing size of the noise between 15-35° 2θ and the increasing dominance a peak characteristic of GeO_2 at 26° 2θ.

Such results seemed to show that the rearrangement process with the use of high concentrations of 12M HCl was not possible. One explanation for this behaviour is the different channel systems between **UTL** and **ITG**. Unlike **UTL**, which consists of a 2D channel system with 14- and 12-ring channels, separated by dense ferrierite-like layers, **ITG** has a 3D channel system, consisting of 12-, 10- and 10-rings. Without the presence of dense layers of silicate, the framework structure is much more vulnerable to high acid concentrations. This resulted in an increasingly less crystalline material due to the gradual breakdown of the framework as the exposure time was increased rather than resulting in the rearrangement of the structure to form *s4r* linkages. This suggests that the less dense

character of the **ITG** layers makes them particularly vulnerable to higher acid concentrations.

5.5.3.4.2 Organisation with 0.1 M HCl

Treatment of ITQ-38 with 0.1 M HCl resulted in a similar change in the PXRD pattern as seen with treatment with 12 M HCl (Figure 5.24).

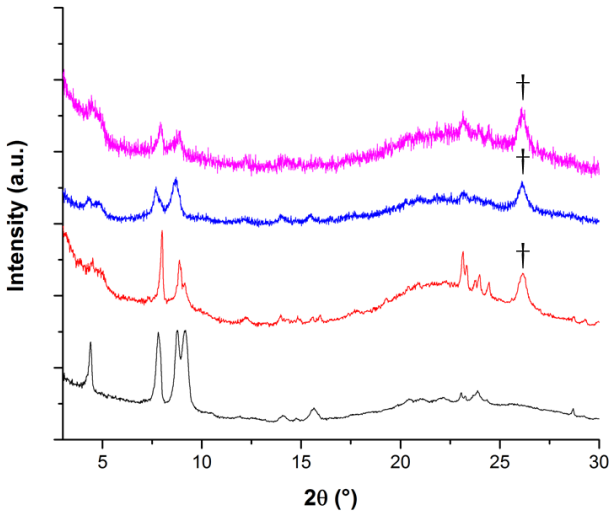

Figure 5.24 Shows the impact of 0.1 M HCl on ITQ-38 over time. After 1 hr (black) a similar powder pattern is seen compared with the just hydrolysed sample. Increasing the time of exposure led to an increasing loss of crystallinity as previously seen under highly acidic conditions (12 hr (red), 24 hr (blue), 48 hr (pink)). The presence of rutile GeO_2 peak was also seen (†).

After 12 hours the PXRD pattern was dominated by 2 peaks as seen after treatment with 12 M HCl. Beyond 12 hours, the PXRD pattern similarly lost a lot of crystallinity. One difference between treatment with 0.1 M HCl and 12 M HCl is that these two peaks remained unchanged as the loss of crystallinity of the sample increased; whereas treatment with 12 M HCl resulted in some movement in the peaks creating a large area of intensity. This is perhaps an indication of the dominance of the deintercalation process under weakly acidic conditions. This is because the weak acid is unable to promote the formation of new Si-O-Si bonds and so no rearrangement process can take place. Both results indicate that the ITQ-38 material is unsuited for organisation with acid treatment. Previous observations suggest that, depending on the treatment conditions, framework Si–O–Si groups may be selectively cleaved. Under conditions involving liquid water the process involves the hydrolysis of terminal Si–O–Si–OH groups, creating a defect, which propagated inward throughout the zeolite lattice. The presence of Ge and B sites in the layers would provide an additional avenue for this process of degradation.[15–18]

The combination of the low density of the layers, the presence of Ge in the layers and the large pores penetrating these layers seems to make ITQ-38P susceptible to break down under the harsh and relatively gentle conditions required for organisation with acid treatment. Due to such results, it was clear that it was possible to disassemble ITQ-38 therefore creating a layered material, however the subsequent treatment of that material should be optimised to account for the fragility of the layered intermediate. The use of acid to accomplish the organisation of these layers was too harsh for the structures.

5.5.3.4.3 Organisation Using Intercalating Agents

Another method for the organisation of the layers is the use of intercalating agents. The organisation of the ITQ-38P layers with intercalating agents, was employed to minimise the exposure of the layers to the harsh acidic condition used previously. To minimise the exposure of ITQ-38P to harsh acidic conditions the hydrolysis step was conducted for 1 hour as initial analysis showed that after this time the layered materials had formed. This disassembled material was collected after 1 hour and then treated accordingly (Section 5.5.2.5).

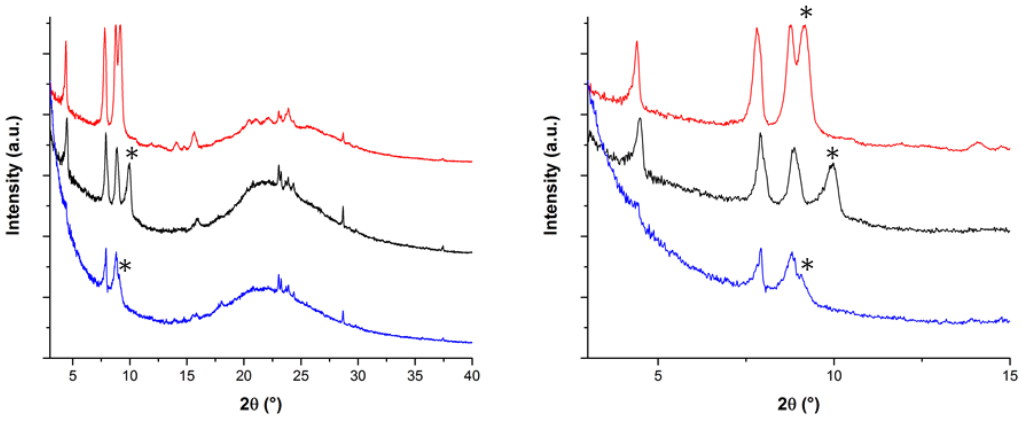

Figure 5.25 Shows the PXRD patterns for ITQ-38P (red), ITQ-38P treated with octylamine (black) and DEDMS (blue). The octylamine shows some movement of the 010 peak (*), due to organisation of the layers, while treatment with DEDMS resulted in a decrease in crystallinity of the material.

Treatment of layered materials with non-bonding agents like octylamine resulted in organisation of the layers, by disrupting the hydrogen bonding between the interlayer silanols.[20] Treatment of ITQ-38P with octylamine showed a minimal but important difference compared to the original material in the PXRD pattern (Figure 5.25). While the first three peaks, corresponding to the (001), $(\bar{1}01)$ and $(00\bar{2})$ remained consistent at 4.49 °, 7.93 ° and 8.86 ° 2θ; the peak corresponding to the (010) reflection moved to higher 2θ

angle (from 9.17 ° to 9.97 ° 2θ). This indicated a lower d-spacing due to the formation of a layered material and that these layers could be manipulated, resulting in better organisation of the layers. Secondly the position of the 010 peak at 9.97° 2θ corresponded to a total decrease in the interlayer distance. This value of 3.82 Å is closer to the values associated with the loss of the *d4r* and the organisation of the layers for the formation of direct O-linkages. The minimal difference between 010 peak position of the initial hydrolysed ITQ-38P layers and the organised ITQ-38P seems to indicate that the disassembly process was very quick and that the layers had indeed collapsed together during hydrolysis after the removal of the *d4r*.

The organisation step was then also attempted with the bonding agent DEDMS, which should form covalent bonds between interlayer silanols, which can then condense together during reassembly to form *s4r*. The use of DEDMS has been successfully used to form these *s4r* linkages between the IPC-1P layers as seen in the formation of IPC-2 from **UTL** (Figure 5.25).[2] Another sample of ITQ-38P was therefore treated with DEDMS in 1M HNO_3 at elevated temperatures.[19] Treatment of ITQ-38P under these conditions seemed to result in a similar material as that seen for the treatment of ITQ-38P under weakly acidic conditions. A large decrease in the crystallinity of the sample was seen, with two peaks dominating the PXRD pattern. The additional 010 peak was not determinable due to the poor quality of the material. Although it may be present in the pattern as an additional shoulder to the right of the $\bar{1}01$ peak at 8.77° 2θ. This may show some success in increasing the interlayer distance to a higher *d*-spacing, compared with treatment with octylamine, which is associated with the formation of the silica columns between the layers. However, such conclusion are simply conjecture as the quality of the material is imperfect, most likely due to the use of high temperatures and acidic conditions, required for the intercalation of DEDMS. The poor quality of such material shows that the ADOR process is incredibly complex, consisting of many steps with different qualities that can be impacted by the framework properties of the parent zeolite. In this case, the weakness of the ITQ-38P layers to acidic mediums make it hard to perform the standard procedures required to properly organise the layers.

5.5.3.5 Reorganisation of the Layers

Reorganisation of the layers was attempted on the samples intercalated with octylamine and with DEDMS. Both samples, whether intercalated with octylamine or DEDMS seemed to produce a similar pattern upon calcination (Figure 5.26).

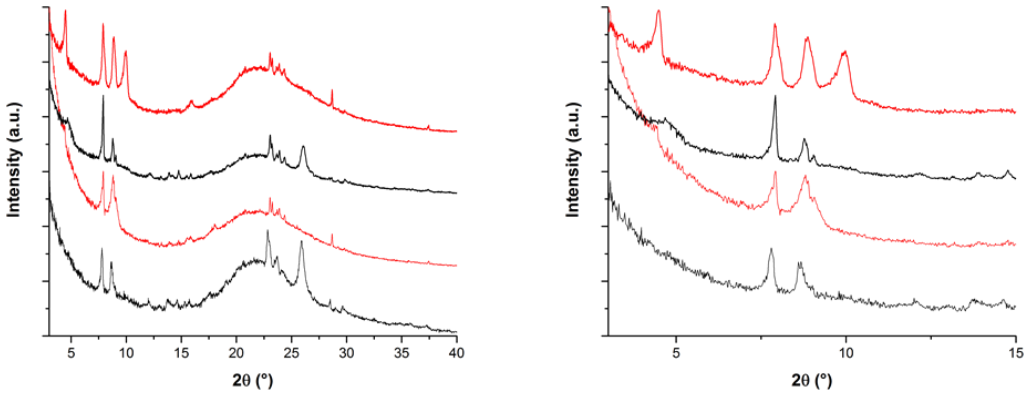

Figure 5.26 Shows the PXRD Patterns before (red) and after calcination (black) for ITQ-38P intercalated with octylamine (top) and DEDMS (bottom), a close-up of the PXRD pattern between 3-15 ° 2θ (right).

Both patterns were dominated by a peak at 7.95 ° 2θ followed by an additional peak at 8.79 ° 2θ. The sample intercalated with octylamine seemed to be better defined and it was possible to observe an additional peak at 9.06 ° 2θ.

The low quality of the PXRD patterns was perhaps indicative of a poorly defined reorganisation step. The similarity of the two patterns despite the different conditions seemed to infer that the formation of the different interlayer linkages between the ITQ-38P layers was not possible.

SEM and EDX analysis of the samples treated with octylamine and DEDMS showed a very high Si/Ge ratio, 83.87 and 83.03 respectively (Figure 5.27).

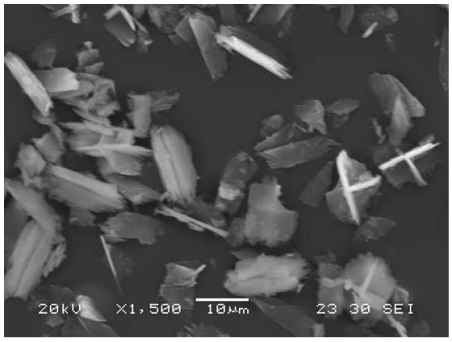

Elemental Analysis (Atomic Percent)

Spectrum	O	Si	Ge	Total
1	76.12	23.6	0.29	100
2	76.97	22.73	0.3	100
3	74.34	25.28	0.38	100
4	67.63	32.08	0.29	100
5	77.67	22.1	0.23	100
Average	74.55	25.16	0.30	

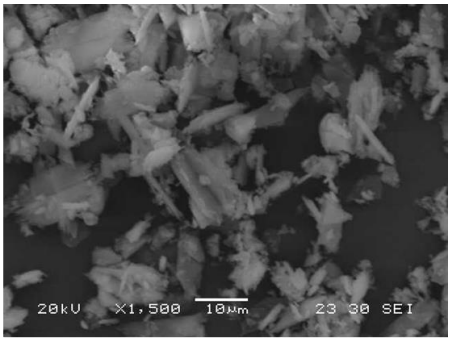

Elemental Analysis (Atomic Percent)

Spectrum	O	Si	Ge	Total
1	75.82	23.82	0.36	100
2	76.94	22.86	0.19	100
3	72.45	27.25	0.3	100
4	74.63	25.05	0.32	100
5	74.1	25.59	0.31	100
Average	74.79	24.91	0.30	

Figure 5.27 Shows the SEM and EDX analyses for resultant materials after reassembly, depending on if the layers were treated with octylamine (left) or DEDMS and acid (right). Both showed a high Si/Ge ratio with the sample treated with DEDMS and acid showing a greater lack of uniformity in the crystal morphology.

The decrease in the crystals' uniformity when treated with DEDMS and acid seemed to confirm that such conditions were too harsh for the relatively weak layers.

Ascertaining the nature of the daughter zeolites that were present was therefore vital. One advantage of the ADOR process is the ability to predict the products from the ADOR process. The isoreticular relationship of the daughter zeolites to the parent germanosilicate makes it easier to predict the resultant product from the synthesis. Structures were therefore generated for the two expected daughter zeolites ITQ-38-octylamine and ITQ-38-DEDMS using Diamond.[21] This was achieved by removing the T and O atoms in the *d4r* to produce the layers. One layer was then translated so that the distance between the two layers was equivalent to that expected for the desired daughter zeolite. T atoms for the *s4r* were then added (if required), the atoms reconnected, and the unit cell length reduced by the amount the layer was translated by. The two predicted daughter zeolites ITQ-38-octylamine and ITQ-38-DEDMS should have the same layers as ITQ-38 but with direct O-linkages and *s4r* linkages between the layers respectively (Figure 5.28).

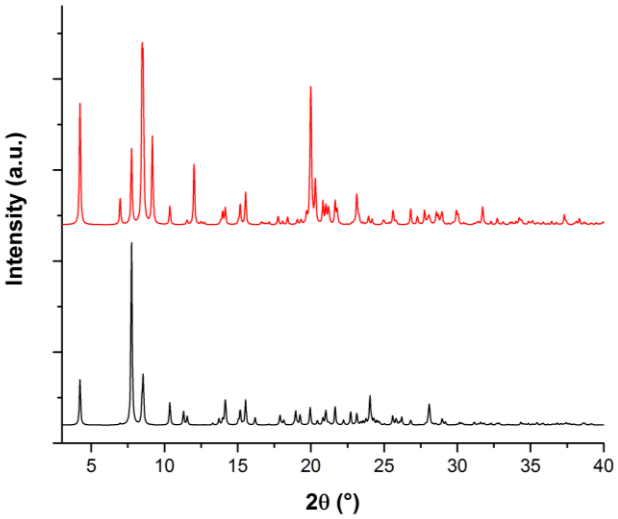

Figure 5.28 Shows the predicted PXRD patterns for ITQ-38-octylamine (black) and ITQ-38-DEDMS (red).

By looking at the predicted structures, ITQ-38-octylamine and ITQ-38-DEDMS seem to show some major differences. Both should have a prominent 100 peak at 6.97 ° 2θ. ITQ-38-octylamine should be dominated by the $(\bar{1}01)$ reflection at 7.75 ° 2θ and show an additional peak at 8.50 ° 2θ corresponding to the $(00\bar{2})$ and (101) reflections. In comparison to this, ITQ-38-DEDMS seems to show an additional peak at 9.17 ° 2θ. This corresponds to interlayer (010) reflection in the PXRD pattern. In the case of ITQ-38-octylamine this reflection is severely reduced in intensity and at a lower angle (11.30 ° 2θ).

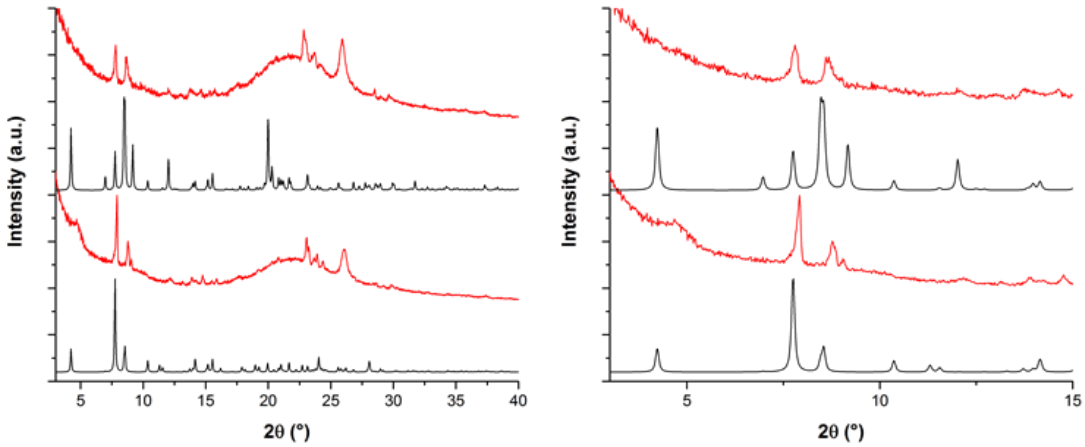

Figure 5.29 Shows a comparison of the generated (black) and the experimental (red) PXRD patterns with ITQ-38-DEDMS shown above and ITQ-38-octylamine shown below. The range between 3-15 ° 2θ is also shown (right).

By taking these generated PXRD patterns and comparing with the experimental patterns obtained (Figure 5.29) some important conclusions can be made. The experimental conditions traditionally used for making *s4r* linkages between the layered materials was unsuccessful in the case of ITQ-38P. Both patterns seemed to show a significant

resemblance to the predicted PXRD pattern for the ITQ-38-octylamine, where direct O-linkages connect the layers.

Such results suggest that the intercalation of the DEDMS was unsuccessful at producing the desired ITQ-38-DEDMS product with *s4r* linkages between the layers. However, from the results with octylamine, the layers can be manipulated with intercalating agents. Such results are a sign of the complexities and issues that surround the ADOR process. The issues surrounding the DEDMS and not the octylamine would perhaps suggest that the ITQ-38P layers are particularly weak to the conditions used for the formation of *s4r* linkages between the layers. There could also be an additional characteristic of the ITQ-38 framework that may lead to an inefficient organisation of the layers with DEDMS.

The results were further complicated after analysis of the samples with BET adsorption (Figure 5.30).

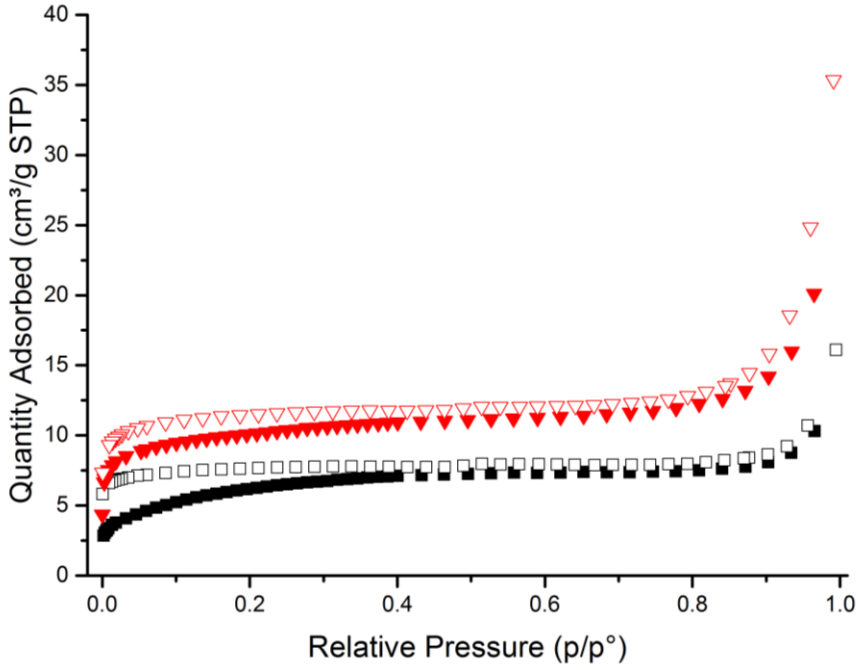

Figure 5.30 Shows the adsorption isotherms for the ITQ-38P layers treated with octylamine (black) or DEDMS and acid (red), with the adsorption represented by filled symbols and desorption by empty symbols.

Both samples showed a severely reduced adsorption compared to the originally reported BET surface area of 367 m^2/g for the ITQ-38 material.[10] ITQ38-octylamine showed a BET surface area of 21.7 m^2/g and ITQ-38-DEDMS showed a BET surface area of 37.38 m^2/g. Although it is promising that the ITQ-38-DEDMS has a slightly higher BET surface area compared to ITQ38-38-octylamine, as would be expected, the reduced surface area is a clear indication of the reduced capacity of the structure. Especially as the original ITQ-38

structure has 10- and 12-rings running in the [010] direction, which should be unaffected by the reduction of the interlayer distance between the layers. There are several factors, which could lead to this reduced surface area. Firstly, the instability of the layers would lead to a disintegration of the surface area as the layers degrade, secondly the process itself could lead to a reduction of the surface area, and thirdly the reduced surface area could suggest a disorderly organisation and reassembly of the layers. It is most likely a combination of these factors that could lead to a decrease in the surface area of the material. The unsuccessful organisation and reassembly of the layers was further supported by results obtained from the ^{29}Si solid-state MAS NMR (Figure 5.31).

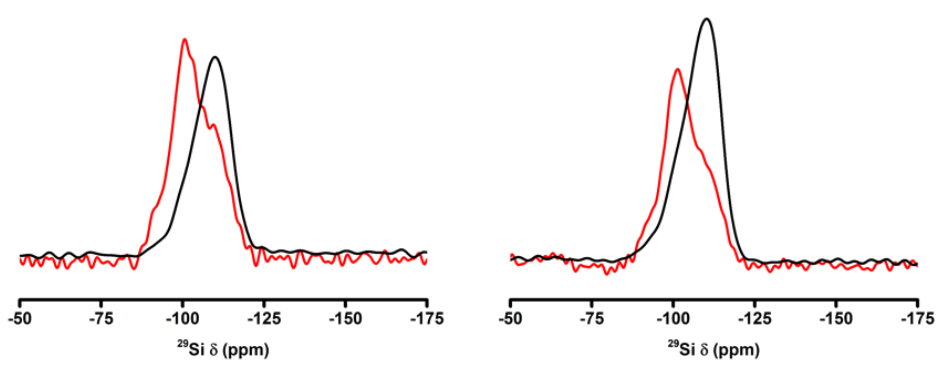

Figure 5.31 Shows the ^{29}Si MAS NMR spectra (black) and {^{1}H} ^{29}Si cross-polarisation MAS NMR (red) for the ITQ-38P layers after treatment with octylamine (left) and with DEDMS and acid (right). Both clearly show the presence of non-Q^{4} sites and underline that such materials have been unsuccessfully organised and reassembled.

The ^{29}Si MAS NMR of the materials showed a broad peak focused around -110 ppm with a large shoulder at around -105 ppm, indicating the presence of Q^4 and Q^3 sites. These Q^3 sites were also highlighted in the {1H} ^{29}Si cross-polarisation MAS NMR as belonging primarily to Si-OH units present in the material. The cross-polarisation MAS NMR also indicated the presence of a large number of Q^2 sites in the material as a result of $Si(OH)_2$ groups. Such results are indicative of an unsuccessful organisation and reassembly of both materials. As previously discussed above the reasoning for the unsuccessful formation of the fully reconnected materials suggests that the problems with the organisation and reassembly are present in both cases and not just because of the different conditions used.

The first suggestion would therefore be the instability of ITQ-38P to the relatively harsh conditions used in the ADOR process. It was already noted from the attempts to organise ITQ-38P with acid that the structures, while easily disassembled, were also weak to the conditions used and seemed particularly prone to breakdown. The apparent lack of crystallinity of the material after treatment with DEDMS and acid, compared to treatment

with octylamine, seemed to support this. This is most likely as a result of the cleavage of Si-O-Si bonds in the presence of water, which is accelerated by the presence of Si-O-Si-OH, Ge and B in the layers and these layers being penetrated with pores.[15–18]

The second suggestion is that ITQ-38 has an issue during the organisation and reassembly steps due to the framework properties of the parent zeolite that are then transferred to the layered ITQ-38P structure. One factor that plays an important role in the organisation of the layer is the orientation of the interlayer silanols. The advantage of the ADOR process is that the disassembly of the *d4r* units is supposed to produce well defined quadruplets of silanols that provide the ability to direct the formation of silica columns that condense together to form *s4r*. when looking at the structure of ITQ-38P and comparing it to IPC-1P (derived from **UTL**) there are some major differences that may explain the different behaviours of the two materials during organisation and reassembly (Figure 5.32).

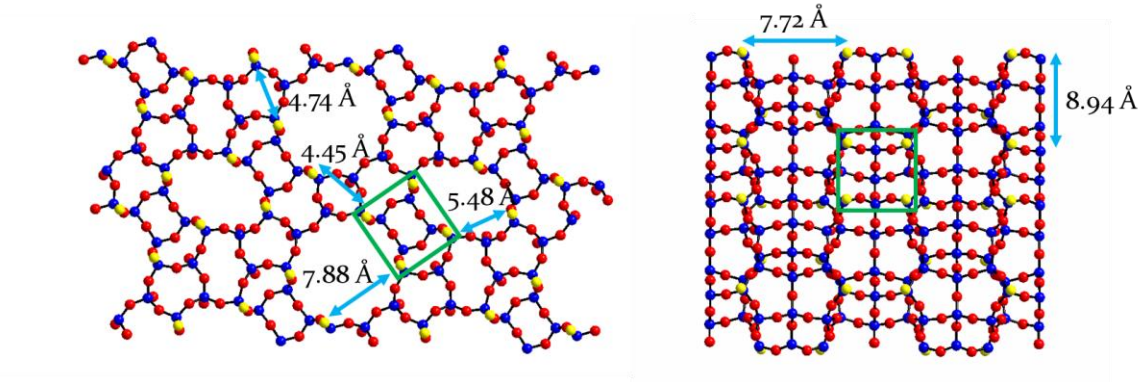

Figure 5.32 Shows the structures of ITQ-38P (left) and IPC-1P (right) when viewing above the interlayer silanol groups. An example of a silanol quadruplet is highlighted (green) and the distances between silanol quadruplets marked (blue arrows). T-atoms are blue, oxygens red and silanol oxygens yellow.

The most notable difference between ITQ-38P and IPC-1P is the orientation of the resultant silanols from the disassembly of the *d4r*. In the case of **UTL** the silanol quadruplets are easy to spot, even without highlighting, as they form clearly defined squares of 4.75 Å x 5.05 Å, representing a close distance between silanols in the same quadruplet. These quadruplets are well spaced as the distance between nearest neighbour silanol quadruplets is either 7.72 Å or 8.94 Å. These two characteristics, a small distance between silanols within the quadruplets and a larger distance between silanols of different quadruplets, helps make **UTL** such a successful ADORable zeolite. This shows that, after disassembly, **UTL** leaves a layered material with clearly orientated and defined silanol groups that are spaced out enough to allow for easy ordering of the layers. ITQ-38P on the other hand pales in comparison to this ideal candidate. The silanol quadruplets (highlighted in green) are hard to distinguish due to the greater distance between silanols

within the quadruplet (6.43 Å and 5.31 Å). This larger distance would not be an issue however were it not for the distances seen between silanol quadruplets. Some of the distances between silanols from different quadruplets are less than 5 Å. This means that the nearest neighbour to an individual silanol is more than likely to be a member of a different silanol quadruplet rather than other members of its own quadruplet. This key difference, the larger distance between silanols in the same quadruplet and the smaller distance between silanol quadruplets, results in an inability to properly organise the layers and repeat the success seen with IPC-1P.[2,19] The organisation step relies heavily on the distribution and orientation of these silanol quadruplets. If these quadruplets are clearly defined, then it provides an energetically favourable orientation of the layers to provide the best interlayer bonding interactions. This allows for ordering of the layers and promotes the formation of daughter zeolites with well-ordered layers.

The ability to still form a material related to ITQ-38-octylamine indicates that the impact of the silanol distribution is less of an issue when organizing the layers with octylamine. Firstly, the reaction conditions are less harsh; slowing down the rate of Si-O-Si cleavage, helping to keep the ITQ-38P layers relatively intact. Secondly the behaviour of the PXRD after organisation of the layers with octylamine showed that the layers could be manipulated. The formation of ITQ38-octylamine with octylamine is less demanding of the orientation of the silanols as it is a non-covalent bonding agent and does not need to have specific ordering of the silanols to successfully organise and reassemble the layers to form a fully connected zeolite. In contrast, the incorporation of DEDMS (a covalent bonding agent), to form *s4r* linkages, is more particular and requires the silanol quadruplets to be well defined and distinguishable from each other. This is so that the DEDMS pillars are in clearly defined quadruplets that will then preferential condense together to form *s4r* linkages between the layers after calcination.

5.5.4 Summary of Results

The results clearly showed the potential of ITQ-38 as a candidate for the ADOR process. The original and hazardous synthesis used by Moliner *et al* was shown to be easily avoidable.[10] The use of STAB to synthesis the intermediate MPP structure resulted in the successful formation of the desired SDA with no impact on the yield and purity while avoiding the dangerous formation of HCN. Using this SDA, investigations into varying the Si/Ge ratio of the initial gel did not result in a significant change in the PXRD pattern or in the Si/Ge ratio observed for the resultant crystals. The crystals formed during syntheses with a higher Ge content seemed more well-defined but also resulted in the formation of

a GeO_2 impurity; another indication that the incorporation of Ge could not be improved further. Application of the disassembly process resulted in a rapid and significant change in the material. The PXRD pattern showed that ITQ-38 showed some of characteristics traditionally associated with the disassembly of a germanosilicate into a layered structure.[19] The pattern was dominated by fewer peaks and the peak associated with the interlayer spacing (010) gained prominence and was seen to have moved to a lower 2θ angle; those peaks associated with reflections with a *k* value greater than 0 were lost, while those that had a *k* value of 0 were preserved. It was noted that the (101) reflection was lost despite this assertion, however this was due to the electron density in the reflection primarily originating from the *d4r*. This meant that the 101 peak was lost with disassembly of the germanosilicate and the loss of the *d4r*. The ($\bar{1}$01) reflection gained far more prominence compared to the original PXRD pattern, because, unlike the (101) reflection, its electron density originates from within these layers. SEM/EDX analysis of the material confirmed a severe reduction in the Ge content of the zeolite and the preservation of the crystal morphology associated with the original **ITG** crystals. The presence of the silanols, due to the removal of the *d4r*, was confirmed by ^{29}Si NMR. The presence of many Q^3 sites because of the formation of Si-OH groups was noted. The spectrum also hinted at the presence of some Q^2 sites, most likely as a result of the removal of Ge that was originally incorporated in the layers creating $Si(OH)_2$ groups in the material. Organisation of the layers was attempted with acid and showed some limitations. The use of concentrated acid and dilute acid resulted in an increasingly loss of crystallinity in the material; this did occur in a much quicker manner in 12 M HCl compared to 0.1 M HCl and was most likely as a result of the layers being particularly weak due to their lower density and being permeated with pores. This resulted in a faster degradation of the structure through the cleavage of Si-O-Si bonds. The use of intercalating agents on the other hand seemed to result in a minor change in peak positions, with treatment with octylamine not increasing the loss of crystallinity in the product as much as seen under acidic conditions. Both the covalent and non-covalent bonding agents resulted in a slight shifting of the (010) reflection with octylamine showing the greatest impact. This indicated that the layers could be manipulated by such methods. The material organised with DEDMS showed a decrease of crystallinity due to the use of nitric acid, traditionally required for the formation of interlayer silicate columns. Reorganisation of these two materials did not result in the two expected daughter zeolites. It seemed that both materials formed materials whose PXRD patterns were closely associated with the expected PXRD pattern

for ITQ-38-octylamine. BET and MAS NMR analysis of the materials also indicated the non-ideal behaviour of the ITQ-38P layers. The BET surface area for both materials was extremely low and the MAS NMR indicated the presence of many Q^3 and Q^2 sites. All these results indicate that the organisation of the ITQ-38P material has a non-ideal behaviour. These results could be due to the increased presence of an impurity, due to breakdown of the layers as well as the inherently bad crystallinity of products of the ADOR process. It is believed that one important factor is the distribution and orientation of the interlayer silanols. Compared to ideal ADOR candidates like **UTL** the silanol quadruplets in ITQ-38P, originating from the dissolution of the Ge-dominated *d4r* in ITQ-38, are too close together. This results in a less clear energetically favourable orientation of the layers, making it more difficult to organise the layers effectively. This is further complicated as the silanols within a quadruplet are further away from each other than they are from the next silanol quadruplet. It is believed that this severely hampered the organisation of the layers particularly for the formation of ITQ-38-DEDMS, as it requires the correct orientation of these silanols to allow for the correct condensation of the layers and the formation of *s4r* linkages between the layers. The formation of an ITQ-38-octylamine-like structure is most likely because of a collapsing of the layers. The organisation of the layers with octylamine is less fastidious and so should be easier to form. However, while the PXRD results were promising, there were still some issues fully confirming the successful formation of ITQ-38-octylamine based on the BET and MAS NMR data of the sample.

ITQ-38 is still a potential candidate for the ADOR process. The zeolite could undergo all the steps necessary to form a new product akin to ITQ-38-octylamine, although it was unable to form the ITQ-38-DEDMS structure. Both structures indicated that the organisation and reassembly steps for ITQ-38 were more difficult compared to ideal frameworks like **UTL**. This does not mean that ITQ-38 should be dismissed as an ADORable candidate. Such behaviour was previously noted in the formation of IPC-12 from **UOV**,[4] indicating that there is still an incomplete understanding of all the factors that can affect each of these steps of the ADOR process.

5.6 Application of the ADOR Process on IM-20 (UWY)

5.6.1 Introduction

The synthesis of IM-20 was first published in 2010 by Dodin *et al*.[9] and was assigned the official three-letter code **UWY** in 2011.[5] The germanosilicate is characterised as containing a 3-dimenional channel system, consisting of straight 12- and 10-rings running in the [001]

direction, these channels are intersected by a single 10 ring channel in the [100] direction and by two separate 10 ring channels running in the [010] direction. The structure contains layers constructed of *stf,* and *lau* CBUs and these layers are then connected by *d4r* running in the [010] direction (Figure 5.33).

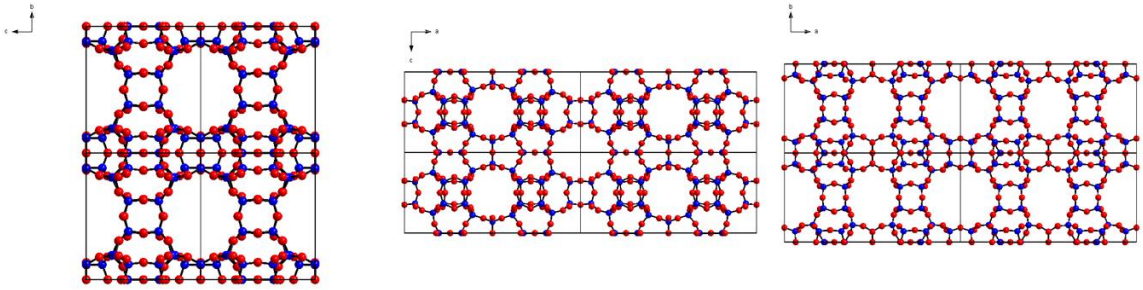

Figure 5.33 Shows the framework structure of UWY when viewed in the *a*, *b*, and *c* direction (left to right). Blue atoms represent T-atoms, red represent oxygen atoms.

Initial analysis seemed to suggest that IM-20 was a potential candidate for the ADOR process and the ^{19}F NMR analysis from the original paper suggested that the germanium dominated *d4r* running in the [010] direction should separate cleanly as the Si present in the *d4r* were separated, preventing preservation of silicate linkages between the layers after hydrolysis.[9]

However, the IM-20 (**UWY**) framework has several issues that would make it a less than ideal candidate for the ADOR process. Firstly IM-20 has a 3D channel system and two separate 10-ring channels penetrate these layers, making these layers more unstable compared to the denser layers originating from other ADORable zeolites like **UTL**. The IM-20 structure contains *d4r* within the layers, which run in the [100] direction. However, these *d4r* should be relatively stable under hydrolysis conditions as they are preferentially occupied by Si (with an occupancy of 0.89). However, the presence of Ge in these positions of the framework could increase the instability of the layers. This is further compounded as the location of Ge in the layers is not limited to these positions. The distribution of Ge in IM-20 seems to show a more dispersed pattern, rather than being solely present in the Ge-dominated *d4r* with some of these sites showing a maximum Ge-occupancy of 0.36 (Figure 5.34).

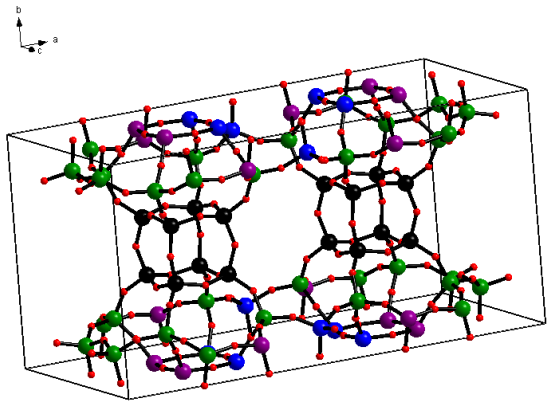

Figure 5.34 Shows the IM-20 unit cell with the T-atoms highlighted based on their Ge occupancy: less than 0.1 (blue), 0.11-0.19 (green), 0.19 - 0.36 (purple) and greater than 0.5 (black). Oxygen atoms are red and reduced in size for clarity.

The best behaved ADORable zeolites (like **UTL**) are typified by dense layers, without penetrating channel systems, that contain wholly silicon. The presence of a 3D channel system, with two channel systems penetrating the layers, and the presence of Ge throughout the layers may add complications to the manipulation of the layers and the stability of the layered material later during the ADOR process.

5.6.2 Experimental Procedures

5.6.2.1 Synthesis of SDA (3-butyl-1-methyl-3H-imidazol-1-ium hydroxide)

1-Methylimidazole (30 mL, 376 mmol) and 1-bromobutane (40 mL, 372 mmol) were combined and heated at 70 °C for 36 hours with constant stirring. The product was then dried under high vacuum to yield the final product BMI bromide (70.02 g, 92 %), that was determined pure by ^{1}H NMR. The bromide salt was then converted to its hydroxide form with the use of ion-exchange resin.

5.6.2.2 Synthesis of Zeolite UWY

The synthesis of **UWY** was attempted using the same synthesis procedure as that reported by Dodin *et al*. for IM-20.[9] Germanium dioxide (1.0461g, 10 mmol) was added to a stirring solution of BMI hydroxide (13.44 mL, 12.5 mmol). After homogenisation fumed silica (0.901 g, 15 mmol) was added and the solution stirred until the correct water ratio had been reached. Once complete hydrofluoric acid (0.45 mL, 12.5 mmol) was added and the gel left to homogenise for 30 minutes. Once complete additional water was added to ensure a gel molar composition of 0.6 SiO_2 : 0.4 GeO_2 : 0.5 BMI(OH) : 0.5 HF : 10 H_2O. The gel was then placed in a Teflon lined autoclave and heated at 175 °C for 14 days. The SDA containing zeolite was then calcined at 575 °C for 7 hours.

Investigations were also conducted into varying the Si/Ge content of the gel without varying the other components of the gel.

5.6.2.3 Formation of UWY-P

The hydrolysis of **UWY** was investigated under various conditions and with varying molarities of acid. The Solid was placed in a stirring solution with a solid to solvent ratio of 0.1g/100ml ratio. Hydrolysis solvents included water, ethanol and HCl of various concentrations. These were then heated or left stirring at room temperature for a defined time of between 1 and 48 hrs. The resultant solid was then filtered and washed with additional water.

5.6.2.4 Intercalation of UWY-P

5.6.2.4.1 Octylamine

UWY-P (0.150 g) was placed in octylamine (15 mL), stirred at 70 °C for 3 hours and then continued stirring for another 16 hours at room temperature. The resultant solid was then filtered and dried to give the intercalated product (yield = 0.145 g).

5.6.2.4.2 DEDMS

UWY-P (0.150 g) was placed in a Teflon liner containing nitric acid (1 M, 15 mL) and DEDMS (68.9 μL,). After 10 minutes of stirring the liner was placed in a steel autoclave and heated at 175 °C for 16 hours. The solid was the isolated by filtration and dried in air to give the intercalated product (yield = 0.108 g).

5.6.3 Results and Discussion

5.6.3.1 Varying the Si/Ge Ratio of UWY

As discussed previously the presence of Ge throughout the IM-20 structure is not ideal for the ADOR process, as this adds instability to the layered material. The original IM-20 synthesis involves an initial Si/Ge ratio of 1.5 in the synthesis gel. It was therefore hoped that by decreasing the Ge content of the initial gel this would lead to a decrease in the amount of Ge in the layers without impacting on the dominance of Ge in the *d4r*, as Ge should still preferentially locate in the *d4r*. As discussed previously the effect of batch composition can have serious implications on the crystallised product. Therefore, the first step was to try and gradually increase the Si/Ge ratio of the initial gel, while observing the impact on the quality of the final product.

The original IM-20 initial Si/Ge gel ratio was synthesised (Si/Ge = 1.5) and the procedure was adjusted to gradually increase the Si/Ge ratio (Table 5.3), while maintaining the ratio of the other reactants in the gel.

Table 5.3 Shows the Si/Ge Ratios investigated and their corresponding identifiers.

Name	Si/Ge Ratio
UWY-1.5	1.5
UWY-2.33	2.33
UWY-3	3
UWY-4	4
UWY-5	5

Initial PXRD analysis showed that the original **UWY**-1.5 had indeed been successfully synthesised and compared favourably with the generated PXRD pattern of **UWY**. The decrease in Ge content of the initial gel seemed to have a minor impact on the PXRD patterns obtained for the crystalline product up to a point (Figure 5.35).

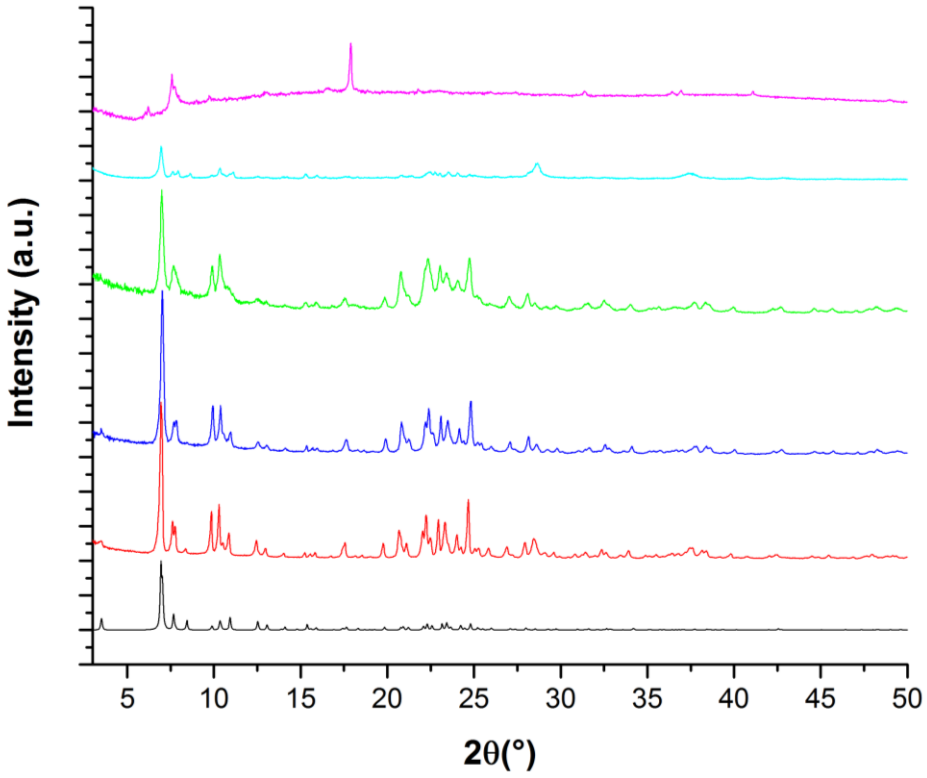

Figure 5.35 Shows the expected PXRD pattern for IM-20 (UWY) and the experimental PXRD patterns for UWY-1.5 (red), UWY-2.33 (blue), UWY-3 (green), UWY-4 (cyan) and UWY-5 (magenta). Clearly showing the increased lack of crystallinity in the material as the Si/Ge ratio was increased.

It seemed that the decrease in the Ge content of the initial gel still resulted in the successful formation of **UWY**. Even at **UWY**-4 a hint of **UWY** material could be observed, although this material was largely lacking crystallinity. Finally, at UWY-5 the resultant material was clearly not **UWY** and was predominantly non-crystalline. This suggests that

the decrease in Ge content could be experimentally done until an impasse was reached at a Si/Ge ratio of 4.

Once it was ascertained that **UWY** could be obtained with a lower Ge content initial gel it was important to ascertain if the decreased Ge content of the initial gel was transposed onto the final crystalline product, and if the morphology of the sample had changed because of the altered syntheses.

SEM analysis showed promise for this concept, unlike the results obtained for ITQ-38. The SEM images of the **UWY**-2.33 and **UWY**-3 showed the characteristic needle-like crystals (Figure 5.36), that were obtained in the original **UWY**-1.5 synthesis. The crystal size averaged between 10-20 μm and showed that the obtained materials were monophasic.

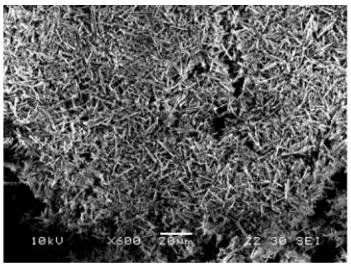

Elemental Analysis (Atomic Percent)				
Spectrum	O	Si	Ge	Total
1	65.18	23.97	10.85	100
2	66.29	23.17	10.54	100
3	67.48	22.71	9.81	100
4	64.18	24.87	10.95	100
5	66.58	23.41	10.01	100
Average	65.94	23.63	10.43	

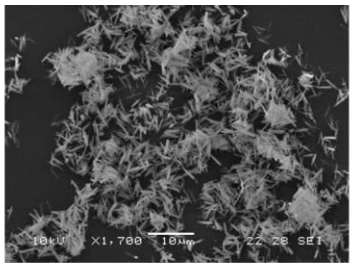

Elemental Analysis (Atomic Percent)				
Spectrum	O	Si	Ge	Total
1	69.78	22.95	7.27	100
2	69.94	22.72	7.34	100
3	70.57	22.34	7.09	100
4	71.56	21.77	6.67	100
5	70.46	22.51	7.03	100
Average	70.46	22.46	7.08	

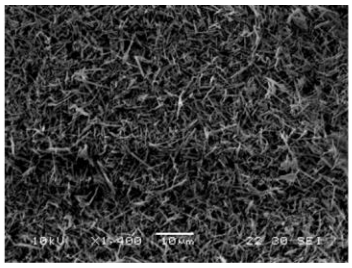

Elemental Analysis (Atomic Percent)				
Spectrum	O	Si	Ge	Total
1	71.45	22.04	6.51	100
2	67.59	24.45	7.96	100
3	68.25	24.36	7.39	100
4	71.23	21.97	6.80	100
5	68.64	23.58	7.78	100
Average	69.43	23.28	7.29	

Figure 5.36 Shows the SEM images obtained for UWY-1.5, UWY-2.33 and UWY-3 with their corresponding EDX elemental analysis (left to right). This confirmed that increasing the Si/Ge ratio of the initial gel did lead to an increase in the Si/Ge ratio of the final crystalline product, without leading to a degradation in crystal morphology or compromising the monophasic behaviour of the material.

EDX analysis of the materials did show an increase in the Si/Ge ratio of the materials (from 2.26 to 3.17 and 3.19), which was consistently higher than the increasing Si/Ge ratio of the initial gels (1.5 to 2.33 to 3 respectively). However, the similarity of the Si/Ge ratios for **UWY**-2.33 and **UWY**-3, despite different initial gel compositions, indicates that increasing the Si/Ge ratio of the initial gel had limitations. Although both samples showed PXRD patterns and SEM images comparable to pure phase **UWY**-1.5, **UWY**-3 did not show any further increase in its Si/Ge ratio compared to **UWY**-2.33. This in conjunction with the results from samples **UWY**-4 and **UWY**-5 seemed to indicate that the Si/Ge ratio had an impact on the formation of the product. It seems that between **UWY-2.33** and **UWY-3** the synthesis was still able to produce the crystalline product, but the Si/Ge ratio of the

product formed had reached its maximum. When the Si/Ge ratio of the gel was increased further then the synthesis was unable to cope leading to the formation of primarily non-crystalline material.

These initial results showed there was a limit to decreasing the Ge content of the **UWY** framework by increasing the initial gel Si/Ge ratio. However, the increase of the Si/Ge ratio from 2 to 3 was enough to warrant investigating the materials to ascertain their potential for the ADOR process. It is hoped that the preferential location of Ge into the *d4r* would mean that the decrease in Ge content of IM-20 would lead to a targeted reduction of the Ge within the layers, without decreasing the Ge content of the *d4r*.

5.6.3.1.1 Calcination of **UWY** Samples

Calcination of the **UWY** samples seemed to also confirm the different behaviours of the frameworks based on their Si/Ge ratio seen in the EDX analyses (Figure 5.37).

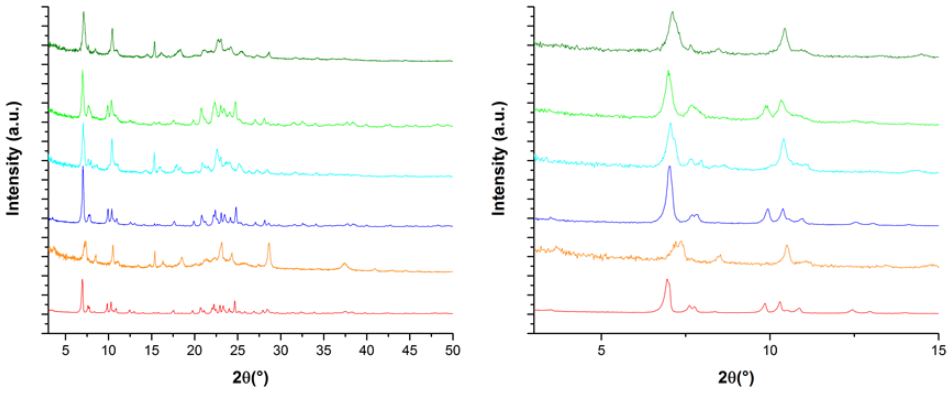

Figure 5.37 Shows the PXRD patterns of IWY-1.5 (red) IWY-1.5 calcined (orange), IWY-2.33 (blue), IWY-2.33 calcined (cyan), IWY-3 (green) and IWY-3 calcined (dark green). After calcination, the sample IWY-1.5 PXRD pattern deteriorates and the predominant peak at 6.96 ° 2θ moves to a higher 2θ angle. This is most likely as a result of the instability of the material due to the higher germanium content. In comparison, the IWY-2.33 and IWY-3 seem less affected by the calcination indicating that both materials have a better stability due to the higher Si/Ge ratio of the materials.

The standard **UWY**-1.5 showed an immediate change after calcination. The well-defined PXRD pattern had deteriorated with the major peak at 6.96° 2θ decreasing in intensity and moving to 7.28 ° 2θ angle. The peak at 6.96° in the original material is associated with the (010) and the (200) reflections; the movement of this peak position is therefore indicative of the degradation of the sample due to the frameworks hydrolytic instability. If the disassembly process was taking place, then the 200 peak would be preserved as it does not run in the same direction as the stacking of the layers. Such a result would be typically associated with the large amount of germanium throughout the structure and not just in the *d4r*. this behaviour suggests that **UWY**-1.5 is unsuited for the ADOR

process. In comparison samples **UWY**-2.33 and **UWY**-3 did not show much change after calcination, indicating that both samples showed a much greater stability compared with **UWY**-1.5. The PXRD patterns of both calcined materials retained the key peak positions associated with the **UWY** framework. This provided further confirmation that increasing the Si/Ge ratio of the synthesis had led to a more siliceous product with greater stability than the original IM-20 material.

5.6.3.2 The Disassembly of UWY

Treatment of the three **UWY** samples with 0.1 M HCl (Section 5.6.2.3) resulted in some dramatic changes to the PXRD patterns. After 1 hour at 95 °C the samples all showed a dramatic decrease in intensity of the powder patterns (Figure 5.38).

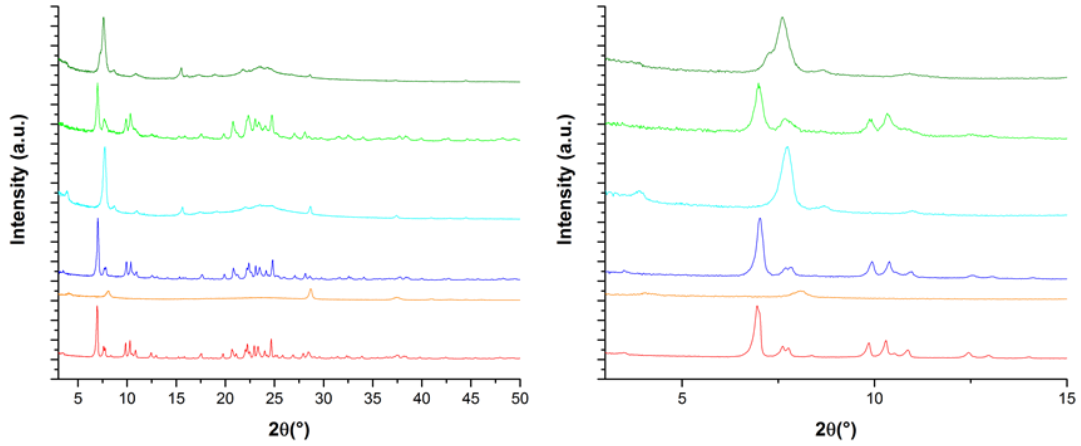

Figure 5.38 Shows the PXRD patterns of IWY-1.5 (red) IWY-1.5 hydrolysed (orange), IWY-2.33 (blue), IWY-2.33 hydrolysed (cyan), IWY-3 (green) and IWY-3 hydrolysed (dark green). After hydrolysis, the sample IWY-1.5 PXRD pattern has deteriorated dramatically, because of its high germanium content, showing one major broad peak at 7.96 ° (an additional peak is seen at 28.7 ° 2θ corresponding to GeO_2). The samples IWY-2.33 and IWY-3 show the same characteristic major peak as IWY-1.5 but are far less deteriorated. This is indicative of the formation of a layered material.

The PXRD pattern of **UWY**-1.5 showed the most dramatic change in the PXRD pattern. The quality of the pattern was the worst of the three materials showing one very broad peak of low intensity at 7.96 ° 2θ (an additional peak at 28.7° 2θ corresponded to GeO_2). This result confirmed the original suspicion, that the Si/Ge ratio was too low in original IM-20 (**UWY**-1.5). This makes the layers too weak to hydrolysis because of their high Ge content. The movement of the peak and the loss of crystallinity shows the inability to retain the structure after removal of the germanium.

In comparison to **UWY**-1.5, the samples **UWY**-2.33 and **UWY**-3 showed very different PXRD patterns, more in keeping with those typically seen for a successful disassembly process. Both PXRD patterns of the hydrolysed materials exhibited loss of a large number of peaks and are dominated by a small number of peaks. The dominant peak of the

patterns was about 7.75 ° 2θ corresponding not only to the interlayer reflection (010) but also the unmoved 001 peak. Other peaks in the PXRD pattern of note were at 3.93 ° (in **UWY**-2.33), 7.28 ° (in **UWY**-3), 8.72 ° 11.04 ° and 15.66 ° 2θ. These five peaks correspond to the retained (100), (200), (101), (201) and (002) reflections, as these reflections are unaffected by the disorder of the stacking of the layers in the [010] direction as their *k* values are 0. The location of the (010) interlayer reflection around 7.75 ° 2θ seems to be a less than ideal shift from 6.94 ° to 7.75 ° 2 θ as this corresponds to a movement of 1.62 Å, which is smaller than seen for the disassembly other zeolites.[2] The presence of the (100) reflection in **UWY**-2.33 and (200) reflection in **UWY**-3 is perhaps an indication of the different behaviour of the layers. Both materials also showed a loss of additional peaks originally at 9.94 ° and 10.38 ° 2θ after hydrolysis of the samples. This is due to the reliance of these peaks on ordering in the [010] direction as they correspond to reflections with a *k* value greater than 0 ((210) and (011) reflections respectively). After hydrolysis, the ordering of the layers in the [010] direction is lost and so this loss of order results in the limited number of peaks being observed in the PXRD pattern.

SEM and EDX analysis of the samples showed similar results seen for other disassembled materials (Figure 5.39).

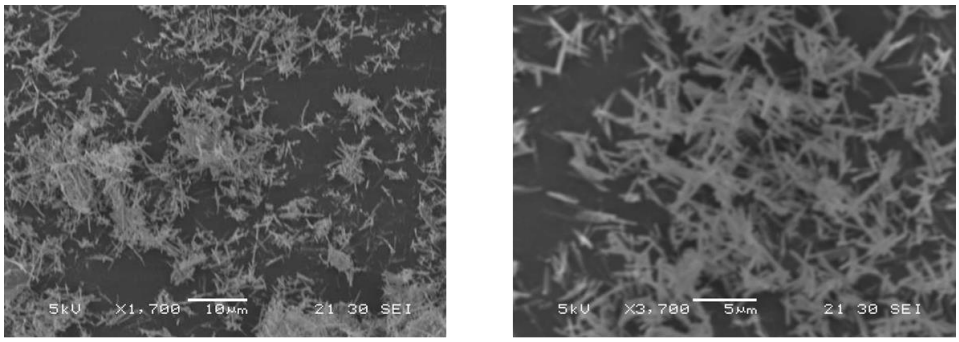

Elemental Analysis (Atomic Percent)

Spectrum	O	Si	Ge	Total
1	76.81	22.71	0.48	100
2	80.61	18.74	0.65	100
3	81.50	17.58	0.92	100
4	76.52	23.02	0.46	100
5	76.78	22.54	0.68	100
Average	78.44	20.92	0.64	

Elemental Analysis (Atomic Percent)

Spectrum	O	Si	Ge	Total
1	86.18	13.59	0.23	100
2	88.14	11.47	0.39	100
3	86.38	13.08	0.54	100
4	87.42	12.54	0.04	100
5	84.25	15.22	0.53	100
Average	86.47	13.18	0.35	

Figure 5.39 Shows the SEM images and EDX analysis obtained for UWY-2.33 (left) and UWY-3 (right).

Both showed a preservation of the needle-like crystal morphology, but with a dramatically increased Si/Ge ratio (32.69 and 37.66). This confirmed the successful removal of the germanium from the structure without complete dissolution of the structure.

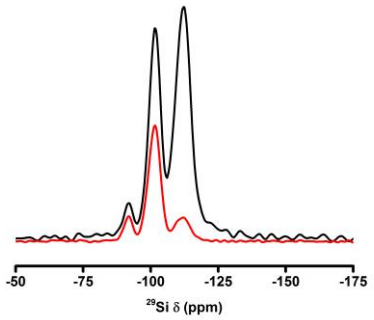

Figure 5.40 Shows the ^{29}Si MAS NMR spectra (black) and {^{1}H} ^{29}Si cross-polarisation MAS NMR (red) of hydrolysed UWY-3P clearly showing the presence of Q^3 sites as a result of the formation of silanols. Also, the presence of some Q^2 sites indicates may indicate the deterioration of some of the layers as well.

The removal of germanium from the **UWY**-3 structure led to the formation of a material that did not consist of just silicon connected to 4 other T-atoms by bridging oxygens; the ^{29}Si MAS NMR (Figure 5.40) showed the presence Q^3 sites (~ -100 ppm); associated with the formation of silanols in the interlayer region caused by the removal of the Ge-atoms. CP analysis of this confirmed that these Q^3 corresponded to the formation of a layered material with the presence of Si-OH groups most likely present in between the layers due to the removal of the Ge-dominated *d4r*. However, the ^{29}Si MAS NMR and CP experiments showed the presence of some Q^2 sites in the **UWY**-3P material. This was most likely due to presence of some Ge in the layers of **UWY**-3 that was subsequently removed during the hydrolysis; if the layers had been wholly Si then there should be just Q^3 sites formed. This suggests that attempts to increase the Si/Ge ratio were not enough to totally remove the presence of Ge in the layers.

Analysis of the materials under disassembly conditions showed that by decreasing the Ge content of the **UWY** framework it was possible to increase the stability of the framework under hydrolysis conditions. **UWY**-1.5 completely collapsed, although a single broad peak dominated the PXRD pattern most likely corresponding to the interlayer reflection. Both **UWY**-2.33 and **UWY**-3 showed this reflection, while also retaining some form of stability of the layers to produce a more detailed PXRD pattern. These PXRD patterns showed that the **UWY**-2.33P and **UWY**-3P followed a similar pattern observed for other ADORable zeolite during disassembly. The PXRD patterns were dominated by the (010) reflection, corresponding to the interlayer reflection; other peaks that were unaffected by the disorder introduced in the [010] direction were preserved. However, peaks that previously dominated the materials like the (210) and (011) reflections were lost due to loss of order in the stacking of the layers in the [010] direction after hydrolysis. The SEM and EDX

analysis of both **UWY**-2.33P and **UWY**-3P showed a preservation of the crystal morphology and the severe reduction in Ge content of the crystals. The ^{29}Si MAS NMR of **UWY**-3 also indicated the presence of silanol groups in the new materials. All indicating that **UWY** was a promising candidate for the ADOR process.

5.6.3.3 Organisation of UWY

Due to the weakness of **UWY**-1.5 and the relatively similar behaviour of **UWY**-2.33 and **UWY**-3 to the disassembly process, the organisation and reassembly steps were attempted on the sample **UWY**-3.

5.6.3.3.1 Organisation with 12 M HCl

The treatment of both samples with 12M HCl had a similar impact on the material as previously seen for **ITG** and produced a similar trend in the PXRD patterns (Figure 5.41).

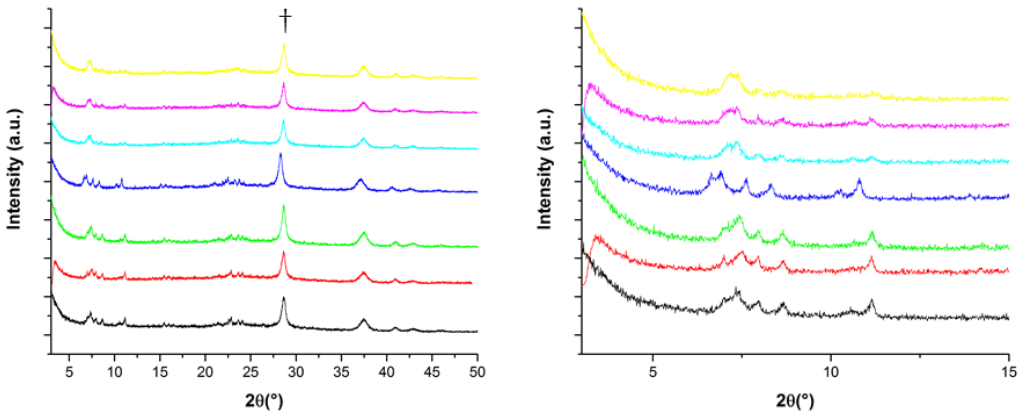

Figure 5.41 Shows the impact of 12M HCl on UWY-3 over time: 1 hr (black), 2 hr (red), 6 hr (green), 12 hr (blue), 24 hr (cyan), 48 hr (pink) and 72 hr (yellow).The PXRD patterns between 3-15 ° 2θ is highlighted on the right. The peak corresponding to GeO_2 is shown (†).

The material showed far greater loss of crystallinity under the 12M HCl conditions than seen when the material was just disassembled with 0.1M HCl. This may be a result of the harsher acid strength, which is used as it is strong enough to allow for a rearrangement process through the formation of new Si-O-Si bonds.[19,22] The formation of a large amount of GeO_2 (†) very soon after contact with the acid is indicative of the removal of Ge from the framework, so indicates that the material has been disassembled with the acid. The strong acid should promote the formation of Si-O-Si bonds, which is perhaps indicated by the movement seen in some of the peaks at about 7.5 ° 2θ. However, the increasingly loss of crystallinity of the material, prevented any conclusive evidence that the rearrangement was occurring. The loss of crystallinity indicates that the strength of the acid is perhaps too much for the **UWY** layers. This confirms initial suspicions that the **UWY** layers would

be weaker due to their lower density compared to ideal ADORable zeolites like **UTL**.[2,9] Previous observations suggested that depending on the treatment conditions the Si–O–Si groups may be broken leading to collapse of the framework. Water often induces this change by the hydrolysis of terminal Si–O–Si–OH groups. This creates a defect, which then propagates inward throughout the zeolite structure. Such a process would also be accelerated by the presence of Ge in layers, that would be removed selectivity, providing additional defects for this process to propagate (perhaps indicated by the Q^2 sites in the ^{29}Si MAS NMR).[15–18] The presence of multiple channels penetrating the layers would also accelerate this process as the surface area of the layers is increased, making them far more unstable under such harsh conditions. A combination of these factors would lead to the increasing loss of crystallinity in the material as the layers breakdown, preventing the successful implementation of the rearrangement process.

5.6.3.3.2 Organisation with 0.1 M HCl

The treatment of the **UWY**-3 with 0.1 M HCl also showed similar results to those obtained for 12 M HCl (Figure 5.42).

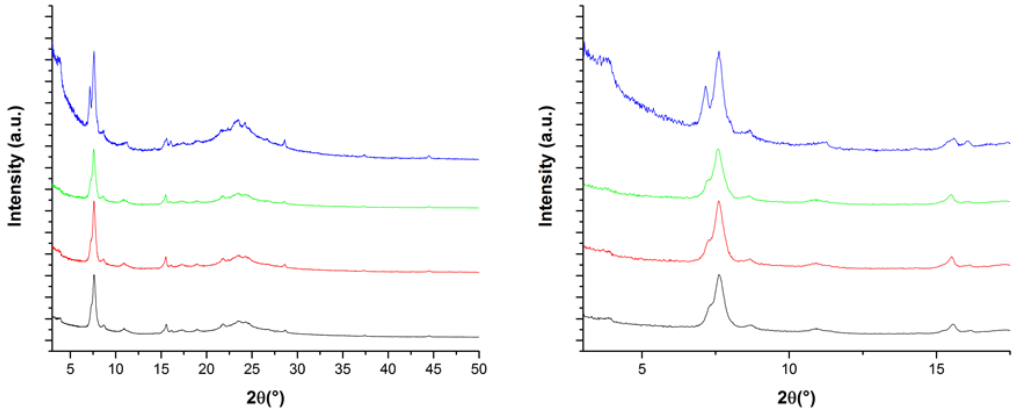

Figure 5.42 Shows the PXRD Patterns for UWY-3 over time: 1 hr (black), 6 hr (red), 12 hr (green) and 24 hr (blue). Unlike the 12M HCl the GeO_2 peak at ~27 ° 2θ is not observed, the PXRD is dominated by the two major peaks seen in the original disassembly, however as time increase the distinction between these two major peaks increases, suggestion some element of organisation as the layers become more ordered producing less broadness and overlap.

Treatment of **UWY**-3 with 0.1 M HCl showed a similar but slightly muted behaviour compared to treatment with 12 M HCl. The use of 0.1 M HCl preserved the two major peaks initially observed in the disassembled PXRD pattern at 7.30 and 7.96 ° 2θ. Contact with the weaker acid did not lead to as much of an loss of crystallinity compared to the stronger acidic conditions. This suggests that the layers were perhaps less vulnerable than initially expected and less vulnerable compared to **ITG**. There was little change in the two

major peaks except for them becoming more distinct from each other. This is because the weak acid is not strong enough to promote the rearrangement process and the formation of Si-O-Si bonds; only the deintercalation process is observed, where over time the species in between the layers are removed and the layers are allowed to self-order.[19] This increased prominence of the (100) reflection under these conditions also adds credence to the theory that the layers were able to self-organise under these conditions. The increased sharpness of the (100) reflection and separation of the 200 and the 010 peaks with increased exposure to the acid is clearly a reflection of the increased ordering of the layers with longer exposure to the acid treatment. However, the increased order was lost with calcination as the material showed a complete lack of crystallinity.

The organisation of the layered material **UWY**-P highlighted that **UWY** was a non-ideal candidate for the ADOR process. The weakness of the layers initially predicted was confirmed under strongly acidic conditions. The use of strong acid resulted in an increasing loss of crystallinity with increased contact time. This was most likely due to degradation of the inherently weak layers due to the accelerated cleavage of Si-O-Si bonds from the presence of Ge in the layers and channels penetrating these layers. Some evidence of rearrangement may have been seen but was mostly inconclusive. The use of weak acid did not result in complete destruction of the layers, suggesting that the Si-O-Si bond cleavage process was slower due to the less harsh conditions and that these layers had greater stability borne out of the increased Si/Ge ratio of the parent germanosilicate. The sharpening of some of the peaks also indicated that the deintercalation of the layers also allowed for some element of self-organisation to take place. However, the pattern still remained less crystalline than seen for other ADORable zeolites. This shows that the **UWY** layered material can undergo some form of organisation with acid, but to a lesser extent than other ADORable zeolites and only under weakly acidic conditions. This therefore means the acid can only be used for deintercalation and not as a means for inducing rearrangement.

5.6.3.3.3 Organisation Using Intercalating Agents

The use of intercalating agents was attempted to help accommodate the relative instability of the **UWY**-P layers and see if a greater degree of organisation could take place. This resulted in some minor changes in the PXRD patterns (Figure 5.43).

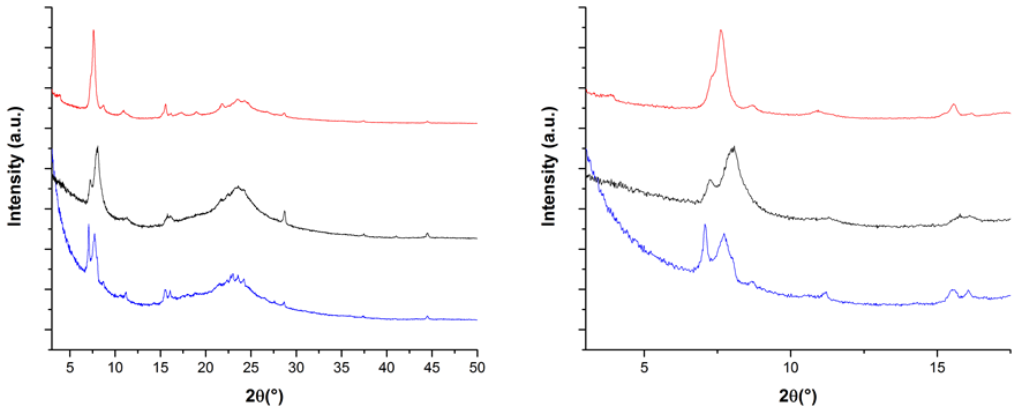

Figure 5.43 Shows the PXRD patterns for UWY-3P (red), UWY-3P treated with octylamine (black) and DEDMS (blue). The octylamine clearly shows a similar behaviour to that seen with 0.1 M HCl with a sharpening of the 200 and 010 peaks from the organisation of the layers (*). Treatment of the UWY-3P material with DEDMS resulted in a similar behaviour but with a much sharper increase in the loss in crystallinity.

Treatment of **UWY**-3P with octylamine showed a similar pattern to that treated with 0.1 M HCl. The first two peaks at 7.24 ° and 8.08° 2θ, corresponding to the (002) and (010)/(100) reflections that remained consistent with the original material. The two peaks showed greater separation than previously seen. However, the peak corresponding to the (010)/(100) reflection showed a certain amount of broadening perhaps indicating a decrease in the interlayer spacing but a less than ideal ordering of the layers.

The organisation step was then also attempted with DEDMS to attempt the formation of the *s4r* linkages between the layers as seen in the formation of IPC-2 from **UTL**. Another sample of **UWY**-3P was treated with DEDMS in 1M HNO_3 at elevated temperatures. Such a treatment seemed to result in a similar material as that seen for the treatment with octylamine. The sharpness of the 200 peak at 7.24 ° 2θ was increased compared with the original material suggesting some ordering had taken place. However, the second peak seemed to develop an even greater shoulder to the right than seen with octylamine perhaps as a result of some ordering not possible through the use of octylamine. The material did show a greater loss of crystallinity due to the harsher conditions used, most likely due to degradation of the structure through the accelerated Si-O-Si cleavage rate under these harsher conditions. Such results seem to suggest that the organisation of the layers using traditional methods was not ideal for **UWY**-P layers.

5.6.3.4 Reassembly of the Layers

Reorganisation of the layers was attempted on the samples intercalated with octylamine and DEDMS. Both samples, whether intercalated with octylamine or DEDMS seemed to produce similar patterns upon calcination (Figure 5.44).

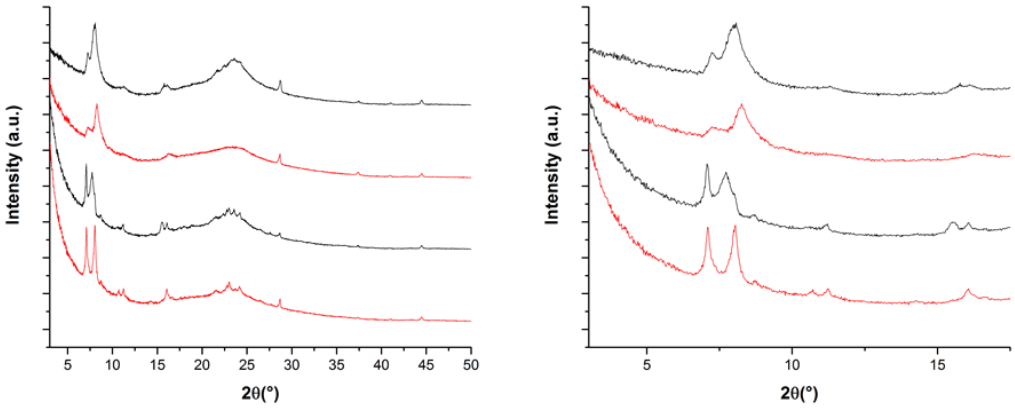

Figure 5.44 Shows the PXRD Patterns before (red) and after calcination (black) for UWY-3P intercalated with octylamine (top) and DEDMS (bottom), a close-up of the PXRD pattern between 3-17.5 ° 2θ (right).

However, it is possible to make some interesting conclusions based on these results. Firstly, the material treated with octylamine showed little difference between the PXRD patterns taken before and after calcination, this suggests that the ordering that had taken place after treatment with octylamine was preserved in the final reassembled material. The reassembly of the material with DEDMS seemed to result in a more dramatic change in the PXRD pattern. The material produced two sharper peaks after calcination at 7.11 ° and 8.05 ° 2θ. the first corresponds to the (200) reflection, but it is more difficult to ascertain which reflection the peak at 8.05 ° 2θ corresponds to, although it is most likely due to the (010) reflection.

The low quality of the PXRD pattern was perhaps indicative of a poorly defined reorganisation step. The lack of change in the sample intercalated with octylamine and the change seen in that treated with DEDMS seems to suggest that the production of the new daughter zeolites from the **UWY**-P layers may be somewhat limited. In addition, the SEM and EDX analysis seemed to suggest that the materials had remained relatively intact despite the different treatments and retained a high Si/Ge ratio (Figure 5.45).

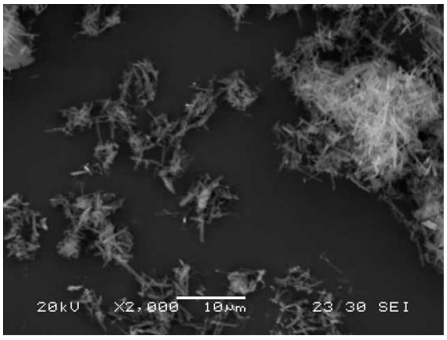

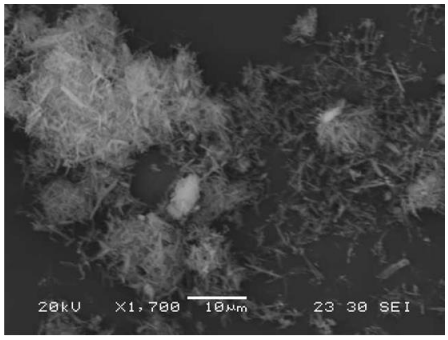

Elemental Analysis (Atomic Percent)				
Spectrum	O	Si	Ge	Total
1	77.94	21.6	0.46	100
2	80.08	19.55	0.37	100
3	77.52	22.05	0.43	100
4	81.52	18.21	0.27	100
5	81.85	17.63	0.52	100
Average	79.78	19.81	0.41	

Elemental Analysis (Atomic Percent)				
Spectrum	O	Si	Ge	Total
1	77.68	22.13	0.19	100
2	79.1	20.63	0.26	100
3	76.78	23.06	0.16	100
4	79.06	20.71	0.24	100
5	80.35	19.34	0.3	100
Average	78.59	21.17	0.23	

Figure 5.45 Shows the SEM and EDX analysis of the UWY layers after treatment with either octylamine (left) or DEDMS and acid (right) followed by calcination. Both showed a preservation of the crystal morphology and the higher Si/Ge ratios associated with the successfully reassembled material.

Further comparisons of the two materials were made using N_2 adsorption data (Figure 5.46).

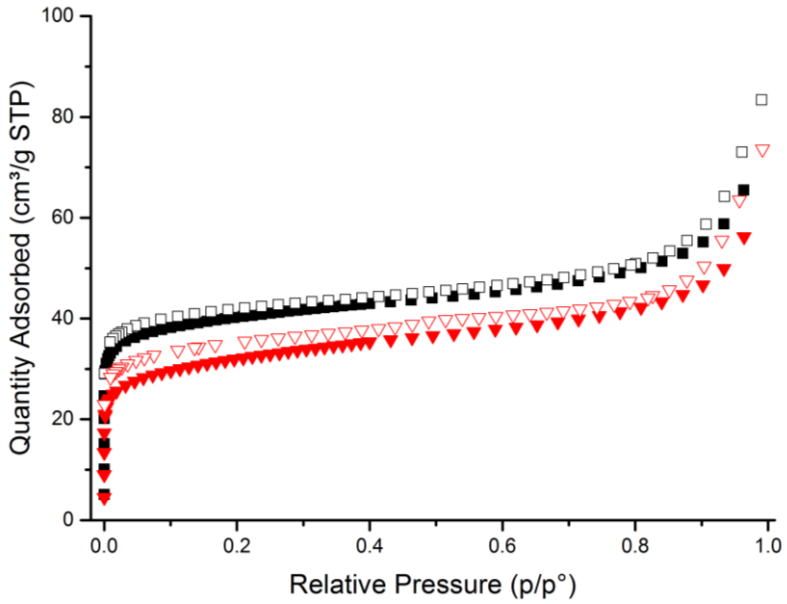

Figure 5.46 Shows the adsorption isotherms for the UWY layers treated with octylamine (black) or DEDMS and acid (red), with the adsorption represented by filled symbols and desorption by empty symbols.

The isotherm data revealed some interesting issues regarding the two products. Firstly, both materials showed a less ideal type I isotherm compared to original IM-20 material, perhaps indicative of the disordered nature of the rearranged materials. Secondly the BET surface area was severely reduced; treatment with octylamine resulted in a BET surface

area of 152 m^2/g and treatment with acid and DEDMS resulted in a BET surface area of 115 m^2/g. Compared to the BET surface area of the original IM-20 material of 401 m^2/g these values seem particularly low. In the case of **UWY**-octylamine such a reduced BET surface area is to be expected as all the channels in the *a* and *c* directions are reduced by the removal of the *d4r* and the formation of direct O-linkages between the layers. This would reduce all the 10-ring channels to 6-ring, which are essentially non-porous. However, it would therefore be expected that an increase in the interlayer linkages (from direct O-linkages to *s4r*) would result in an increase in the surface area. This is clearly not the case, the **UWY** layers treated with DEDMS and acid did not show a greater BET surface area than that for that those layers treated with octylamine. Such results lead further credence to theory that the **UWY** layers are not ideal for the ADOR process.

Further suspicions as to the degree of success of the organisation and reassembly steps on the **UWY** layers were raised in the analysis of the materials by solid-state ^{29}Si MAS NMR (Figure 5.47).

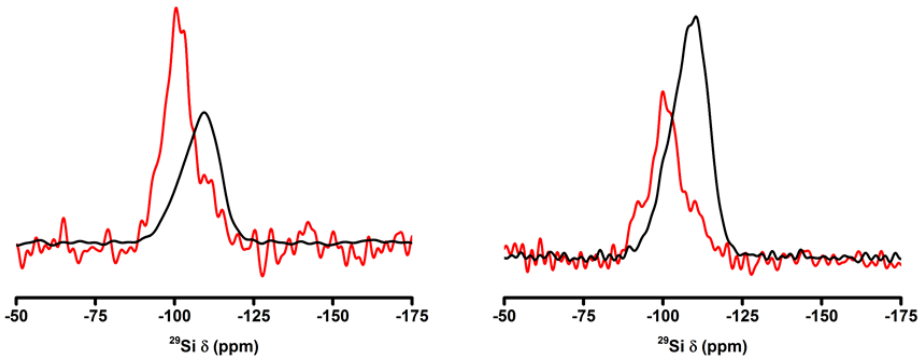

Figure 5.47 Shows the ^{29}Si MAS NMR spectra (black) and $\{^1H\}$ ^{29}Si cross-polarisation MAS NMR (red) for the UWY layers after treatment with octylamine (left) and with DEDMS and acid (right). Both clearly show the presence of non-Q^4 sites and underline that such materials have been unsuccessfully organised and reassembled.

The MAS ^{29}Si NMR spectra for both material showed that the organisation and reassembly steps had been unsuccessful in producing two new fully connected daughter zeolites. Both spectra initially showed the presence of Q^4 sites with large shoulders relating to the presence of Q^3 sites. Such results would therefore show the presence of many Si-OH groups in the calcined material, suggesting that in both cases the reassembly process had not resulted in fully connected layers. This would suggest that the orderly reassembly of the materials was somehow prevented. Also of interest would be the shape of the cross-polarisation experiments, hinting at the presence of additional Q^2 sites in the materials reorganised with the use of DEDMS and acid. This would perhaps hint at the formation of large numbers of Q^2 sites, that would be because of degradation of the structure by

further treatment with acid or due to the introduction of DEDMS and its subsequent inability to fully condense and form *s4r* resulting in the presence of $Si(OH)_2$ groups. It is most likely that a collection of factors are responsible for the unsuccessful reassembly of the product. Firstly, the instability of the layers under the treatment conditions could result in an increasing loss of crystallinity in the product, secondly these results are perhaps an indication that the **UWY** layers are particularly incapable of the organisation and reassembly steps, or these results could be partly due to the ADOR process itself as it is known to give poorly crystalline materials.

To fully reason such results, ascertaining the nature of the daughter zeolite that was present was therefore vital. One advantage of the ADOR process is the ability to predict the products from the ADOR process. The isoreticular relationship of the daughters to the parent germanosilicate makes it easier to predict the resultant product from the synthesis. Structures were generated for the two expected daughter zeolites, **UWY**-octylamine and **UWY**-DEDMS, using the same method that was used to generate the structures for ITQ-38-octylamine and ITQ-38-DEDMS. **UWY**-octylamine and **UWY**-DEDMS were therefore related to the parent germanosilicate **UWY** as they have the same layers but with direct O-linkages and *s4r*-linkages respectively instead of *d4r* linkages.

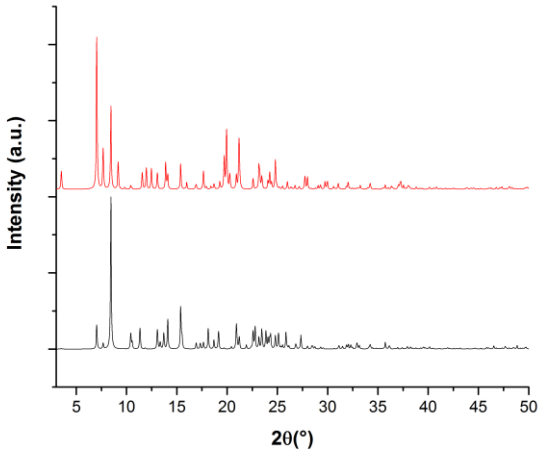

Figure 5.48 Shows the generated PXRD patterns for UWY-DEDMS (red) and UWY-octylamine (black).

By looking at the predicted structures for the **UWY**-octylamine and **UWY**-DEDMS seem to show some major differences. **UWY**-DEDMS shows the unchanged 100 peak at 3.89° 2θ, while **UWY**-octylamine seems to lose this peak. The PXRD pattern for **UWY**-DEDMS seems to be dominated by a group of four peaks between 5 ° and 10 ° 2θ with two of these peaks being the most prominent, the 200 peak at 7.04 ° 2θ and the 101 peak at 8.44 ° 2θ.

The two additional peaks in this quartet are the (001) and the (010) reflection at 7.68 ° and 9.17 ° 2θ respectively. The latter being the now moved interlayer reflection. **UWY**-octylamine is dominated by a single peak at 8.44 ° 2θ corresponding to the (101) reflection. The generated PXRD pattern also shows the 200 and 101 peaks. But these reflections seem to be severely reduced in intensity. The second most prominent peak in the PXRD pattern is at 15.40 ° 2θ which is caused by the (002), (211) and (310) reflections. The (010) reflection is reduced to a minor peak in the pattern at 11.35 ° 2θ.

By comparing these generated PXRD patterns with the experimental it is possible to ascertain the nature of the materials that have been produced through intercalation and calcination (Figure 5.49).

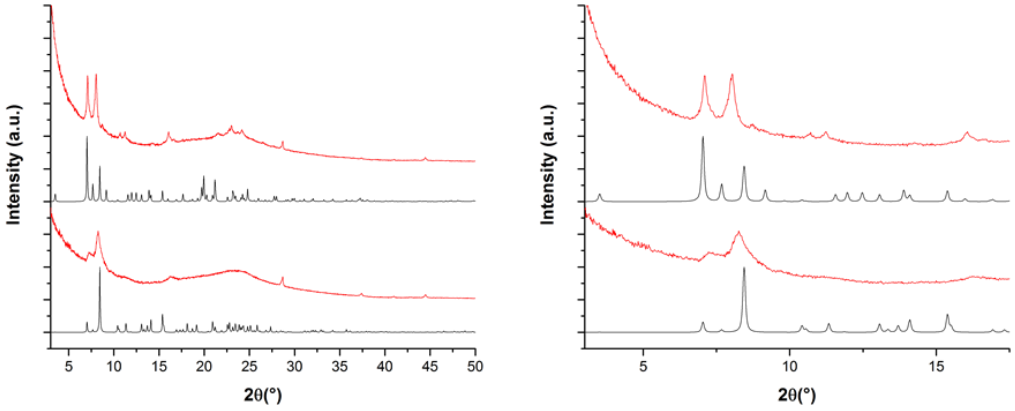

Figure 5.49 Shows a comparison of the generated (black) and the experimental (red) PXRD patterns with UWY-DEDMS shown above and UWY-octylamine shown below. The range between 3-17.5 ° 2θ is also shown (right).

Looking at the comparison between these powder patterns it is possible to infer some conclusions. Firstly, both patterns showed some loss in crystallinity, making it harder to ascertain the true nature of the materials. However, it seems that both experimental PXRD patterns seem to reflect the key characteristics of the generated patterns for the expected materials. The pattern for **UWY**-DEDMS is dominated by two peaks at 7.10 ° and 8.05 ° 2θ, which reasonably matches the two equally dominant peaks of the expected first four peaks of the generated **UWY**-DEDMS. Meanwhile the **UWY**-octylamine experimental is dominated by two peaks at 7.24 ° and 8.14 ° 2θ with the expected difference in intensities between them. These seem to indicate that the experimental procedures used could produce something like the expected materials, but not with high purity required to confidently confirm these materials.

These results suggest that **UWY** has issues during the organisation and reassembly steps. The biggest impact on this step is the role played by the silanols present in the **UWY**-P structure. The advantage of the ADOR process is that the disassembly of the *d4r* units is supposed to produce well defined quadruplets of silanols that provide the easier organisation of the layers, including directing the formation of silica columns that condense together to form *s4r*. Looking at the structure of **UWY**-P and comparing it to IPC-1P (derived from **UTL**) there are some major differences between the two that can explain the issues encountered (Figure 5.50).

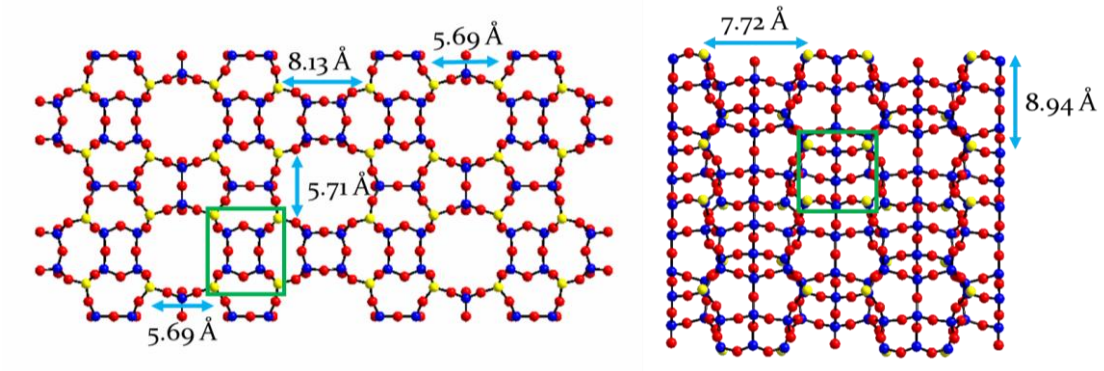

Figure 5.50 Shows the structures of UWY-P (left) and IPC-1P (right) when viewing above the interlayer silanol groups. An example of a silanol quadruplets is highlighted (green) in UWY-P the distance between silanols within the same quadruplet is 5.74 Å x 5.65 Å and in IPC-1P the distance between silanols within the same quadruplet is 4.75 Å x 5.05 Å. The distances between silanol quadruplets are marked (blue arrows). T-atoms are shown in blue, oxygens red and silanol oxygens yellow.

The most notable difference between **UWY**-P and IPC-1P is the orientation of the resultant silanols from the disassembly of the *d4r*. In the case of IPC-1P the silanol quadruplets are easy to spot, even without highlighting, as they form clearly defined quadruplets of 4.75 Å x 5.05 Å, representing a close distance between silanols in the same quadruplet. These quadruplets are well spaced as the distance between nearest neighbour silanol quadruplets is either 7.72 Å or 8.94 Å. These two characteristics, a small distance between silanols within the quadruplets and a larger distance between silanols of different quadruplets, helps make **UTL** such a successful ADORable zeolite. After disassembly **UTL** leaves a layered material with clearly orientated and defined silanol groups that provides for better ordering of the layers for optimal organisation and reassembly. In **UWY**-P the distance between silanols within a quadruplet (5.74 Å x 5.65 Å) is like that seen in IPC-1P. In contrast to IPC-1P, the distance between silanols in separate quadruplets is smaller in **UWY**-P (5.71 Å and 5.69 Å). A larger distance is seen between silanol quadruplets for those separated by the 10-ring channels (8.13 Å). With the silanol quadruplets less defined in

UWY-P compared to IPC-1P, due to the smaller distance between silanols from different quadruplets, the organisation and reassembly step becomes severely hampered.

The clearly defined quadruplets help to ensure that during organisation with octylamine the layers are orientated in a way to reduce the energy of the system. In IPC-1P, where the silanol quadruplets are well defined, the stacking of the layers to form IPC-2 in reassembly is favoured as it minimises the energy. In **UWY**-P the closeness of the silanols means that there are other orientations and stacking of the layers that can be just as favourable as that ideal for **UWY**-octylamine. This could lead to the lack of order in the final **UWY**-octylamine material seen in the PXRD pattern.

For the formation of the *s4r* linkages between the layers (**UWY**-DEDMS) the organisation step relies even more on these silanol quadruplets being clearly defined. This is not just because the clearly defined quadruplets are required for preferential stacking of the layers to form a well-ordered material. It is also required to direct the formation of the *s4r*. During organisation with DEDMS the silica columns form in between the silanols of each layer. In the case of IPC-1P the clearly defined silanol quadruplets leads to the formation of quadruplets of silica columns in between the layer that can easily condense together to form *s4r*. In the case of **UWY**-P this lack of distinction between the silanol quadruplets leads to these silanol columns being unable to condense together in an ordered fashion to form perfectly ordered layers of *s4r*. The increased disorder seen in the PXRD pattern for the **UWY**-DEDMS compared to **UWY**-octylamine seems to suggest this increased disorder. However, the two products formed from the different procedures suggest that the **UWY**-P layers were able to undergo some sort of organisation similar to that seen for IPC-1P to form a disordered form of the expected product. This may be due to the presence of some larger distances between the silanol quadruplets, which can therefore allow for some manipulation of the layers to occur, although the organisation process is perhaps not fully understood and so these are merely suggestions.

5.6.4 Summary of Results

Early attempts to synthesise the **UWY** framework structure showed that it was possible to reduce the amount of Ge compare to the originally reported synthesis.[9] However the Si/Ge ratio could only be increased to a maximum of 3.19 compared to the 2.26 when the original synthesis was repeated. Despite the limitation in increasing the Si-content, an impact on the framework was already seen, as the structures **UWY**-2.33 and **UWY**-3 were shown to be more stable to calcination than the original **UWY**-1.5. Application of the disassembly

process to the three materials also confirmed the increase in stability of the materials with a greater Si/Ge ratio. **UWY**-1.5 lost almost all crystallinity upon contact with weak acid. Most likely due to the presence of Ge in the layers, resulting in a dissolution of the structure. Meanwhile both **UWY**-2.33 and **UWY**-3 showed PXRD patterns that would be expected of a disassembled material. Both became dominated by a single peak, with peaks unaffected by the movement of the 010/interlayer distance still being observed. SEM/EDX analysis also confirmed the preservation of the crystal morphology of these two materials and the reduction of the Ge content (Si/Ge ratio > 32). ^{29}Si MAS NMR showed the formation silanols as a result of the dissolution of the Ge-dominated *d4r*, the CP experiment also highlighted the presence of some additional Q^2 sites, most likely as a result of the removal of some Ge that was still present in the layers. Organisation of the layers with strong acid resulted in destruction of the materials, due to the increased speed of the rate of Si-O-Si bond cleavage. Most likely as a result of the presence of Ge in the layers creating defect sites and the ease of accessibility to these defects, due to the lower density of these layers. Although some of the peak movement that occurred may suggest that a rearrangement process was also taking place. However, the increasing loss of crystallinity in the material was the predominant theme. Organisation of the material with weak acid seemed to follow the pattern expected, with deintercalation taking place without any additional Si-O-Si bond formation. Attempts to organise the layers with the use of intercalating agents proved somewhat fruitful with the PXRD patterns changing, showing a better distinction between the relatively close peaks between 7-8 ° 2θ and the presence of the (100) reflection. However, the change was relatively minimal, leading to suspicions of issues surrounding the organisation step. Reassembly of the products organised with octylamine and DEDMS produced materials whose PXRD patterns hinted towards the expected **UWY**-octylamine and **UWY**-DEDMS materials, but not with the quality PXRD patterns expected for a perfectly organised and reassembled sample. The BET surface area and MAS NMR of the materials also highlighted the non-ideal behaviour of these materials during the organisation and reassembly steps. The low BET surface area of the materials and the presence of Q^2 and Q^3 sites indicated that the final reassembly of the materials were not successful. It is suggested that the issues with the organisation and reassembly are due to the relative instability of the layers and the orientation and distribution of the silanols in between the layers, after removal of the Ge-dominated *d4r*. The closeness of separate silanol quadruplets leads to a lack of ordering of the layers, as there is no single energetically favourable orientation, resulting in stacking faults and

disordering of the layers during reassembly and formation of **UWY**-octylamine. These issues are then exacerbated during the formation of **UWY**-DEDMS as the lack of orientation of the layers leads to the inability for the formation of ordered layers of *s4r*. Such results clearly show that **UWY** is a partially ADORable zeolite, clearly able to undergo the assembly and disassembly processes, however the orientation of its interlayer silanols and the instability of the layers seem to make it a less than ideal candidate for the organisation and reassembly steps (especially when compared to **UTL**).

5.7 Conclusions

The limited number of ADOR candidates was highlighted and four candidates for the ADOR process were drawn up based on criteria discussed and relative interest. The frameworks NUD-1 and ITQ-33 were shown to be non-ideal candidates for the ADOR process. It was shown that both frameworks avoided the incorporation of more silicon. By increasing the Si-content of the initial gel, as the materials produced became less crystalline products. This was most likely due to the high concentration of *d4r* in the structures, which require a high Ge content to maintain their stability and aid their formation. Both materials only showed Si/Ge ratios that were similar to those already reported in the literature.[7,8] Attempts to disassemble the materials showed the impact of the high Ge content of these frameworks. Both frameworks were destroyed after 5 mins under relatively gentle conditions. This suggests that both NUD-1 and ITQ-33 are unsuitable candidates for the ADOR process.

The ITQ-38 (**ITG**) material showed far more promise. The synthesis of the SDA was successfully modified to avoid the release of HCN as in the original procedure.[10] This SDA was then used to successfully synthesise the **ITG** framework, however when the Ge content was varied the Si/Ge content of the gel seemed to remain unchanged and the formation of a GeO_2 impurity was noted. The material was successfully disassembled as the PXRD pattern showed a loss of peaks with reflections that required ordering in the same direction as the stacking of the layers. The material also showed the loss of Ge in the EDX analysis, the formation of silanol groups in the ^{29}Si MAS NMR and a preservation of the crystal morphology in the SEM images. The **ITG** layers were shown to be particularly unstable to organisation with acid. In 12 M HCl and 0.1 M HCl the material showed an ever-increasing loss of crystallinity, although there were some hints of a rearrangement process taking place in the stronger acid and the lower acid strength led to a slower rate of degradation of the framework. The use of intercalating agents to organise the layers

resulted in a slight change with the use of octylamine showing the characteristic movement of the interlayer reflection to a higher 2θ value. Use of DEDMS and acidic conditions seemed to result in a degradation of the structure, mainly due to the weakness of the layers under the harsher conditions used. reorganisation of both materials resulted in similar products, which matched the daughter zeolite with the layers connected by direct O-linkages. The process also showed a decrease in the crystallinity of the pattern and the material. The poor quality of the material suggested a property of the framework was interfering in the successful organisation of the layers. It is suggested that unlike, **UTL**, ITQ-38 has a non-ideal arrangement of silanols. The silanol quadruplets are not well-defined leading to a less obvious energetically favourable orientation of the layers that would maximise their organisation. The lack of any clear quadruplets seems to lead to the material only forming the ITQ-38-octylamine structure.

The synthesis of IM-20 was conducted and attempts to reduce the amount of Ge in the framework by increasing the Si/Ge ratio of the starting gel were relatively successful. The increasing Si/Ge ratio did hit an impasse before the synthesis resulted in a primarily non-crystalline material. Both **UWY**2.33 and **UWY**-3 showed an increased Si-content, while maintaining the crystal morphology and purity of the material. The original **UWY**-1.5 showed the expected fragility due to its higher Ge content and was almost destroyed after calcination and disassembly. In comparison both **UWY-2.33** and **UWY-3** remained stable and displayed some of the key characteristics of the disassembly of a zeolite. The PXRD pattern showed a loss of peaks with reflections that required ordering in the same direction as the stacking of the layers. The material also showed the loss of Ge in the EDX analysis, the formation of silanol groups in the ^{29}Si MAS NMR and a preservation of the crystal morphology in the SEM images. The interlayer reflection for these materials showed a less dramatic shift corresponding to a less dramatic decrease in the interlayer distance than expected for the removal Ge-dominated *d4r*. The attempted organisation of the **UWY**-3P material with 12M showed similar results to that seen for ITQ-38. The layers seemed to dramatically lose crystallinity with increasing contact time with the acid, due to their relative instability. Although some changes in peak positions was seen which may have alluded to a rearrangement process occurring. Under weakly acidic conditions the material showed a lower rate of degradation and some degree of self-ordering, which was not seen for ITQ-38. Attempts to reassemble this material were however unsuccessful. Organisation of the layers with octylamine and DEDMS seemed to result in a slight change in the PXRD patterns, with the material after treatment with octylamine showing a similar

pattern to that after treatment with weak acid. The use of DEDMS resulted in a decrease in crystallinity of the material and a similar if less ordered PXRD pattern to the disassembled product. Reassembly of the layers by calcination led to the formation of two materials that seemed to closely relate to the expected materials, although the increasing loss of crystallinity in the materials made it hard to conclusively prove. It is suggested that **UWY**-P suffers from a similar issue to that already seen for the ITQ-38-P layers; the non-ideal arrangement of silanols. The silanol quadruplets are not well-defined compared to those in IPC-1P and these lead to a less well defined favourable orientation of the layers to maximise their organisation of the layers. The ability for the **UWY**-P layers, unlike ITQ-38P, to form two seemingly different materials under the conditions used; suggests that there may be some better ordering of the layers. It is suggested that this may be because **UWY**-P silanols do have some areas where the distance between silanol quadruplets is larger, this would help define some of the quadruplets and allow for the development of some ordering and the formation of a material like **UWY**-octylamine or **UWY**-DEDMS. In the case of ITQ-38-P there is no such zoning taking place, making it harder to organise the layers, resulting in a similar material despite the different methodologies used. Another factor may be the relative stability of the layers. It was clear, from the SEM images of the resultant materials, that the **UWY** layers were more stable after treatment with DEDMS and acid. In comparison, the ITQ-38-P layer showed a far greater loss of crystallinity. This would perhaps suggest that the ITQ-38P layers were breaking down while the Si connections were forming resulting in a closer distance between the layers and the increasing loss of crystallinity in the material. The stability of the **UWY** layers (as seen in the SEM) would therefore suggest that the issues organizing the layers were primarily due to the orientation of the silanols and not due to degradation of the material.

From this research, it is clear that the ADOR process is far more fastidious than expected and that its potential may be severely limited with the currently known framework materials. While some materials were unable to undergo the ADOR process (ITQ-33 and NUD-1) others could undergo all steps of the ADOR process (ITQ-38 and **UWY**). However, the relative success of these materials was particularly hampered by the fragility of the layers and the non-ideal orientation of the silanols. This prevented the ordering of the layers to the degree required to definitively prove the formation of the daughter zeolites expected.

5.8 Future Work

Future work should involve further evaluation of other germanosilicate materials to see if they are also suited for the ADOR process. The organisation of the layers of the ITQ-38 and **UWY** may have to be investigated computationally to ascertain the relatively favourability of certain orientations of the layers. Also, further investigations should be conducted to ascertain if a better ordering of the layers could be obtained with the use of other intercalating agents.

5.9 References

(1) Mazur, M.; Wheatley, P. S.; Navarro, M.; Roth, W. J.; Položij, M.; Mayoral, A.; Eliášová, P.; Nachtigall, P.; Čejka, J.; Morris, R. E. Synthesis of "Unfeasible" Zeolites. *Nat. Chem.* **2015**, *8* (1), 58–62.

(2) Roth, W. J.; Nachtigall, P.; Morris, R. E.; Wheatley, P. S.; Seymour, V. R.; Ashbrook, S. E.; Chlubná, P.; Grajciar, L.; Položij, M.; Zukal, A.; et al. A Family of Zeolites with Controlled Pore Size Prepared Using a Top-Down Method. *Nat. Chem.* **2013**, *5* (7), 628–633.

(3) Chlubná-Eliášová, P.; Tian, Y.; Pinar, A. B.; Kubů, M.; Čejka, J.; Morris, R. E. The Assembly-Disassembly-Organization-Reassembly Mechanism for 3D-2D-3D Transformation of Germanosilicate IWW Zeolite. *Angew. Chemie* **2014**, *126* (27), 7168–7172.

(4) Kasneryk, V.; Shamzhy, M.; Opanasenko, M.; Wheatley, P. S.; Morris, S. A.; Russell, S. E.; Mayoral, A.; Trachta, M.; Čejka, J.; Morris, R. E. Expansion of the ADOR Strategy for the Synthesis of Zeolites: The Synthesis of IPC-12 from Zeolite UOV. *Angew. Chemie* **2017**, *129* (15), 4388–4391.

(5) Baerlocher, C.; McCusker, L. B. Database of Zeolite Structures http://www.iza-structure.org/databases/.

(6) Sastre, G.; Vidal-Moya, J. A.; Blasco, T.; Rius, J.; Jordá, J. L.; Navarro, M. T.; Rey, F.; Corma, A. Preferential Location of Ge Atoms in Polymorph C of Beta Zeolite (ITQ-17) and Their Structure-Directing Effect: A Computational, XRD, and NMR Spectroscopic Study. *Angew. Chemie Int. Ed.* **2002**, *41* (24), 4722–4726.

(7) Chen, F.-J.; Xu, Y.; Du, H.-B. An Extra-Large-Pore Zeolite with Intersecting 18-, 12-, and 10-Membered Ring Channels. *Angew. Chemie Int. Ed.* **2014**, *53* (36), 9592–

9596.

(8) Corma, A.; Díaz-Cabañas, M. J.; Jordá, J. L.; Martínez, C.; Moliner, M. High-Throughput Synthesis and Catalytic Properties of a Molecular Sieve with 18- and 10-Member Rings. *Nature* **2006**, *443* (7113), 842–845.

(9) Dodin, M.; Paillaud, J. L.; Lorgouilloux, Y.; Caullet, P.; Elkaïm, E.; Bats, N. A Zeolitic Material with a Three-Dimensional Pore System Formed by Straight 12- and 10-Ring Channels Synthesized with an Imidazolium Derivative as Structure-Directing Agent. *J. Am. Chem. Soc.* **2010**, *132* (30), 10221–10223.

(10) Moliner, M.; Willhammar, T.; Wan, W.; González, J.; Rey, F.; Jorda, J. L.; Zou, X.; Corma, A. Synthesis Design and Structure of a Multipore Zeolite with Interconnected 12- and 10-MR Channels. *J. Am. Chem. Soc.* **2012**, *134* (14), 6473–6478.

(11) Qian, K.; Wang, Y.; Liang, Z.; Li, J. Germanosilicate Zeolite ITQ-44 with Extra-Large 18-Rings Synthesized by Using Commercial Quaternary Ammonium as Structure-Directing Agent. *RSC Adv.* **2015**, *5*, 63209–63214.

(12) Kamakoti, P.; Barckholtz, T. A. Role of Germanium in the Formation of Double Four Rings in Zeolites. *J. Phys. Chem. C* **2007**, *111* (9), 3575–3583.

(13) Liu, L.; Yu, Z. B.; Chen, H.; Deng, Y.; Lee, B. L.; Sun, J. Disorder in Extra-Large Pore Zeolite ITQ-33 Revealed by Single Crystal XRD. *Cryst. Growth Des.* **2013**, *13* (10), 4168–4171.

(14) Morris, R. E.; Čejka, J. Exploiting Chemically Selective Weakness in Solids as a Route to New Porous Materials. *Nat. Chem.* **2015**, *7* (5), 381–388.

(15) Vjunov, A.; Fulton, J. L.; Camaioni, D. M.; Hu, J. Z.; Burton, S. D.; Arslan, I.; Lercher, J. A. Impact of Aqueous Medium on Zeolite Framework Integrity. *Chem. Mater.* **2015**, *27* (9), 3533–3545.

(16) Mokaya, R. Al Content Dependent Hydrothermal Stability of Directly Synthesized Aluminosilicate MCM-41. *J. Phys. Chem. B* **2000**, *104* (34), 8279–8286.

(17) Verboekend, D.; Keller, T. C.; Milina, M.; Hauert, R.; Pérez-Ramírez, J. Hierarchy Brings Function: Mesoporous Clinoptilolite and L Zeolite Catalysts Synthesized by Tandem Acid-Base Treatments. *Chem. Mater.* **2013**, *25* (9), 1947–1959.

(18) Shen, S.-C.; Kawi, S. Understanding of the Effect of Al Substitution on the Hydrothermal Stability of MCM-41. *J. Phys. Chem. B* **1999**, *103* (42), 8870–8876.

(19) Eliášová, P.; Opanasenko, M.; Wheatley, P. S.; Shamzhy, M.; Mazur, M.; Nachtigall, P.; Roth, W. J.; Morris, R. E.; Čejka, J. The ADOR Mechanism for the Synthesis of New Zeolites. *Chem. Soc. Rev.* **2015**, *44* (20), 7177–7206.

(20) Mazur, M.; Chlubná-Eliášová, P.; Roth, W. J.; Čejka, J. Intercalation Chemistry of Layered Zeolite Precursor IPC-1P. *Catal. Today* **2014**, *227*, 37–44.

(21) Brandenburg, K. Diamond - Crystal and Molecular Structure Visualization. Kreuzherrenstr. 102, 53227 Bonn, Germany.

(22) Morris, S. A.; Bignami, G. P. M.; Tian, Y.; Navarro, M.; Firth, D. S.; Čejka, J.; Wheatley, P. S.; Dawson, D. M.; Slawinski, W. A.; Wragg, D. S.; et al. In Situ Solid-State NMR and XRD Studies of the ADOR Process and the Unusual Structure of Zeolite IPC-6. *Nat. Chem.* **2017**, *9*, 1012–1018.

6 Investigating the Use of Biphenyl SDAs for the Synthesis of New Zeolites

6.1 Aim

This chapter will discuss the shortcomings of the ADOR process and the first investigations into the synthesis of new ADORable zeolites using a group of selected organic SDAs, based on a rigid biphenyl backbone. The synthesis of these SDAs will be discussed, along with their use in traditional hydrothermal syntheses and the successes and shortcomings of such SDAs and their implications on future SDA designs.

6.2 Introduction

6.2.1 The ADOR Process

The ADOR process has had many successes during its brief history. However, as seen in the previous chapter, the ADOR process does have some limitations. A material requires a very specific set of framework properties to be considered a possible candidate for the ADOR process, including Ge-dominated monodirectional *d4r*, stable silicate layers and large pores.[1]

ABW	ACO	AEI	AEL	AEN	AET	AFG	AFI	AFN	AFO	AFR	AFS
AFT	AFV	AFX	AFY	AHT	ANA	APC	APD	AST	ASV	ATN	ATO
ATS	ATT	ATV	AVL	AWO	AWW	BCT	*BEA	BEC	BIK	BOF	BOG
BOZ	BPH	BRE	BSV	CAN	CAS	CDO	CFI	CGF	CGS	CHA	-CHI
-CLO	CON	CSV	CZP	DAC	DDR	DFO	DFT	DOH	DON	EAB	EDI
EEI	EMT	EON	EPI	ERI	ESV	ETL	ETR	EUO	*-EWT	EZT	FAR
FAU	FER	FRA	GIS	GIU	GME	GON	GOO	HEU	IFO	IFR	-IFU
IFW	IFY	IHW	IMF	IRN	IRR	-IRY	ISV	ITE	ITG	ITH	*-ITN
ITR	ITT	-ITV	ITW	IWR	IWS	IWV	IWW	JBW	JNT	JOZ	JRY
JSN	JSR	JST	JSW	KFI	LAU	LEV	LIO	-LIT	LOS	LOV	LTA
LTF	LTJ	LTL	LTN	MAR	MAZ	MEI	MEL	MEP	MER	MFI	MFS
MON	MOR	MOZ	*MRE	MSE	MSO	MTF	MTN	MTT	MTW	MVY	MWF
MWW	NAB	NAT	NES	NON	NPO	NPT	NSI	OBW	OFF	OKO	OSI
OSO	OWE	-PAR	PAU	PCR	PHI	PON	POS	PSI	PUN	RHO	-RON
RRO	RSN	RTE	RTH	RUT	RWR	RWY	SAF	SAO	SAS	SAT	SAV
SBE	SBN	SBS	SBT	SEW	SFE	SFF	SFG	SFH	SFN	SFO	SFS
*SFV	SFW	SGT	SIV	SOD	SOF	SOS	SSF	*-SSO	SSY	STF	STI
*STO	STT	STW	-SVR	SVV	SZR	TER	THO	TOL	TON	TSC	TUN
UEI	UFI	UOS	UOV	UOZ	USI	UTL	UWY	VET	VFI	VNI	VSV
WEI	-WEN	YUG	ZON								

Figure 6.1 Shows the 232 unique zeolite framework structures after the application of the selection criteria for the ADOR process. Frameworks highlighted are ruled out due to: not containing *d4r* (red), not currently known to contain Ge-dominated *d4r* (green) and not containing stable silicate layers (blue). Those 12 left over (white) are deemed to satisfy the selection criteria.

By applying these loose selection criteria to the currently known frameworks in the IZA database only 12 of 232 unique frameworks are left that may be able to undergo the ADOR process (Figure 6.1Figure 5.2). Of these 12 frameworks, three have already been researched with varying degrees of success (**IWW**, **UOV** and **UTL**).[2–4] Even those potential candidates that were deemed suitable through these selection criteria (**ITG** and **UWY**) were shown to be less than ideal candidates. It is imperative to form new ADORable zeolites, through hydrothermal synthesis, if the ADOR process is to be advanced further and to ensure the ADOR process is seen as a viable pathway to the synthesis of new pure-silicate frameworks.

6.2.2 Hydrothermal Synthesis

Hydrothermal synthesis has had a long and successful history in the synthesis of zeolites and other materials. Using hydrothermal synthesis, researchers have increased the number of unique zeolite framework structures to over 230.[5–7] The design and synthesis of new zeolite frameworks have advanced with the increasing knowledge and understanding of the various factors that impact the crystallisation process.

One of the most successful advances in the synthesis of new zeolite frameworks has been the development of new organic structure directing agents and understanding their role in framework formation.[8] As discussed previously, structure directing agent (SDA) is used as a collective term to encompass the three main roles played by organic agents in zeolite synthesis including: space filling, true templating and structure directing agents. Most SDAs do not fulfil the 'true-templating agent' role but generally fulfil a space filling or structure directing agent role. As defined by Lobo *et al.*, a structure directing agent is as an additive whose presence is required to direct the synthesis to a specific product, whose formation is impossible with another additive, but is not necessarily unique.[9,10] The interaction between the SDA and the framework is typified as 'host-guest interactions' through Van der Waals interactions. This leads to a framework that tends to correlate with the size and shape of the SDA used. Therefore, by designing new SDAs of different sizes and shapes it is possible to synthesise new frameworks.

6.2.3 The Role of the SDA

Some of the most important factors in determining the role an SDA plays in the zeolite synthesis have been summarised by Lobo *et al.* who linked the structure directing abilities of molecules to several factors including:

1) The molecule must have room within the particular cage of the zeolite.

2) The guest compound must be stable in the presence of water under synthesis conditions.
3) The guest compound should fit the inner surface of the cage with as many Van der Waals contacts as possible without deformation.
4) The tendency of the guest substance to form complexes in solvent should be weak; those molecules with higher stiffness will tend to form a cage/pore.
5) The tendency to form a cage/pore will increase with basicity or polarisability of the molecule.[9]

With regards to specific organic molecules and their structure-directing abilities, Zones *et al*. have shown a relationship between the size (or C+N number) of quaternary ammonium molecules and their selectivity for a specific framework.[11] It was shown that as a molecule increases in size they generally became more selective, as larger molecules placed more stringent requirements on the framework to provide enough room for the molecule and favourable Van der Waals interactions. These requirements can then be maximised by increasing the rigidity of the SDA, limiting the number of favourable Van der Waals interactions, as a more flexible molecule can achieve a greater number of conformations decreasing its selectivity.

6.2.4 The Choice of SDA

By taking these factors into account a 'wish list' was created, determining the ideal properties looked for in an organic SDA:

1) The organic SDA should be large and rigid.
2) The organic SDA should dissolve and be stable in water
3) Synthesis of the organic SDA should be relatively easy and cheap.

Taking these criteria into consideration the biphenyl molecule was selected to act as a basis for the new SDAs (Figure 6.2).

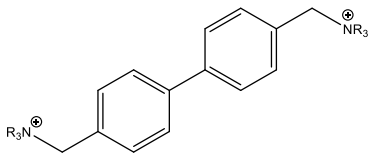

Figure 6.2 Shows the biphenyl SDA selected for the investigations conducted in this chapter.

This biphenyl SDA ammonium salt has previously been investigated for use in catalysis and for antibacterial and antifungal purposes.[12,13] The biphenyl SDA backbone seemed to be an ideal candidate for the synthesis of new zeolite frameworks. The presence of the two

phenyl rings linked together by a direct bond provide for a larger molecule with the rigidity required, as suggested by Zones *et al.*[11] The terminal chlorines on the commercially available 4,4′-Bis(chloromethyl)-1,1′-biphenyl allowed for the easy formation of terminal ammonium cations, which could be easily varied depending on the amine chosen. It was hoped that the backbone rigidity, combined with the opportunity for the variation of the ammonium cations, would help with the design and synthesis of new and interesting zeolite frameworks. This, in combination with the ease of synthesis of such SDAs increased interest in conducting investigations into SDAs based on this organo-cation.

6.3 Experimental Section

6.3.1 Synthesis of SDAs

6.3.1.1 Synthesis of Biphy-TEA SDA

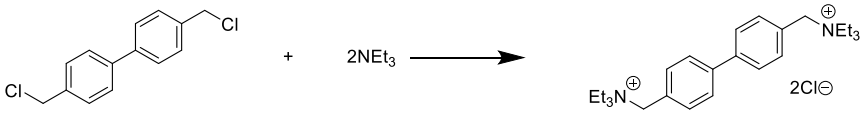

Figure 6.3 Shows the reaction scheme to form N,N'-([1,1'-biphenyl]-4,4'-diylbis(methylene))bis(N,N-diethylethanaminium) dichloride (Biphy-TEA).

4,4′-Bis(chloromethyl)-1,1′-biphenyl (30 g, 119.4 mmol), acetonitrile (300 mL) and triethylamine (33.3 mL, 238.8 mmol) were placed in a round bottom flask and heated at 70 °C for 72 hours. The resultant solid was then collected and filtered with acetonitrile to yield a white solid (48.47 g, 89.5 %). The chloride salt was converted to the hydroxide form with the use of ion-exchange resin in water.

6.3.1.2 Synthesis of Biphy-Im SDA

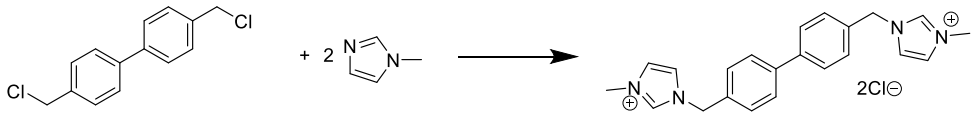

Figure 6.4 Shows the reaction scheme to form 1,1'-([1,1'-biphenyl]-4,4'-diylbis(methylene))bis(3-methyl-1H-imidazol-3-ium) dichloride (Biphy-Im).

4,4′-Bis(chloromethyl)-1,1′-biphenyl (30 g, 119.4 mmol), acetonitrile (250 mL) and 1-methylimidazole (19 mL, 238.4 mmol) were placed in a round bottom flask and heated at 70 °C for 72 hours. The resultant solid was then collected and filtered with acetonitrile to yield a white solid (44.85 g, 90.4 %). The chloride salt was converted to the hydroxide form with the use of ion-exchange resin in water.

6.3.1.3 Synthesis of Biphy-DABCO SDA

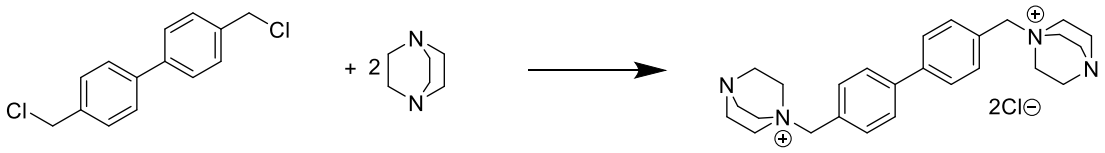

Figure 6.5 Shows the reaction scheme to form 1,1'-([1,1'-biphenyl]-4,4'-diylbis(methylene))bis(1,4-diazabicyclo[2.2.2]octan-1-ium) dichloride (Biphy-DABCO).

4,4′-Bis(chloromethyl)-1,1′-biphenyl (20 g, 79.6 mmol), acetonitrile (150 mL) and DABCO (17.86 g, 159.2 mmol) were placed in a round bottom flask and heated at 70 °C for 72 hours. The resultant solid was then collected and filtered with acetonitrile and ethyl acetate to yield a white solid (31.73 g, 83.8 %). The chloride salt was converted to the hydroxide form with the use of ion-exchange resin in water.

6.3.2 Synthesis of Zeolites

The synthesis gels were varied according to the desired conditions for the reaction. The general procedure involved the placement of germanium and/or boric acid in a stirring solution of the SDAOH. After 1 hour, the silica source was then added, and the gel stirred for a further 3 hours, or overnight depending on the silica source. The reaction weight was monitored to ensure the desired water ratio was reached, then HF acid (48 wt.%) was added if desired. After stirring for an hour, the gel was weighed to ensure the desired molar ratio was present and then transferred to a steel-lined autoclave and heated at a specified temperature and time.

6.3.2.1 Example of ITQ-38 (ITG) Synthesis

Boric acid (0.12 g, 2.33 mmol) was added to a stirring solution of a Biphy-SDA solution (2.33 mmol). After 30 minutes germanium dioxide (0.244 g, 2.33 mmol) was then added. After stirring the solution for one hour, colloidal silica (0.81 mL, 7 mmol) was added. Once the homogeneous solution reached the desired molar ratio (3 SiO_2 : 1 GeO_2 : 1 $SDA(OH_2)$: 0.08 H_3BO_3 : 80 H_2O) the liner was placed in a steel-lined autoclave and the synthesis was heated to 175 °C for 14 days. The resultant solid was then filtered and washed with water.

6.3.2.2 Example of IM-12 (UTL) Synthesis

Germanium dioxide (1.255 g, 12 mmol) was added to a stirring solution of a Biphy-SDA solution (9 mmol) in a Teflon liner. After 30 mins fumed silica (1.44 g, 24 mmol) was added and the solution stirred until homogeneous. Once homogeneous, and once the gel had reached the correct molar ratio (0.8 SiO_2 : 0.4 GeO_2 : 0.3 $SDA(OH_2)$: 30 H_2O) the

liner was placed in a steel-lined autoclave and the synthesis heated to 175 °C for 14 days. The resultant solid was then filtered and washed with water.

6.3.2.3 Example of IM-20 (UWY) Synthesis

Germanium dioxide (0.418 g, 4 mmol) was added to a stirring solution of a Biphy-SDA solution (2.5 mmol) in a Teflon cup. After 30 minutes fumed silica (0.360 g, 6 mmol) was added and the solution stirred until homogeneous. Once the gel had reached the desired weight 48 wt.% hydrofluoric acid (181 µL, 5 mmol) was added and the gel allowed to stir for 30 minutes. Once the gel had reached the desired molar ratio (0.6 SiO_2 : 0.4 GeO_2 : 0.25 $SDA(OH_2)$: 0.5 HF : 10 H_2O) the gel was transferred from the Teflon cup to a steel-lined autoclave and heated to 175 °C for 14 days. The resultant solid was then filtered and washed with water.

6.3.2.4 Example of ITQ-26 (IWS) Synthesis

Germanium dioxide (0.314 g, 3 mmol) was added to a stirring solution of a Biphy-SDA solution (3.75 mmol) in a Teflon cup. After 30 minutes TEOS (2.68 mL, 12 mmol) was added and the solution stirred overnight to allow for hydrolysis. Once the gel had reached the desired weight 48 wt.% hydrofluoric acid (272 µL, 7.5 mmol) was added and allowed to stir for 30 minutes. Once the gel had reached the desired molar ratio (0.8 SiO_2 : 0.2 GeO_2 : 0.25 $SDA(OH_2)$: 0.5 HF : 7.5 H_2O) gel was transferred from the Teflon cup to a steel-lined autoclave and heated to 150 °C for 14 days. The resultant solid was then filtered and washed with water.

6.4 Results and Discussion

6.4.1 Investigating the Synthesis of Biphenyl SDAs

The synthesis of these new SDAs was conducted on a smaller scale before the larger scale production. These syntheses involved the reaction of 4,4′-Bis(chloromethyl)-1,1′-biphenyl with the desired amine to form the chloride salt.

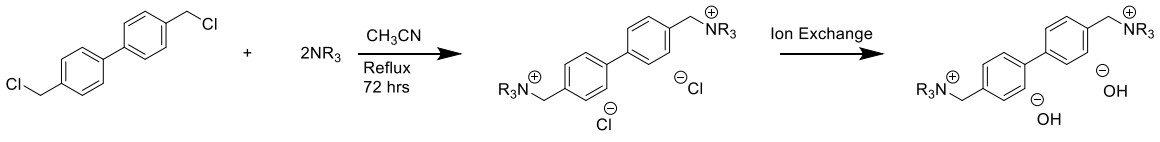

Figure 6.6 Shows the general reaction scheme for the formation of the Biphy-ammonium hydroxide SDAs from reaction of the 4,4′-Bis(chloromethyl)-1,1′-biphenyl with a chosen tertiary amine to form the corresponding diammonium salt. Ion exchange then follows this to form the hydroxide form.

This salt could then be easily converted to the hydroxide form using standard ion exchange procedures (Figure 6.6). The syntheses were monitored by TLC and when the reaction was observed as complete the success was determined by ^{1}H NMR.

6.4.1.1 Synthesis of Biphy-TEA

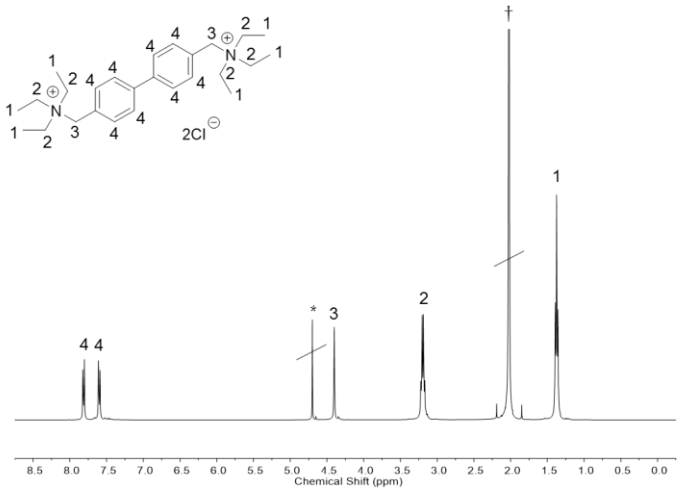

No.	Peak Position (ppm)	Integration
1	1.37	18.87
2	3.20	12.31
3	4.40	4.00
4	7.60, 7.81	4.26,4.12

Figure 6.7 Shows the ^{1}H NMR spectrum (left) of the synthesised Biphy-TEA chloride SDA using the stated synthesis procedure. The Biphy-TEA chloride structure is overlaid with the different environments labelled. The table (right) shows the peak position and their corresponding environment and the integration when peak 3 is normalised to 4.00. A line indicates impurity peaks from acetonitrile (†) and water (*).

The results of the NMR (Figure 6.7) showed that the adapted procedure had indeed produced the target cation.[13] The presence of acetonitrile was noted, but drying the sample overnight easily removed these impurities. The NMR was then assigned, as seen in Figure 6.7. The ^{1}H NMR showed the characteristic triplet (peak 1) and quartet (peak 2) at positions 1.37 ppm and 3.20 ppm associated with the terminal triethylammonium groups, including an integration value of 18.87 and 12.31 respectively, very close to the expected values of 18 and 12. The peak at 4.40 ppm corresponded to the CH_2 groups (peak 3) connecting the biphenyl rings with the terminal triethylammonium groups. When this peak was normalised to 4.00 the integration of the other peaks also corresponded to their expected values. The final doublet of doublet at 7.60 ppm and 7.82 ppm (peak 4) corresponded to the expected biphenyl peaks. This confirmed the successful synthesis of Biphy-TEA, which was repeated on a larger scale with a good yield and purity (Section 6.3.1.1).

6.4.1.2 Synthesis of Biphy-Im

With the successful synthesis of Biphy-TEA the synthesis of Biphy-Im was attempted. From the ^{1}H NMR it was possible to assign these peaks (Figure 6.8).[13] The singlet (peak 1) at 3.73 ppm corresponded to the CH_3 in the terminal methylimidazolium group, and

showed an integration value of 6.13 corresponding closely to the expected value. Peak 2 corresponded to the expected singlet for the CH_2 groups connecting the methylimidazolium groups to the biphenyl backbone. The peak at 7.30 ppm is indicative of the aromatic CH in the methylimidazolium group that are bordered by a single nitrogen (peak 3). This was further corroborated when the integrated value of 4.12 was close to the expected value of 4. The characteristic doublet of doublets (peak 4) at 7.34 ppm and 7.54 ppm was seen for the biphenyl hydrogens with an integration value close to the expected 8. The final peak at 8.66 ppm (peak 5) with an integration of 2.09 matches the expected value for the aromatic CH bonded to two nitrogens in methylimidazolium group. This leads to more deshielding and the higher ppm values compared to the other hydrogens in the methylimidazolium group. The only impurity seen in the ^{1}H NMR was seen for water associated with the deuterated solvent D_2O used.

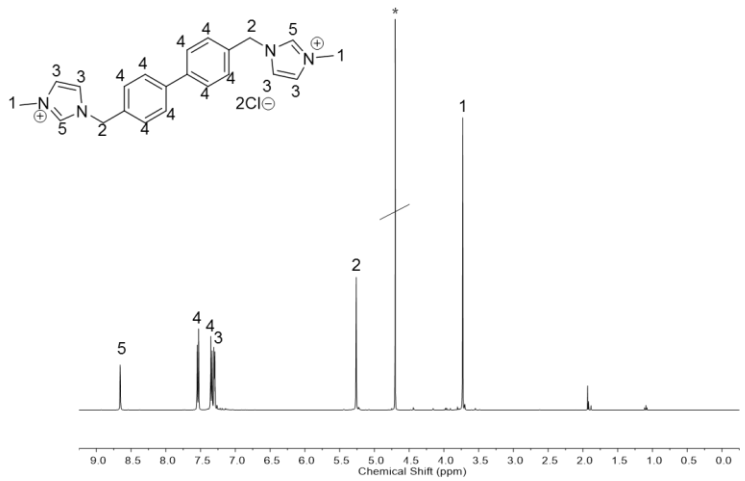

No.	Peak Position (ppm)	Integration
1	3.73	6.13
2	5.26	4.00
3	7.30	4.12
4	7.34, 7.54	4.04, 4.28
5	8.66	2.09

Figure 6.8 Shows the ^{1}H NMR spectrum (left) of the synthesised Biphy-Im chloride SDA using the stated synthesis procedure. The Biphy-Im chloride structure is overlaid with the different environments labelled. The table (right) shows the peak positions and their corresponding environment and the integration when peak 2 is normalised to 4.00. A line indicates an impurity peak from water (*).

The successful preparation of the Biphy-Im SDA was again repeated on a larger scale with a good yield and purity (Section 6.3.1.2).

6.4.1.3 Synthesis of Biphy-DABCO

The final SDA synthesis that was synthesised was the Biphy-DABCO SDA. The ^{1}H NMR spectrum strongly indicated the successful formation of the desired chloride salt (Figure 6.9).

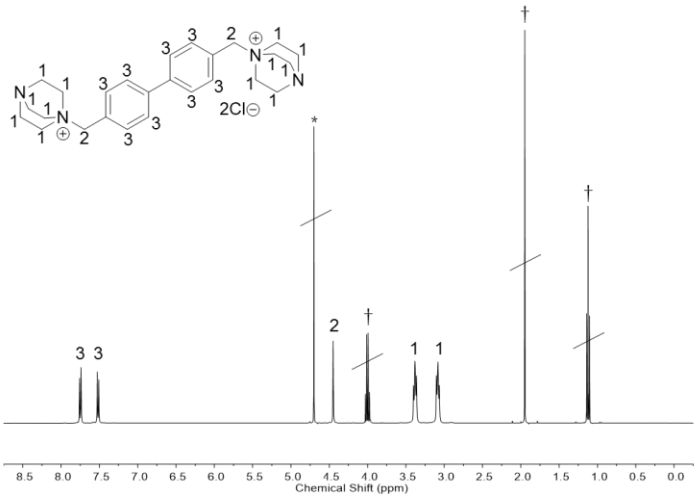

No.	Peak Position (ppm)	Integration
1	3.08, 3.38	12.01,12.18
2	4.45	4.00
3	7.52, 7.75	3.97, 3.98

Figure 6.9 Shows the ^{1}H NMR spectrum (left) of the synthesised Biphy-DABCO chloride SDA using the stated synthesis procedure. The Biphy-DABCO chloride structure is overlaid with the different environments labelled. The table (right) shows the peak positions and their corresponding environment and the integration when peak 2 is normalised to 4.00. A line through the peak indicates an impurity peak from water (*) and ethyl acetate (†).

The Biphy-DABCO ^{1}H NMR was dominated by impurity peaks from the ethyl acetate used to wash the product as well as the target SDA.[13] The peaks at 1.12 ppm 1.95 ppm and 4.00 ppm corresponded to the peaks seen for ethyl acetate. The SDA showed three characteristic peaks corresponding to the expected environments. The doublet of triplets at 3.08 and 3.38 ppm were indicative of the DABCO environment, and the integration values of 12.01 and 12.18 corresponded well to the expected value of 24. The singlet at 4.45 ppm (peak 2) corresponded to the CH_2 connecting the biphenyl backbone with the terminal DABCO groups, and the integration was normalised to 4.00. The final doublet of doublets at 7.52 ppm and 7.75 ppm correlated with that expected for the biphenyl groups, which was further corroborated with an integration (3.97 and 3.98) that closely matched the expected value of 8. Again, the successful synthesis of Biphy-DABCO SDA was confirmed, and the synthesis was repeated on a larger scale to produce enough SDA for investigations into its applications in zeolite synthesis.

The successful syntheses of these three SDAs confirmed that the choice of SDA had achieved the third of the priorities set out in the introduction. The syntheses were relatively easy, relatively cheap and were possible to produce in large amounts with high purity.

6.4.2 Using Biphenyl SDAs to Produce Zeolites

The successful synthesis of the SDAs on a large scale had indeed confirmed the choice of SDA as a suitable one. From the organic synthesis perspective, these SDAs were relatively

simple and cheap to make. However, the next step was to investigate the use of such SDAs in the formation of new zeolite frameworks.

Initial investigations were conducted by simply repeating other zeolite syntheses but using these three new biphenyl SDAs in the synthesis gel instead. The first syntheses that were inspired by ITQ-38 (**ITG**),[14] IM-12 (**UTL**),[15] IM-20 (**UWY**),[16] and ITQ-26 (**IWS**).[17] These syntheses were all used to form germanosilicates but show enough variation to evaluate the potential of these biphenyl SDAs for the formation of ADORable zeolites (Table 6.1).

Table 6.1 Shows the syntheses used to investigate the potential of biphenyl SDAs to form ADORable zeolites.

Synthesis	Ratios			Additives (T atom/Additive)	Silica Source
	Si/Ge Ratio	H_2O/T atoms	T atoms/SDAOH		
ITQ-38	3	20	4	Boric Acid (50)	Colloidal Silica
IM-12	2	25	4	-	Fumed Silica
IM-20	1.5	10	4	Fluoride (2)	Fumed Silica
ITQ-26	4	7.5	4	Fluoride (2)	TEOS

The four syntheses show a degree of variation in their Si/Ge ratio to analyse its impact on *d4r* formation, which can be promoted with different germanium content. The syntheses also vary in their water content with ITQ-38 and IM-12 having a higher water content than IM-20 and ITQ-26. These lower water syntheses are complimented with the use of hydrofluoric acid as an additive, as it is known to promote the formation of *d4r*.[18] The synthesis of ITQ-38 also included boric acid as another additive. Finally, the changing silica source may also be a potentially important factor in these zeolite syntheses. The variety of conditions and reactants in these syntheses makes them ideal for determining if the biphenyl SDAs are suitable for the formation of ADORable zeolites.

6.4.2.1 ITQ-38 Style Syntheses

The syntheses inspired by ITQ-38 involved the use of boron with the hope of seeing the impact that it would have on the successful synthesis of a zeolite (Figure 6.10).

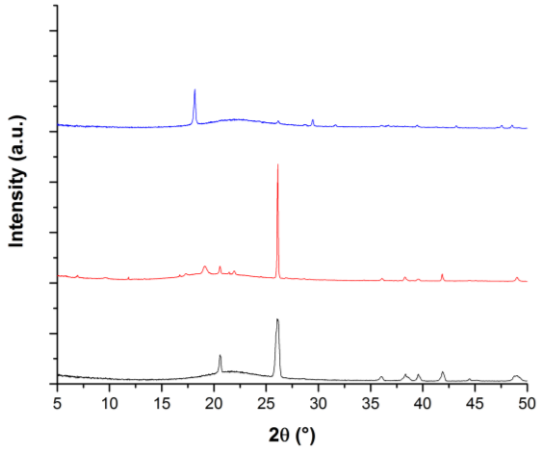

Figure 6.10 Shows the PXRD patterns for the materials obtained for Biphy-TEA (black), Biphy-DABCO (red) and Biphy-Im (blue) under the conditions that had previously been reported for the synthesis of ITQ-38. All showed dominant peaks at high angles, indicating the presence a small unit cell associated with dense phases.

The approach of using an ITQ-38 style synthesis promised very little in the way of results. The presence of very few peaks in the PXRD patterns of all three Biphy syntheses and their relatively high angle made it harder to specifically identify any structure that was formed. Biphy-TEA and Biphy-DABCO were both dominated by a peak at 26.1 ° 2θ, with additional peaks at 20.6, 36.2, 39.6, 40.3 and 41.9 ° 2θ. These peaks are clear indicators of the presence of predominantly GeO_2 in the material. Such a result clearly shows that the conditions were unsuitable for the formation of a zeolite under the conditions chosen. Biphy-Im seemed to form a different phase under these conditions. The PXRD pattern was dominated by a single peak at 18.2 ° 2θ. However, the lack of additional peaks and the amorphous character of the product were a severe hindrance for any conclusive results from a database search.

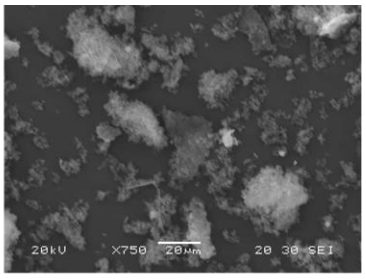

Elemental Analysis (Atomic Percent)

Spectrum	O	Si	Ge	Total
1	75.78	23.48	0.74	100
2	76.57	22.70	0.73	100
3	78.51	20.78	0.71	100
4	78.91	20.26	0.83	100
5	76.21	23.01	0.77	100
Average	77.20	22.05	0.76	

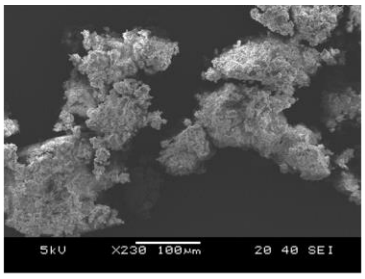

Elemental Analysis (Atomic Percent)

Spectrum	O	Si	Ge	Total
1	75.65	22.31	2.04	100
2	75.04	23.24	1.71	100
3	35.02	60.55	4.43	100
4	77.62	20.02	2.36	100
5	79.15	14.99	5.86	100
Average	68.50	28.22	3.28	

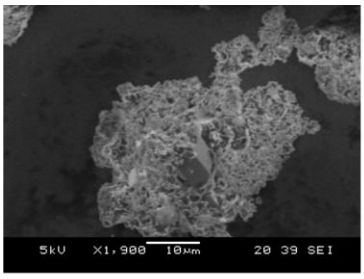

Elemental Analysis (Atomic Percent)

Spectrum	O	Si	Ge	Total
1	40.03	53.57	6.40	100
2	77.57	19.04	3.39	100
3	50.67	47.23	2.11	100
4	74.51	21.82	3.67	100
5	79.44	18.91	1.65	100
Average	64.44	32.11	3.44	

Figure 6.11 Shows the EDX and SEM analysis for (left to right) Biphy-TEA, Biphy-DABCO and Biphy-Im syntheses under similar conditions used to synthesise ITQ-38.

SEM and EDX analysis also confirmed the amorphous character of the materials obtained in this synthesis (Figure 6.11). There was an indication of some other more crystalline material in the Biphy-Im synthesis. However further repetitions of the synthesis did not result in the successful formation of the material. The relatively amorphous character of the material and the low Ge content compared to the initial synthesis gels seems to indicate that an approach like that taken for the synthesis of ITQ-38 would be unsuitable for the synthesis of ADORable zeolites. The reaction conditions were clearly subpar for the formation of any kind of high quality zeolitic material. The formation of a germanosilicate material is often aided by the presence of fluoride in the synthesis. It was therefore hoped that the syntheses inspired by IM-20 and ITQ-26 would yield more promising results.

6.4.2.2 IM-20 Style Synthesis

The syntheses inspired by IM-20 were of interest as, in comparison to ITQ-38, the synthesis involves a much lower Si/Ge ratio, a lower water content, and the use of fluoride. These three key differences would hopefully have an impact on the success of the syntheses as such an approach has already been used to produce many new low-density germanosilicates.

The initial PXRD patterns did indeed tell a very different story compared to those obtained for the ITQ-38 syntheses (Figure 6.12).

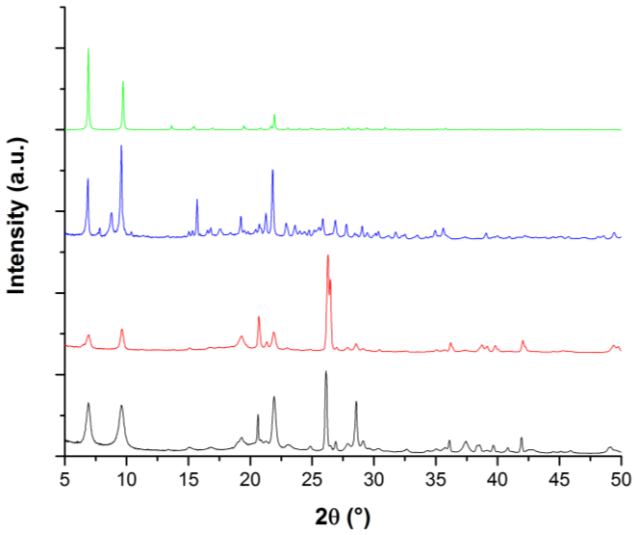

Figure 6.12 Shows the PXRD patterns for the materials obtained for Biphy-TEA (black), Biphy-DABCO (red) and Biphy-Im (blue) under the conditions that had previously been reported for the synthesis of IM-20. The generated PXRD pattern for BEC is also shown for comparison (green)

All 3 PXRD patterns showed two peaks at 6.88 ° and 9.58 ° 2θ that indicated the presence of a structure with a lower density than that obtained with the ITQ-38 synthesis. These

two peaks and the rest of the pattern showed a close correlation to an already known phase **BEC**. The results for Biphy-DABCO and Biphy-TEA showed additional peaks related to Quartz and GeO_2 (26.3 ° and 26.5 ° 2θ), while Biphy-Im seemed to show additional peaks from an impurity (7.9 ° and 8.8 ° 2θ), which could not be determined.

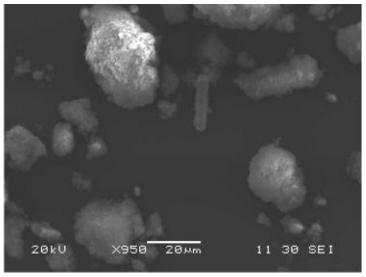

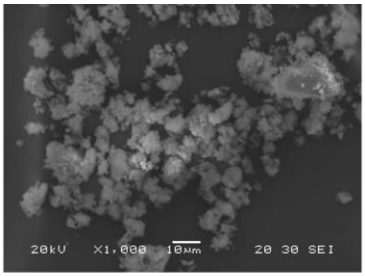

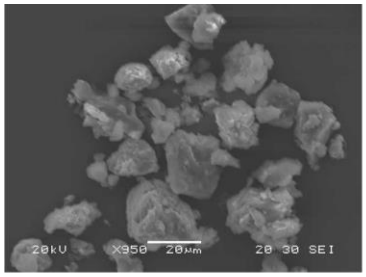

Elemental Analysis (Atomic Percent)

Spectrum	O	Si	Ge	Total
1	70.75	19.59	9.66	100
2	55.40	33.60	11.00	100
3	67.99	22.33	9.68	100
4	70.67	17.62	11.71	100
5	72.25	19.04	8.71	100
Average	67.41	22.44	10.15	

Elemental Analysis (Atomic Percent)

Spectrum	O	Si	Ge	Total
1	68.08	21.96	9.96	100
2	62.91	26.74	10.35	100
3	57.11	31.88	11.02	100
4	69.98	20.84	9.18	100
5	67.75	22.39	9.87	100
Average	65.17	24.76	10.08	

Elemental Analysis (Atomic Percent)

Spectrum	O	Si	Ge	Total
1	46.09	34.31	19.60	100
2	44.37	41.69	13.95	100
3	65.67	24.59	9.73	100
4	43.22	45.29	11.49	100
5	57.70	32.27	10.04	100
Average	51.41	35.63	12.96	

Figure 6.13 Shows the EDX and SEM analysis for (left to right) Biphy-TEA, Biphy-DABCO and Biphy-Im syntheses under similar conditions used to synthesise IM-20.

SEM and EDX analysis of the materials obtained (Figure 6.13) seemed to also confirm the results obtained for the IM-20 syntheses. Biphy-TEA seemed to show some crystals that closely resembled those previously reported for **BEC**,[19] while Biphy-DABCO showed a mostly amorphous character and Biphy-Im seemed to consist of a mixture of phases. The Si/Ge ratios for the materials were higher than that achieved in the ITQ-38 synthesis (2.21, 2.46 and 2.74 respectively). These ratios are similar to those reported for the synthesis of ITQ-17 (**BEC**) indicating that these similar synthesis conditions were leading to a similar product despite the different SDAs used.[20]

Zeolite Beta is a highly-faulted intergrowth between polymorphs A and B. **BEC** (polymorph C) is a known phase of zeolite Beta that was first reported by Liu *et al.* in 2001.[21] The structure is similar to polymorphs A and B but differs in the arrangement of the layers.[22] The polymorph C structure is generated by the recurrent application of a shear operation along both a and b axes to the Polymorph A layers when building framework. This subtle difference results in polymorph C having a completely linear three-dimensional channel system compared to polymorphs A and B where one of the channels exhibits sinusoidal properties.[23] This arrangement of the layers means that polymorph C, unlike polymorphs A and B, contains *d4r* as SBUs, the high tension in these

units is stabilised by the presence of germanium. For this reason, polymorph C was not formed under the conditions traditionally associated with zeolite Beta (traditionally Si based). Corma *et al.* were able to form pure phase **BEC** under a multitude of synthesis conditions, with the use of germanium and fluoride.[19] **BEC** was not only formed with a variety of Si/Ge ratios but also with a wide range of SDAs (Figure 6.14).

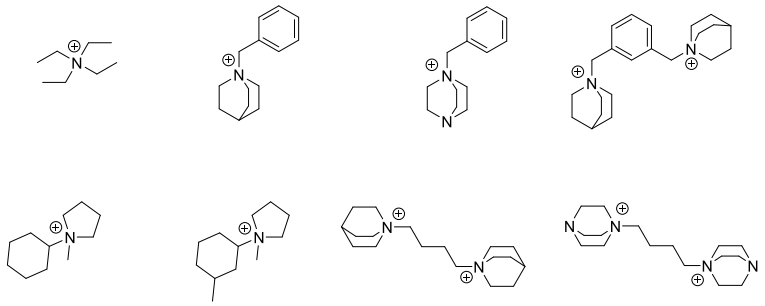

Figure 6.14 Shows the variety of SDAs used by Corma *et al.* that could achieve pure BEC with the use of Ge and fluoride.

This shows the incredible directing power of germanium and fluoride towards *d4r* and consequently towards **BEC**. Without the use of germanium or fluoride these SDAs produced a variety of SiO_2 zeolites including zeolite Beta, ITQ-4 and ZSM-12.

The prevalence of polymorph C (**BEC**) in the syntheses despite the use of different SDAs suggests that the directing effect of the SDAs was overpowered by that of the Ge and fluoride. It is of interest that Corma *et al.* reported the use of several dications with DABCOs connected by benzyl and aliphatic groups.[19] This would suggest that the Biphy-based SDAs used in this chapter are similar enough to those used by Corma *et al*. to give to give a similar framework. It is also clear that the **BEC** framework is extremely prevalent and not particularly selective with regards to the SDAs required to form it. With the high amount of Ge and fluoride used possibly playing a factor, it was hoped that other syntheses with lower amounts of these reactants could yield a different framework structure.

6.4.2.3 ITQ-26 Style Synthesis

The ITQ-26 synthesis was of interest as it used germanium and fluoride, just like IM-20. However, the synthesis uses a higher Si/Ge ratio and an even lower water content. This slight variation would be of interest as it would show how powerful the directing effect of Ge and fluoride was on the final phase. If that reported by Corma *et* al. was true then the mere presence of Ge and fluoride would lead once again to polymorph C (**BEC**).[19]

The PXRDs obtained for this material were conclusive with respect to this hypothesis (Figure 6.15).

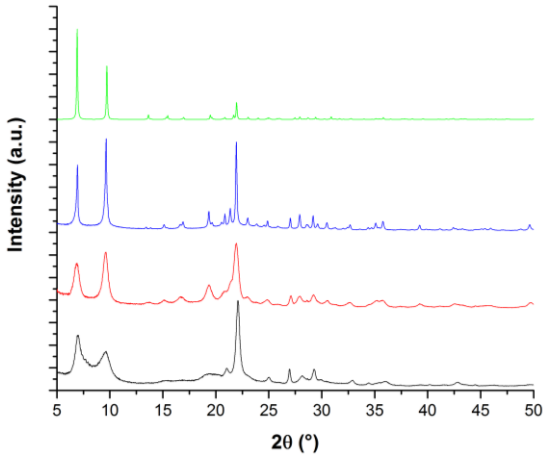

Figure 6.15 Shows the PXRD patterns for the materials obtained for Biphy-TEA (black), Biphy-DABCO (red) and Biphy-Im (blue) under the conditions that had previously been reported for the synthesis of ITQ-26. The generated PXRD pattern for BEC is also shown for comparison (green)

The PXRDs for all three biphenyl SDAs showed once again the formation of polymorph C (**BEC**). In comparison to the results with an IM-20 style synthesis the resultant materials were very pure, although there was a difference in the crystallinity of some samples. Biphy-TEA and Biphy-DABCO seemed to show a more amorphous character compared to the material obtained with Biphy-Im. This confirmed the results reported by Corma *et al*. that even a reduced Ge content of the synthesis gel would still lead to pure phase polymorph C (**BEC**).[19] This once again confirmed the overpowering effect of Ge and fluoride against the SDAs to promote the formation of a framework with a high proportion of *d4r*.

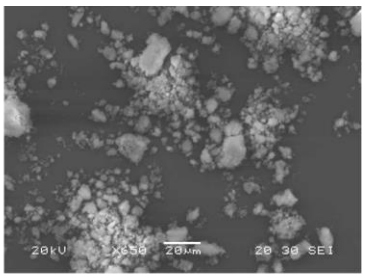

Elemental Analysis (Atomic Percent)				
Spectrum	O	Si	Ge	Total
1	70.98	23.72	5.30	100
2	70.83	23.71	5.47	100
3	69.60	24.93	5.46	100
4	60.62	32.56	6.82	100
5	65.11	28.80	6.09	100
Average	67.43	26.74	5.83	

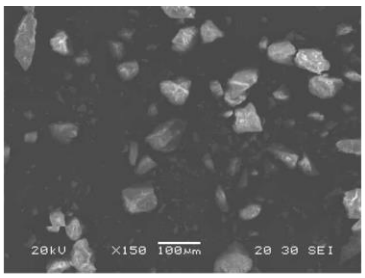

Elemental Analysis (Atomic Percent)				
Spectrum	O	Si	Ge	Total
1	55.55	37.67	6.78	100
2	66.58	27.73	5.69	100
3	65.73	28.25	6.02	100
4	73.64	21.31	5.05	100
5	71.10	23.57	5.32	100
Average	66.52	27.71	5.77	

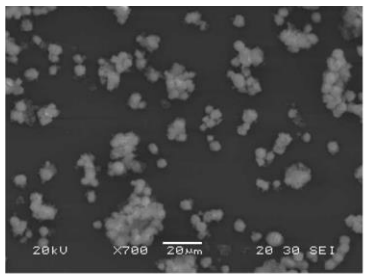

Elemental Analysis (Atomic Percent)				
Spectrum	O	Si	Ge	Total
1	55.25	39.16	5.59	100
2	66.99	26.79	6.22	100
3	70.75	23.43	5.82	100
4	71.11	22.94	5.95	100
5	69.35	24.11	6.53	100
Average	66.69	27.29	6.02	

Figure 6.16 Shows the EDX and SEM analysis for (left to right) Biphy-TEA, Biphy-DABCO and Biphy-Im syntheses under similar conditions used to synthesise ITQ-26.

SEM and EDX analysis showed similar results to those seen for the syntheses conducted using conditions for the synthesis of IM-20 (Figure 6.16). The materials seemed to show a

variation in morphology, varying from irregular crystals to a more spherical species. The Si/Ge ratios obtained for these materials were similar to the initial Si/Ge ratio of the initial gels (4.59, 4.80, 4.53), suggesting that the change in Ge content had an impact on the Ge content of the end product but was not enough to change the framework that was formed. In a similar manner to that for the IM-20 syntheses these ITQ-26 syntheses showed a prevalence for the formation of polymorph C (**BEC**) with an even greater purity and crystallinity compared to the former. No difference in phase was seen between the SDAs suggesting that either the directing effect of Ge and fluoride had overpowered the directing effect of the SDAs, or that the SDAs do not show enough dissimilarity to result in a change of phase. The crystallinity of the samples seemed to increase with the Biphy-Im SDA compared to Biphy-DABCO and Biphy-TEA, but reasons as to why were not forthcoming.

6.4.2.4 Just Silicon Synthesis

At this point the prevalence for the formation of polymorph C (**BEC**) by these three SDAs in the presence of germanium and fluoride was clear. The work by Croma *et al.* showed that very different phases were formed when purely silicon was used including zeolite Beta.[19] It was decided to investigate the products of the synthesis when only silicon was used.

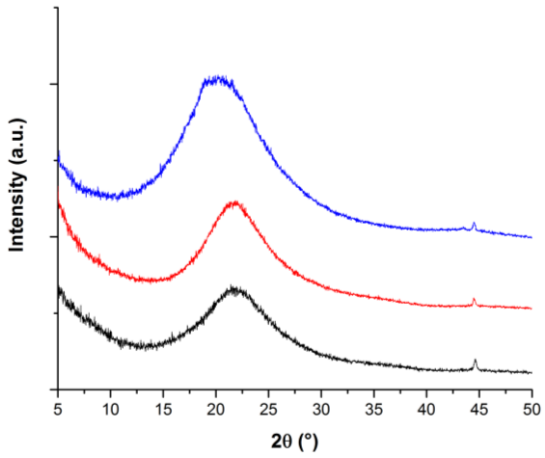

Figure 6.17 Shows the PXRD patterns for the materials obtained for Biphy-TEA (black), Biphy-DABCO (red) and Biphy-Im (blue) under the conditions that had previously been reported for the silicon-only synthesis.

The resultant PXRD patterns (Figure 6.17) clearly showed that these SDAs had not formed a different phase under the silicon-only conditions used. Such results clearly showed the need for these syntheses to be carried out with Ge being present, if a product was to be formed.

6.4.2.5 IM-12 Style Synthesis

With the formation of just Polymorph C (**BEC**) under the conditions involving the use of germanium and fluoride and the lack of any phase under a wholly silicon-based synthesis. It was decided to investigate the impact of just germanium on the synthesis. This was based on the IM-12 synthesis, which used no fluoride, a relatively large amount of germanium and an increased amount of water in the synthesis.[15] It was hoped that these factors would aid in the formation of a different phase, hopefully of a similar ADORable calibre as IM-12 (**UTL**).

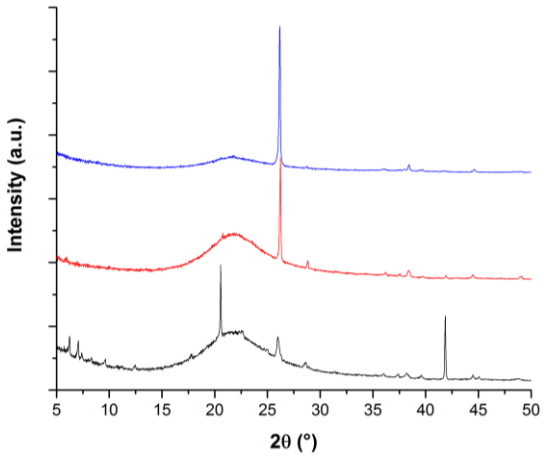

Figure 6.18 Shows the PXRD patterns for the materials obtained for Biphy-TEA (black), Biphy-DABCO (red) and Biphy-Im (blue) under the conditions that had previously been reported for the IM-12 style synthesis.

The PXRD results (Figure 6.18) showed that the synthesis had resulted in some different behaviour between these materials. Biphy-TEA seemed to show the formation of a minor phase, that looked almost like IM-12 (**UTL**), while Biphy-DABCO and Biphy-Im showed the presence of just germanium dioxide, indicating that such syntheses had not worked.

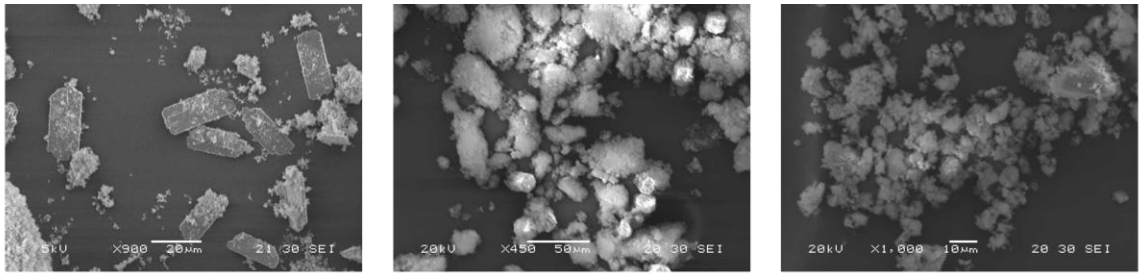

Elemental Analysis (Atomic Percent)				
Spectrum	O	Si	Ge	Total
1	62.96	33.95	3.09	100
2	68.87	27.19	3.94	100
3	73.44	24.53	2.03	100
4	51.30	46.87	1.83	100
5	74.03	24.35	1.62	100
Average	66.12	31.38	2.50	

Elemental Analysis (Atomic Percent)				
Spectrum	O	Si	Ge	Total
1	70.08	28.33	1.60	100
2	69.53	29.75	0.72	100
3	63.46	34.28	2.26	100
4	65.35	32.13	2.52	100
5	59.93	39.60	0.46	100
Average	65.67	32.82	1.51	

Elemental Analysis (Atomic Percent)				
Spectrum	O	Si	Ge	Total
1	61.94	34.71	3.35	100
2	69.29	26.94	3.76	100
3	61.19	35.30	3.51	100
4	68.71	27.79	3.49	100
5	71.49	23.94	4.57	100
Average	66.52	29.74	3.74	

Figure 6.19 Shows the EDX and SEM analysis for (left to right) Biphy-TEA, Biphy-DABCO and Biphy-Im syntheses under similar conditions used to synthesise UTL.

SEM and EDX analysis (Figure 6.19) of the materials confirmed the PXRD results; both Biphy-DABCO and Biphy-Im showed a highly amorphous character, while Biphy-TEA showed a mainly amorphous character with some crystals that showed a similar rectangular morphology to that previously seen for **UTL**. The Si/Ge ratios of these materials were quite varied (12.55, 21.73 and 7.95 respectively) perhaps indicative of the highly amorphous character of the materials. The low values obtained for Biphy-TEA suggest that the predominantly silicate material interfered with an accurate determination of the Ge content of these **UTL** crystals.

The presence of IM-12 (**UTL**) as a minor impurity in the PXRD pattern lead to a repetition of the synthesis to maximise the formation of such a phase as previously shown by the work of Shamzhy *et al*.[24] The pH was accurately measured and the reaction was monitored to see if any phases had formed (Figure 6.20).

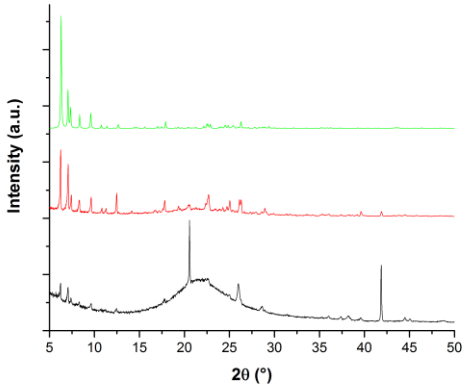

Figure 6.20 Shows the PXRD patterns for the materials obtained for the IM-12 style synthesis with the Biphy-TEA SDA including: The initial PXRD pattern (black), the repeated synthesis (red) and the expected IM-12 PXRD pattern (green).

Repetition of the synthesis using these conditions resulted in the formation of IM-12 (**UTL**). The repetition of this synthesis for the Biphy-Im and Biphy-DABCO SDAs did not result in this phase selectivity. This suggests that with regards to the synthesis of IM-12 (**UTL**) the Biphy-TEA SDA was uniquely selective for that phase compared to the others. This also showed that without fluoride the phase selectivity of Biphy-TEA changed from **BEC** to **UTL**, perhaps indicating the increased directing power of the SDA without the presence of fluoride in the synthesis. The fact that **UTL** is a germanosilicate with a lower concentration of *d4r* in its framework compared to **BEC**, as it consists of *d4r* connecting silicate layers, whereas **BEC** can be built using almost wholly *d4r*. This is indicative of the decreased direction towards the formation of *d4r* by the removal of fluoride from the synthesis.

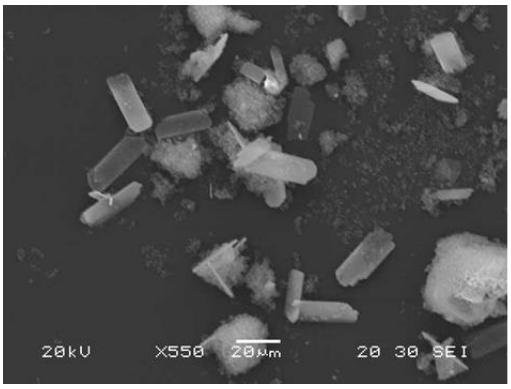

Elemental Analysis (Atomic Percent)

Spectrum	O	Si	Ge	Total
1	68.91	26.10	4.99	100
2	72.81	22.45	4.74	100
3	80.33	16.97	2.70	100
4	71.02	24.46	4.52	100
5	78.50	17.25	4.25	100
Average	74.31	21.45	4.24	

Figure 6.21 Shows the SEM/EDX analysis of the Biphy-TEA UTL. It shows the distinctive tombstone like morphology and a Si/Ge ratio similar to that expected for UTL. The extra siliceous-like material indicates that the synthesis was not completely one phase, but this impurity seems to have a relatively minor impact on the properties of the UTL.

SEM and EDX analysis (Figure 6.21) showed a dominant **UTL** phase with a minor siliceous impurity. The rectangular/platelet morphology of the crystals correlated well with that

expected for **UTL** and the Si/Ge ratio also showed a similar value for that obtained for previous **UTL** samples.[24] This showed that the germanium was incorporated into the **UTL** framework. The presence of Ge without fluoride aided the formation of a *d4r*-containing framework (**UTL**) without the drive to form *d4r* overpowering the synthesis and forming a *d4r*-dominated framework like **BEC**.

It was therefore of interest to prove that the SDA designed had indeed been incorporated into the **UTL** structure. To this end the most impressive evidence was collected using ^{13}C CP MAS NMR (Figure 6.22).

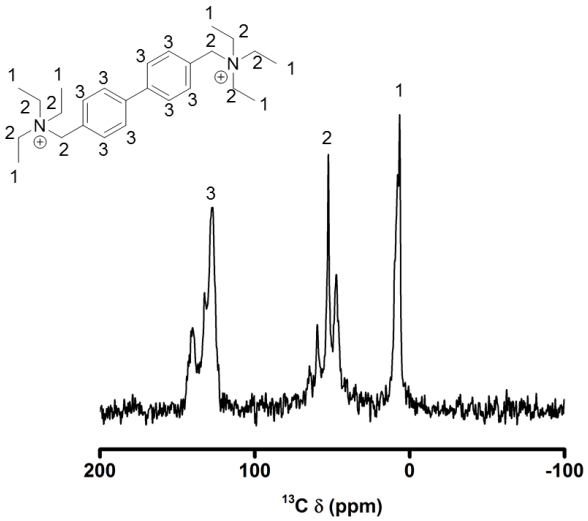

Figure 6.22 Shows the ^{13}C CP MAS NMR for the Biphy-TEA SDA present within the UTL zeolite formed. The SDA is pictured, and the corresponding environments labelled.

The ^{13}C CP MAS NMR showed three distinct environments that correlate well to that expected for the Biphy-TEA SDA, if it was intact in the framework. The first peak at 7.5 ppm corresponds well to the expected peak for the terminal CH_3 groups (peak 1). The second peak also corresponded well with the expected position for the TEA and the bridging CH_2 groups at 52.8 ppm. The final peak at 133.1 ppm also correlated well with the biphenyl CH groups. When integrated, the peaks showed values 5.2, 6.6 and 8.0 respectively. While these values are generally treated with caution as ^{13}C CP MAS NMR does not provide accurate integration values the fact that these values are close to those expected is a good indicator that the molecules are intact. More importantly the presence of the TEA C-atoms and the lack of the C-OH expected for biphenol is a clear indication that Biphy-TEA had indeed been incorporated intact into the **UTL** framework and had remained intact during this incorporation.

6.4.2.5.1 Applying the ADOR Process to Biphy-TEA UTL

Using the Biphy-TEA SDA it was possible to reproduce the already known ADORable zeolite IM-12 (**UTL**). To ensure that the **UTL** produced using this SDA was in fact an ADORable zeolite. The standard procedure for the ADOR process was then applied to a sample of the **UTL** produced by Biphy-TEA (Figure 6.23).

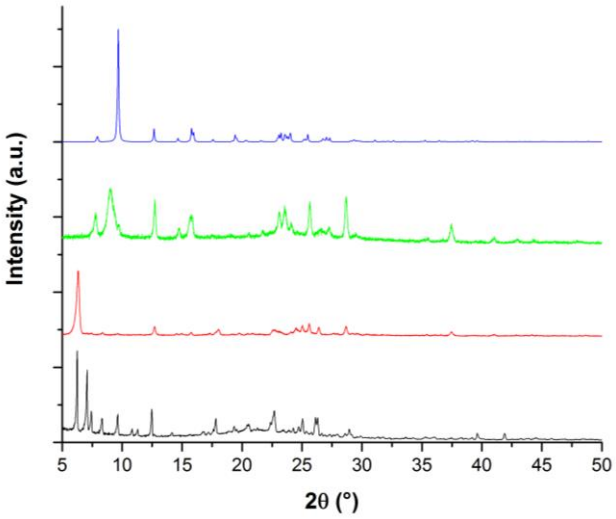

Figure 6.23 Shows the PXRD patterns for Biphy-TEA UTL (black), after treatment with 0.1 M HCl (red) and after direct calcination (green). Showing that Biphy-TEA UTL can undergo the ADOR process and form an IPC-4 type material a generated pattern of IPC-4 is shown (blue).

PXRD analysis of the samples showed that upon contact with weak acid the Biphy-TEA UTL sample underwent hydrolysis forming the IPC-1P structure, with the PXRD pattern becoming dominated by the interlayer peak (6.34 ° 2θ). Upon calcination the PXRD pattern showed that the layers had collapsed together to form a rather disordered material that correlated with the expected IPC-4 materials, perhaps more in line with IPC-1,[25] consisting of direct O-linkages between the IPC-1P layers.[4]

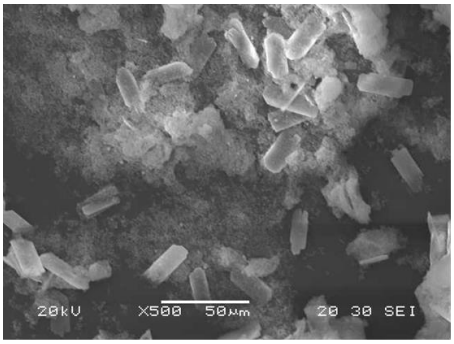

Elemental Analysis (Atomic Percent)

Spectrum	O	Si	Ge	Total
1	78.32	21.22	0.46	100
2	75.56	24.11	0.33	100
3	71.11	28.37	0.52	100
4	74.25	25.11	0.64	100
5	79.62	20.19	0.19	100
Average	75.77	23.80	0.43	

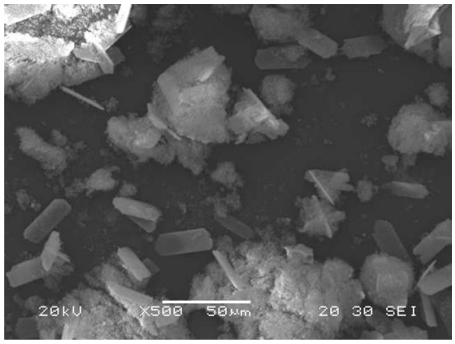

Elemental Analysis (Atomic Percent)

Spectrum	O	Si	Ge	Total
1	69.93	29.40	0.67	100
2	74.56	25.17	0.27	100
3	76.25	23.58	0.17	100
4	78.14	21.15	0.71	100
5	80.13	19.45	0.42	100
Average	75.80	23.75	0.45	

Figure 6.24 Shows the SEM and EDX analysis for hydrolysed (left) and then calcined (right) samples of Biphy-TEA UTL.

The SEM and EDX analysis (Figure 6.24) also showed a preservation of the crystal morphology with a decrease in the Ge content of the sample typically associated with the successful application of the ADOR process. A large amount of siliceous material was also noted; the presence of this material was already seen in the parent Biphy-TEA **UTL** and so had simply been unaffected by the reaction conditions during the ADOR process, but had also not had an impact on it.

This clearly showed that the use of these newly designed biphenyl SDAs were able to produce an ADORable zeolite. Unfortunately, the formation of the already known **UTL** was the result. This is perhaps unsurprising as, in a similar manner to the formation of **BEC**, many SDAs have been shown to form **UTL** under the right conditions.[26] All of these SDAs, like Biphy-TEA, were bulky, with rigid backbones and some were dications (Figure 6.25).

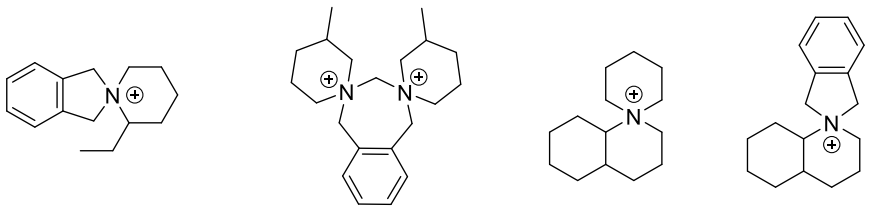

Figure 6.25 Shows some of the SDAs that have been shown to direct the formation of UTL

It seems that the formation of **UTL** is not unique to a specific SDA, 13 of the 25 SDAs tested by Schvets *et al.* formed highly crystalline **UTL**. Perhaps of interest was the C/N ratio of

Biphy-TEA (13) was close to the value of those dications that could produce **UTL**.[26] This underlines that the chosen SDA did suit the requirements for the formation of an ADORable zeolite that was able to undergo the ADOR process;[4] forming the layered IPC-1P material under weakly acidic conditions and then forming the IPC-4 structure upon calcination.

6.4.2.6 Issues Surrounding SDAs

One of the issues that was discussed when selecting a suitable SDA for zeolite synthesis was the stability of the SDA. During the synthesis of these materials it was noted that when the autoclave was removed from the oven, cooled, and opened, a lot of white solid was seen. This white solid was not removed with water but the solid was severely reduced upon contact with organic solvents like ethanol and acetone. This same material then reappeared when water was added to the filtrate. These observations hinted at the presence of an organic compound that had formed during the synthesis, since the SDAs were shown to dissolve perfectly in water and not in organic solvents. It was therefore imperative to determine the nature of the product that was formed. The solid was first isolated by filtration, dried and analysed using SEM and EDX.

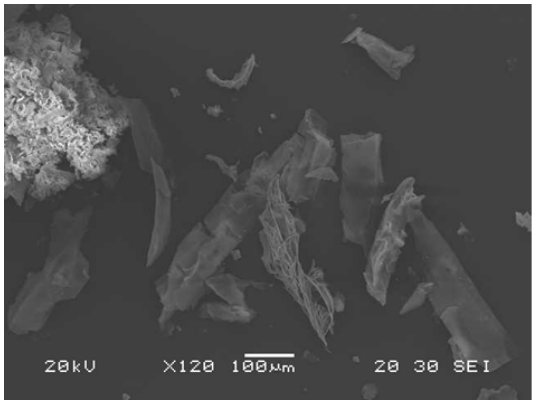

Elemental Analysis (Atomic Percent)

Spectrum	C	O	Si	Ge	Total
1	73.91	24.56	0.18	1.36	100
2	69.23	25.82	0.41	4.54	100
3	65.12	31.13	0.85	2.91	100
4	71.19	25.12	0.47	3.22	100
5	46.38	38.21	1.56	13.84	100
Average	65.17	28.97	0.69	5.17	

Figure 6.26 Shows SEM and EDX analysis of the material obtained after isolation and drying, the low content of Si and Ge hinted at the presence of some organic material, with the presence of some GeO_2.

Analysis of the material obtained showed a mixture of phases. But two dominant phases prevailed. The first phase was an amorphous material with a similar appearance to that seen for amorphous Si- and Ge-containing material (predominantly Ge). The second phase contained a large amount of carbon containing material, whose crystals appeared more platelet-like (Figure 6.26).

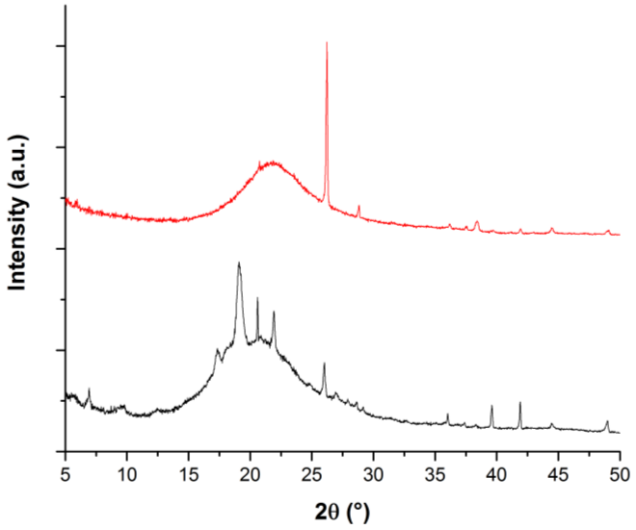

Figure 6.27 Shows the PXRD pattern for the material obtained from the filtrate before (black) and after calcination (red).

PXRD analysis of the materials also heightened suspicions that the material was mostly organic in character (Figure 6.27). The large hump between 15 and 27 ° 2θ suggested that the material was highly amorphous in character. There were some peaks observed at low angle including a large peak at about 19 ° 2θ. However, a lot of these peaks were lost after calcination perhaps indicative of the organic nature of the material, as this would have been burnt off during the calcination process. The resultant material was then dominated by a single large peak at 26.2 ° 2θ pertaining to GeO_2.

Due to the clearly organic nature of the material further investigations were conducted using NMR. The organic material was separated from the other amorphous material and then dissolved in a chlorinated solvent and studied with solution state ^1H NMR (Figure 6.28).

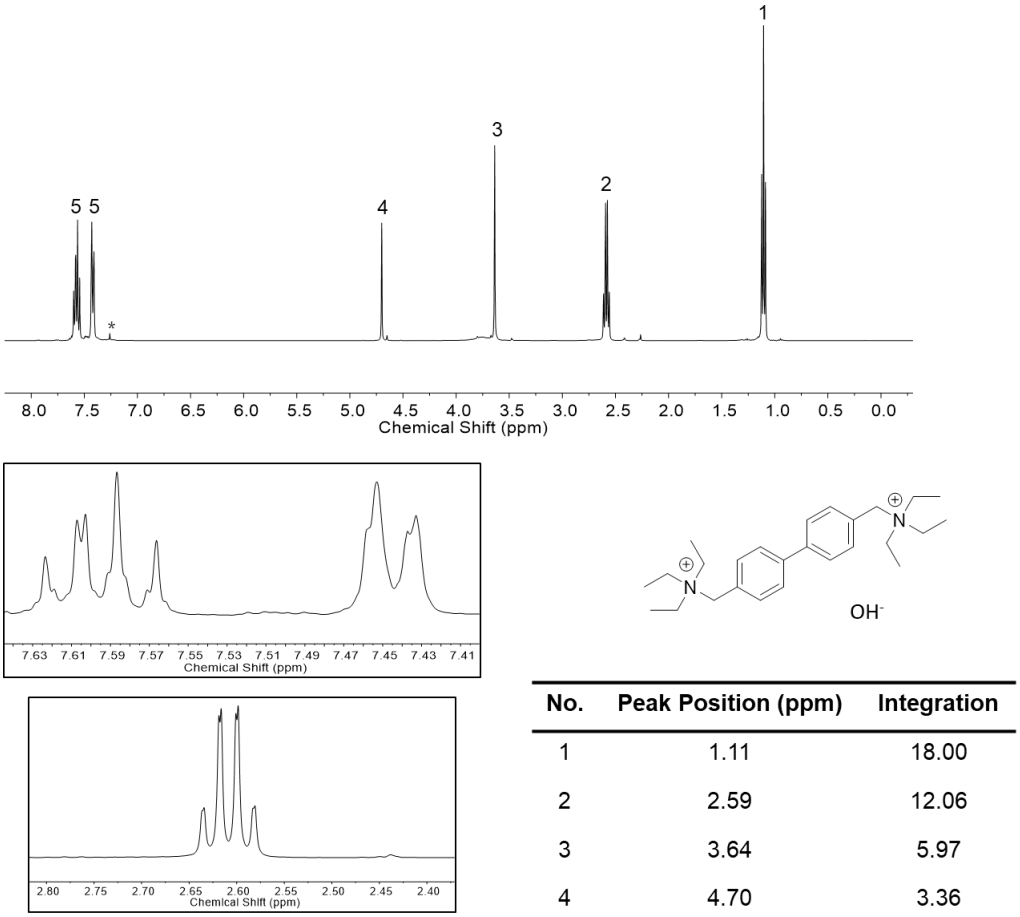

No.	Peak Position (ppm)	Integration
1	1.11	18.00
2	2.59	12.06
3	3.64	5.97
4	4.70	3.36
5	7.42, 7.57	9.48, 9.97

Figure 6.28 Shows the ^{1}H NMR of the recovered filtrate after the hydrothermal synthesis of Biphy-TEA UTL (top) with key parts of the spectrum highlighted (left), the original Biphy-TEA molecule is shown (right). $CDCl_3$ is denoted as * in the spectrum.

The most obvious change in the spectra was seen between 3.5 and 5 ppm. In the spectrum of the original material (Figure 6.7) there had been a single peak at 4.40 ppm. This peak corresponded to the CH_2 groups connecting the Biphy-backbone with the triethylamine triethylammonium cations. In the ^{1}H NMR of the material obtained from the filtrate after the hydrothermal synthesis of Biphy-TEA **UTL** there were now two peaks at 3.64 and 4.70 ppm. This indicated the presence of a new H-environment that was not present before, its position in the spectrum indicative that it was perhaps a similar group, but shifted due to a change in its surroundings. Suspicions were intensified after integration of the peaks. When the peaks with the CH_3 groups of the TEA cation were normalised to 18, the only peak with the expected integration value belonged to the CH_2 in the TEA cation at 2.59 ppm. Integration of the peaks associated with the Biphy backbone (7.42 and 7.57 ppm) resulted in a total integration of about 19.45. Looking closer at the peaks it seems that the second peak at 7.57 ppm was a combination of two different environments. Also, a closer

look at the peak at 2.59 showed that all the peaks were doubled and suggested the presence of two separate but very similar environments for the TEA-CH_2 groups. The results showed some of the SDA had under gone a change during the hydrothermal synthesis.

To ascertain the full nature of the product obtained solution state ^{13}C NMR and 2D NMR experiments were run (Figure 6.29).

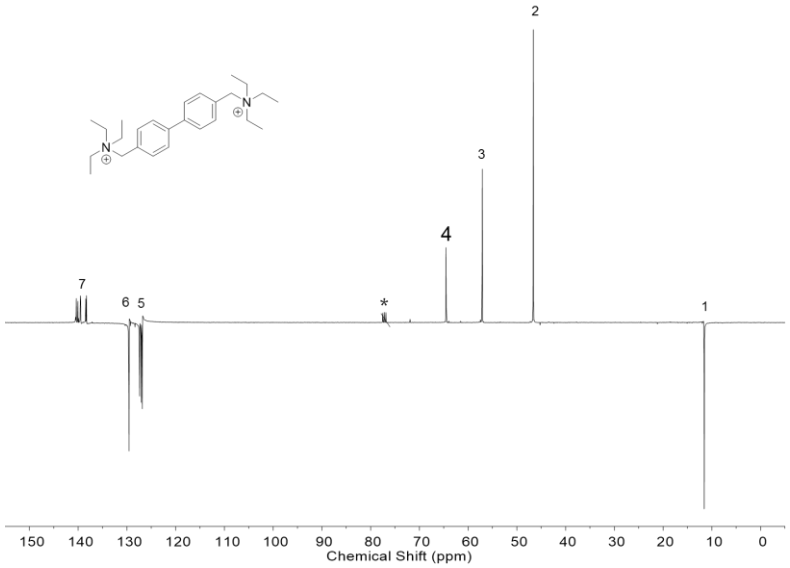

No.	Peak Position (ppm)
1	11.53
2	46.60
3	57.07
4	64.47
5	126.80
6	138.33, 139.48
7	140.03, 140.35

Figure 6.29 Shows the ^{13}C NMR spectra with multiplicity editing the peaks are numbered and $CDCl_3$ is denoted with *. The spectrum seems to confirm the same as the ^{1}H NMR, that there is a presence of an additional peak associated with a CH_2 group at 64.47 ppm.

The ^{13}C NMR confirmed the suspicion that there was indeed another new CH_2 environment present in the material analysed. The peak at 57.07 ppm seemed to confirm that there was a new environment at a higher ppm, similar to the additional peak seen in the ^{1}H NMR. This suggests that this new group was in a more deshielding environment than that associated with the CH_2 group in the original Biphy-TEA SDA. By conducting a HSQC 2D NMR experiment it was possible to match the connecting ^{13}C and ^{1}H environments (Figure 6.30). Heteronuclear single quantum correlation (HSQC) is a 2-dimensional spectrum with one axis for proton and the other for a non-proton nucleus (in this case carbon). This results in a peak for each unique proton attached to the carbon under investigation. This is achieved by the transfer of magnetisation from the proton to the carbon, after a time delay the magnetisation is then transferred back to the proton and the signal recorded. Because of this method HSQC is typically associated with a short number of bond distances.

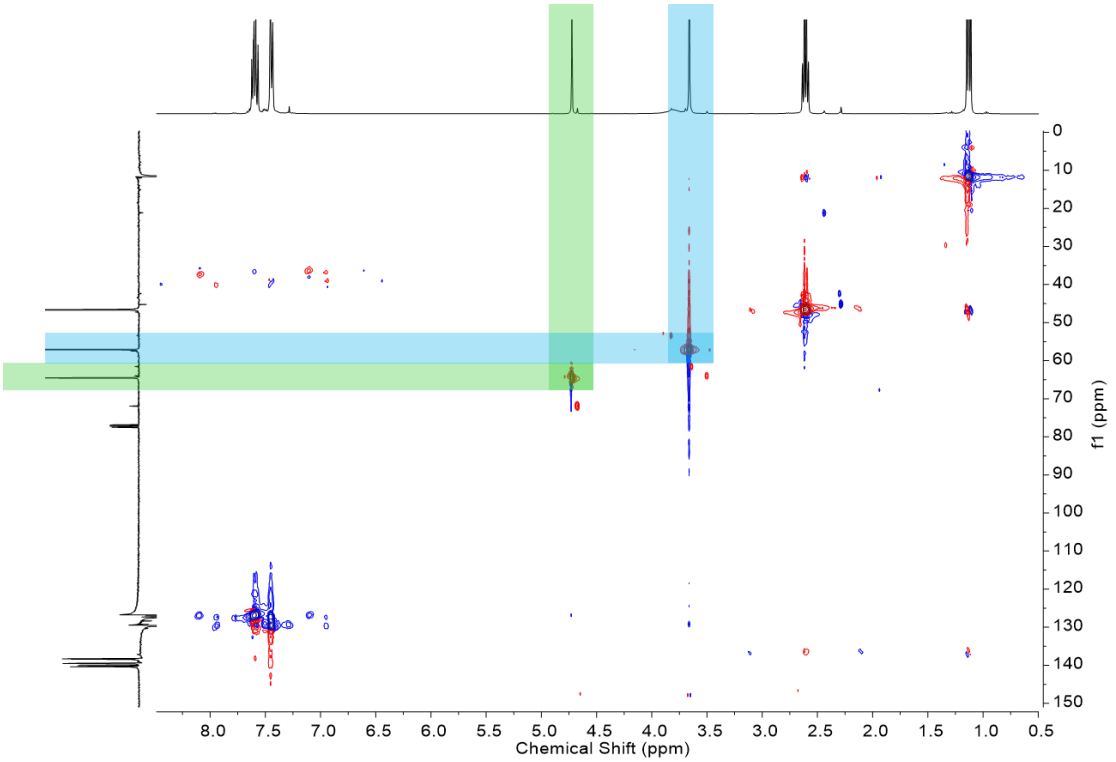

Figure 6.30 Shows the HSQC experiment conducted on the material. The two different CH_2 environment are highlighted in blue and green, confirming the correlation of the less deshielded C environment with the less deshielded H environment.

The HSQC experiment confirmed that the more deshielded CH_2 group in the ^{1}H NMR spectrum corresponded to the more deshielded group in the ^{13}C NMR spectrum. The correlation experiment also confirmed that the other environments that were already seen in the original SDA, also correlated to the expected environments in the ^{13}C NMR. The correlation experiment also further confirmed that the sample being analysed was a mixture of compounds including the original SDA.

The final experiment was a 2D heteronuclear multiple bond correlation (HMBC) experiment. HMBC typically shows correlations between protons and heteronuclei over a wider number of bonds than seen in HSQC experiments (between 2 and 4 bonds). The results of the HMBC experiment are shown in Figure 6.31.

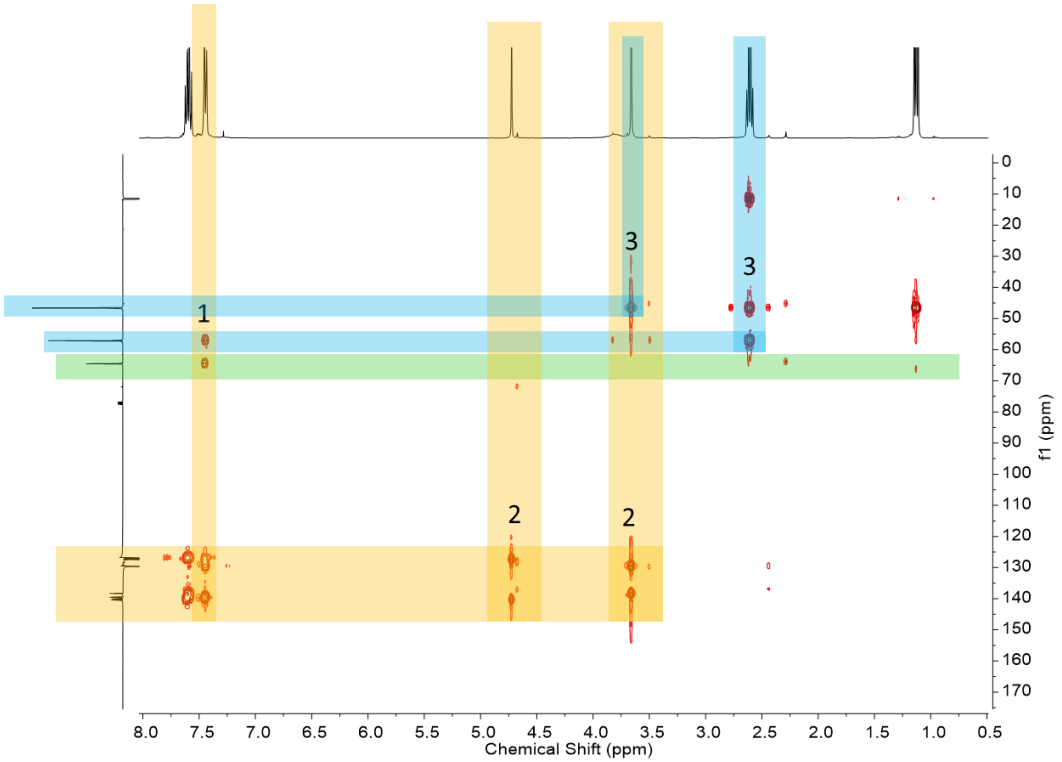

Figure 6.31 Shows the HMBC correlation experiment for the mixture obtained after the synthesis of Biphy-TEA UTL. Indicating that the CH_2 environments between 55 ppm and 75 ppm correlated to two different products. The correlations between the bridging CH_2 and biphenyl groups are highlighted in orange, the correlation between the original bridging CH_2 and the TEA CH_2 is highlighted in blue, the lack of correlation between the new bridging CH_2 group and the TEA molecule is highlighted in green.

The HMBC correlation experiment also confirmed that there was a mixture of products in the material obtained after the formation of Biphy-TEA **UTL**. The two bridging CH_2 environments in the ^{13}C NMR at 57.07 ppm and 64.47 ppm showed different correlation behaviours. Both peaks as expected showed that they were close to the H environments associated with the Biphy backbone (highlighted in orange, cross point 1). This trend was also reciprocated by the ^{13}C NMR peaks (138.33, 139.48, 140.03 and 140.35 ppm), corresponding to the biphenyl environments, showing correlation with both bridging CH_2 groups (highlighted in orange, cross points 2). However, the only peak that showed correlation with the CH_2 group in the TEA cation corresponded to original bridging CH_2 (highlighted in blue, cross point 3). The new peak also showed no such correlation with the TEA part of the molecule (highlighted in green). Such results clearly indicated the presence of a mixture of molecules in the recovered material. This included the original Biphy-TEA SDA and another product, based on the integration data from the ^{1}H NMR and the experiments it was clear that this new molecule consisted of the biphenyl backbone with a more deshielded CH_2 group. Based on these results and the knowledge of the hydrothermal conditions used it is predicted that the most likely culprit was the alcohol product [1,1'-biphenyl]-4,4'-diyldimethanol (Figure 6.32).

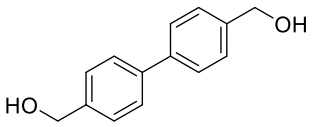

Figure 6.32 Shows the predicted impurity formed during the hydrothermal synthesis of the product.

This product would be formed by elimination of the NEt_3 groups due to attack by the hydroxide resulting in the formation of the alcohol product. Shvets *et al*. noted that methylene groups between N atoms are unstable and will often undergo Hoffman degradation in highly alkaline conditions.[26] The degradation of larger SDAs to smaller molecules has also been described by Conradsson *et al*. where they showed that DABCO decomposed to NMe_3 during hydrothermal synthesis, but did not discuss the mechanism by which it occurred. [27]

Due to the impossibility of observing the OH group in the ^1H NMR an IR spectrum for the material was obtained for this material and confirmed the suspicions indicated by the NMR (Figure 6.33).

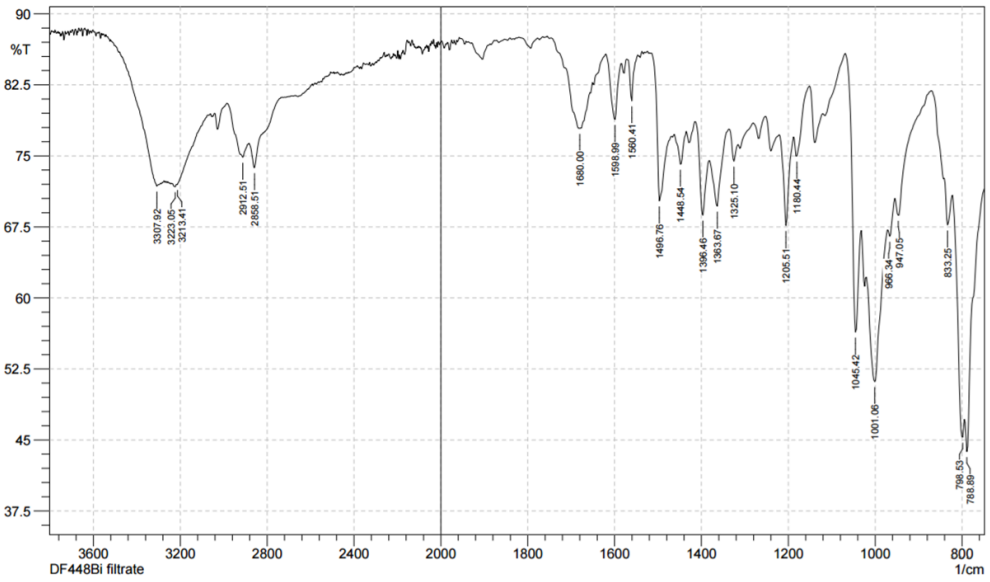

Figure 6.33 Shows the IR spectrum for the material obtained after the formation of Biphy-TEA UTL. The spectrum shows the characteristic peaks corresponding to the O-H stretch (3308, 3223 cm^{-1}), C-O stretch (1001 cm^{-1}) due to the presence of the alcohol.

The IR spectrum showed the presence of key peaks associated with the presence of an alcohol including: peaks at 3308 cm^{-1}, 3223 cm^{-1} and 1396 cm^{-1} relating to the O-H stretch and peaks at 1045 cm^{-1} and 1001 cm^{-1} relating to the C-O bond. The IR spectrum also showed peaks associated with the presence of alkane and aromatic groups including: peaks at 2913 cm^{-1}, 2859 cm^{-1}, 1449 cm^{-1} and 1364 cm^{-1} relating to the C-H alkane bond stretch, 799 cm^{-1} and 789 cm^{-1} for the C-H aromatic stretch, 1680 cm^{-1}, 1599 cm^{-1} and 1497

cm^{-1} for the C-C stretch associated with the aromatic ring. An absorption at 1206 cm^{-1} may be associated with the C-N stretch from an amine or the ammonium cation in the product.

Such results confirmed initial suspicions that some of the SDA had decomposed during the hydrothermal synthesis. The NMR data showed a mixture of the original Biphy-TEA SDA and another unknown compound. This molecule seemed to have the same biphenyl backbone and a shifted CH_2 peak. The mismatch of the integration values with the TEA CH_3 groups suggested the formation of a product without the terminal TEA cations. 2D experiments confirmed that the shifted CH_2 peak did not interact with these terminal TEA cations, but still interacted with the biphenyl groups. The molecule was confirmed to be an alcohol due to the observance of a large OH absorbance in the IR spectrum.

Confirmation of the degradation of the SDA into the alcohol may also explain some of the issue with regards to the syntheses conducted. The presence of alcohols in hydrothermal synthesis is known to have a complex and sometimes detrimental impact on the final product.[28] In particular an increasing amount of alcohol in a synthesis is known to lead to an increase in amorphous character of the product and a change in morphology. This is perhaps most obvious in the SEM and EDX results obtained for the Biphy-TEA **UTL** material. The morphology of the crystals seems to be slightly rounded in comparison to the more rectangular crystals typically expected for **UTL**. This suggests that the crystals began crystallising in a rectangular fashion but as the alcohol content increased, due to decomposition of the Biphy-TEA SDA, it started to affect the crystallisation process leading to the more rounded morphology seen. In addition, the large number of small particulates seem to indicate the increased amorphous character of the material obtained, due to the increased alcohol content leading to a decrease solubilisation of germanium- and silicon- containing species and the slower rate of crystallisation caused by the presence of the alcohol.[29] It is noted that unlike ethanol used in these previously reported syntheses the biphenyl alcohol has a higher melting point and is insoluble in water. It is suggested that the biphenyl alcohol added extraneous difficulties for zeolite synthesis as it would form and then crash out of the solution inhibiting the crystallisation process by impacting the solvation ability of silicate species and organocations. However, it is not possible to fully appreciate the full impact of this process without proper in-situ analysis.

6.5 Conclusions

This chapter reported the successful synthesis of a group of new biphenyl quaternary ammonium cations and the resultant zeolitic materials that were obtained from their use

under hydrothermal conditions. The biphenyl SDAs were selected as they seemed to fit the requirement for an organic SDA including rigidity, solubility, and stability. The synthesis of these SDAs was easily conducted using relatively cheap materials with a high yield and degree of purity. Investigations into the use of these SDAs into the synthesis of new ADORable zeolite resulted in mixed results. Syntheses that used a higher water content with boron and with just silicate resulted in amorphous and/or dense phase material. However, the use of fluoride in combination with germanium resulted in the crystallisation of a poorly defined **BEC** phase. This structure is dominated by *d4r* and has a high Ge content making it a non-ideal candidate for the ADOR process. The presence of large concentration of *d4r* also indicated that the structure directing power of the fluoride and the Ge, which tends towards the formation of *d4r*, was overpowering the directing effects of the SDAs used. Using a synthesis with Ge and no fluoride, to decrease the preference for the formation of *d4r*, resulted in the synthesis of an ADORable zeolite, but unfortunately this was an already known ADORable zeolite **UTL**. Using ^{13}C MAS NMR it was confirmed that the SDA was present in the framework and so had directed its formation. It was also shown that this form of **UTL** could also undergo the ADOR process to form an IPC-4-like structure. This confirmed that it was possible to design an SDA and synthesis to form an ADORable zeolite. Unfortunately that said ADORable zeolite was already known and has been synthesised with a wide variety of SDAs.[26] However the SDAs were also shown to be less than ideal under conditions typically associated with hydrothermal synthesis. It seemed that hydrothermal conditions lead to decomposition of the biphenyl quaternary ammonium cations into a biphenyl alcohol and the amine as observed in the NMR and IR spectra. It is believed that the formation of this alcohol would have interfered in the synthesis of the **UTL** zeolite. This lead to the slight change in the morphology of the normally rectangular **UTL** crystals and the presence of a large amount of amorphous material as this decomposition product interfered with the complex interactions between the many components of the synthesis.

6.6 Future Work

Future work should involve the formation of other SDAs based on this material with the aim of preventing its degradation.[26] Also further investigations should be conducted into the stability of these SDAs under hydrothermal conditions and the impact of the products of these SDAs on the system. Particularly the formation of amorphous material, through slowing crystallisation rates and the impact on crystal morphology. Investigations should also be conducted into the impact on the rate of decomposition by changing conditions

such as lowering synthesis temperatures, lowering pH and lowering crystallisation periods.

6.7 References

(1) Eliášová, P.; Opanasenko, M.; Wheatley, P. S.; Shamzhy, M.; Mazur, M.; Nachtigall, P.; Roth, W. J.; Morris, R. E.; Čejka, J. The ADOR Mechanism for the Synthesis of New Zeolites. *Chem. Soc. Rev.* **2015**, *44* (20), 7177–7206.

(2) Chlubná-Eliášová, P.; Tian, Y.; Pinar, A. B.; Kubů, M.; Čejka, J.; Morris, R. E. The Assembly-Disassembly-Organization-Reassembly Mechanism for 3D-2D-3D Transformation of Germanosilicate IWW Zeolite. *Angew. Chemie* **2014**, *126* (27), 7168–7172.

(3) Kasneryk, V.; Shamzhy, M.; Opanasenko, M.; Wheatley, P. S.; Morris, S. A.; Russell, S. E.; Mayoral, A.; Trachta, M.; Čejka, J.; Morris, R. E. Expansion of the ADOR Strategy for the Synthesis of Zeolites: The Synthesis of IPC-12 from Zeolite UOV. *Angew. Chemie* **2017**, *129* (15), 4388–4391.

(4) Roth, W. J.; Nachtigall, P.; Morris, R. E.; Wheatley, P. S.; Seymour, V. R.; Ashbrook, S. E.; Chlubná, P.; Grajciar, L.; Položij, M.; Zukal, A.; et al. A Family of Zeolites with Controlled Pore Size Prepared Using a Top-Down Method. *Nat. Chem.* **2013**, *5* (7), 628–633.

(5) Baerlocher, C.; McCusker, L. B. Database of Zeolite Structures http://www.iza-structure.org/databases/.

(6) Cundy, C. S.; Cox, P. A. The Hydrothermal Synthesis of Zeolites: History and Development from the Earliest Days to the Present Time. *Chem. Rev.* **2003**, *103* (3), 663–701.

(7) Cundy, C. S.; Cox, P. A. The Hydrothermal Synthesis of Zeolites: Precursors, Intermediates and Reaction Mechanism. *Microporous Mesoporous Mater.* **2005**, *82* (1–2), 1–78.

(8) Burton, A. W.; Zones, S. I. Chapter 5 - Organic Molecules in Zeolite Synthesis: Their Preparation and Structure-Directing Effects. In *Studies in Surface Science and Catalysis*; Čejka, J., Corma, A., Bekkum, H. van, Schüth, F., Eds.; Elsevier, 2007; Vol. 168, pp 137–179.

(9) Lobo, R. F.; Zones, S. I.; Davis, M. E. Structure-Direction in Zeolite Synthesis. *J. Incl.*

Phenom. Mol. Recognit. Chem. **1995**, *21* (1–4), 47–78.

(10) Davis, M. E.; Lobo, R. F. Zeolite and Molecular Sieve Synthesis. *Chem. Mater.* **1992**, *4* (4), 756–768.

(11) Zones, S. I.; Nakagawa, Y.; Lee, G. S.; Chen, C. Y.; Yuen, L. T. Searching for New High Silica Zeolites Through a Synergy of Organic Templates and Novel Inorganic Conditions. *Microporous Mesoporous Mater.* **1998**, *21* (4–6), 199–211.

(12) Lee, L.-W.; Yang, H.-M. Combination of a Dual-Site Phase-Transfer Catalyst and an Ionic Liquid for the Synthesis of Benzyl Salicylate. *Ind. Eng. Chem. Res.* **2014**, *53* (31), 12257–12263.

(13) Shibata, S.; Nagata, T.; Kourai, H.; Kume, M.; Harada, K. Novel Quaternary Ammonium Salt Compounds, Process for Producing the Same and Use Thereof. WO Patent. 2,002,060,856, 2002.

(14) Moliner, M.; Willhammar, T.; Wan, W.; González, J.; Rey, F.; Jorda, J. L.; Zou, X.; Corma, A. Synthesis Design and Structure of a Multipore Zeolite with Interconnected 12- and 10-MR Channels. *J. Am. Chem. Soc.* **2012**, *134* (14), 6473–6478.

(15) Paillaud, J.-L.; Harbuzaru, B.; Patarin, J.; Bats, N. Extra-Large-Pore Zeolites with Two-Dimensional Channels Formed by 14 and 12 Rings. *Science* **2004**, *304* (5673), 990–992.

(16) Dodin, M.; Paillaud, J. L.; Lorgouilloux, Y.; Caullet, P.; Elkaïm, E.; Bats, N. A Zeolitic Material with a Three-Dimensional Pore System Formed by Straight 12- and 10-Ring Channels Synthesized with an Imidazolium Derivative as Structure-Directing Agent. *J. Am. Chem. Soc.* **2010**, *132* (30), 10221–10223.

(17) Corma, A.; Diaz, M. J.; Rey, F.; Strohmaier, K. G.; Dorset, D. L. ITQ-26, new crystalline microporous material. US Patent. 8,114,378 B2, 2012.

(18) Pulido, A.; Sastre, G.; Corma, A. Computational Study of 19F NMR Spectra of Double Four Ring-Containing Si/Ge-Zeolites. *ChemPhysChem* **2006**, *7* (5), 1092–1099.

(19) Corma, A.; Navarro, M. T.; Rey, F.; Rius, J.; Valencia, S. Pure Polymorph C of Zeolite Beta Synthesized by Using Framework Isomorphous Substitution as a Structure-Directing Mechanism . *Angew. Chemie Int. Ed.* **2001**, *40* (12), 2277–2280.

(20) Sastre, G.; Vidal-Moya, J. A.; Blasco, T.; Rius, J.; Jordá, J. L.; Navarro, M. T.; Rey, F.; Corma, A. Preferential Location of Ge Atoms in Polymorph C of Beta Zeolite (ITQ-17) and Their Structure-Directing Effect: A Computational, XRD, and NMR Spectroscopic Study. *Angew. Chemie Int. Ed.* **2002**, *41* (24), 4722–4726.

(21) Liu, Z.; Ohsuna, T.; Terasaki, O.; Camblor, M. A.; Diaz-Cabañas, M. J.; Hiraga, K. The First Zeolite with Three-Dimensional Intersecting Straight-Channel System of 12-Membered Rings. *J. Am. Chem. Soc.* **2001**, *123* (22), 5370–5371.

(22) Newsam, J. M.; Treacy, M. M. J.; Koetsier, W. T.; Gruyter, C. B. D. Structural Characterization of Zeolite Beta. *Proc. R. Soc. A Math. Phys. Eng. Sci.* **1988**, *420* (1859), 375–405.

(23) Goretsky, A.; Beck, L.; Zones, S.; Davis, M. Influence of the Hydrophobic Character of Structure-Directing Agents for the Synthesis of Pure-Silica Zeolites. *Microporous Mesoporous Mater.* **1999**, *28* (3), 387–393.

(24) Shamzhy, M. V; Shvets, O. V; Opanasenko, M. V; Yaremov, P. S.; Sarkisyan, L. G.; Chlubná, P.; Zukal, A.; Marthala, V. R.; Hartmann, M.; Čejka, J. Synthesis of Isomorphously Substituted Extra-Large Pore UTL Zeolites. *J. Mater. Chem.* **2012**, *22* (31), 15793.

(25) Roth, W. J.; Shvets, O. V.; Shamzhy, M.; Chlubná, P.; Kubů, M.; Nachtigall, P.; Čejka, J. Postsynthesis Transformation of Three-Dimensional Framework into a Lamellar Zeolite with Modifiable Architecture. *J. Am. Chem. Soc.* **2011**, *133* (16), 6130–6133.

(26) Shvets, O. V; Kasian, N.; Zukal, A.; Pinkas, J.; Čejka, J. The Role of Template Structure and Synergism Between Inorganic and Organic Structure Directing Agents in the Synthesis of UTL Zeolite. *Chem. Mater.* **2010**, *22* (11), 3482–3495.

(27) Conradsson, T.; Dadachov, M. . S.; Zou, X. . D. Synthesis and Structure of $(Me_3N)_6[Ge_{32}O_{64}]\cdot(H_2O)_{4.5}$, a Thermally Stable Novel Zeotype with 3D Interconnected 12-Ring Channels. *Microporous Mesoporous Mater.* **2000**, *41* (1–3), 183–191.

(28) Huang, Y.; Yao, J.; Zhang, X.; Kong, C. (Charlie); Chen, H.; Liu, D.; Tsapatsis, M.; Hill, M. R.; Hill, A. J.; Wang, H. Role of Ethanol in Sodalite Crystallization in an Ethanol–Na_2O–Al_2O_3–SiO_2–H_2O System. *CrystEngComm* **2011**, *13* (14), 4714.

(29) Cheng, C.-H.; Shantz, D. F. Silicalite-1: Growth from Clear Solution: Effect of

Alcohol Identity and Content on Growth Kinetics. *J. Phys. Chem. B* **2005**, *109* (41), 19116–19125.

7 *A Priori* Design of a 'Propagated' Synthesis Forming an Isoreticular Family of Zeolites

7.1 Aim

This chapter will discuss the first *a priori* design and synthesis of an ADORable zeolite, by traditional hydrothermal synthesis, and its subsequent propagation to produce its daughters, producing a new isoreticular family of zeolites. The design principles taken into consideration will be discussed and the parent germanosilicates' structural and chemical properties fully characterised, including its suitability for the ADOR process. This single parent germanosilicate will then be propagated to form several new daughter products, with their differing framework and chemical properties discussed.

7.2 Introduction

As discussed in the previous chapter, both hydrothermal synthesis and the ADOR process have helped advance the field of zeolite synthesis. Hydrothermal synthesis has resulted in the synthesis of many highly crystalline materials.[1,2] However hydrothermal synthesis has been shown to have one major disadvantage, especially when it comes to the synthesis of new materials. The reversibility of crystallisation has resulted in the hydrothermal system being able to avoid higher energy arrangements. This has led to the now infamous zeolite conundrum, best illustrated by the energy-density correlation that is seen for hydrothermally prepared zeolites (Figure 7.1).[3–5]

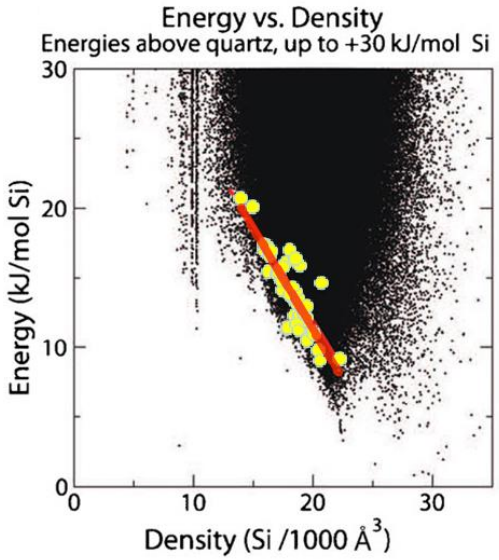

Figure 7.1 Shows an Energy vs. Density plot for computationally predicted zeolite structures, known zeolite structures are shown in yellow with the linear fit highlighted in red. Adapted from reference 4.

The presence of all currently known zeolites on a specific gradient of energy vs density indicated that a large majority of theoretical zeolite structures were completely unattainable as a result of the use of traditional hydrothermal synthesis.[5–8] Attempts to vary hydrothermal synthesis, including the use of ionothermal and low water syntheses,[9] proved unable to produce structure beyond the energy vs density gradient.

7.2.1 The ADOR Process

The ADOR process has shown the most promise in providing an alternative route for the synthesis of new zeolite framework structures.[10,11,12] The method has now resulted in the formation of 8 new high silica zeolites (Table 7.1), unattainable by traditional hydrothermal synthesis. Take into consideration that there are only 50 unique high silica zeolite frameworks currently known, this represents an almost 20% success rate in 4 years, and compares favourably to hydrothermal synthesis, which has already had 60 years.[11,13–15]

Table 7.1 Shows the currently known ADORable germanosilicate frameworks (left) and their resultant daughter zeolites (right).

Parent Zeolite	ADOR Daughters
UTL	IPC-2, IPC-4, IPC-6, IPC-7, IPC-9, IPC-10
IWW	IPC-5
UOV	IPC-12

Not only has the ADOR process been used to synthesise new unique high silica zeolite frameworks, but it has been used to synthesise the first 'unfeasible' zeolites.[12] IPC-9 and IPC-10 were formed using choline hydroxide to arrange a shift in the silicate layers. These shifted layers after reassembly produce two new daughter zeolites with odd membered rings. IPC-9 and 10 are both more strained zeolite structures farther to the right of the energy vs density line than zeolites synthesised by traditional hydrothermal synthesis.

However, the ADOR process has been shown to have some sever limitations. As discussed in previous chapters the ADOR process requires a very specific set of framework properties of the parent germanosilicate. Even those that were singled out as potential ADORable zeolites were found to be non-ideal candidates for the process (Chapter 5).

7.2.2 The Approach

To advance the synthesis of new zeolitic materials the issues surrounding both traditional hydrothermal synthesis and the newer ADOR process need to be confronted. By combining the two methods it was hoped that it would be possible to overcome the issues that both syntheses have. The use of traditional hydrothermal synthesis (with a new SDA) could produce a new parent germanosilicate and then the ADOR process could be applied to propagate that synthesis and increase the number of new zeolites. Instead of one new hydrothermal synthesis producing one new zeolite, combining these two techniques, it could be possible to produce three or more new zeolites. Previous attempts to synthesise a new germanosilicate using a new SDA were partially successful (Chapter 6). It was hoped that by using a different SDA and a more systematic approach to the design of the synthesis a new parent germanosilicate could be synthesised.

7.2.3 Design Principles

To combine these two methods, it was a priority to first consider the key characteristics of hydrothermal synthesis to outline the correct principles and factors to make the approach a success. To design, *a priori*, a hydrothermal synthesis that will produce a material suitable for further manipulation using the ADOR process it is vital to increase the likelihood of producing the necessary structural and compositional features in the final product that would make it an ADOR candidate.

The formation of Ge-dominated *d4r* units is promoted through the addition of germanium to a zeolite synthesis. The likelihood of producing *d4r* units can be enhanced further through minor adjustments to the chemical synthesis. Firstly, the use of fluoride also promotes the formation of *d4r* units. The addition of fluoride also aids in the formation of

larger pores as the synthesis gel becomes less alkaline. This is because higher alkalinity will often lead to a smaller pored zeolite, as the larger pores are more unstable under highly alkaline conditions.[16] The sources of silica can also aid in the promotion of *d4r* different silica sources have differing rates of reactivity, if a silica source is used, and is too reactive, it could override the *d4r* driving power of germanium leading to the formation of a zeolite without any *d4r* units.[17] The final and most important part of the design concept step is the use of the correct organic SDA. The use of a bulky large SDA allows for the promotion of *d4r* units and large pores as the zeolite accommodates the SDA molecule.[18,19] The SDA should also not be too large as a small charge to mass ratio leads to the SDA being unable to dissolve into the synthesis gel.[20]

7.2.4 The Design

Taking all these factors into consideration a set of synthesis conditions were designed that would be ideal for the synthesis of a perfect candidate parent germanosilicate. The SDA that was ideal for such a synthesis was determined to be a naphthalene derivative 1-methyl-3-(naphthalen-1-ylmethyl)-imidazolium cation. The SDA was based on a previously known SDA (1-methyl-3-(naphthalen-2-ylmethyl)-imidazolium cation) that was used to produce the germanosilicate NUD-1. Both SDAs combined the large bulky naphthalene sub-unit with the cationic charge of the imidazolium subunit. The presence of both units together formed a particularly rigid body organic SDA. It was therefore of interest to see if the movement of the imidazolium cation from the 2- to the 1-position would change the space-filling and Van der Waals requirements on the synthesis and result in a different framework.[21]

With the ideal organic SDA candidate selected it was also key to ensure that the ideal synthesis conditions were also used. This included the use of a large amount of germanium oxide and hydrofluoric acid, to promote the formation of *d4r* units and large pores.

7.3 Experimental Section

7.3.1 Synthesis of the Organic SDA

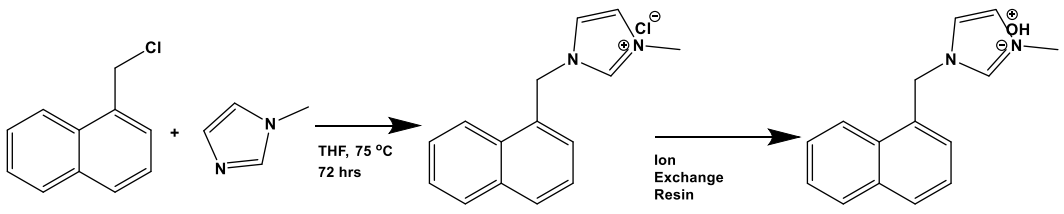

Figure 7.2 Shows the synthesis procedure for the designed SDA 1-methyl-3-(naphthalen-1-ylmethyl)-imidazolium hydroxide

The desired SDAOH was synthesised as shown in Figure 7.2. 1-(chloromethyl)naphthalene (58.43 g, 330 mmol) was placed in THF (250 mL) with subsequent addition of a stoichiometric amount of 1-methyl-1H-imidazole (31.35 mL, 330 mmol) and refluxed for 3 days. The resulting white solid was filtered and washed with more THF and allowed to dry overnight yielding a white solid, which was determined pure by ^{1}H and ^{13}C NMR (yield= 72.5 g, 84.9 %). ^{1}H NMR (400 MHz, Deuterium Oxide) δ 8.39 ppm (*s*, 1H), 7.81 ppm (*m*, 2H), 7.70 ppm (*m*, 1H), 7.44 - 7.39 ppm (*m*, 4H), 7.23 - 7.19 ppm (*m*, 2H), 5.55 ppm (*s*, 2H), 3.60 ppm (*s*, 3H). ^{13}C NMR (126 MHz, Deuterium Oxide) δ 135.41, 133.32, 130.19, 130.09, 128.82, 128.77, 128.07, 127.34, 126.41, 125.52, 123.35, 122.06, 121.84, 50.20, 35.45.

The chloride salt was then converted to the hydroxide salt by anion exchange. The final concentration of the ion exchanged SDAOH solution was determined by titration with HCl (0.1 M), the yields of the ion exchange were over 90 %.

7.3.2 Investigating the Synthesis of Parent Germanosilicate

The synthesis of the zeolite consisted of adding germanium oxide to a stirring solution of the anion exchanged SDA-OH. After 30 minutes tetraethyl orthosilicate or Cab-O-Sil™ was added and the solution stirred overnight to allow for hydrolysis of the TEOS and/or loss of water. HF solution was then added, and the gel was stirred to reach the desired water ratio by evaporation. Once the desired molar composition had been reached the resultant white paste was placed in a Teflon-lined autoclave and heated at 150 °C for 14 days. The final product was then filtered and washed with distilled water and finally a small amount of ethanol. This synthesis procedure was used with varying amounts of the reactant to produce a wide range of reaction mixture compositions with varying different reactant molar ratios.

7.3.3 Example Syntheses

7.3.3.1 Example Synthesis of SAZ-1

The synthesis of the zeolite consisted of adding germanium oxide (1.046 g, 10 mmol) to a stirring solution of the anion exchanged SDAOH (10 mmol). After 30 minutes Cab-O-Sil™ (1.202 g, 20mmol) was added and the solution stirred overnight to allow for hydrolysis of the loss of water. HF (48 %) solution (0.725 mL, 20 mmol) was then added and the gel was allowed to reach the desired water ratio by evaporation resulting in a final molar composition of 1 SiO_2 : 0.5 GeO_2 : 1 SDAOH : 1 HF : 15 H_2O. The resultant white paste was placed in a Teflon lined autoclave and heated at 150 °C for 14 days. The final product was then filtered and washed with distilled water (approx. 1 L) and finally a small amount of

ethanol. The product was then calcined at 575 °C to produce the SDA-free germanosilicate.

7.3.3.2 Synthesis of SAZ-1P

The calcined zeolite (0.50 g) was placed in 0.1 M HCl (100 mL) and heated at 95 °C for 16 hours. The resultant solid was filtered, washed with distilled water, and dried. The recovered product is named SAZ-1P (yield = 0.324 g).

7.3.3.3 Synthesis of SAZ-2

For SAZ-2 hydrolysed SAZ-1 (0.324 g) was placed in octylamine (20 mL). This was then stirred at 70 °C for 3 hours followed by room temperature overnight. The product was then filtered, washed, and calcined at 575 °C (yield = 0.242 g).

7.3.3.4 Synthesis of SAZ-3

For SAZ-3 hydrolysed SAZ-1 (0.324 g) was placed in an autoclave containing nitric acid (1 M, 20 mL) and diethoxydimethylsilane (0.05 g) stirred at room temperature for 10 minutes and heated at 175 °C for 16 hours. The product was then filtered and washed with water and calcined at 575 °C (yield = 0.234 g).

7.3.3.5 Synthesis of Al-SAZ-1P

Al-SAZ-1P was prepared by placing calcined SAZ-1 (0.50 g) in a mixture of acetic acid (1 M, 75 mL) and aluminium nitrate (1 M, 50 mL) and was then refluxed at 95 °C for 16 hours. The product was then filtered and washed with 0.01 M acetic acid (yield = 0.349 g).

7.3.3.6 Synthesis of Al-SAZ-2

Al-SAZ-1P (0.175 g) was stirred in dilute HCl (0.01 M, 15 mL) for ten minutes at room temperature. This was then filtered and dried before being placed in octylamine (5 mL) and heated at 75 °C for 3 hours. This was followed by subsequent stirring at room temperature for a further 16 hours. The product was then filtered and dried before then being calcined at 575 °C (yield = 0.139 g).

7.3.3.7 Synthesis of Al-SAZ-3

Al-SAZ-1P (0.175 g) was placed in an autoclave containing nitric acid (1 M, 10 mL) and diethoxydimethylsilane (0.05 g) stirred at room temperature for 10 minutes and heated at 175 °C for 16 hours. The product was then filtered and washed with water and calcined at 575 °C (yield = 0.153 g).

7.3.3.8 Acid Site Formation of Al-SAZ-2 and Al-SAZ-3

The zeolite (0.100g) was added to an aqueous solution of ammonium chloride (0.3 M, 10 mL) and stirred at room temperature overnight. The product was then filtered and allowed to dry (this process was then repeated three times). The sample was then calcined at 575 °C (yield= 0.094 g).

7.3.3.9 Copper Site Formation of Cu-Al-SAZ-2 and Cu-Al-SAZ-3

The Zeolite (0.100g) was added to a stirring solution of Copper nitrate solution (0.3 M, 100 mL) and heated under reflux for 16 hours. The resultant solid was then filtered, washed with water, and dried overnight to yield a faintly blue product (0.899 g, 89.9 %).

7.3.3.10 Synthesis of SAZ-1PS

SAZ-1PS was prepared by placing calcined SAZ-1P (0.50 g) in a solution of choline hydroxide/chloride (50 wt. %, 1.3 moldm^{-3} with respect to OH^-, 25 mL) and stirring at room temperature for 5 hours. The product was then filtered and washed with a small amount of water and then allowed to dry (yield = 0.495 g).

7.3.3.11 Synthesis of SAZ-2S

SAZ-2S was prepared by taking SAZ-1PS (0.200 g) and calcining at 575 ˚C (yield = 0.196 g).

7.3.3.12 Synthesis of SAZ-3S

SAZ-1PS (0.200 g) was placed in an autoclave containing nitric acid (1 M, 10 mL) and diethoxydimethylsilane (0.05 g) stirred at room temperature for 10 minutes and heated at 175 °C for 16 hours. The product was then filtered and washed with water and calcined at 575 °C (yield = 0.151 g).

7.4 Results and Discussion

7.4.1 Initial Investigations into Synthesis of Parent Germanosilicate

Taking the design principles discussed into account the naphthalene derivative 1-methyl-3-(naphthalen-1-ylmethyl)-imidazolium cation was selected and synthesised according to a similar procedure reported by Chen *et al*.[21]

7.4.2 Synthesis of SAZ-1 Germanosilicate

A series of reactions were conducted varying the molar ratios of various reactants. It was hoped that by conducting the reaction under the same conditions, but with the reaction gel mixture adjusted an optimal synthesis mixture and procedure could be achieved. The gel mixtures were varied per their water content, ratio of fluoride to T atoms, ratio of Ge/Si and the source of silica (Table 7.2). The SDAOH remained constant compared with the

HF, to maintain the reaction gels at a relatively low pH typically required for the synthesis of large pore zeolites.

Table 7.2 Shows the synthesis conditions explored during the synthesis of SAZ-1. The H_2O/T,HF/T and Ge/Si ratios of the gel compositions is shown (SDAOH/HF ratio was 1 and remained constant throughout) and the source of silicon used. The resultant phases are then highlighted (D = Dominant phase, I = Impurity/Minor phase and blank = Not present)

Sample	H_2O/T	HF/T	Ge/Si	Si Source	SAZ-1	LTA	Amorphous
DF301A	6.6667	0.66667	0.5	Fumed Silica	D		
DF301B	6.6667	0.66667	0.5	TEOS	D	I	
DF311A	5	0.5	1	Fumed Silica	D		I
DF311B	5	0.5	1	TEOS	D	I	I
DF312A	10	0.5	1	Fumed Silica	D		I
DF312B	10	0.5	1	TEOS	I		D
DF313A	15	0.5	1	Fumed Silica			D
DF313B	15	0.5	1	TEOS			D
DF318A	17.77778	0.88889	0.125	Fumed Silica	I		D
DF318B	17.77778	0.88889	0.125	TEOS		I	D
DF319	8.8889	0.88889	0.125	TEOS			D
DF320	8	0.8	0.25	TEOS		D	I
DF321	16	0.8	0.25	TEOS			D
DF326	10	1	0	TEOS			D
DF344	4	0.4	0.25	TEOS	I	I	D
DF346A	10	0.66667	0.5	Fumed Silica	D		
DF346B	10	0.66667	0.5	TEOS	D	I	
DF359	6.6667	0.66667	0.3333	TEOS		I	D
DF360	10	0.66667	0.3333	TEOS	I	D	I
DF361	6.6667	0.33333	0.3333	TEOS		I	D
DF362A	10	0.33333	0.5	Fumed Silica	I		D
DF362B	10	0.33333	0.5	TEOS	I	D	I
DF363	8	0.4	0.25	TEOS		I	D
DF366A	7.50	0.50	1	Fumed Silica	D		
DF366B	7.5	0.5	1	TEOS	I	D	
DF367	11.6667	0.58333	0.75	TEOS	I	D	
DF368	13.33	0.667	1	TEOS			D
DF369	8.88889	0.88889	0.5	TEOS			D
DF370A	16	0.8	0.6	Fumed Silica	I		D
DF370B	16	0.8	0.6	TEOS		D	
DF371A	13.3333	0.66667	0.5	Fumed Silica	D		I
DF371B	13.333	0.66667	0.5	TEOS		I	D
DF373	10	0.6667	0.6	TEOS		D	
DF374A	8.00	0.80	1	Fumed Silica	D		
DF374B	8	0.8	0.6	TEOS		D	
DF375A	6.67	0.67	1	Fumed Silica	D		I
DF375B	6.6667	0.66667	0.75	TEOS		D	I
DF379	10	1	0.5	TEOS		D	I
DF380A	17.7778	0.6667	0.5	Fumed Silica			D
DF380B	17.7778	0.6667	0.5	TEOS	I		D
DF381	6.667	0.6667	0.25	TEOS		D	I
DF391A	6.6667	1	0.5	Fumed Silica	D		I
DF391B	6.667	1	0.5	TEOS			D

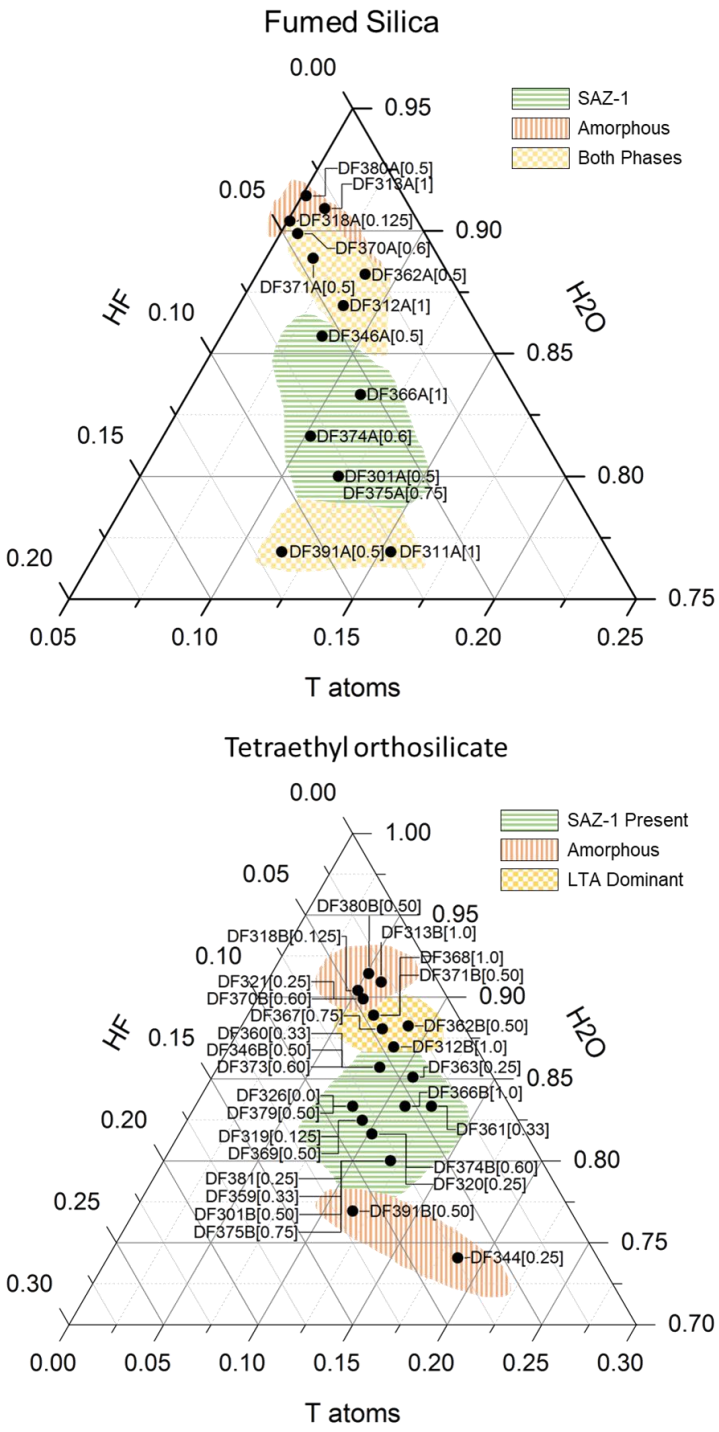

Figure 7.3 Shows two ternary plots for those syntheses conducted with fumed silica (top) and TEOS (bottom). Both plots compare the ratio of T atoms, HF and H_2O. The Ge/Si ratio is also shown next to the sample number (for example DF344 [0.25] represents a Ge/Si ratio of 0.25). The plots clearly show a distinct difference between the behaviours of the silica sources, but also shows the effect of gel composition on the product composition.

From the initial PXRD patterns obtained, there was the strong indication of the formation of a new material (later identified as SAZ-1). It was clear that this new phase was only present over a narrow range of synthesis conditions and so the changing reaction gel ratios did have an impact on the resultant product formed (Figure 7.3).

7.4.2.1 The Role of Silica Source

Initial investigations first involved the use of TEOS before moving on to the use of fumed silica. The most notable trend seen when comparing the ternary plots is the clear difference between these two different silica sources (Figure 7.3). Both silica sources show a similar range where the synthesis conditions would lead to a new crystalline phase (SAZ-1). However, when TEOS was used another phase (**LTA**) appeared as an impurity or as the dominant phase in the final product.

The presence of **LTA** in a lot of resultant products was interesting due to its framework properties. **LTA** (Linde Type A) is a well-known zeolite with its structure known as early as 1956.[22] The **LTA** framework code includes about 15 related materials including SAPO-42, [Ga-P-O]-LTA and the germanosilicate ITQ-29.[23–25] The **LTA** framework consists of 8 *sod* cages arranged in a cube connected by sharing *s8r* and surrounding a central *lta* cage. These central *lta* cages are connected to 8 other *lta* cages by *d4r* in all directions. This structure is therefore not able to undergo the ADOR process as all T-atoms are connected to a *d4r* unit, making it impossible to have stable silicate layer after their removal.

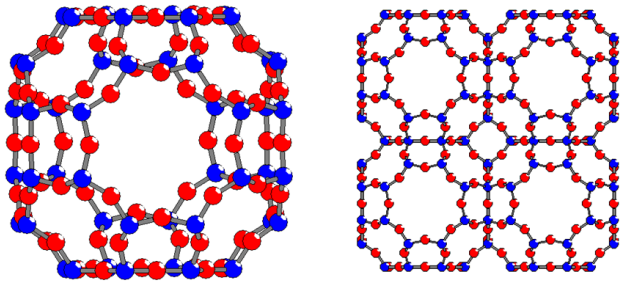

Figure 7.4 Shows the *sod* cage structure (left), 8 *sod* cages are then combined in a cubic fashion, connected by shared *s8r* surrounding a central *lta* cage (right). This *lta* cage is connected to other *lta* by *d4r* in all directions this means that LTA in unable to undergo the ADOR process and so is an undesired product.

It is already known that the source of silica has a huge impact on the crystal size and morphology, but there is very little evidence of selectivity of phases with the two different silica sources used, although the aluminium content of silica sources is shown to play a key role. While TEOS and fumed silica do not differ hugely in their aluminium content, their relative solubilities are vastly different. TEOS has a larger surface area than fumed silica as the silica is provided in a molecular form, $Si(OC_2H_5)_4$, and so dissolves faster into solution than fumed silica, which has a much lower surface area and so takes longer to dissolve.[17,26]

As previously mentioned in the experimental the reaction mixture was stirred to allow the correct water content to be reached before the addition of hydrofluoric acid. This means the silica source was stirred in a higher pH solution. The pH was then reduced by the addition of hydrofluoric acid before the reaction was placed in the oven. Generally, it is found that at higher pH, the silicate species most probably present are $[SiO_2(OH)_2]_2^-$ or $[SiO(OH)_3]^-$. At lower pH the concentration of dimers and four-membered ring species increases. This range is closely associated with the crystallisation of more siliceous zeolites with five-membered rings in their structure.[27,28]

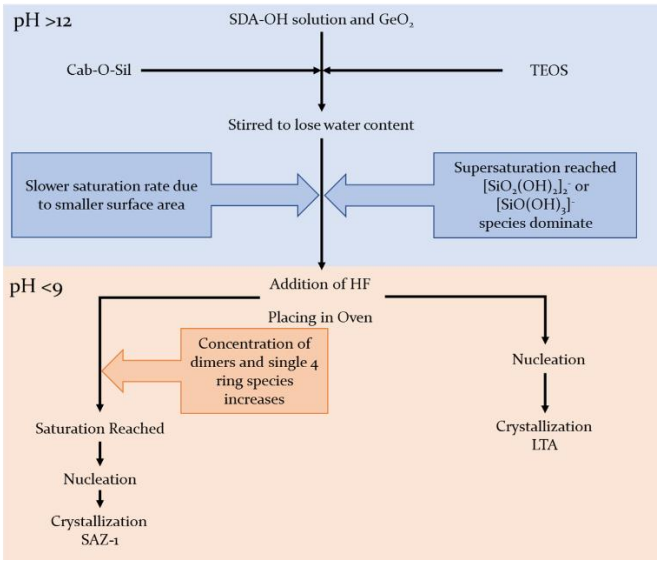

Figure 7.5 Shows the effect of the experimental procedure and different silica sources on the synthesis of the two crystalline phases SAZ-1 and LTA.

It is therefore likely that a combination of these two factors, the behaviour of the silicate source and the experimental procedure played a key role in determining the formation of **LTA** vs SAZ-1 (Figure 7.5). The higher saturation rate of TEOS means that the reaction reached supersaturation faster that those reactions using fumed silica. Therefore, the reaction mixture reached supersaturation very quickly after the addition of hydrofluoric acid and subsequent placement in the oven. This meant that silica species present in the TEOS reaction mixture consisted primarily of $[SiO_2(OH)_2]_2^-$ or $[SiO(OH)_3]^-$ which had formed under the higher alkaline conditions.[17,28] In comparison those reactions using fumed silica were slower to reach saturation. The saturation rate was therefore slower and so the dominant silica species present were dimers and four-membered ring species by the time crystallisation occurred. This therefore favoured the formation of a more siliceous zeolite SAZ-1.

It was clear that the use of fumed silica was key to the preventing the formation of LTA and promoting the formation of SAZ-1.

7.4.2.2 Effect of H_2O/T

In comparison to the HF/T and Ge/Si ratio the ratio of water to T atoms seemed to show the greatest effect on the product of the synthesis gel. When comparing both ternary plots, the formation of a crystalline product is hindered by H_2O/T ratios that are too high or too low, whether the silica source is fumed silica or TEOS. It is well documented that the water content has an important role in zeolite syntheses.[17,26] Water acts as the solvent in the synthesis and so increasing the water content leads to a lower concentration of reactants in the gel and so lowers the crystallisation rate. This was observed for both silica sources and can be used to explain the formation of some SAZ-1 with TEOS in gel composition with a higher water content. The higher water content prevented supersaturation of the gel when the mixture was placed in the oven. This allowed the formation of larger building units before crystallisation and so disfavoured the formation of **LTA**. In the case of fumed silica an increase in amorphous character was seen due to the slower rate of reaction caused by dilution of the gel.[2] These experiments were all given the same amount of time and so with increased time it is reasonable to assume that the full crystallisation of the zeolite would have occurred. With lower water content, there was an increase in amorphousness (as seen in DF391A and DF311A). It is also known that a lower water content in F^- medium can have a phase selectivity effect. So most likely the increased amorphous character seen under very low water content conditions is because of the lowered selectivity towards SAZ-1.[26]

7.4.2.3 Effect of Ge/Si

The desire to produce an ADORable zeolite means that the inclusion of Ge was imperative and as with many syntheses the Ge content of the gel tends to be higher to ensure the formation of *d4r* dominated by germanium. Limiting the amount of Ge was therefore undesirable. From the results, there seems to be an ideal Ge/Si ratio required to result in the formation of SAZ-1. This effect was particularly noted when TEOS was used as the silica source in the synthesis gel. It is observed that experiments that appeared on the same point of the ternary plot and so only differed in their germanium content showed different dominant phases in the final product. This is most readily seen in the comparison between DF375B, DF301B, DF359 and DF381. All four of these experiments showed different phases despite having the same molar ratios of HF, T-atoms, and H_2O. The only difference between these syntheses was the Ge/Si ratio. DF375B and DF301B (Ge/Si= 0.75

and 0.5) showed a dominant SAZ-1 phase while DF359 and DF381 (Ge/Si= 0.33 and 0.25) showed LTA as the dominant phase in the final product. Further to this the only experiment without Ge present (DF326) yielded a material that had a wholly amorphous character. Germanium is well known for its ability to stabilise the formation of *d4r* and enhance the rate of formation.[29] It has also been observed that with increasing Ge content the reaction media produces larger nanoparticles in the crystallisation process and so leads to the more rapid formation of stabilised zeolite building blocks early on in the reaction, this therefore allows for the ordering of the zeolite framework to occur more quickly.[29]

It is therefore possible that the increase in germanium counteracts the formation of just **LTA**, by allowing for the quicker formation of large zeolite building blocks, thus minimising the effects of the supersaturation when TEOS is used as the silica source. However, it should be noted most of the phases where SAZ-1 dominated still contained a **LTA** impurity.

In the cases where fumed silica was used the difference caused by changing the germanium content seemed limited. It is important to note that the different Ge/Si ratios were not properly investigated for fumed silica due to time constraints, limited resources and the trends indicated by results already obtained for TEOS.

7.4.2.4 Effect of HF/T

It was clear that the amount of HF in the synthesis gel played an important role in the resultant product of the synthesis gel. In both cases the HF ratio needed to be within a certain ratio (0.05 and 0.08) to ensure the formation of a crystalline product. This is to be expected as fluoride plays a key role in zeolite crystallisation. Fluoride acts as a mineralising agent, in much the same way as hydroxide, resulting in the formation of highly crystalline products.[16,18] However, it is well documented that fluoride favours the formation of *d4r* and so this,[30] in conjunction with high Ge/Si ratios, seems to be required to direct the formation of SAZ-1. This is most likely due to the stabilisation of building blocks under lower pH conditions, which is associated with higher density zeolites. In comparison those syntheses with lower Ge/Si ratios and lower HF/T seem to show a lower preferential for SAZ-1 formation. An example of this can be seen in both ternary plots. In the case of fumed silica syntheses lower HF concentrations (like DF380A and DF313A) remained amorphous. Simply increasing the HF content (DF370A and DF371A) lead to the formation of some crystalline products, even if there was still a certain amount of

amorphous material still present. This trend is also seen with TEOS as the silica source, when comparing DF363 and DF361 with DF366B and DF346B. Where the former, with lower HF/T ratios, showed a preferential formation of LTA, while higher HF/T ratios in the latter lead to the preferential formation of SAZ-1. This clearly showed that increasing HF/T showed an increasing likelihood towards the formation of a crystalline product.

7.4.3 Assembly of Parent Germanosilicate SAZ-1

An eventual ideal molar ratio was found and used as described in the experimental section (Section 7.3.3.1), to consistently produce a new germanosilicate. The initial PXRD pattern (Figure 7.6) of this material suggested a crystalline material had been formed and maybe new as it did not match patterns from available databases.

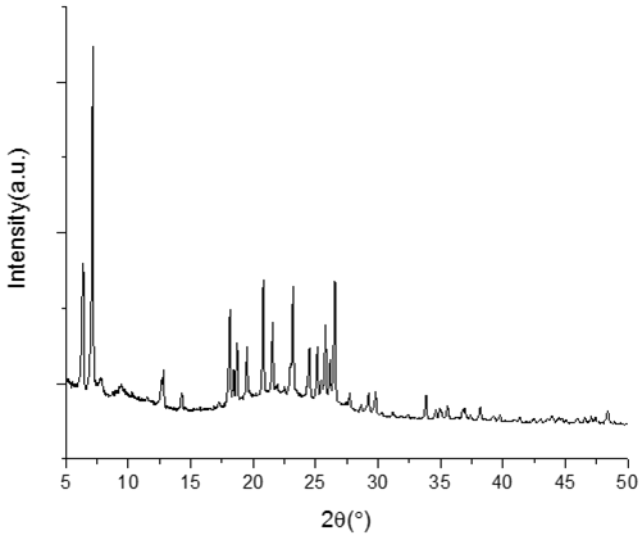

Figure 7.6 Shows the powder X-ray diffraction pattern of SAZ-1, which when checked against databases was found to not match any previously known frameworks.

These initial results suggested that the new material was perhaps a novel zeolitic framework and was therefore designated SAZ-1.

7.4.3.1 Assessing the Role of the SDA

To prove that the design principles used in the synthesis were valid it was important to confirm that the choice of SDA played a key role in the successful synthesis of SAZ-1. Therefore, it was important to prove that the SDA was present in the final zeolite product. Initial TGA analysis (Figure 7.7) showed that SAZ-1 had a weight loss of about 25%. This is a typical profile seen for zeolites with an organic SDA present in the pores and so indicated the presence of an organic SDA in the pores of the as-made zeolite.

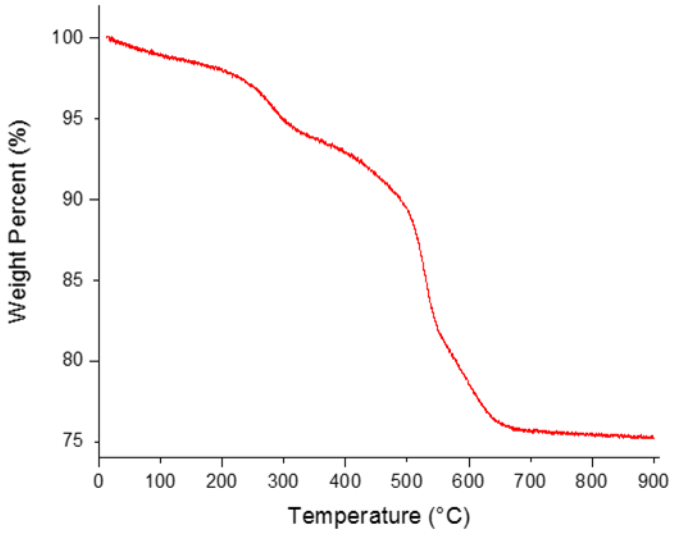

Figure 7.7 Shows the Thermogravimetric analysis of SAZ-1 with the typical two humps seen for zeolites, with the first smaller hump caused by the loss of water and the second larger weight loss caused by the decomposition and removal of the SDA from the zeolite pores.

While it was proven that there was an organic SDA present in the SAZ-1 pores this did not conclusively prove that the designed SDA was intact within the pores. There are examples of SDAs used in zeolite synthesis, where it is the resultant products from the decomposition of the initial molecule to smaller subunits that then direct the formation of the zeolite. This means that these decomposition products and not the original SDA are found in the pores of the synthesised zeolite.[31] To prove that the organic present in the pores of SAZ-1 was indeed the intact SDA and not a product of decomposition ^{13}C MAS NMR analysis was conducted on the as-made sample.

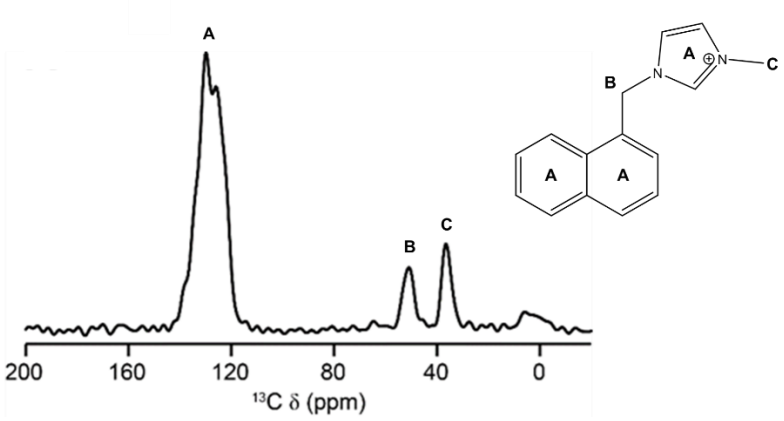

Figure 7.8 ^{13}C MAS NMR spectrum from SAZ-1 showing peaks consistent with the intact SDA within the zeolite SAZ-1

The spectrum collected on the as-made SAZ-1 sample showed the presence of 4 key peaks (Figure 7.8). Two peaks between 120-135 ppm (A)correlate to the aromatic carbons present

in the imidazole and naphthalene rings, which was originally observed in the solution state ^{13}C NMR. The peak at about 50 ppm (B) corresponds to the peak for the CH_2 carbon connecting the two rings and the final peak at about 37 ppm (C) corresponds to the CH_3 carbon attached to the imidazole ring. This result not only confirmed the presence of an intact organic SDA within SAZ-1, but confirmed that the SDA present was the intact SDA that had been designed.

7.4.3.2 Characterisation of SAZ-1 Structure

7.4.3.2.1 ^{29}Si MAS NMR

With confirmation that the designed SDA was indeed intact within the zeolite it was therefore of interest to fully characterise SAZ-1 and to ascertain if it was a suitable candidate for the ADOR process.

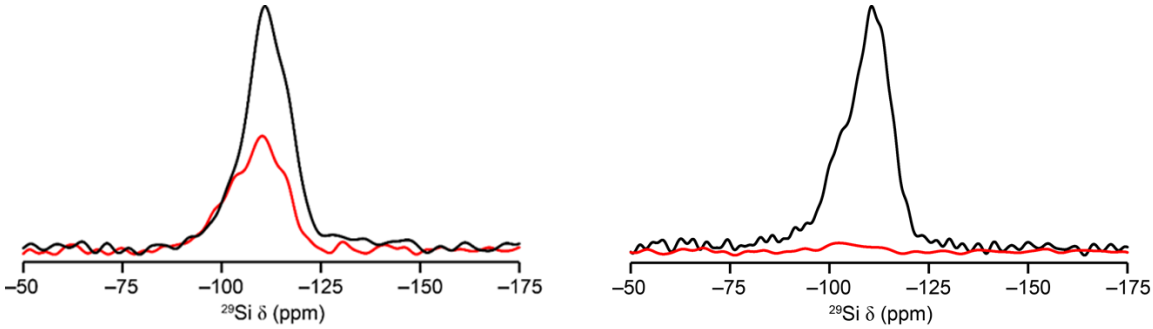

Figure 7.9 . ^{29}Si MAS NMR spectra (black) and {^{1}H} ^{29}Si cross-polarisation MAS NMR (red) of SAZ-1 as-made (left) and calcined (right). SAZ-1 shows a small number of Q^3 sites caused by the disorder present in the germanosilicate and the presence of the SDA in the structure, the majority of this signal is lost upon calcination indicating that the SDA is responsible for the majority of Q^3 sites seen.

The ^{29}Si MAS NMR spectra (Figure 7.9 black) showed the presence of predominantly Q^4 sites (~ -110 ppm) in both the as-made (left) and calcined forms of the zeolite (right). This suggests that SAZ-1 is a zeolite framework dominated by fully connected tetrahedral atoms. The {^{1}H} ^{29}Si cross-polarisation MAS NMR spectra (red) showed the presence of more Q^3 sites in the as-made zeolite compared to the calcined material. These can be attributed to the presence of the SDA in the pores of the zeolite. There was still a small number of Q^3 sites (~ -100 ppm) present in the structure even after removal of the SDA, this is perhaps indicative of some possible disorder present in the zeolite SAZ-1.

7.4.3.2.2 N_2 Adsorption Data

Nitrogen adsorption isotherms (77 K) of the calcined material showed a type I isotherm with a BET surface area of 257 m^2/g (Figure 7.10). This indicated that SAZ-1 showed the typical adsorption properties seen in zeolites.

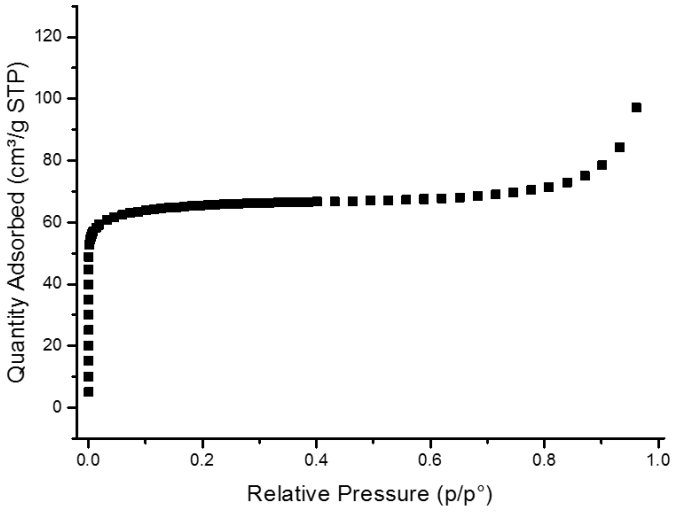

Figure 7.10 Shows the nitrogen adsorption isotherm for calcined SAZ-1 indicating that SAZ-1 had a typical type 1 adsorption isotherm observed for zeolites.

It was clear that SAZ-1 had the typical properties expected for a fully connected zeolite this confirmed that the designed synthesis had indeed led to the formation of a zeolite. It was therefore of interest to see if SAZ-1 had the chemical properties suitable for the ADOR process.

7.4.3.2.3 SEM and EDX Analysis

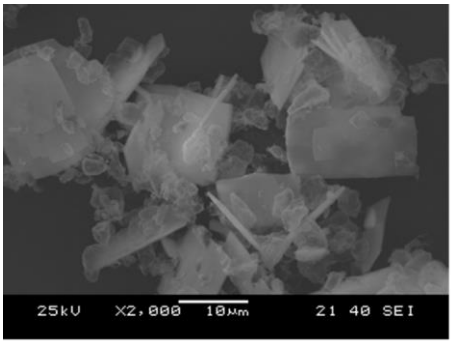

Element Analysis (Atomic percent)

Spectrum	O	Si	Ge	Total
1	70.83	25.35	3.82	100
2	51.65	45.03	4.32	100
3	58.14	38.65	3.21	100
4	62.73	33.52	3.75	100
5	65.95	30.04	4.01	100
Average	61.86	34.52	3.82	

Figure 7.11 SEM images and EDX analysis for as made SAZ-1 clearly showing

SEM and EDX analysis (Figure 7.11) further confirmed that the synthesis designed was successful in synthesising a possible ADOR candidate zeolite. The SEM imaging confirmed the presence of some minor non-regular shaped amorphous solid present as an impurity. Much of the bulk solid was observed to consist of crystals with a thin platelet-like morphology with the crystal size averaging about 15 µm in length. Such crystal morphology and size has typically been seen in previously researched ADORable zeolites like **UTL**. Energy-Dispersive X-ray spectroscopy conducted on the SAZ-1 crystals showed the presence of germanium and silicon in the structure. Although the Si/Ge ratio seen in

the crystals is lower than that in the initial reaction mixture (9.03 and 2 respectively). The amount of germanium incorporated into the crystals showed that the design principles that had been implemented were correct and germanium had been incorporated into the crystal structure, therefore providing a strong indication that SAZ-1 was a possible candidate for ADOR process.

7.4.3.2.4 Single Crystal Analysis of SAZ-1

From the analytical techniques used previously it was clear that SAZ-1 had the physical and chemical properties ideal for a candidate to undergo the ADOR process. While SEM/EDX analysis indicated and ideal Si/Ge ratio in the SAZ-1 structure, it was not clear what the SAZ-1 framework structure was and therefore hard the determine the positions occupied by germanium in the framework structure. As previously discussed the ADOR process requires a specific set of framework and chemical properties and so it was important to determine if the SAZ-1 framework showed these ideal characteristics. The SEM analysis showed that the crystal size and morphology of SAZ-1 made them suitable for analysis by single crystal X-ray diffraction allowing for easy determination of the SAZ-1 framework structure and its suitability as a candidate for the ADOR process.

The structure of the material was partially solved by Professor Alexandra Slawin (See Appendix) from a small single crystal of the material using direct methods and refined using least-squares methods. The single crystal analysis was hampered by the poor quality of the crystals, but did indicate that the SAZ-1 framework was new at the time. The framework was like that seen for CIT-13 and NUD-2, which were developed at the same time as SAZ-1.[32,33] All three had the same framework but were made using different SDAs.

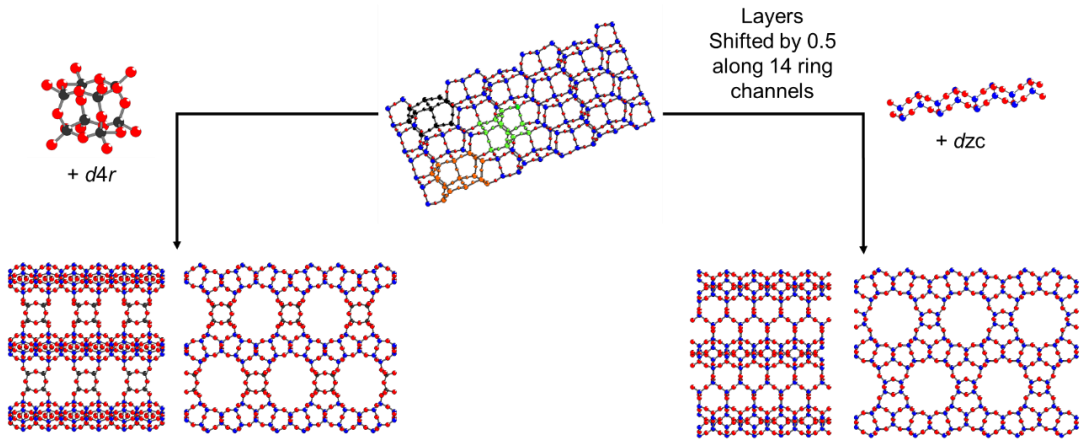

Figure 7.12 Shows the *cfi* layers with the composite building units *ton* (orange), *cas* (red) and *mtt* (green) highlighted. With the resultant zeolite structures, SAZ-1 (left) and CFI (right), with the different connectivity of the layers highlighted.

SAZ-1, like CIT-13 and NUD-2, comprised of the desired structural features ideal for the ADOR process. Dense silica-rich layers define the SAZ-1 framework. These layers have also been seen in the framework **CFI**,[34] which are like other silica rich ferrierite layers but not the same as they comprise of *cas*, *mtt*, and *ton* composite building units (Figure 7.12). Unlike SAZ-1 where the *cfi*-layers are linked together, through germanium-rich *d4r* units, into a three-dimensional structure, the layers in **CFI** are shifted by half a unit cell along the 14-ring channels and connected by double zigzag chains to form the 1-dimensional 14-ring channels. In SAZ-1 the use of *d4r* linkages produces a large-pore zeolite with 2 dimensional channels of 14- and 10-ring (Figure 7.13).

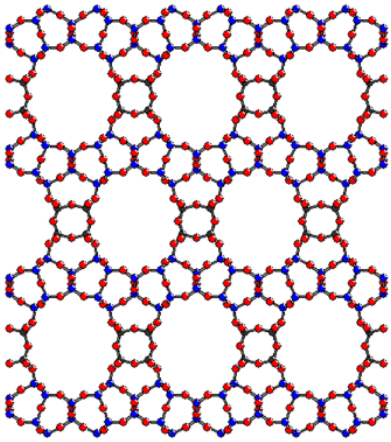

Figure 7.13 Shows the crystal structure of SAZ-1 when viewing the 14-rings ([001] direction). SAZ-1 consists of dense ferrierite-like layers dominated by silicon (blue) connected by germanium (grey) dominated *d4r* linkages, oxygen is also shown (red).

The size of the pores confirmed that the combination of a bulky SDA and the use of germanium and fluoride helped to promote *d4r* in the SAZ-1 structure. In particular when compared to the synthesis of CIT-5, which involved the use of a bulky organic SDA, inorganic cations and no germanium or fluoride in the reaction mixture and so did not promote the formation of *d4r* units.[34]

7.4.3.3 SAZ-1 A Disordered Structure

From the single crystal analysis, it was clear that SAZ-1 was a very clear candidate for the ADOR process. However, an additional distinctive feature of the SAZ-1 framework was noticed. While the 14-rings were very clearly ordered when the SAZ-1 structure was viewed in the direction of the 10-ring channels there was a severe amount of disorder in the *d4r* units connecting the layers (Figure 7.14).

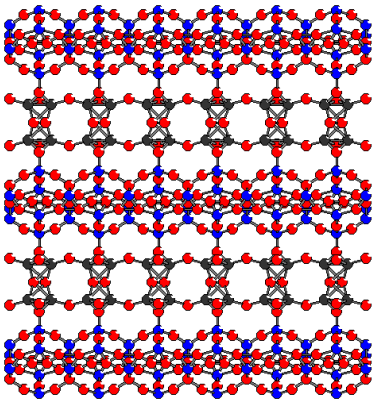

Figure 7.14 Shows the single crystal structure of SAZ-1 viewed along what should be the 10-ring channels. However, the Ge-dominated *d4r* units (black) are severely disordered across two sites.

The refined crystal therefore suggests that the oxygens connecting the *d4r* and silicate layers have 3 bonds. As this cannot be the case it is suggested that the *d4r* units are disordered over two sites, this leads to disorder of the *d4r* units in not just one but two directions.

This disorder is incredibly interesting as the presence of one *d4r* dictates the formation of *d4r* in the [001] direction but does not dictate the disorder of the *d4r* units in the [100] direction. It is easy to see why this is the case when the connecting oxygens in the interlayer region are highlighted and the *cfi* layers are viewed from directly above.

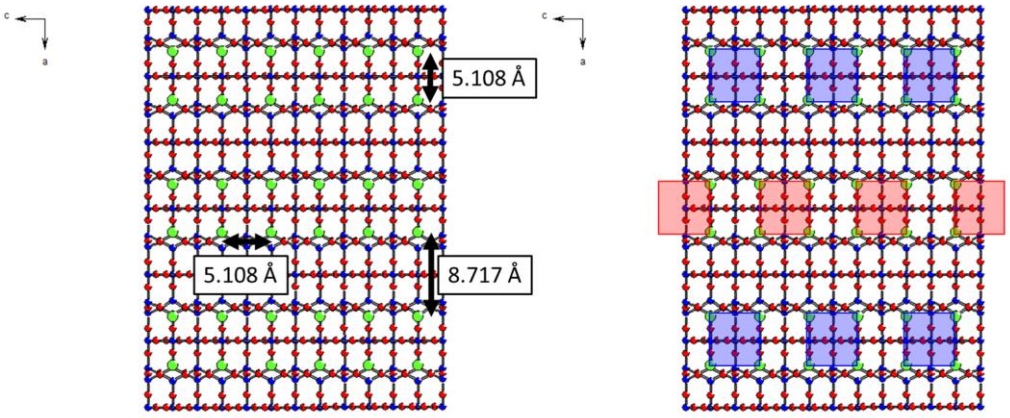

Figure 7.15 Shows the SAZ-1 layer viewed in the [010] direction with the connecting oxygens (green) and the distances between them highlighted(left). The different *d4r* orientations are highlighted blue or red (right), where whole rows of blue or red *d4r* units run in the [001] direction but alternate in the [100] direction. This leads to the disorder of the 10-ring channels as it runs parallel with the direction of this disorder.

The oxygens connected to the *d4r* units in between the layers (Figure 7.15) can be described as oxygen pairs (separated by 5.108 Å in the [100] direction) running in the [001] direction and repeating every 5.108 Å, each of these rows of oxygen pairs are then

separated from each other by 8.717 Å. The closeness of the oxygen pairs within these rows means that once a *d4r* unit is formed it dictates the orientation of the *d4r* units in the rest of the row running in the [001] direction (leading to rows of *d4r* in the [001] direction being all blue or all red). The larger distance between these rows of oxygen pairs in the [100] direction (8.72 Å) means that each row of *d4r* units running in the [001] direction behaves independently of those running parallel with it. This can lead to the formation of fully alternating rows of blue-red-blue *d4r* running in the [100] direction. This leads to disorder running parallel with the 14-rings but perpendicular to the 10-rings leaving the 14-ring channels intact while the 10-ring channels are blocked.

However, SAZ-1 is a 3D framework and so this intralayer disorder is repeated with every layer of *d4r* connecting the silicate layers in the [010] direction. As the orientation of one layer of *d4r* units is unable to dictate the orientation of the *d4r* units in the next layer (interlayer disorder).

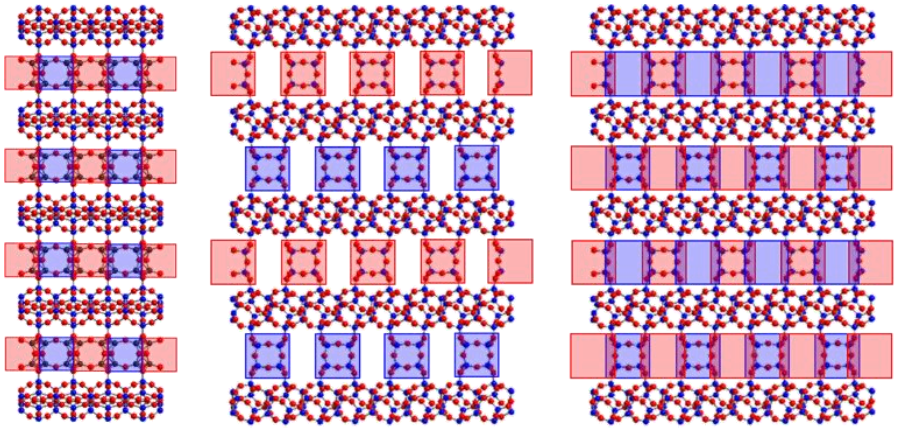

Figure 7.16 Highlights the full degree of disorder present in SAZ-1. The initial crystal structure (left) with two different *d4r* unit orientations highlighted in red or blue. An example of disorder in the [010] direction is then shown with alternating red-blue-red *d4r* linkages between each layer (middle). The combination of this disorder in the [010] is then combined with the disorder previously discussed running in the [001] direction leading to a fully disordered structure in both directions.

As shown in Figure 7.16 (middle) this interlayer disorder can result in alternating (red-blue-red) rows of *d4r* units running in the [010] direction. By then combining this interlayer layer disorder with the intralayer disorder already shown in Figure 7.15. The degree of disorder seen in SAZ-1 can be fully appreciated. With fully alternating rows of blue and red *d4r* units running in the [100] and [010] direction, the 10-ring channels become completely lost while the 14-ring channels remain fully intact.

The disorder implied by the single crystal analysis of SAZ-1 was proven beyond doubt with the images produced from high-resolution spherical aberration corrected (C_s-corrected) scanning transmission electron microscopy (STEM) analysis (Figure 7.17).

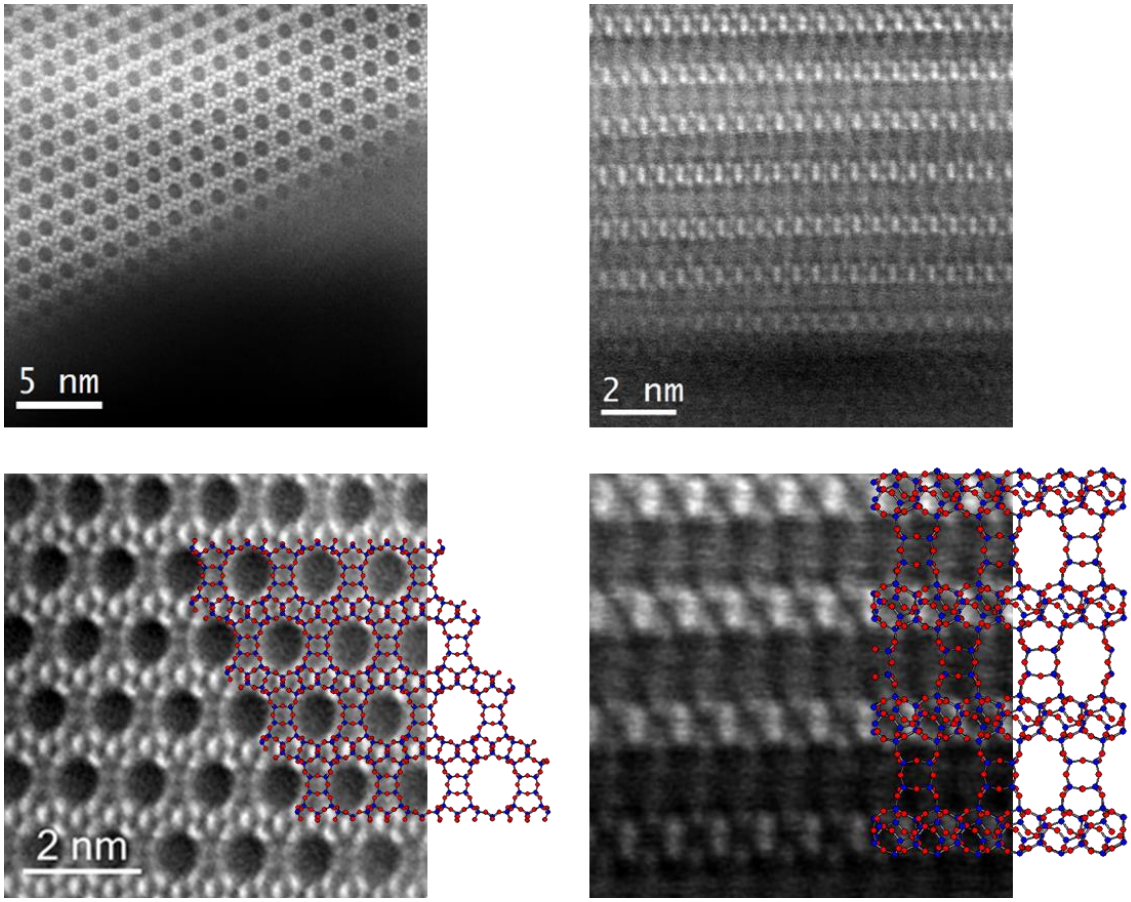

Figure 7.17 HADDF STEM images of SAZ-1 viewed along the 14-ring channels (left) and 10-ring channels (right). The images were then overlaid with the SAZ-1 framework (bottom). The images show the 14-ring channels intact and well-defined matching the predicted SAZ-1 structure (bottom left), while the 10-ring channels are fully disordered resulting in a blurring of the interlayer region and the image not matching predicted SAZ-1 structure where the 10-rings are ordered.

The images collected by Alvaro Mayoral substantiated the single crystals analysis. Not only were the predicted *cfi*-layers clearly visible, these layers were clearly connected by *d4r* units. The 14-ring channels were ordered and well-defined, as expected, as these channels were unaffected by the disorder observed in the single crystal analysis. When viewed in the 10-ring direction the silicate layers were clearly defined, but the 10-ring channels were not visible and the *d4r* units were ill-defined. Instead a 'smudging' this interlayer region was seen, clearly showing that the disorder seen in the single crystal analysis was indeed present in the SAZ-1 framework.

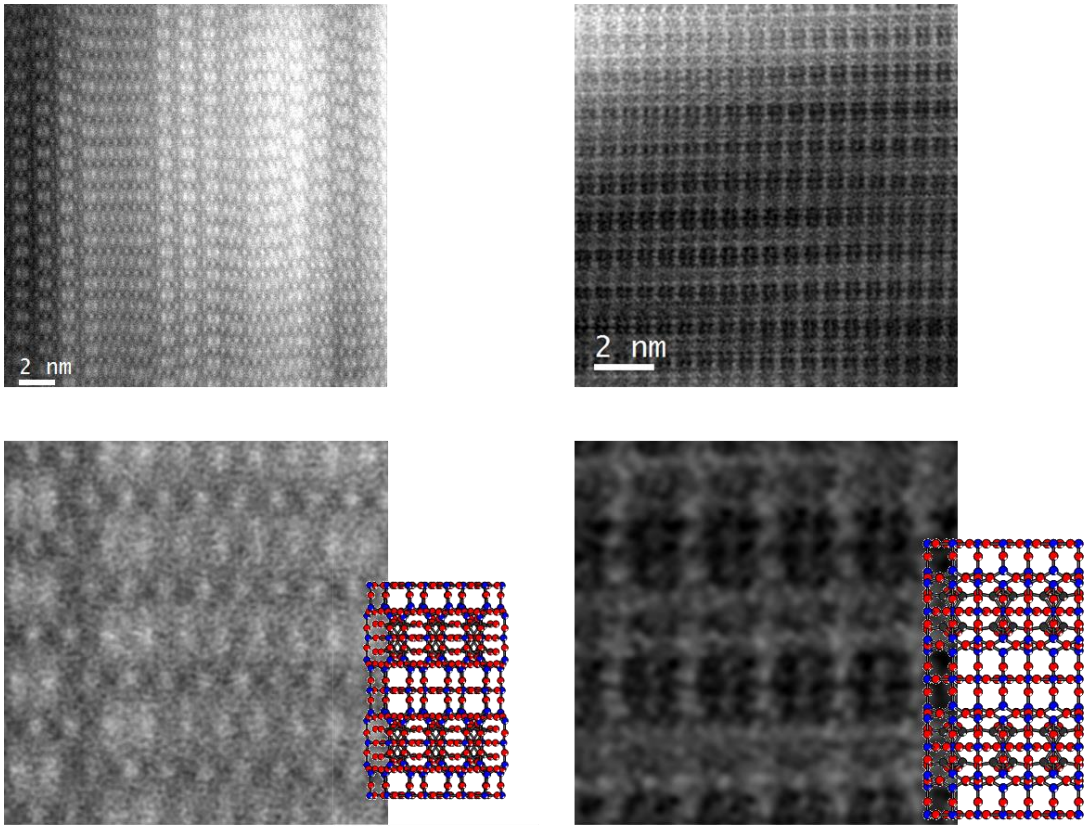

Figure 7.18 Shows the STEM images of SAZ-1 viewed in the [110] and [010] directions (top left and top right). The [110] direction shows the severe faulting of the crystals, while the [010] direction shows the view of the crystal looking down onto the layers. Both TEM images compare favourably with the generated structures superimposed on them.

Further STEM images collected by Alvaro Mayoral of SAZ-1 also revealed some significant faulting/twinning of the crystals (Figure 7.18) when seen in the [110] direction. Although it is not clear the cause of this faulting it is possibly an additional effect of the disorder of the *d4r* discussed previously. Additional TEM images of the crystal when viewed directly on top of the layers compared very favourably with the superimposed crystal structure.

7.4.3.4 An ADORable Zeolite Assembled

From the full characterisation of SAZ-1 it was irrefutable to conclude that the design principles discussed in the synthesis strategy had succeeded. Not only had these principles produced a zeolite under hydrothermal conditions, but the zeolite produced was a new unique zeolite framework. SAZ-1 showed the ideal chemical and framework properties to be an ADOR process candidate. The analysis used showed that SAZ-1 consisted of dense silicate layers connected by *d4r* units, although these *d4r* units were found to be severely disordered this should have no effect on the application of the ADOR process. It should be noted that during the period of these experiments papers were published on structures NUD-2 and CIT-13 that have a similar framework structure as SAZ-1.[32,33]

7.4.3.5 Applying the ADOR Process

Given the successful assembly of the new germanosilicate SAZ-1, the next question to be answered was whether the ADOR process could be successfully applied. One of the great advantages of the ADOR process is that once the framework of the parent zeolite is known it is easy to computationally predict the structure of the disassembled layers and the subsequent daughter zeolites (Figure 7.19).

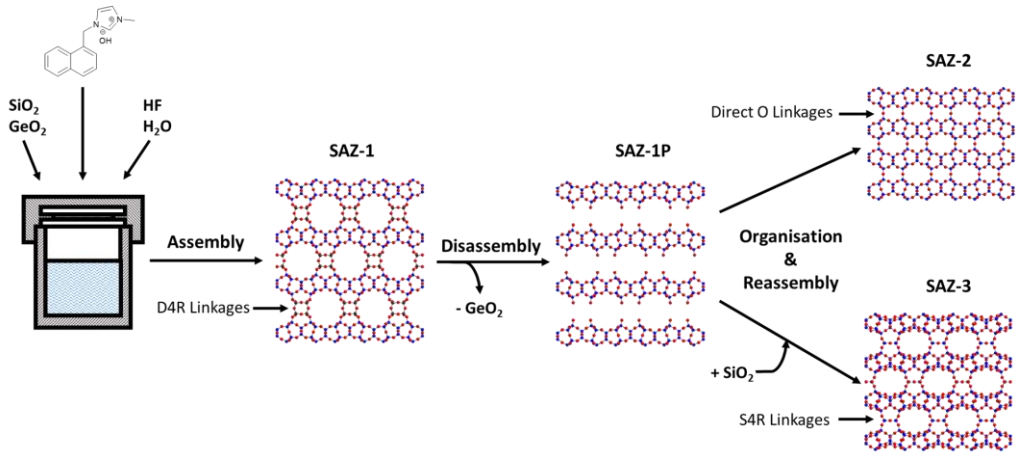

Figure 7.19 Shows a schematic representation of the ADOR process applied to SAZ-1. Firstly, the successful hydrothermal synthesis of SAZ-1 (assembly) with its clearly defined *d4r* linkages between the silicate layers. Secondly, the removal of Ge-containing *d4r* connections between the layers to form the lamellar product SAZ-1P (disassembly). SAZ-1P can then be organised and reassembled into the two daughter zeolites SAZ-2 and SAZ-3, where the *cfi*-layers are connected by direct O-linkages or *s4r* linkages respectively

In the case of SAZ-1 the disassembly step caused by the removal of the Ge-dominated *d4r* (disassembly) results in the formation of a high silica layered material, SAZ-1P consisting of the *cfi* layers with silanol groups in the interlayer region. By organizing and reassembling these layers without additional silicon it is possible to form the daughter zeolite SAZ-2 with direct O-linkages between the layers. With the addition of silicon, the *cfi* layers are connected by *s4r* linkages between the layers to form the zeolite SAZ-3. Through this process 3 different zeolites are formed. These layers remain the same but contain different interlayer linkages and so have differing channels. With SAZ-1 containing 14- and 10-ring channels, SAZ-2 10- and 6-ring channels and SAZ-3 12- and 8-ring channels a new isoreticular family of zeolites can be made.

7.4.4 Disassembly of SAZ-1

Although the analysis of SAZ-1 indicated it had all the ideal characteristics to be a candidate for the ADOR process. It would not be until the ADOR process had been put into practise that its suitability could be fully examined. The next step of the ADOR process (disassembly) involves the treatment of the parent germanosilicate with acid. The weakness of germanium to hydrolysis results in the destruction of the *d4r* linkages

between the silicate layers and consequently their removal from the structure, while the dense silicate layers remain intact. The removal of these linkages should lead to the contraction of the layers together as the *d4r* supports are removed and the formation of many silanols in the space between these layers.

7.4.4.1 Initial PXRD Pattern

Treatment of SAZ-1 with 0.1 M HCl (Section 7.3.3.2) resulted in a dramatic change in the PXRD pattern. In comparison to the PXRD pattern of SAZ-1, SAZ-1P showed far fewer peaks and a broader PXRD pattern (Figure 7.20).

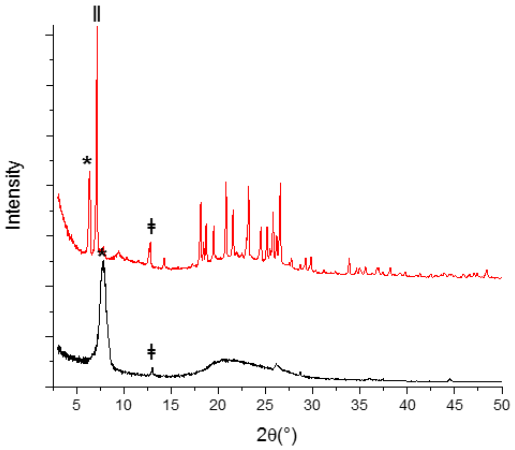

Figure 7.20 Shows the PXRD patterns of SAZ-1 (red) compared with the SAZ-1P (black). The pattern of SAZ-1P includes very few peaks, with the 200 peak (*) becoming dominant and shifting to lower d-spacing. Most other peaks relating to interlayer reflection are lost. The preservation of the 040 peak (ǂ) and the loss of the 110 peak (‖) is also noted.

The disassembly step resulted in a dominance of the peak corresponding to the (200) reflection (*), and its shift towards a higher scattering angle (from 6.3° to 7.9° 2θ). This is because the (200) reflection corresponds to the stacking of the *cfi* layers. An increase in the scattering angle must indicate a decrease in the *d*-spacing between layers because of the removal of the *d4r* linkages. The PXRD pattern of SAZ-1P also showed that a large majority of the peaks that were originally present in SAZ-1 had disappeared. This is another indication of the successful disassembly of the parent germanosilicate and formation of a layered material.[10] This is because the disassembly process results in the loss of all other peaks with a reflection value in the same direction as the movement of the layers, as order in the *a* direction is lost. This means that, in the case of the transformation of SAZ-1 to SAZ-1P, any other reflection with a *hkl* value where $h>0$ is lost and so is the corresponding peak in the powder pattern. In this example, the 110 peak (‖) that had previously dominated SAZ-1 completely disappears with the removal of the Ge-dominated *d4r*. In contrast reflections with a corresponding *hkl* value where $h=0$ are still preserved

and their peaks remain unchanged. This explains the preservation of the 040 peak (‡) from the original SAZ-1 PXRD pattern in the disassembled product SAZ-1P. Such observations strongly suggest that the Ge-dominated *d4r* in SAZ-1 had been disassembled and the lamellar material (SAZ-1P) had been formed.

7.4.4.2 Characterisation of SAZ-1P

With the promising results from the initial PXRD pattern of the disassembled SAZ-1P material a better resolution powder pattern was obtained at Diamond Light Source in Oxfordshire. The obtained powder pattern of SAZ-1P was then compared to the generated unit cell by a Pawley fit conducted by Sam Morris(Figure 7.21).[35]

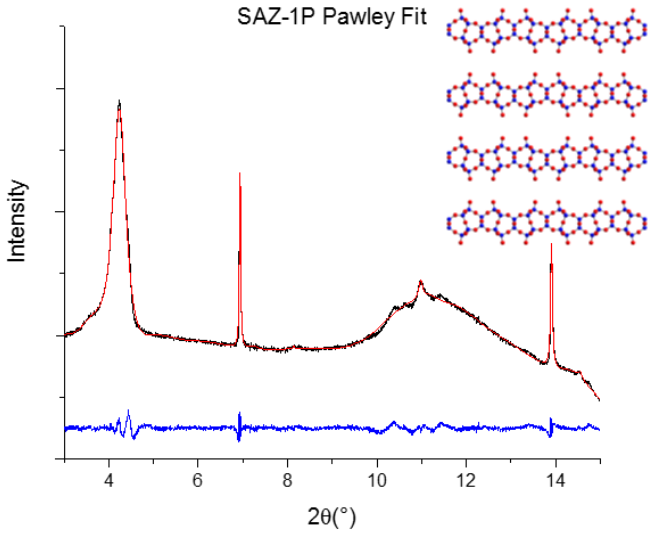

Unit Cell SAZ-1P	
Space Group	*Cmmm*
R_{wp}	0.94
R_{exp}	0.63
a	22.274(3) Å
b	13.6359(5) Å
c	4.9708(6) Å

Figure 7.21 Pawley fit of SAZ-1P with the predicted structure as viewed along the *c* axis. The Pawley fit shows the experimental PXRD (black), calculated (red) and difference curves (blue). The pattern showed a reasonably good fit for the predicted unit cell with a R*wp*= 0.94 % and R*exp*= 0.63 % and χ^2= 2.23.

When fitted against the generated unit cell for SAZ-1P a reasonably good fit was achieved, despite the limited peaks. However, while the χ^2 is above 1 (2.23), the fit should be approached with some caution. The limited number of peaks and the high amount of background noise makes determining the accuracy of the fit difficult. This does not rule out the disassembly of the product, but merely is a symptom of the difficulty modelling a complex layered material with any degree of certainty. The unit cell values obtained for SAZ-1P from the Pawley fit matched those of SAZ-1, except for the *a* axis, where the distance was 22.274 Å compared 27.193 Å. This contraction of the cell in the *a* axis clearly indicated the collapse of the distance between the silicate layers, due to the removal of the interlayer linkages. The difference between the *a* axes is of note as 4.919 Å is close to the expected value consistent with the removal of the *d4r* units from the inter-layer space.

The removal of the *d4r* linkages from the interlayer space removed the channel system present in SAZ-1. This was demonstrated in the much-reduced sorption capacity of SAZ-1P (158.68 m^2/g) in comparison to SAZ-1 (257.94m^2/g).

SEM analysis of the material showed the preservation of the original SAZ-1 morphology, with the SAZ-1P crystals resembling small platelet-like structures (Figure 7.22), indicating that the material was related to the parent germanosilicate and some ordering was preserved in the structure. EDX analysis of the SAZ-1P crystals showed a dramatic decrease in the Ge content of the crystals with the average Si/Ge ratio of the material increasing from 9.03 to 23.79. confirming the removal of germanium from the structure due to the hydrolysis of the Ge-dominated *d4r* linkages.

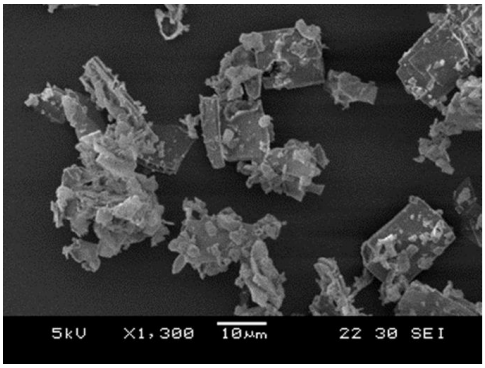

Element Analysis (Atomic percent)				
Spectrum	**O**	**Si**	**Ge**	**Total**
1	80.01	19.24	0.74	100
2	78.75	20.38	0.87	100
3	78.68	20.41	0.91	100
4	77.82	21.24	0.94	100
5	79.64	19.58	0.78	100
Average	78.98	20.17	0.848	

Figure 7.22 Shows the SEM image and EDX analysis of SAZ-1P from the disassembly of SAZ-1. The resultant crystals show a preservation of the original crystal morphology, with a dramatically increased Si/Ge ratio strongly indicating the successful targeted removal of the Ge-dominated *d4r* linkages.

Final confirmation of the successful disassembly of SAZ-1 and nature of the interlayer space between the silicate layers of the material SAZ-1P was confirmed through ^{29}Si MAS NMR (Figure 7.23).

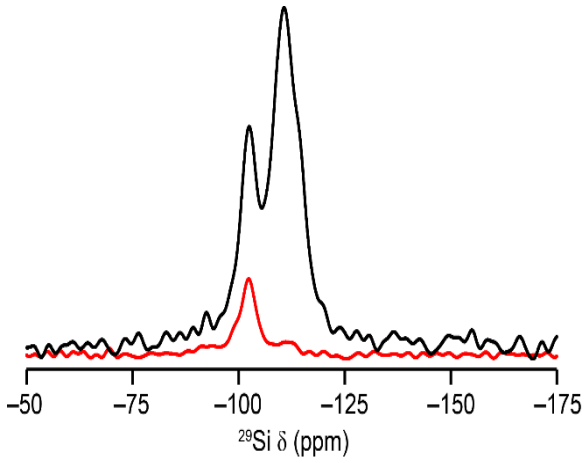

Figure 7.23 Shows the ^{29}Si MAS NMR (black) and {^{1}H} ^{29}Si cross-polarisation MAS NMR (red) spectra of SAZ-1P. SAZ-1P shows a large number of Q^{3} sites compared to the parent zeolite SAZ-1 caused by the removal of the Ge-dominated *d4r* linkages between the layers and the formation of large concentration of silanols in the interlayer region.

The resulting ^{29}Si MAS NMR spectrum (black) showed two key peaks corresponding to presence of many Si Q^{3} sites (at ~ -100 ppm) as well as the expected Q^{4} sites (at ~ -110 ppm). This indicated the presence of silicon atoms that were now no longer connected to other T-atoms by a bridging oxygen. These Si Q^{3} sites were then confirmed to be silanols (Si-OH) using {^{1}H} ^{29}Si cross-polarisation (red line), indicating that the T-atoms had been replaced with a H atom. This confirmed that the parent germanosilicate had been disassembled, the Ge-dominated *d4r* had been removed from the interlayer space and this had resulted in the formation of large numbers of silanols in the interlayer space and as expected a layered material.[15]

From the analysis of SAZ-1P it was clear that SAZ-1 had fulfilled all the promises indicated. SAZ-1 could undergo the disassembly step of the ADOR process. The Ge-dominated *d4r* linkages had been removed from between the *cfi* layers resulting in the decreased Ge content of SAZ-1P. The removal of these linkages caused the formation of many silanols resulting in the increased number of Q^{3} sites in the ^{29}Si MAS NMR. The dense silicate layers, free from the constraints set by of the *d4r* linkages, then subsequently contracted closer together. This resulted in a decrease in the d-spacing of the interlayer reflection and a decrease in the unit cell in the direction of the layers. This also led to a destruction of the interlayer channel system present in SAZ-1 and the dramatic loss BET surface area seen in the adsorption isotherm of SAZ-1P.

7.4.5 Organisation and Reassembly of SAZ-1P to Make SAZ-2 and SAZ-3

With the successful disassembly of SAZ-1 to form the layered material SAZ-1P the next step was to apply the organisation and reassembly steps and so produce new daughter

zeolites related to their parent zeolite SAZ-1. The formation of these two daughters SAZ-2 and SAZ-3 differed depending on the nature of the interlayer linkages.

7.4.5.1 Formation of SAZ-2 and Characterisation of SAZ-2

Treatment of SAZ-1P with octylamine to organise the layers followed by calcination to remove the octylamine and force the formation of Si-O-Si linkages resulted in the formation of a new 3D framework zeolite SAZ-2 (Section 7.3.3.3).

The initial PXRD pattern for SAZ-2 fitted well with the calculated pattern from a DFT-optimised model (provided by Miroslav Položij). This model comprised of SAZ-1P layers connected by direct oxygen linkers. However, to really prove the accuracy of this model a Pawley fit was conducted by Sam Morris, with data acquired from the Diamond Light Source in Oxfordshire (Figure 7.24).

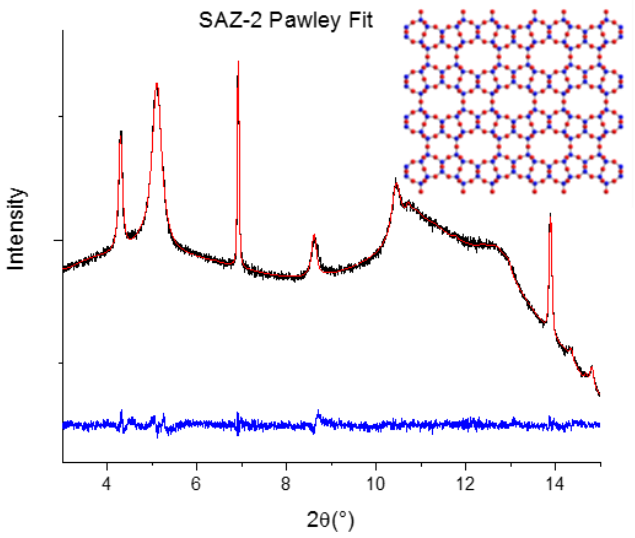

Unit Cell SAZ-2	
Space Group	*Cmmm*
R_{wp}	0.73
R_{exp}	0.66
a	18.489(2) Å
b	13.651(1) Å
c	4.972(1) Å

Figure 7.24 Pawley fit of SAZ-2 with the predicted structure as viewed along the *c* axis. The Pawley fit shows the experimental PXRD (black), calculated (red) and difference curves (blue). The pattern showed a very good fit for the predicted unit cell with a R*wp*= 0.73 % and R*exp*= 0.66 % and χ^2= 1.22.

The Pawley fit was extremely good with a χ^2 value of 1.22, a value very close to one, indicating a very good correlation between the modelled unit cell of SAZ-2 and the experimental PXRD pattern collected. The unit cell showed the same dimensions as previously seen in SAZ-1 and SAZ-1P. The only exception was once again in the *a* axis where a further contraction to 18.489 Å was seen in SAZ-3, compared to SAZ-1 and SAZ-1P (27.193 Å and 22.274 Å respectively). This indicated the formation of the direct O-linkages, which had forced a further contraction of the *cfi* layers, as the layers condensed together during

the reassembly step. These initial results showed that SAZ-1P had been successfully organised and reassembled to form the new daughter zeolite SAZ-2.

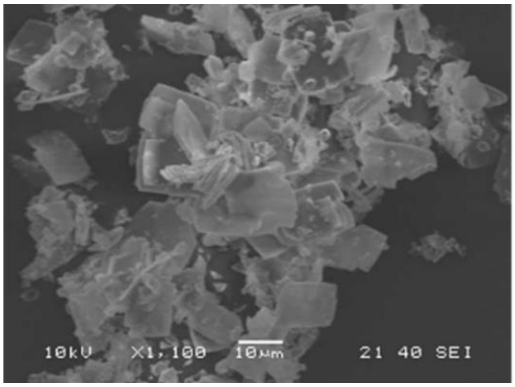

Element Analysis (Atomic percent)				
Spectrum	O	Si	Ge	Total
1	73.66	25.64	0.70	100
2	68.21	31.15	0.64	100
3	74.72	24.61	0.66	100
4	72.96	26.33	0.71	100
5	69.14	30.25	0.61	100
Average	71.74	27.60	0.66	

Figure 7.25 Shows the SEM image and EDX analysis of SAZ-2 from the organisation and reassembly of SAZ-1P. The SEM shows a preservation of the crystal morphology seen in SAZ-1 and SAZ-1P. The EDX analysis a similar Si/Ge ratio as seen in SAZ-1P.

From the SEM and EDX analysis confirmed that SAZ-2 showed the same thin-platelet like morphology as seen in its parent zeolite SAZ-1 strongly indicating the formation of a layered material from the parent material instead of its dissolution. The EDX analysis confirmed that the Si/Ge ratio had further decreased in comparison to SAZ-1P with the average Si/Ge ratio now reaching 41.81. This is most likely explained as the additional synthesis step results in further opportunities for the germanium to be removed from the system.

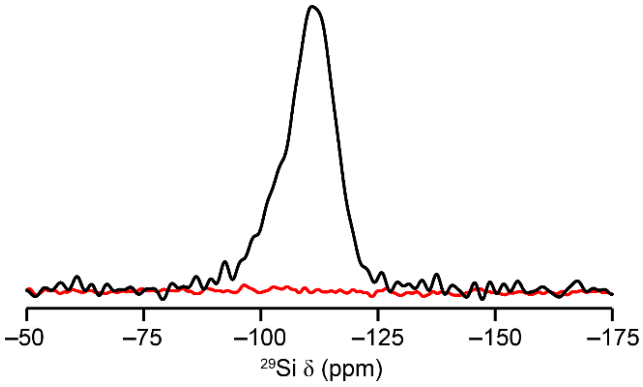

Figure 7.26 Shows the ^{29}Si MAS NMR (black) and {^{1}H} ^{29}Si cross-polarisation MAS NMR (red) spectra of SAZ-2. SAZ-2 shows a large number of Q^4 sites and very few Q^3 sites indicating that the SAZ-1P had been successfully fully reconnected to form the daughter zeolite SAZ-2.

The resulting ^{29}Si MAS NMR spectrum (Figure 7.26) showed the complete loss of the Q^3 sites that had been present in the layered product SAZ-1P, this strongly indicated the loss of the silanols that had formed in the interlayer space. This analysis was corroborated in the {^{1}H} ^{29}Si cross-polarisation where there was little to no signal traditionally associated with the presence of Si-OH species in the material (~ -100 ppm). This confirmed that the

silanols in the SAZ-1P layers had been fully reconnected to form a fully connected daughter zeolite SAZ-2. It also showed that the interlayer region of SAZ-2 did not suffer from the same degree of disorder as seen in the *d4r* of SAZ-1. This is because the formation of direct O-linkages between the layer negates the very strict orientation of the interlayer oxygens (as discussed in Section 7.4.3.3). It is therefore possible to say that this new daughter zeolite SAZ-2 has not inherited the 'genetic' disorder of its parent zeolite SAZ-1.

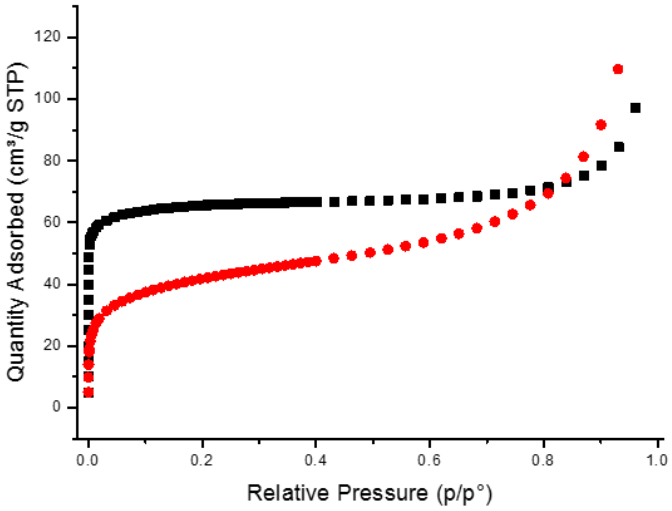

Figure 7.27 Shows the nitrogen adsorption isotherms for SAZ-1 (black) and SAZ-2 (red) indicating the decreased sorption capacity of SAZ-2 compared with SAZ-1.

The further contraction of the unit cell and layers was demonstrated in the reduced sorption capacity (Figure 7.27) of SAZ-2 (148 m^2/g) compared to SAZ-1P (158.68 m^2/g) in comparison to SAZ-1 (257.94m^2/g), however such low values were not seen for other zeolites like IPC-2 and IPC-4.[11]

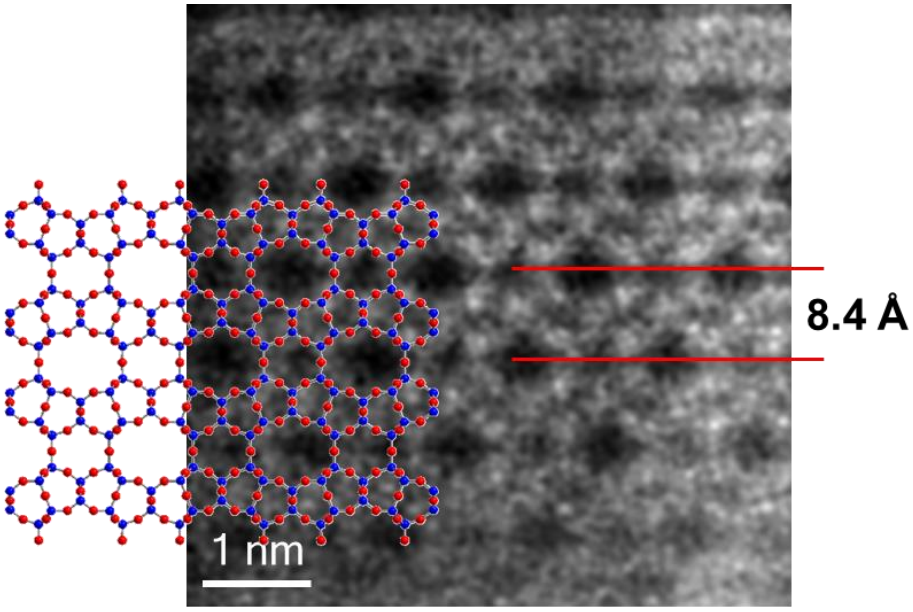

Figure 7.28 HADDF STEM images of SAZ-2 viewed along the 10-ring channels, the image is overlaid with the SAZ-2 framework and the distance between the interlayer linkages.

The final conclusive evidence was provided through high-resolution spherical aberration corrected (C_s-corrected) scanning transmission electron microscopy (STEM) analysis of SAZ-2 (Figure 7.28). The high-resolution STEM images obtained showed the different channel sizes of SAZ-2 compared with SAZ-1. When viewed along the *c* axis the 14-rings have now been transformed into 10-rings and the *d4r* linkages have been replaced with direct O-linkages resulting in the formation of 6-rings between the 10-ring channels, perhaps adding to the reduced sorption capacity seen in SAZ-2. The distance between repeating linkages (8.4 Å) matched that expected for the presence of direct O-linkages between the layers and confirmed the contraction of the silicate layers compared to SAZ-1 (where the distance was 12.1 Å).

From all the evidence, it was clear that the organisation and reassembly steps of the ADOR process had been successfully applied to SAZ-1P. This resulted in the first successful synthesis of a daughter zeolite from a newly synthesised parent germanosilicate. Indicating that the design principles considered, and the approach taken, in synthesising SAZ-1, had been excellent in providing an ADORable zeolite.

7.4.5.2 Formation and Characterisation of SAZ-3

Treatment of SAZ-1P with a source of silicon under acidic conditions, to form silicon columns between the layers, with subsequent calcination to force the formation of Si-O-Si linkages resulted in the formation of another new 3D framework zeolite SAZ-3 with *s4r* linkages between the layers (Section 7.3.3.3).

The initial PXRD pattern for SAZ-3 fitted well with the calculated pattern from a DFT-optimised model (provided by Miroslav Položij) that comprises of the SAZ-1P layers connected by *s4r* linkers. Again, to really prove the accuracy of this model a Pawley fit was conducted by Sam Morris, with data acquired from Diamond (Figure 7.29).

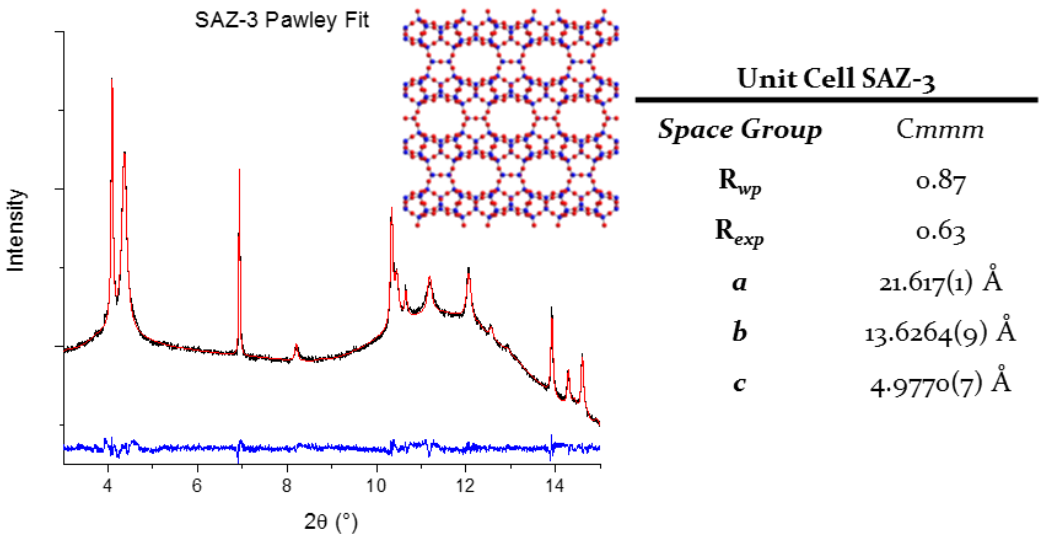

Figure 7.29 Pawley fit of SAZ-3 with the predicted structure as viewed along the *c* axis. The Pawley fit shows the experimental PXRD (black), calculated (red) and difference curves (blue). The pattern showed a very good fit for the predicted unit cell with a R*wp*= 0.87 % and R*exp*= 0.63 % and χ^2= 1.91.

The Pawley fit was extremely good with a χ^2 value of 1.91, a value close to one, indicating a very good correlation between the modelled unit cell of SAZ-3 and the experimental PXRD pattern collected. The value was slightly higher than that obtained for SAZ-2, however this was perhaps to be expected with the disorder present (as discussed later). The unit cell showed the same dimensions as previously seen in SAZ-1, SAZ-1P and SAZ-2 except in the *a* axis. SAZ-3 (21.617) showed a contraction of the unit cell in the *a* direction compared to SAZ-1 and SAZ-1P (27.193 Å and 22.274 Å respectively) but an expansion of the unit cell compared to SAZ-2 (18.489 Å). This indicated that SAZ-3 consisted of the SAZ-1 layers connected by smaller linkages than SAZ-1 (*d4r*) but larger than those of SAZ-2 (direct O-linkages). This strongly suggested the formation of *s4r* linkages between the layers and so showed that SAZ-1P had been successfully organised and reassembled to form another new daughter zeolite SAZ-3.

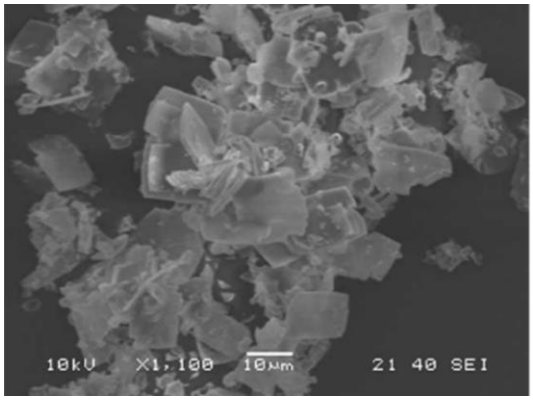

Element Analysis (Atomic percent)				
Spectrum	O	Si	Ge	Total
1	70.12	29.09	0.74	100
2	68.24	31.20	0.87	100
3	72.54	26.77	0.91	100
4	66.48	32.65	0.87	100
5	70.81	28.55	0.64	100
Average	69.64	29.65	0.81	

Figure 7.30 Shows the SEM image and EDX analysis of SAZ-3 from the organisation and reassembly of SAZ-1P. The SEM shows a preservation of the crystal morphology seen in SAZ-1 and SAZ-1P. The EDX analysis a similar Si/Ge ratio as seen in SAZ-1P.

From the SEM and EDX analysis (Figure 7.30) the preservation of the crystal morphology was confirmed as SAZ-3 showed the same thin platelet-like morphology as seen for SAZ-1 and SAZ-2 samples. The EDX analysis confirmed that the Si/Ge ratio in SAZ-3 (like in SAZ-2) had also decreased in comparison to SAZ-1P with the average Si/Ge ratio now reaching 36.60. This is also most likely explained as the additional synthesis steps results in further opportunities for the germanium to be removed.

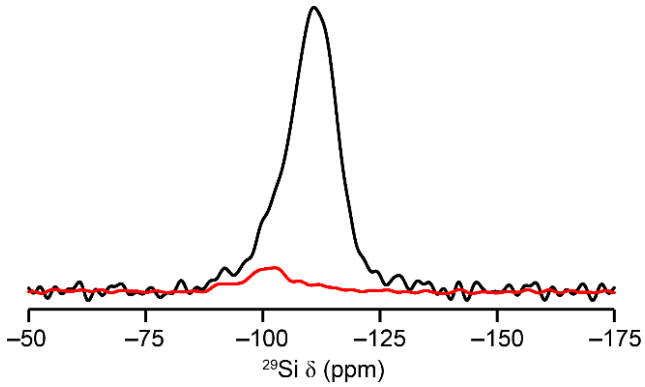

Figure 7.31 Shows the ^{29}Si MAS NMR (black) and {^{1}H} ^{29}Si cross-polarisation MAS NMR (red) spectra of SAZ-3. SAZ-3 shows a large number of Q^4 sites and a large reduction in the number of Q^3 sites indicating that the SAZ-1P had been successfully fully reconnected to form the daughter zeolite SAZ-3.

The resulting ^{29}Si MAS NMR spectrum (Figure 7.31) showed the dramatic loss of the Q^3 sites (~ -100 ppm) that had been present in the layered product SAZ-1P. Once again, a strong indication of the loss of the silanols after formation of fully tetrahedrally coordinated Si atoms during reassembly. However, there was still the presence of a small amount of Q^3 sites and a new peak for Q^2 sites (~ -90 ppm) was seen in the {^{1}H} ^{29}Si cross-polarisation. This confirmed that the reassembly had been successful but that there was also some interesting behaviour in SAZ-3, which had not been seen in SAZ-2. The presence of these additional Q^2 and Q^3 sites indicated that some Si present in the structure were

not fully connected. The reassembly step of the ADOR process is an irreversible step, this means that some silicon pillars formed between the layers may be placed incorrectly, preventing the condensation of perfect *s4r* units between the layers. This is due to the proximity of silanols in between the SAZ-1P layers. These pillars react between the layers and so are then unable to move during the calcination step. This means that some are unable to form fully connected *s4r* linkages. However, it seems that the silanols in SAZ-1P are orientated well enough that fully connected *s4r* linkages are still in the majority, unlike the results seen for zeolites **UWY** and **ITG** in the previous chapter. This is perhaps that the *d4r* are still in ordered rows and are only disordered within these rows. Such issues have clearly been inherited from the parent zeolite SAZ-1, where disorder of the *d4r* linkages was also observed. It is therefore clear that the 'genetic' disorder of the parent SAZ-1 was not passed on to SAZ-2 but was still inherited by SAZ-3.

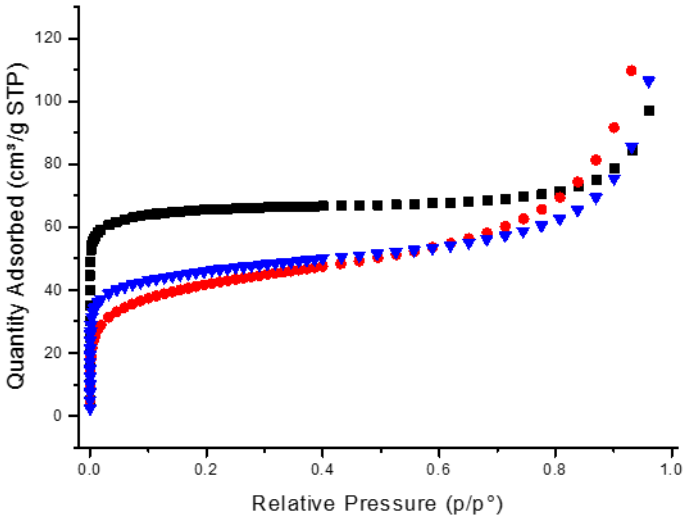

Figure 7.32 Shows the nitrogen adsorption isotherms for SAZ-1 (black) and SAZ-2 (red) and SAZ-3 (blue) indicating the decreased sorption capacity of SAZ-3 compared with SAZ-1 but its increased capacity compared with SAZ-2.

The nitrogen adsorption isotherm for SAZ-3 (Figure 7.32) confirmed the expected surface area properties of SAZ-3. With the new daughter zeolite showing a better sorption capacity (159 m^2/g) than its sister zeolite SAZ-2 (148 m^2/g) but fared worse compared to SAZ-1P (158.68 m^2/g) and SAZ-1 (257.94m^2/g). It is perhaps to be expected as the formation of SAZ-1 was under hydrothermal conditions, where the ability to make and break bonds allowed for better ordering of the interlayer *d4r*-linkages. The ADOR process does not have this ability and so the disorder present in this interlayer region may have contributed to the lower than expect sorption capacity.

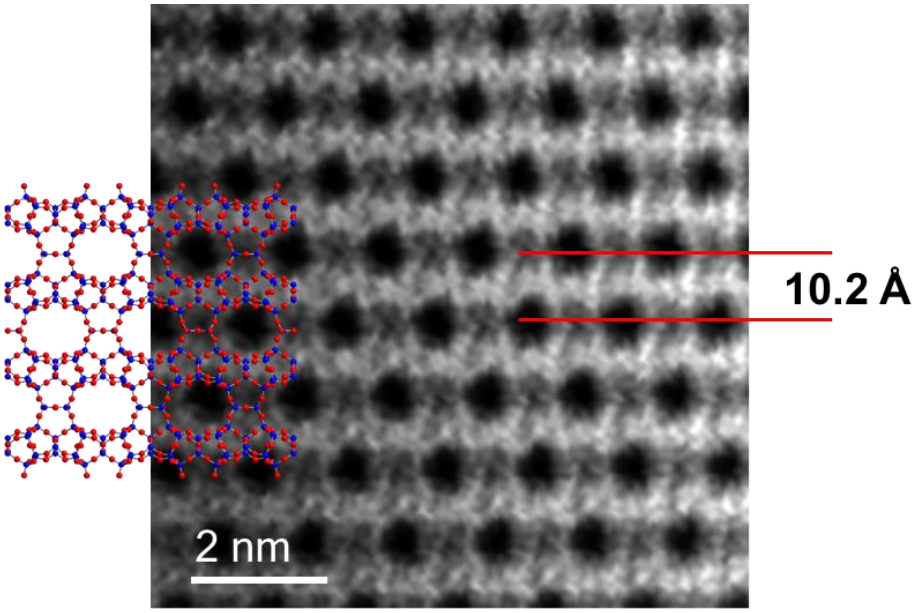

Figure 7.33 HADDF STEM images of SAZ-3 viewed along the 12-ring channels, the image is overlaid with the SAZ-3 framework and the distance between the interlayer linkages.

The final conclusive evidence was provided once again through high-resolution spherical aberration corrected (C_s-corrected) scanning transmission electron microscopy (STEM) analysis of SAZ-3 (Figure 7.33). The high-resolution STEM images obtained showed the different channel size of SAZ-3 compared with SAZ-1 and SAZ-2. When viewed along the *c* axis, the 12-ring channels were clearly defined and the *s4r*-linkages between the 12-rings are also observed (instead of *d4r* or 6-rings). The distance between repeating units (10.2 Å) matches that expected from the formation of *s4r* between the layers and shows that SAZ-2 lies somewhere in between SAZ-1 and SAZ-3 (12.1 Å and 8.4 Å).

From all the evidence, it was clear that the organisation and reassembly steps of the ADOR process had once again been successfully applied to SAZ-1P. This resulted in the synthesis of another new daughter zeolite from SAZ-1.

7.4.6 An Aluminated Family

One of the other great attractions of the ADOR process is the ability to not only form new zeolite frameworks, but also to incorporate new elements into these frameworks to impart new interesting chemical properties on these structures that the parent zeolite did not contain.[36] With the successful synthesis of SAZ-2 and SAZ-3 the next step was to see if both structures could be aluminated. The introduction of aluminium into the T sites of the zeolite framework generates an additional negative charge for each aluminium atom present. This is because silicon has a formal charge of +4 and aluminium +3. This negative charge is then compensated for by the formation of H^+ ions near a bridging Si-O-Al bond

and so results in the formation of Brønsted acid sites in the zeolite framework (Figure 7.34).

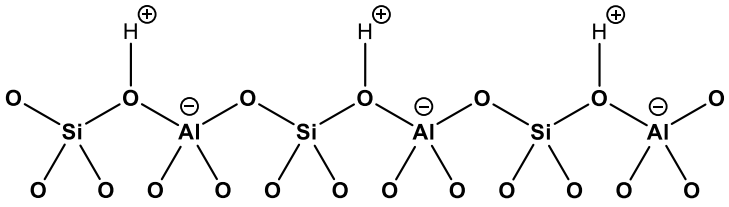

Figure 7.34 Shows the Brønsted acid sites formed by the incorporation of negatively charged aluminium into the zeolite framework.

With the addition of aluminium atoms, the zeolite can act as a catalyst for many reactions. Of interest for the Morris group is the release of biologically active NO for stents as described in Chapter 1.

It was therefore of great interest to see if, using the ADOR process, it was possible to increase the SAZ-1 family even further. By introducing aluminium into the SAZ-1P structure making Al-SAZ-1P it would then be possible to synthesise two more daughter zeolites Al-SAZ-2 and Al-SAZ-3, with the same zeolite framework as their sisters but different chemical properties thanks to the addition of aluminium.

The procedure involved the assembly of SAZ-1, disassembly into SAZ-1P, followed by alumination to form Al-SAZ-1P. This Al-SAZ-1P could then be organised and reassembled to form Al-SAZ-2 and Al-SAZ-3.

7.4.6.1 Formation of Al-SAZ-1P

The formation of Al-SAZ-1P was confirmed using PXRD, SEM and EDX analysis. The PXRD pattern of Al-SAZ-1P also showed the same dominant (200) reflection. This confirmed that a similar structure to SAZ-1P had been formed (Figure 7.35).

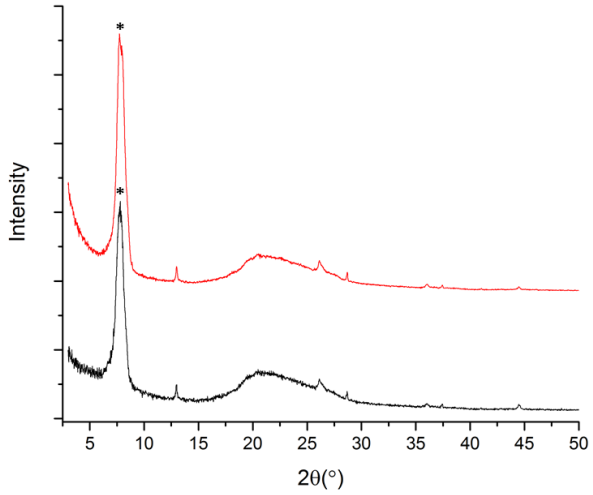

Figure 7.35 Shows the powder patterns of SAZ-1P (red) with Al-SAZ-1P (black) the dominant (200) reflection is highlight (*).

The SEM images confirmed the preservation of the original SAZ-1 crystal morphology and confirmed the minimal formation of extra-framework aluminium also known as aluminium zoning, which is usually seen as bright small particulates on the crystal surface. EDX analysis of the crystals confirmed that the formation of Al-SAZ-1P had removed much of the germanium from the zeolite structure. Al-SAZ-1P showing a Si/Ge ratio of about 48, a similar low value to that achieved for SAZ-1. EDX analysis (Figure 7.36) also confirmed the incorporation of aluminium into the SAZ-1P layers. The Si/Al ratio achieved in SAZ-1P was about 58.43, which while somewhat low in comparison to other aluminium zeolites but hopefully would be enough to allow the formation of Brønsted acid sites within the daughter zeolites formed.

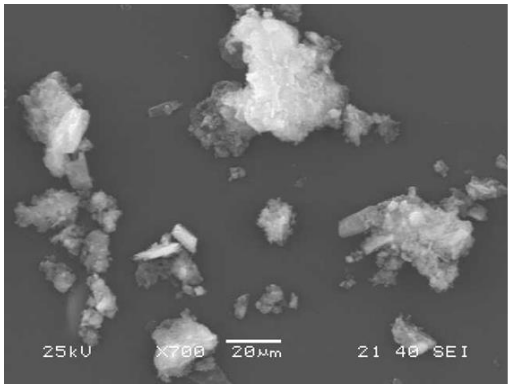

Element Analysis (Atomic percent)

Spectrum	O	Al	Si	Ge	Total
1	77.27	0.24	22.02	0.47	100
2	78.51	0.52	20.48	0.49	100
3	78.25	0.49	20.72	0.54	100
4	76.23	0.26	23.03	0.48	100
5	78.14	0.33	21.27	0.26	100
Average	77.68	0.368	21.504	0.448	

Figure 7.36 Shows the SEM and EDX analysis of Al-SAZ-1P. The images show some preservation of the crystal morphology, while the EDX analysis confirmed the low Ge content and the presence of Al.

7.4.6.2 Formation of Al-SAZ-2 and Al-SAZ-3

Al-SAZ-2 was successfully prepared in the same way as SAZ-2 but with the use of Al-SAZ-1P (Section 7.3.3.6). Al-SAZ-3 was also prepared in the same way as the preparation of SAZ-3 but with Al-SAZ-1P instead of SAZ-1P (Section 7.3.3.7).

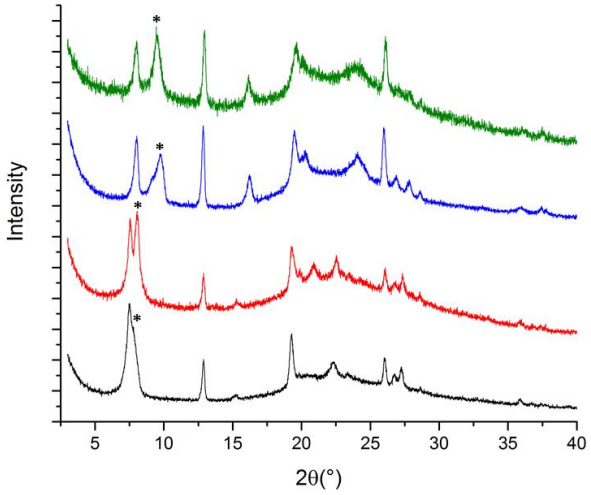

Figure 7.37 Compares the PXRD patterns of SAZ-2 (green), Al-SAZ-2 (blue), SAZ-3 (red) and Al-SAZ-3 (black) both aluminated daughter zeolites compared favourably with their non-aluminated sister zeolites.

The PXRD patterns of Al-SAZ-2 and Al-SAZ-3 compared favourably with the PXRD patterns seen for standard SAZ-2 and SAZ-3 (Figure 7.37). The only difference seen between the patterns was a slight disordering of the 200 peaks (*). This was perhaps due to some disordering within the stacking of the layers, caused by the inclusion of aluminium in the framework structure.

SEM and EDX analysis (Figure 7.38) showed some preservation of crystal morphology and the Si/Al ratio achieved in the final daughter zeolite was approximately 36.53 and 47.80 respectively.

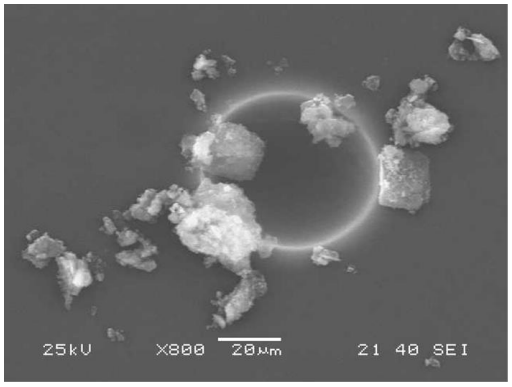

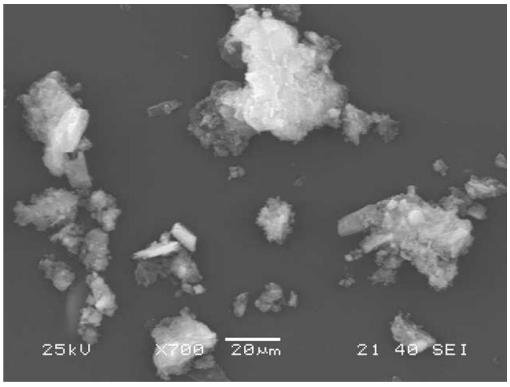

Element Analysis (Atomic percent)

Spectrum	O	Al	Si	Ge	Total
1	79.76	0.50	19.65	0.09	100
2	77.12	0.64	22.05	0.19	100
3	77.21	0.60	22.10	0.09	100
4	77.34	0.67	21.87	0.12	100
5	77.24	0.54	22.07	0.15	100
Average	77.73	0.59	21.55	0.13	

Element Analysis (Atomic percent)

Spectrum	O	Al	Si	Ge	Total
1	78.39	0.48	20.72	0.41	100
2	77.22	0.52	22.02	0.24	100
3	78.68	0.53	20.48	0.31	100
4	76.52	0.27	23.03	0.18	100
5	75.46	0.51	23.68	0.35	100
Average	77.25	0.46	21.99	0.30	

Figure 7.38 Shows the SEM and EDX analysis for Al-SAZ-2 (left) and Al-SAZ-3 (right).

7.4.6.3 Catalytic Results of the Aluminated Family

As discussed, the addition of aluminium into the zeolite framework structure results in the addition of Brønsted acid sites and results in the development of catalytic activity. This catalytic activity is of interest for the Morris group to produce medicinal NO. Therefore, it was of interest to test the catalytic activity of Al-SAZ-2 and Al-SAZ-3. This experimental procedure (described in section 7.3.3.8) involves the formation of Brønsted acid sites through ammonium ion exchange followed by calcination. These sites can then react with nitrite to produce NO. The samples were tested by placing Al-SAZ-2 and Al-SAZ-3 in water and injecting a solution of sodium nitrite (0.05 M, 250 µL), the release of NO was then monitored (further details in Section 3). The resulting profiles showed that both daughter zeolites had the ability to produce NO (Figure 7.39). Though the amount produced was relatively low, this clearly showed that the alumination procedure had been successful and that these daughter zeolites, whose framework is the same as their sister zeolites, showed different reactivity.

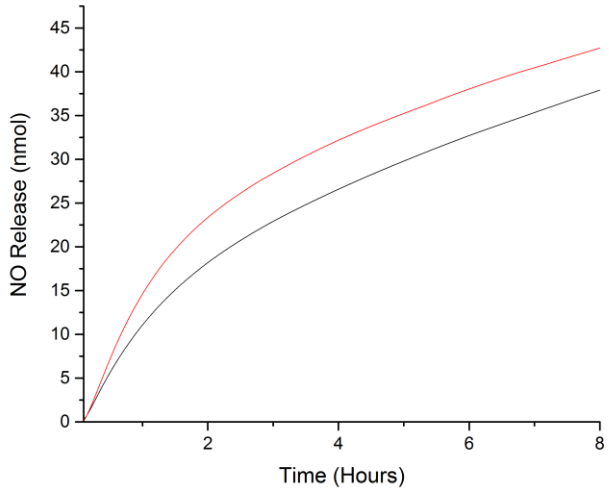

Figure 7.39 Shows the NO production profiles of SAZ-2 (black) and SAZ-3 (red)

Both Al-SAZ-2 and Al-SAZ-3 showed similar release profiles, with the only difference being that Al-SAZ-3 showed a greater maximum release, as indicated by the steeper gradient of the NO release curve. After about 2 hours both samples slowed to about the same rate. This difference between the two daughters is still rather minimal. This is to be expected as the frameworks are isoreticular and do not differ radically from each other. Both should contain 2-dimensional channels and similar Si/Al ratios as both were synthesised from the same Al-SAZ-1P sample. However, this small difference can be explained by comparing the channels in the two zeolites, as Al-SAZ-2 contains 10 and 6 channels while Al-SAZ-3 contains 12 and 8 channels. This indicates that the difference in activity is simply due to this relatively small size in the pores. However, the smaller difference between the two is perhaps because of the disorder associated with both samples.

The results from the analysis clearly shows that the SAZ-1 family had been expanded. The ADOR process had been used to produce two zeolite frameworks related to their sisters' in structure, but with different chemical properties. The addition of aluminium imparted the ability for these two new daughter zeolites to have new catalytic properties unattainable by the parent or sisters in the SAZ-1 family of zeolites. The addition of aluminium was confirmed through SEM and EDX and the ability to produce NO from nitrite was analysed.

7.4.7 A Cuprous Family

The formation of Brønsted acid sites was of interest, however such sites are finite and once used there are no currently known techniques that can be used to regenerate them. For many applications, a catalytic system is preferred. This led to the investigation of copper sites in zeolites. The potential of placing copper sites for the catalytic production of NO, has already been investigated by Russel *et al.*[37] Therefore the results of the alumination of SAZ-2 and SAZ-3, while positive, showed how limited Brønsted acid sites were. It was hoped that by placing copper in the zeolite, the resultant Cu-Al-SAZ-2 and Cu-Al-SAZ-3 would show greater activity and would be regenerative.

7.4.7.1 Formation of Cu-Al-SAZ-2 and Cu-Al-SAZ-3

The creation of copper sites involved the heating of Al-SAZ-2 and Al-SAZ-3 in a copper nitrate solution (Section 7.3.3.9). PXRD results of the two copper-exchanged samples, showed no change compared with the original Al-SAZ-2 and AL-SAZ-3.

EDX/PXRD analysis of Cu-Al-SAZ-2 and Cu-Al-SAZ-3 showed that the zeolites had lost a lot of the well-defined crystallinity, compared to the original parent SAZ-1 zeolite. This was mainly due to the number of process that had been forced on these crystals. The original SAZ-1 crystals have been through a total of 4 separate chemical processes to form these Cu-exchanged daughters, with the additional physical processes associated with analysis, such as grinding the sample for PXRD analysis. However, the crystals still showed some examples of the characteristic platelet-like morphology associated with the original SAZ-1 (Figure 7.40).

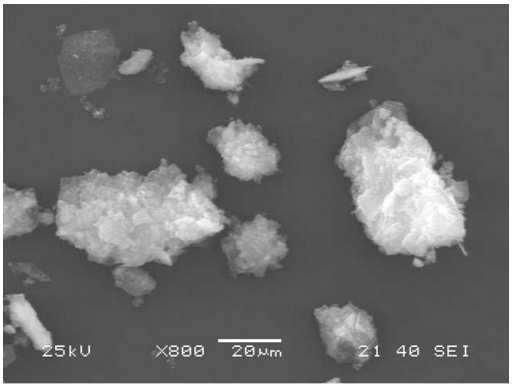

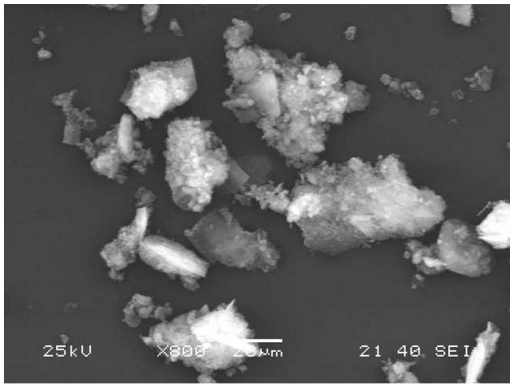

Element Analysis (Atomic percent)					
Spectrum	Si	Al	Ge	Cu	O
1	21.47	0.10	0.46	0.08	77.90
2	24.23	0.35	0.55	0.14	74.73
3	20.80	0.12	0.58	0.10	78.41
4	21.72	0.33	0.64	0.19	77.12
5	21.42	0.60	0.68	0.09	77.21
Average	21.93	0.30	0.58	0.12	77.07

Element Analysis (Atomic percent)					
Spectrum	Si	Al	Ge	Cu	O
1	32.41	0.15	0.45	0.04	66.94
2	24.19	0.25	0.41	0.03	75.13
3	22.02	0.21	0.47	0.03	77.27
4	20.48	0.47	0.49	0.06	78.51
5	20.72	0.43	0.54	0.06	78.25
Average	23.96	0.30	0.47	0.04	75.22

Figure 7.40 Shows the SEM images for Cu-Al-SAZ-2 (left) and Cu-Al-SAZ-3 (right) with their corresponding EDX analysis underneath. The images show some preservation of the original platelet-like crystal morphology, while the EDX analysis showed the incorporation of a small amount of copper corresponding, which did not correspond to the expected Cu/Al ratio of 0.5.

EDX analysis confirmed that the copper was incorporated into the daughter zeolites with the minimal loss of aluminium. The Cu/Al ratio was shown to not be close to the ideal value (0.5), indicating that the maximum incorporation of copper into the zeolite structure had not been achieved.

7.4.7.2 Catalytic Activity of Cu-Al-SAZ-2 and Cu-AL-SAZ-3

The addition of copper into the zeolite structure was hoped to lead to an increase in the catalytic activity of these SAZ-1 daughter zeolites. This is because the incorporation of coppers results in a catalytic cycle whereby cysteine converts the Cu(II) in the incorporated in the framework to Cu(I). This then converts nitrite to NO and reforming Cu(II). However, it was shown that no NO was produced. The reasoning for this is most likely due to a combination of the relatively low aluminium and subsequent copper content, the degree of disorder present in the structures, and the relatively small channels, that could inhibit interaction of the incorporated copper with the cysteine. Previous research in the group has shown that pillaring of IPC-1P and incorporation of Cu did not result in catalytic activity and that this was due to the inability for the cysteine and the nitrite to access the Cu sites due to the disordered pillars of silica.

7.4.8 A High-Energy Family

Another advantage of the ADOR process discussed in Section 1 is the ability for the ADOR process to allow access to 'unattainable' zeolites with much higher energies than those frameworks produced by traditional hydrothermal synthesis.[12]

With the successful expansion of the SAZ-1 family, to now include daughter zeolites with new chemical properties, it was of interest to see if the same ADOR process could be used to produce high energy variations of SAZ-2 and SAZ-3.

7.4.8.1 Formation of SAZ-1PS

To form the desired high-energy framework structures, it is important to control the organisation step of the ADOR process. This involves the breaking of the hydrogen bonding between the SAZ-1P layers and shifting the layers relative to each other into a new orientation. This was achieved with the use of choline hydroxide, as it has been shown to produce the desired shift in the orientation of the layers.[12] This is because the choline cations will preferentially orientate in-between groups of silanols (or quadruplets) with a large excess of choline causing the desired shift in the layers.

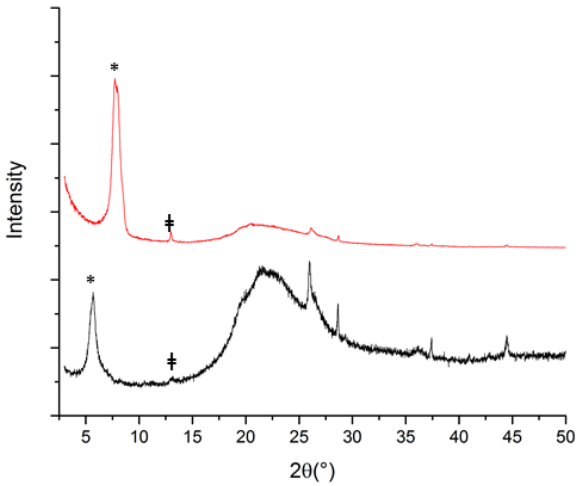

Figure 7.41 Shows a comparison between standard SAZ-1P (red) and SAZ-1PS (black) after treatment with 50 wt. % choline hydroxide solution confirming that the *cfi* layers can shifted with the use of choline hydroxide.

The incorporation of choline hydroxide into SAZ-1P resulted in a significant change in the PXRD pattern (Figure 7.41). The most notable change was a shift of the 200 peak (*), corresponding to the interlayer reflection, to a lower 2θ angle (from 7.9 ° to 5.6 ° 2θ). This indicated a larger d-spacing between layers (an expansion of the interlayer spacing).[38] This confirmed the successful incorporation of a swelling agent in between the layers. Perhaps more interesting is that the 040 peak (‡) was less obvious in the PXRD pattern. The 040

peak corresponds to the reflection running perpendicular to the layer stacking, and was preserved in the original SAZ-1P PXRD pattern (Figure 7.20). It was unaffected by the disorder running in the [100] direction as its *h* value was 0, therefore the electron density in this reflection was still ordered enough to produce a peak in the PXRD pattern. However, with the inclusion of the choline cation and the introduction of disorder in orientation of the layers, effecting the *b* axis reflections, this peak loses intensity.[12] This indicates that the choline cation has not just successfully swollen the layers, but that it also caused a shift in the layers, which could lead to the formation of newer higher energy zeolites. An issue noted with these powder patterns was the increase in the amorphous character between 17 ° and 30° 2θ. This is an unfortunate consequence of the use of choline hydroxide. As strongly alkali conditions often result in dissolution of the zeolite.[26] However, it was found that only the hydroxide could be used to cause the shift desired (Figure 7.42), as the pattern remained unchanged with the use of lower concentrations of choline hydroxide and a higher proportion of choline chloride. This is believed to be a consequence of the hydroxide being required to overcome the hydrogen bonding between the silanols of the interlayer region.[12]

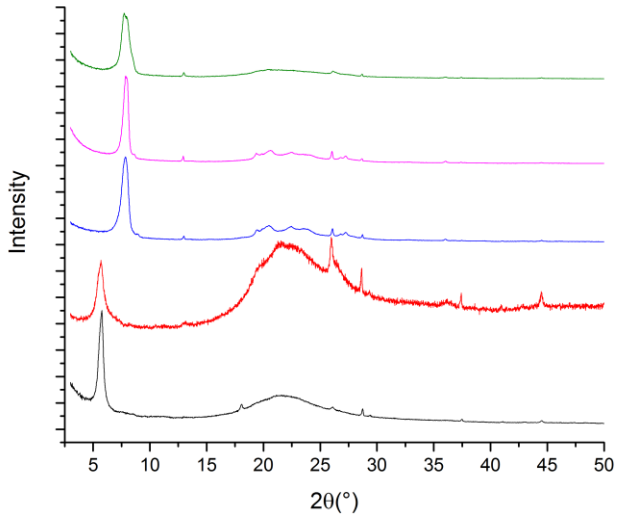

Figure 7.42 Shows a comparison of the PXRD patterns of untreated SAZ-1P (green), SAZ-1P treated with 50 wt. % choline chloride/hydroxide solution with concentrations of 0.5 M hydroxide after 5hrs (pink) and 16 hrs (blue), 2 M hydroxide after 5 hrs (red) and 1.3 M hydroxide after 5hrs (black).

As the increased amorphous content was undesirable it was hoped that by using a mixture of choline chloride and hydroxide rather than a wholly 50 wt. % choline hydroxide solution, the zeolite layers could still be shifted, while minimizing the dissolution effects of the hydroxide solution. Initial PXRD patterns of SAZ-1P layers treated under different

choline concentrations indeed showed this trade-off between the rate of dissolution and the shifting of layers (Figure 7.42). It was found that a 50 wt. % solution of choline chloride/hydroxide with 0.5 M concentration of hydroxide ions was too weak to cause the desired shift in the layers as the main 200 peak remained at 7.9 ° 2θ(*), even after stirring at room temperature for an additional 16 hours. It was also shown that higher concentrations of choline hydroxide (2 M) were too much and led to dissolution of the zeolite and the undesirable increase in amorphous character. It was found that a concentration of choline hydroxide between these values (1.3 M) was suitable and facilitated the movement of the 200 peak to the lower 2θ values, while minimising the dissolution of the structure. The resultant SAZ-1PS showed the characteristic movement of the 200 peak and the loss of the 400 peak. All while displaying a less amorphous character between the 15 ° and 30 ° 2θ values. This concentration was then used as the standard procedure for the formation of SAZ-1PS (section 7.3.3.10).

7.4.8.2 Formation of SAZ-2S and SAZ-3S

With the successful formation of SAZ-1PS the synthesis of SAZ-2S and SAZ-3S was carried out per that stated in Sections 7.3.3.11 and 7.3.3.12. It was hoped that by using similar procedures on SAZ-1PS, as those used to produce SAZ-2 and SAZ-3 from SAZ-1P. It would be possible to form the same interlayer connections between the layers (direct O-linkages and *s4r* linkages respectively). But as these layers are shifted with respect to one another this would produce a more strained 'high energy' structure in a similar manner to the formation of IPC-9 and IPC-10.[12] Initial PXRD patterns of these structures showed that they were quite different to their sister zeolites (Figure 7.43).

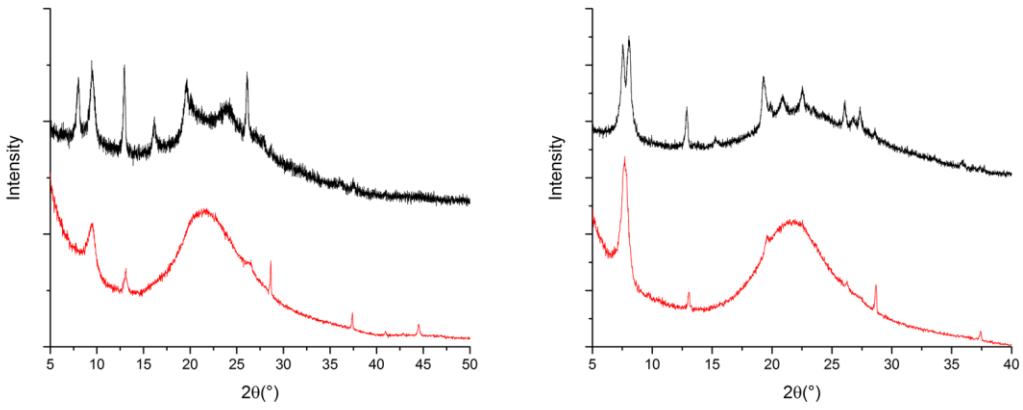

Figure 7.43 Shows PXRD patterns comparing the unshifted (black) and shifted (red) SAZ-2 (left) and SAZ-3 (right).

The most notable issue with regards to the PXRD pattern was the increase in amorphous character with the large humps seen between 17-30° 2θ. This showed that even with the adapted choline hydroxide procedure the final resultant materials were still highly amorphous. This amorphous character may also be indication of the high degree of disorder in these two shifted materials compared with their unshifted sister zeolites.

SEM and EDX analysis of the samples also confirmed the increasingly amorphous character of the materials after contact with choline hydroxide (Figure 7.44).

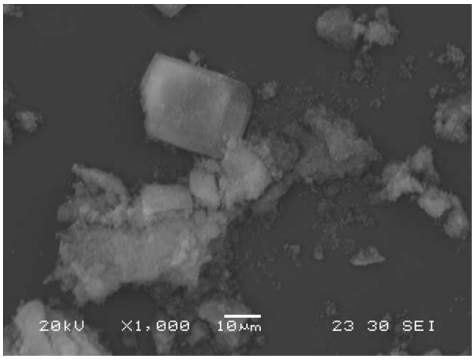

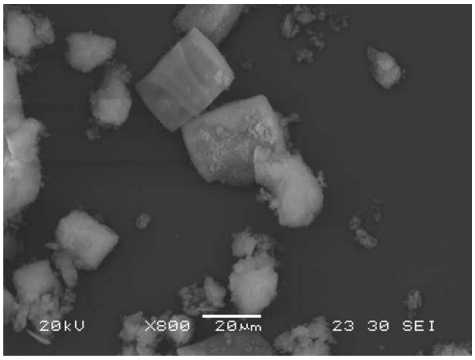

Element Analysis (Atomic percent)

Spectrum	O	Si	Ge	Total
1	77.05	22.61	0.34	100
2	73.22	26.67	0.10	100
3	75.72	24.11	0.17	100
4	78.44	21.35	0.21	100
5	80.03	19.86	0.12	100
Average	76.89	22.92	0.19	

Element Analysis (Atomic percent)

Spectrum	O	Si	Ge	Total
1	77.05	22.61	0.34	100
2	73.22	26.67	0.10	100
3	75.72	24.11	0.17	100
4	78.44	21.35	0.21	100
5	80.03	19.86	0.12	100
Average	76.89	22.92	0.19	

Figure 7.44 Shows the SEM and EDX analysis for SAZ-2S (left) and SAZ-3S (right).

Such results confirmed that even with the reduced concentration of hydroxide used, the material still underwent a severe amount of degradation. Such behaviour is typical for zeolites under alkaline conditions. The increased surface area of the hydrolysed material would lead to an increased rate of degradation compared to other zeolites. Also, the lack of counterions in the framework is also known to lead to the increased instability of zeolites to alkaline conditions.[39]

Computational modelling showed some interesting results. SAZ-2S showed a similar lack of disorder as seen in the SAZ-2 structure caused by the presence of just O-linkages between the layers. This minimises the pathways for much of the disorder seen in the SAZ-1 structures. The shifting SAZ-2 layers resulted in the formation of 8-ring 1-dimensional channels compared with the 10-ring 1-dimensioanl channels seen in unshifted SAZ-2 (Figure 7.45).

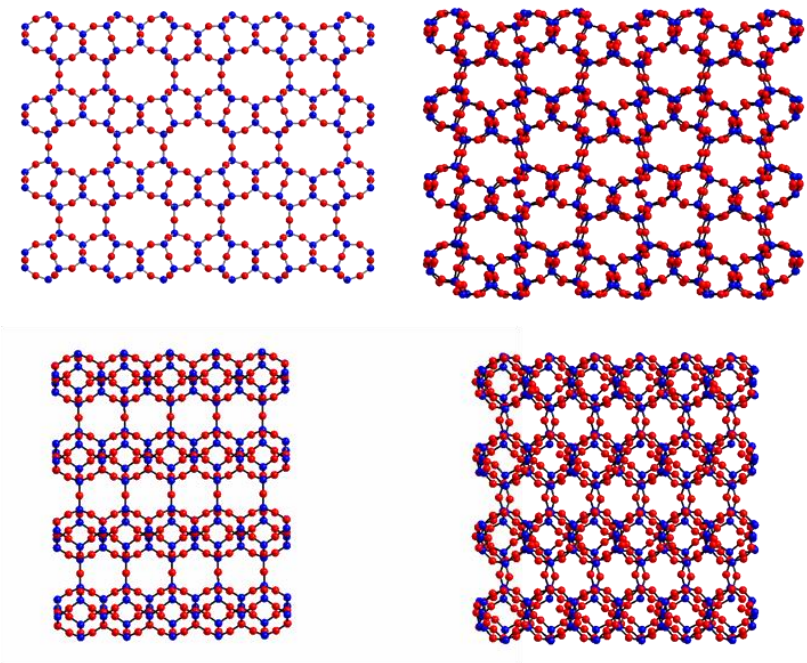

Figure 7.45 Shows the SAZ-2 (left) and SAZ-2S (right) structures. When viewed along the 10-ring or 8-ring channels (top) or along the 6-ring channels(bottom).

This does suggest that the degree of disorder seen in the PXRD pattern is most likely due to the procedure, perhaps due to dissolution of the structure or the inefficiency of the procedure to produce the shifted material in a pure form.

When the PXRD pattern of SAZ-2S was compared to the generated PXRD pattern (Figure 7.46). They seemed to suggest that the material was closely related to the structure, however there is a suggestion that the material has suffered from a lack of ordering of the layers.

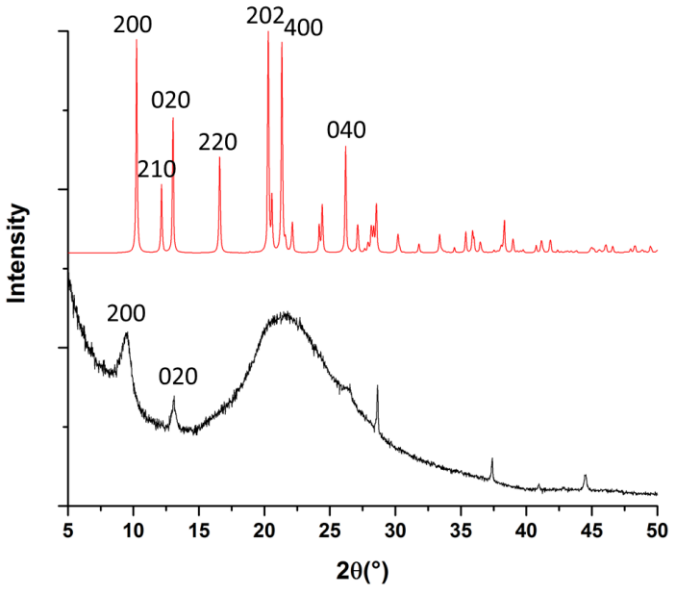

Figure 7.46 Shows the generated (red) and experimental (black) PXRD patterns for SAZ-2S. Some of the important reflections discussed are labelled.

In fact, in a similar manner to that seen with the hydrolysed material the peaks observed are those that remain unaffected by the disorder in the [100] direction. As expected the 200 peak corresponding the interlayer reflection dominates at 9.75 ° 2θ. The only clearly observed peak is the 020 peak at 13.09° 2θ. Most of the peaks expected in the generated PXRD pattern are unobserved. This is perhaps a symptom of disorder in the structure as the peaks missing correspond to reflections that have non-zero h values. This includes the (210), (202) and the (400), this therefore suggests that the SAZ-2S structure was not particularly well ordered.

It was necessary therefore to check that the reassembly step had indeed been a success and ascertain if the new daughter zeolite was indeed a fully connected zeolite. To this end ^{29}Si MAS NMR was used (Figure 7.47).

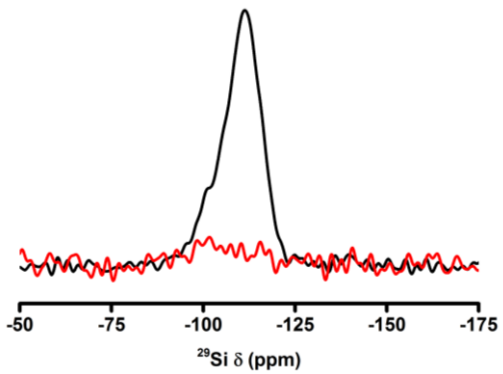

Figure 7.47 Shows the ^{29}Si MAS NMR (black) and {^{1}H} ^{29}Si cross-polarisation MAS NMR (red) spectra of SAZ-2S. SAZ-2S shows a large number of Q^4 sites and a negligible number of Q^3 sites. This indicates that SAZ-1PS had been successfully fully reconnected to form a true zeolite, despite the disorder seen in the PXRD pattern.

The results of the MAS ^{29}Si NMR clearly indicated that the SAZ-2S structure contained wholly Q^4 sites (~ -110 ppm). Indicating that SAZ-2S was a 'true zeolite' as far as the reassembly step had formed a fully connected zeolite even though the PXRD patterns showed a severe amount of disorder in the material.

The disorder in the SAZ-3S material was even more complex than SAZ-2S. Firstly just looking at the ^{29}Si MAS NMR data (Figure 7.48) SAZ-3S showed a far more disordered array of Si sites in its structure. SAZ-3S showed a much larger number of Q^3 and Q^2 sites (~ -100 ppm and -90 ppm respectively) as well as the expected Q^4 sites (~ -110 ppm). This is most likely due to the interlayer silica columns in between the layers, introduced by DEDMS, being unable to fully connect in an organised fashion to form perfectly order *s4r* linkages between the layers.

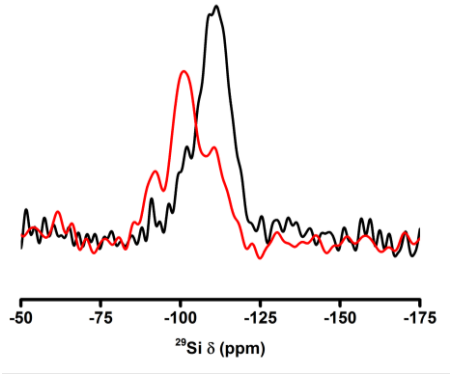

Figure 7.48 Shows the ^{29}Si MAS NMR (black) and {^{1}H} ^{29}Si cross-polarisation MAS NMR (red) spectra of SAZ-3S. SAZ-3S shows a large number of Q^4 sites with also a large number of Q^3 and Q^2 sites. This indicates that silica columns formed by the introduction of DEDMS, were not able to connect together in an organised fashion to form *s4r* linkages between the layers.

A similar situation was seen to a much lesser extent for the formation of the original SAZ-3 material (Figure 7.31).

By looking at the generated structures of SAZ-3S, the degree of disorder was further highlighted (Figure 7.49). In comparison to SAZ-2S, where only one structure was possible with a shift in the layers, and the SAZ-3 structure, where 4 possible arrangements of the *s4r* linkages were possible, the SAZ-3S structure showed 12 possible arrangements. This was due to the presence of inter- and intra-layer disorder. The intralayer disorder results from the *s4r* linkages in the same layer being disordered in not just the 10-ring direction (like SAZ-3 and SAZ-1) but also due to the shifting of the layers in the 12-ring direction. The interlayer disorder is a consequence of disorder of the *s4r* linkages in one layer in comparison to the next layer as they are unable to influence their orientation.

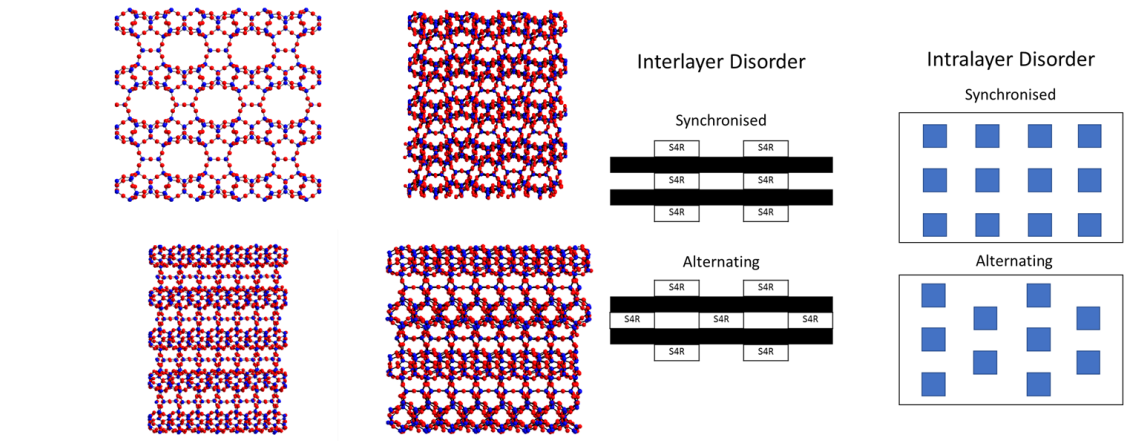

Figure 7.49 The structures of SAZ-3 and the SAZ-3S (left) are shown with a simplified model of the interlayer and intralayer disorder possible (right). In the case of SAZ-3 there is no disorder seen in the 12-ring direction (top left), while in the 10-ring direction there is both interlayer disorder (alternating running up the page) and intralayer disorder (running alternating into the page). In comparison SAZ-3S (right) has both inter- and intra-layer disorder in the 12-ring direction (top right) and the 10-ring direction (bottom right). Si atoms are shown in blue and oxygen atoms in red.

These structures are highly idealised assuming that all the Si columns are successfully connected with each other, to form the *s4r* linkages, during the reassembly step.

Shifting the layers in SAZ-3PS makes it even harder for these connections to be as ordered as seen before. Without the ability to discern which of these possible 12 models it is best to use for the disorder it is harder to compare the generated PXRD pattern with the experimental to ascertain if a structure is favoured.

It is therefore not clear if the SAZ-3S structure has indeed been made. It is clear from the PXRD that a different structure has been formed compared to the original SAZ-3 structure. However, the degree of disorder in the structure makes it impossible to accurately ascertain if it is indeed correct. It seems that SAZ-3S has not just inherited the disorder that was originally associated with the parent SAZ-1 zeolite, but has also developed its own, due to the shifting of the layers relative to each other. However, another suggestion could be that the layers are simply connected without sufficient ordering in a similar fashion to IPC-1 and cannot be conclusively proven to be the shifted structure.[40]

Unlike **UTL** and the formation of IPC-9 and IPC-10, SAZ-1 seems somewhat handicapped in being able to form these higher energy structures. **UTL**'s success stems from the clear distinct silanol quadruplets that provide for the well-ordered formation of linkages between the layers. These well-ordered quadruplets are still defined in the shifted IPC-1P precursor for IPC-9 and IPC-10.[12] SAZ-1 on the other hand does not have as well ordered silanol quadruplets and the shifting of the layers, makes it even harder to distinguish between them. This perhaps suggests that the methodology has produced 'unfeasible'

daughter zeolites, but without the necessary ordering required to definitively prove it. This means that to successfully form and conclusively prove the presence of an 'unfeasible' zeolite from SAZ-1 other methods may have to be investigated. It is also worth noting that this disorder is an inherent issue with the ADOR process and getting good crystallinity is extremely difficult.

7.5 Conclusions

The work conducted throughout this chapter has shown that although the ADOR process is currently limited it still has huge potential for increasing the number of frameworks that can be synthesised. The requirements for monodirectional Ge-dominated *d4r* separating stable dense silicate layers means that very few already known zeolite frameworks can undergo this process. To overcome these issues, a hydrothermal synthesis was conducted with key design principles considered to optimise the synthesis of a new germanosilicate as a candidate for the ADOR process.

This was achieved through the design of a new bulky SDA (1-methyl-3-(naphthalen-1-ylmethyl)-imidazolium hydroxide). Investigations into the synthesis of a new zeolite showed the impact of water content, fluoride content and silica source. It was shown that **LTA** was a competing phase with the new phase SAZ-1. **LTA** was shown to be particularly prevalent when TEOS was used as the silica source. This was due to the rate of saturation and the type of silica species that would then be present at the point of crystallisation. When using TEOS, the saturation rate was quicker. During crystallisation of the zeolite the dominant silica species in solution were the smaller $[SiO_2(OH)_2]_2^-$ or $[SiO(OH)_3]^-$, that had formed in the alkaline conditions before the addition of fluoride. The slower saturation rate of fumed silica resulted in the dominant silica species present being dimers and four-membered rings,[28] typically formed under less alkaline conditions, which favoured the formation of the more siliceous SAZ-1.

An ideal synthesis for SAZ-1 was found, using the right combination of silica source, water, and fluoride content, under the right hydrothermal conditions to produce a at the time unknown zeolite framework called SAZ-1. Analysis of this framework structure showed a close relationship to the previously known germanosilicate **UTL**. SAZ-1 was shown to have mono-directional *d4r* separated by dense *fer*-like silicate layers (*cfi*). The Ge content of the zeolite indicated the presence of a large enough amount of Ge to dominate the *d4r*. These Ge-dominated *d4r* were also easily accessible by the 14 x 10 channels, like the 14 x 12 channels already seen in **UTL**. STEM imaging also confirmed this structure while showing

the disorder of the 10-ring channels. This was due to the smaller distance between potential *d4r* making the *d4r* sites less well defined, which resulted in intra- and inter-layer disorder of the *d4r*. It perhaps also leads to the formation of some marbling/twinning of the crystals as seen in the STEM images. These early indications showed that new zeolite SAZ-1, despite some difficulties, would be an ideal candidate for the ADOR process, as it displayed the classic characteristics for an ADORable zeolite including: dense silicate layer, connected by Ge-dominated *d4r* that can be easily accessed through large pores.

The use of weak acid was strong enough to remove the Ge-dominated *d4r* and form the layered precursor SAZ-1P. The preservation of crystal morphology and the removal of Ge was confirmed by SEM/EDX analysis. PXRD results showed the dominance and movement of the 010 peaks, corresponding to the interlayer reflection. The removal of the Ge-dominated *d4r* resulted in the formation of silanol groups in between the layers, as confirmed by the many Q^3 sites observed in the ^{29}Si MAS NMR.

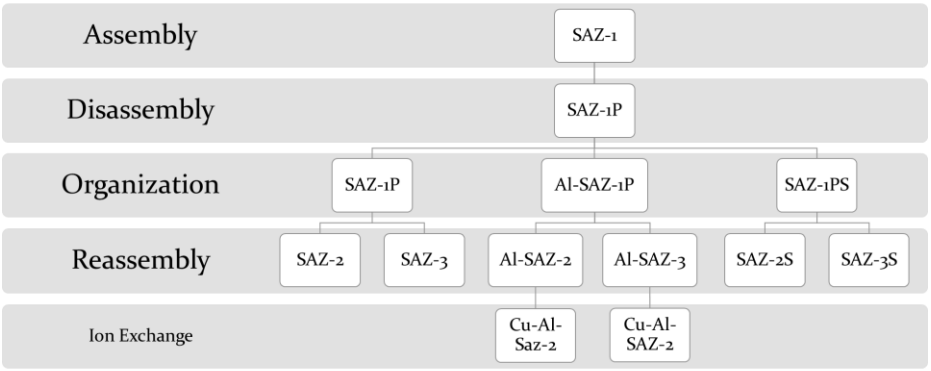

Figure 7.50 Shows the SAZ-1 family included in this chapter. This includes the original newly assembled SAZ-1, the product of its disassembly SAZ-1P, and the multitude of intermediates and daughter zeolites produced by the subsequent organisation and reassembly steps.

It was then shown that using different methods it was possible to produce 6 different daughter zeolites (Figure 7.50). Manipulation of the layers with octylamine and DEDMS produced two new daughter zeolites SAZ-2 and SAZ-3, that had an isoreticular relationship to the parent germanosilicate SAZ-1. Both still possess the *cfi*-type layers, but the interlayer connection was modified with SAZ-2 containing direct O-linkages between the layers, and SAZ-3 containing *s4r* linkages between the layers. These smaller interlayer linkages resulted in a reduced pore size from 14- (SAZ-1) to 12- (SAZ-3) and 10-ring (SAZ-2). This change in pore size was characterised through comparison of the experimental PXRD patterns with the predicted ones, BET surface area, and the use of HRSTEM images. ^{29}Si MAS NMR of SAZ-2 and SAZ-3 showed that SAZ-2 had wholly Q^4 sites and so lost the

disorder associated with the *d4r* in the parent SAZ-1. This was due to formation of direct O-linkages connecting the layers, removing the requirement for ordering of silanol quadruplets. However, SAZ-3 showed the presence of some Q^3 and Q^2 sites in the ^{29}Si MAS NMR. This seemed to suggest that SAZ-3 had inherited this disorder from the parent germanosilicate, the silanol quadruplets are less well defined in SAZ-1P compared to IPC-1P due to their proximity in the [001] direction. This results in silica columns connecting the layers in the same silanol quadruplet being close to members of other potential quadruplets in the [001] direction. This means that during reassembly some of these silanols condense together incorrectly and are unable to form fully connected *s4r* linkages between the layers.

The formation of two additional daughter zeolites could be done through the incorporation of aluminium into the disassembled SAZ-1P structure. This led to the formation of Al-SAZ-2 and Al-SAZ-3 who had the same structure as SAZ-2 and SAZ-3 but the incorporation of aluminium would lead to catalytic activity. The PXRD analysis showed some disorder of these materials compared to their wholly siliceous sister zeolites, most likely as a result of the incorporation of aluminium. EDX and SEM analysis showed the preservation of the crystal morphology and the presence of some aluminium. Catalytic testing showed that these structures could form NO from nitrite, however due to the very small amount of aluminium incorporated into these structures the release profile were relatively poor. Attempts to improve the catalytic activity by incorporation of Cu were unsuccessful, due to the limited incorporation of Al and hence Cu, but also due to the disorder of the structures, leading to the inaccessibility of the Cu by the cysteine molecules.

The final additions to the SAZ-1 family were the shifted series of zeolites. The use of choline hydroxide on the SAZ-1P sample produced a shift in the (200) reflection, corresponding to a movement of the interlayer spacing. The shifting of the layers was also indicated by the loss of the (040) reflection, due to the loss of ordering in this reflection. However, there were issues surrounding the increased amorphous character of the sample, due to the high concentration of hydroxide leading to dissolution of the sample. It was shown that a better sample could be produced with the use of a lower concentration of OH^- by introducing Cl^-, while still shifting the layers. This sample was then used to form SAZ-2S and SAZ-3S, which consisted of the same interlayer linkages as SAZ-2 and SAZ-3, but the shift in the layers produced a slightly different structure. The most successful of these was SAZ-2S. The PXRD pattern showed a close resemblance to the generated PXRD

pattern and ^{29}Si MAS NMR results indicated that the zeolite had been fully reconnected. However, the lack of certain peaks and reflections in the PXRD patterns may indicate that the structure is far more disordered than expected. SAZ-3S was shown to have a different PXRD pattern to SAZ-3 indicating a change in the structure and suggesting that a new material had indeed been made. However, the shifting of the SAZ-1P layers and incorporation of *s4r* linkages between the layers resulted in SAZ-3S not only inheriting the disorder from the parent germanosilicate, but also developing further disorder. As shifting of the layers results in disordering of the layers in the 12-ring direction as well as the 8-ring direction. This was indicated in the ^{29}Si MAS NMR, which showed an even greater number of Q^3 and Q^2 sites compared to SAZ-3. It was clear that while the manipulation of the layers to produce 'unfeasible' zeolite was possible, it is perhaps harder to achieve this with SAZ-1P compared with IPC-1P due to the inherent disorder in the structure.

This chapter has shown that with the right design principles it is possible to design and synthesise a new ADORable zeolite, with hydrothermal synthesis, and then propagate that synthesis using the ADOR process to produce a family of new materials with an isoreticular relationship to one another.

7.6 Future Work

Future work can be divided into two components: 1) Further investigations into the SAZ-1 family and 2) Further investigations into the formation of new ADORable zeolites with newly designed organic SDAs.

The shifting of the SAZ-1P layers with the use of choline hydroxide showed that these layers could be manipulated in a similar manner as the IPC-1P layers. However, the degree of disorder and amorphous character seen in the resultant materials indicates that the syntheses of these shifted materials need to be refined. The use of other swelling agents to induce a shift in the layers may provide an avenue for better ordering of the layers.

The success of 1-methyl-3-(naphthalen-1-ylmethyl)-imidazolium hydroxide would suggest that further investigations could involve modifying the SDA to see the impact on the synthesis. The use of other ammonium cations instead of imidazolium and the use of di-substituted naphthalene could be investigated.

7.7 References

(1) Baerlocher, C.; McCusker, L. B. Database of Zeolite Structures http://www.iza-

structure.org/databases/.

(2) Cubillas, P.; Anderson, M. W. Synthesis Mechanism: Crystal Growth and Nucleation. In *Zeolites and Catalysis: Synthesis, Reactions and Applications*; Wiley-VCH Verlag GmbH & Co. KGaA: Weinheim, Germany, 2010; Vol. 1, pp 1–55.

(3) Blatov, V. A.; Ilyushin, G. D.; Proserpio, D. M. The Zeolite Conundrum: Why are There so Many Hypothetical Zeolites and so Few Observed? A Possible Answer from the Zeolite-Type Frameworks Perceived as Packings of Tiles. *Chem. Mater.* **2013**, *25* (3), 412–424.

(4) Li, X.; Deem, M. W. Why Zeolites Have So Few Seven-Membered Rings. *J. Phys. Chem. C* **2014**, *118* (29), 15835–15839.

(5) Earl, D. J.; Deem, M. W. Toward a Database of Hypothetical Zeolite Structures. *Ind. Eng. Chem. Res.* **2006**, *45* (16), 5449–5454.

(6) Foster, M. D.; Simperler, A.; Bell, R. G.; Friedrichs, O. D.; Paz, F. A. A.; Klinowski, J. Chemically Feasible Hypothetical Crystalline Networks. *Nat Mater* **2004**, *3* (4), 234–238.

(7) Foster, M. D.; Friedrichs, O. D.; Bell, R. G.; Paz, F. A. A.; Klinowski, J. Chemical Evaluation of Hypothetical Uninodal Zeolites. *J. Am. Chem. Soc.* **2004**, *126* (31), 9769–9775.

(8) Pophale, R.; Cheeseman, P. A.; Deem, M. W. A Database of New Zeolite-like Materials. *Phys. Chem. Chem. Phys.* **2011**, *13* (27), 12407–12412.

(9) Morris, R. E. Ionothermal Synthesis of Zeolites and Other Porous Materials. In *Zeolites and Catalysis: Synthesis, Reactions and Applications*; Wiley-VCH Verlag GmbH & Co. KGaA: Weinheim, Germany, 2010; Vol. 1, pp 87–105.

(10) Eliášová, P.; Opanasenko, M.; Wheatley, P. S.; Shamzhy, M.; Mazur, M.; Nachtigall, P.; Roth, W. J.; Morris, R. E.; Čejka, J. The ADOR Mechanism for the Synthesis of New Zeolites. *Chem. Soc. Rev.* **2015**, *44* (20), 7177–7206.

(11) Roth, W. J.; Nachtigall, P.; Morris, R. E.; Wheatley, P. S.; Seymour, V. R.; Ashbrook, S. E.; Chlubná, P.; Grajciar, L.; Položij, M.; Zukal, A.; et al. A Family of Zeolites with Controlled Pore Size Prepared Using a Top-Down Method. *Nat. Chem.* **2013**, *5* (7), 628–633.

(12) Mazur, M.; Wheatley, P. S.; Navarro, M.; Roth, W. J.; Položij, M.; Mayoral, A.; Eliášová, P.; Nachtigall, P.; Čejka, J.; Morris, R. E. Synthesis of "Unfeasible" Zeolites. *Nat. Chem.* **2015**, *8* (1), 58–62.

(13) Chlubná-Eliášová, P.; Tian, Y.; Pinar, A. B.; Kubů, M.; Čejka, J.; Morris, R. E. The Assembly-Disassembly-Organization-Reassembly Mechanism for 3D-2D-3D Transformation of Germanosilicate IWW Zeolite. *Angew. Chemie* **2014**, *126* (27), 7168–7172.

(14) Kasneryk, V.; Shamzhy, M.; Opanasenko, M.; Wheatley, P. S.; Morris, S. A.; Russell, S. E.; Mayoral, A.; Trachta, M.; Čejka, J.; Morris, R. E. Expansion of the ADOR Strategy for the Synthesis of Zeolites: The Synthesis of IPC-12 from Zeolite UOV. *Angew. Chemie* **2017**, *129* (15), 4388–4391.

(15) Morris, S. A.; Bignami, G. P. M.; Tian, Y.; Navarro, M.; Firth, D. S.; Čejka, J.; Wheatley, P. S.; Dawson, D. M.; Slawinski, W. A.; Wragg, D. S.; et al. In Situ Solid-State NMR and XRD Studies of the ADOR Process and the Unusual Structure of Zeolite IPC-6. *Nat. Chem.* **2017**, *9*, 1012–1018.

(16) Zones, S. I.; Hwang, S. J.; Elomari, S.; Ogino, I.; Davis, M. E.; Burton, A. W. The Fluoride-Based Route to All-Silica Molecular Sieves; a Strategy for Synthesis of New Materials Based upon Close-Packing of Guest-Host Products. *Comptes Rendus Chim.* **2005**, *8* (3–4), 267–282.

(17) Yu, J. Chapter 3 - Synthesis of Zeolites. In *Introduction to Zeolite Science and Practice*; Čejka, J., Corma, A., Bekkum, H. van, Schüth, F., Eds.; Elsevier, 2007; Vol. 168, pp 39–103.

(18) Burton, A. W.; Zones, S. I. Chapter 5 - Organic Molecules in Zeolite Synthesis: Their Preparation and Structure-Directing Effects. In *Studies in Surface Science and Catalysis*; Čejka, J., Corma, A., Bekkum, H. van, Schüth, F., Eds.; Elsevier, 2007; Vol. 168, pp 137–179.

(19) Lobo, R. F.; Zones, S. I.; Davis, M. E. Structure-Direction in Zeolite Synthesis. *J. Incl. Phenom. Mol. Recognit. Chem.* **1995**, *21* (1–4), 47–78.

(20) Shvets, O. V; Kasian, N.; Zukal, A.; Pinkas, J.; Čejka, J. The Role of Template Structure and Synergism Between Inorganic and Organic Structure Directing Agents in the Synthesis of UTL Zeolite. *Chem. Mater.* **2010**, *22* (11), 3482–3495.

(21) Chen, F.-J.; Xu, Y.; Du, H.-B. An Extra-Large-Pore Zeolite with Intersecting 18-, 12-, and 10-Membered Ring Channels. *Angew. Chemie Int. Ed.* **2014**, *53* (36), 9592–9596.

(22) Reed, T. B.; Breck, D. W. Crystalline Zeolites. II. Crystal Structure of Synthetic Zeolite, Type A. *J. Am. Chem. Soc.* **1956**, *78* (23), 5972–5977.

(23) Wilson, S. T.; Lok, B. M.; Messina, C. A.; Cannan, T. R.; Flanigen, E. M. Aluminophosphate Molecular Sieves: A New Class of Microporous Crystalline Inorganic Solids. *J. Am. Chem. Soc.* **1982**, *104* (4), 1146–1147.

(24) Simmen, A.; Patarin, J.; Baerlocher, C. Rietveld Refinement of F^- containing GaPO4-LTA. In *Proc. 9th Int. Zeolite Conf.*; Proc. 9th Int. Zeolite Conf., 1993; pp 433–440.

(25) Corma, A.; Rey, F.; Rius, J.; Sabater, M. J.; Valencia, S. Supramolecular Self-Assembled Molecules as Organic Directing Agent for Synthesis of Zeolites. *Nature* **2004**, *431* (7006), 287–290.

(26) Strohmaier, K. G. Synthesis Approaches. In *Zeolites and Catalysis: Synthesis, Reactions and Applications*; Wiley-VCH Verlag GmbH & Co. KGaA: Weinheim, Germany, 2010; Vol. 1, pp 57–86.

(27) The pH-Value and its Importance for the Crystallization of Zeolites http://www.iza-online.org/synthesis/VS_2ndEd/pH.htm (accessed Jan 31, 2017).

(28) Guth, J. L.; Caullet, P.; Seive, A.; Patarin, J.; Delprato, F. New Mobilizing and Templating Agents in the Synthesis of Crystalline Microporous Solids. In *Guidelines for Mastering the Properties of Molecular Sieves*; Barthomeuf, D., Derouane, E. G., Hölderich, W., Eds.; Springer Science & Business Media, 2013.

(29) O'Brien, M. G.; Beale, A. M.; Kuipers, B. W. M.; Erné, B. H.; Lewis, D. W.; Catlow, C. R. A. Role of Germanium on the Nucleation and Growth of Zeolite A from Clear Solutions as Studied by in Situ Small-Angle X-ray Scattering, Wide-Angle X-ray Scattering, and Dynamic Light Scattering. *J. Phys. Chem. C* **2009**, *113* (43), 18614–18622.

(30) Liu, X.; Ravon, U.; Tuel, A. Fluoride Removal from Double Four-Membered Ring (D4R) Units in As-Synthesized Ge-Containing Zeolites. *Chem. Mater.* **2011**, *23* (22), 5052–5057.

(31) Earl, D. J.; Burton, A. W.; Rea, T.; Ong, K.; Deem, M. W.; Hwang, S.-J.; Zones, S. I.

Synthesis and Monte Carlo Structure Determination of SSZ-77: A New Zeolite Topology. *J. Phys. Chem. C* **2008**, *112* (24), 9099–9105.

(32) Gao, Z.-H.; Chen, F.-J.; Xu, L.; Sun, L.; Xu, Y.; Du, H.-B. A Stable Extra-Large-Pore Zeolite with Intersecting 14- and 10-Membered-Ring Channels. *Chem. Eur. J.* **2016**, *22* (40), 14367–14372.

(33) Kang, J. H.; Xie, D.; Zones, S. I.; Smeets, S.; McCusker, L. B.; Davis, M. E. Synthesis and Characterization of CIT-13, a Germanosilicate Molecular Sieve with Extra-Large Pore Openings. *Chem. Mater.* **2016**, *28* (17), 6250–6259.

(34) Yoshikawa, M.; Wagner, P.; Lovallo, M.; Tsuji, K.; Takewaki, T.; Chen, C.-Y.; Beck, L. W.; Jones, C.; Tsapatsis, M.; Zones, S. I.; et al. Synthesis, Characterization, and Structure Solution of CIT-5, a New, High-Silica, Extra-Large-Pore Molecular Sieve. *J. Phys. Chem. B* **1998**, *102* (37), 7139–7147.

(35) Le Bail, A. Whole Powder Pattern Decomposition Methods and Applications: A Retrospection. *Powder Diffr.* **2005**, *20* (4), 316–326.

(36) Shamzhy, M. V.; Eliášová, P.; Vitvarová, D.; Opanasenko, M. V.; Firth, D. S.; Morris, R. E. Post-Synthesis Stabilization of Germanosilicate Zeolites ITH, IWW, and UTL by Substitution of Ge for Al. *Chem. - A Eur. J.* **2016**, *22* (48), 17377–17386.

(37) Russell, S. E.; González Carballo, J. M.; Orellana-Tavra, C.; Fairen-Jimenez, D.; Morris, R. E. A Comparison of Copper and Acid Site Zeolites for the Production of Nitric Oxide for Biomedical Applications. *Dalt. Trans.* **2017**, *46* (12), 3915–3920.

(38) Mazur, M.; Chlubná-Eliášová, P.; Roth, W. J.; Čejka, J. Intercalation Chemistry of Layered Zeolite Precursor IPC-1P. *Catal. Today* **2014**, *227*, 37–44.

(39) Verboekend, D.; Keller, T. C.; Milina, M.; Hauert, R.; Pérez-Ramírez, J. Hierarchy Brings Function: Mesoporous Clinoptilolite and L Zeolite Catalysts Synthesized by Tandem Acid-Base Treatments. *Chem. Mater.* **2013**, *25* (9), 1947–1959.

(40) Roth, W. J.; Shvets, O. V.; Shamzhy, M.; Chlubná, P.; Kubů, M.; Nachtigall, P.; Čejka, J. Postsynthesis Transformation of Three-Dimensional Framework into a Lamellar Zeolite with Modifiable Architecture. *J. Am. Chem. Soc.* **2011**, *133* (16), 6130–6133.

8 Conclusions and Future Work

8.1 Conclusions

To expand the frontiers of the ADOR process investigations were conducted into the incorporation of new elements in the already known ADORable zeolite **UTL**. The incorporation of Al and P between the IPC-1P layers resulted in the formation of a zeolite-AlPO hybrid. The material was shown to reform the layered material IPC-1P under acidic conditions. This indicated that the species in between the layers of the zeolite-AlPO hybrid were unstable, which is atypical of the interconnections seen between the layers of other daughter zeolites from the ADOR process. Further analysis of the material confirmed the zeolite-AlPO hybrid contained fully reconnected layers (by *s4r* linkages) with Al and P present in the material. These Al and P species were shown to be the same as those typically seen in AlPOs. Attempts to enrich the material enough to enable 2D correlation experiments between Si and P could produce an increase in signal, but not to the degree required for 2D correlations experiments. It was therefore not possible to conclusively prove the presence of Si-O-P bonds. However, the increased instability of the materials and the presence of Al and P in the material were strong indications of the formation of such bonds.

Attempts to expand the ADOR process further were then made by applying the ADOR process to other already known germanosilicate frameworks. The candidates were selected based on their chemical and framework properties that indicated they had the potential to undergo the ADOR process. It was found that some of the candidates selected were unable to undergo the disassembly process due to their high germanium content (ITQ-33 and NUD-1). Attempts to vary the synthesis of these structures, and decrease the germanium content, were unsuccessful. These frameworks were therefore deemed unsuitable for the ADOR process. Other frameworks were however more successful. The germanosilicates ITQ-38 and IM-20 were shown (with some slight alterations in their Ge content) to be easily disassembled to form a layered material. These layered materials were shown to be more unstable compared to the more ideally behaved ADORable zeolite **UTL**. Both layered materials degraded rapidly under the acidic conditions typically used to self-organise the layers, indicating that these layers were more unstable. This was most likely due to their lower density, the presence of some Ge in the layers and the penetration of these layer by large pores. The materials were shown to undergo the organisation and reassembly steps with octylamine and DEDMS. But these materials tended to result in less

crystalline daughter zeolites, compared to those derived from **UTL**. The reasoning for this unsatisfactory performance was deemed to be a combination of the instability of the layers and the orientation of the interlayer silanols. Both of the layered materials derived from ITQ-38 and IM-20 lacked clearly defined silanol quadruplets. This was because some silanols in one quadruplet were shown to be closer to silanols in other quadruplets than to those within their own quadruplets. This lack of defined silanol quadruplets makes it harder to organise the layers in an ordered enough fashion, to result in a successful reassembly step, and form a fully-connected true zeolite framework. Such results highlighted that, even with the criteria used to select these candidates, there are still many factors that can play a role in the ADOR process and increase complications. Each step of the ADOR process requires specific framework properties to be successful and it is hard for a framework to fulfil the requirements for each step.

With the unsuccessful attempt to use the ADOR process on already known germanosilicate frameworks. The next logical step involved the use of new SDAs to form new germanosilicates to be considered as new candidates for the ADOR process. The first of these attempts was to investigate the use of a group of SDAs with a biphenyl-backbone and different terminal ammonium cations. The potential of this family of SDAs was highlighted by their easy synthesis and the array of cations available, by varying the ammonium cations. This could provide a huge array of different SDAs that would require very different frameworks to form to accommodate their different sizes. The use of different standard synthesis conditions highlighted the interplay between different synthesis components. The presence of fluoride and germanium seemed to override the directing effect of the SDAs and resulted in the formation of the **BEC** framework, which has a high concentration of *d4r*. The use of neither Ge or fluoride resulted in an amorphous material, highlighting the need for germanium or fluoride for the synthesis to be a success. The use of just germanium and silicon with the Biphy-TEA SDA resulted in the successful synthesis of an ADORable zeolite, the already known **UTL**. This indicated that it was possible to design a synthesis to produce an ADORable zeolite, it was just unfortunate that the framework formed was already known. The biphenyl-TEA SDA is now one of the more than 20 SDAs that are known to produce **UTL**, showing that the formation of **UTL** is perhaps more a result of space-filling rather than true templating behaviour. During these syntheses, it was however noted that the biphenyl SDAs showed some non-ideal behaviour. This was due to the tendency of the biphenyl SDAs to degrade under typical hydrothermal conditions.

With the relatively successful use of the biphenyl-based SDAs other SDAs were investigated. The naphthalene-imidazolium based SDA was designed to specifically target the formation of a zeolite suitable for the ADOR process. The use of this SDA resulted in the formation of the new germanosilicate SAZ-1 (which was developed at the same time as the published CIT-13 and NUD-2 structures). SAZ-1 was shown to contain all the ideal characteristics for an ADORable zeolite. The framework contained dense silicate layers, connected by monodirectional, Ge-dominated *d4r* that were easily accessible by large pores. SAZ-1 was shown to contain some undesirable disorder of the *d4r*, due to the proximity of potential *d4r* sites. This lack of order of the 10-ring channels was noted in the STEM images. SAZ-1 was shown to disassemble in the presence of acid to produce a layered material SAZ-1P. This layered material was then able to undergo organisation and reassembly to form SAZ-2 and SAZ-3. Both daughter zeolites were related to SAZ-1 as they have the same layers. But these layers are connected by direct O-linkages and *s4r* linkages respectively. SAZ-2 was shown to be a fully connected 'true' zeolite framework and had not inherited the disorder from its parent germanosilicate. However, SAZ-3 was shown to have inherited the disorder from its parent germanosilicate. The proximity of the silanols resulted in the less-ordered formation of the *s4r* due to some *s4r* being incorrectly orientated to condense and form fully connected *s4r* linkages. SAZ-1 was also able to produce Al-containing daughter zeolites Al-SAZ-2 and Al-SAZ-3, which resulted in the formation of Brønsted acid sites and catalytic activity. The use of choline also resulted in a shifting of the SAZ-1P layers akin to that already seen for the 'unfeasible' zeolites IPC-9 and IPC-10. However, the materials formed were not found to be of suitable quality to conclusively prove the formation of two new 'unfeasible' daughter zeolites, due to the huge degree of disorder introduced by the shifting and partial dissolution of the layers.

8.2 Future Work

This work highlights the potentials and the limitations of the ADOR process. During the brief period since its first identification the ADOR process has led to an explosion of new high silicate zeolite frameworks.

The successful incorporation of Al and P into the IPC-2 structure indicates the potential for the ADOR process to form new frameworks with potentially interesting framework properties. The use of the ADOR process to incorporate other elements including but not exclusively Sn, Co, P and Al in between the layers should be investigated further.

The results and complications arising from the application of the ADOR process to already known zeolites IM-20 and ITQ-38 show that there are many factors that impact on a germanosilicates suitability to undergo the ADOR process. Further work should look at applying the ADOR process to those already known frameworks. This should include those candidates that are deemed non-ideal. It is possible that with the right conditions and intercalating agents these non-ideal layered materials could be successfully organised and reassembled. The requirement for a germanosilicate to form stable silicate layers that can then be easily manipulated means that the already limited number of candidate frameworks has been squeezed. The ADOR process is clearly limited and has now reached a point where new approaches need to be taken if the frontiers are to be advanced further.

The work of particularly Chapters 6 and 7 shows that the ADOR process does not need to rely on the already known frameworks to succeed. With the right design principles traditional hydrothermal synthesis can be used to synthesise new ADORable zeolites. The synthesis can then be propagated to produce new silicate daughter zeolites and greatly increasing the number of new zeolites from just one procedure. The success of the ADOR process will be dependent on the perfect marriage between this relatively new technique and the much older hydrothermal synthesis. Further work should therefore focus on the formation of new SDAs, using these SDAs to synthesise new germanosilicate frameworks, and investigating these germanosilicates for their potential as ADORable zeolites. Despite the instability of the biphenyl-SDAs in Chapter 6 the degree of variation possible by replacement of the terminal ammonium cation seems to provide the greatest variety of species required. The success of the naphthalene based SDA to form SAZ-1 should not be ignored and further investigations should be conducted into variations of this SDA.

With more research into the synthesis of new germanosilicates the number of ADORable candidates will only increase. This will then lead to the formation of more daughter zeolites by the ADOR process and consequently increase the number of known zeolite frameworks. By furthering the ADOR process and using hydrothermal synthesis to produce new zeolites with a manifold destiny it will be possible to advance the frontiers of the ADOR process even further.

9 Appendix

9.1 Single Crystal Data Obtained

General	
Origin	
Code	shelxl
Database dates	
Common name	
Systematic name	
Structural formula	
Analytical formula	
Bibliographic data	
Author(s)	
Publication title	
Citation	
Mineral name	
Compound source	
Structure type	
Creation method	SHELXL-2014/7
Comments	
Phase data	
Formula sum	C15 H16 Ge20 N2 O41 Si20
Formula weight	2893.9 g/mol
Crystal system	orthorhombic
Space-group	C m m m (65)
Cell parameters	a=13.758(6) Å b=27.562(15) Å c=5.108(2) Å
Cell ratio	a/b=0.4992 b/c=5.3958 c/a=0.3713
Cell volume	1936.94(150) $Å^3$
Z	1
Calc. density	2.48079 g/cm^3
Meas. density	
Melting point	
RAll	0.308
RObs	
Pearson code	oC120
Formula type	N4O7
Wyckoff sequence	r2q3p3on2j2ie

Atomic parameters									
Atom	**Ox.**	**Wyck.**	**Site**	**S.O.F.**	**x/a**	**y/b**	**z/c**	**U [$Å^2$]**	
Ge1		4i	m2m	2	1/2	0.7288(4)	1.00000		
Ge2		8p	..m		0.2899(5)	0.6963(3)	1.00000		
Ge3		8q	..m		0.1971(5)	0.6515(3)	1/2		
Ge4		4j	m2m	2	0	0.7091(4)	1/2		
Ge5		16r	1		0.1129(4)	0.5554(2)	0.3081(15)		
O2		8p	..m		0.132(3)	0.5721(16)	0		
O3		4j	m2m	2	0	0.5687(17)	1/2		
O6		8q	..m		0.0905(16)	0.6758(9)	1/2		
O7		4e	..2/m		1/4	3/4	1.00000		
O8		8p	..m		0.4061(17)	0.6972(9)	1.00000		
O9		8n	m..		0	0.7539(12)	0.624(10)		
O10		16r	1		0.2536(15)	0.6658(9)	0.758(4)		
O11		8o	.m.		0.149(4)	1/2	0.398(10)		
O12		8q	..m		0.1832(18)	0.5924(9)	1/2		
O13		8n	m..		1/2	0.7729(15)	1.166(11)		